

Development of a Software for the Failure Modes and Effects Analysis and Reliability Analysis of Satellite Power Generation Systems

Davide Martelli

©ESA/BepiColombo/MTM, CC BY-SA 3.0 IGO

 TU Delft

Together
ahead. **RUAG**

Development of a Software for the Failure Modes and Effects Analysis and Reliability Analysis of Satellite Power Generation Systems

by

Davide Martelli

to obtain the degree of Master of Science
at the Delft University of Technology,
to be defended publicly on Monday February 28, 2022 at 16:00 PM.

Student number: 4555686
Project duration: June 1, 2021 – January 24, 2022
Thesis Committee: Dr. A. Cervone, TU Delft, Committee Chair
M. S. Uludağ, TU Delft, Thesis Supervisor
Ir. K. J. Cowan, TU Delft, Examiner
Dr. M. Pantaleev, RUAG Space, Team Leader Electrical Engineering

This thesis is confidential and cannot be made public until February 28, 2024.

An electronic version of this thesis is available at <http://repository.tudelft.nl/>.

Executive Summary

Motivation

Today, Photovoltaic Arrays (PVA) are the primary power generation source in Satellite Power Generation Systems (SPGS) for Earth-orbiting systems. Their design is a complex system engineering task: in addition to the traditional mechanical and power performance design, the increased cost, complexity, and lifetime requirements of modern space missions have put a strong focus on system-level reliability. As a consequence, a Failure Modes and Effects Analysis (FMEA), as well as a reliability analysis, is crucial for the design and production of a compliant and fault-tolerant system. This drives the interest in the development of a software in support of the aforementioned activities. The research is carried out in collaboration with RUAG Space, Zürich.

Research Questions and Objectives

The research aims to answer the following research questions:

-
- What are the effects of potential foreseen failures on solar arrays performance?
 - How does the solar array regulator react to the failures?
 - What are the most relevant factors that influence the reliability of a solar array?
-

These constitute a solid framework for the formulation of the research objectives, which drives the methodology followed in this study:

-
- To simulate the electrical performance of the selected solar array, under both healthy and faulty conditions, by implementing a suitable modeling software.
 - To estimate the system reliability by integrating the software with an algorithm that is able to translate the implemented electrical model into a reliability model.
 - To assess the impact of identified factors on the system reliability and provide recommendations for reliability improvement by performing an automated sensitivity analysis run by the software.
-

Research Methodology

The research methodology involves the development of a software able to perform the FMEA and reliability analysis of a solar array. These activities require the implementation of two different models: an electrical model and a reliability model. The research begins with the definition of the electrical modeling approach of the solar array, whose configuration may be defined through the graphical user interface of the software. As requested by the Company, both the single- and double-diode model, two of the most common models for the performance simulation of solar cells, are implemented, with the capability of managing any operating conditions. The solar cells are then series- and parallel-connected according to the defined configuration to build the PVA. As the FMEA extends to the investigation of the solar array regulator (SAR) behavior when subjected to failure, this subsystem is also involved in the modeling process. The current version of the software is limited to the implementation of two SARs: the Sequential Switching Shunt Regulator (S3R) and the Maximum Power Point Tracker (MPPT). The first topology implies a Direct Energy Transfer (DET) method and a regulated bus and it is mainly adopted for GEO missions. The MPPT employs a DC/DC converter to decouple the PVA from the bus and the former is forced to operate at its maximum output power by a controller implemented with a power tracking algorithm. This architecture is particularly suitable for LEO mission characterized by high variations in solar array inputs. The software is also featured with the capability of applying modifications to the original electrical model of the solar array in such a way as to simulate a list of potential failure modes, exclusively related to the PVA. Two types of analysis may be performed to study the effects of the failure modes: a static analysis, which consists of the investigation of the variations experienced by the characteristic curves of the solar array due to the failures, and a dynamic analysis, involving the response of

the SAR.

As far as the reliability analysis is concerned, the software derives the mathematical model associated with the reliability block diagram that is obtained from the solar array configuration. In this way, the system reliability is calculated. Furthermore, the software is able to perform a sensitivity analysis, as required by the research objectives, to assess the influence of different factors on the reliability. Moreover, an attempt to generalize the results obtained from the reliability analysis, which are exclusively applicable to the solar array under investigation, is made by developing a machine learning-based model. The goal is to retrieve an importance ranking of the factors that influence the reliability and study its sensitivity to their different combinations.

Experimental Set-up

The experimental set-up consists of a computer featured with the selected programming language. Among the licensed products purchased by RUAG Space, MATLAB and the MATLAB-based graphical programming environment Simulink are the most suitable for conducting the intended analyses. In particular, Simulink's Simscape Electrical Toolbox allows modeling all the electronic components needed to build a solar array. Moreover, it supports customized model blocks, increasing the flexibility of the software.

Results, Outcome and Relevance

As far as the FMEA is concerned, the outcome depends on the type of analysis performed. For the static analysis, the characteristic curves of the healthy and faulty system are plotted, and the variations in the performance corresponding to the three main operating points (open-circuit, short-circuit, maximum power) are calculated. This allows characterizing the effects of the failures of the Solar Array (SA). Furthermore, a severity classification of the failure modes considered is retrieved. The response of the Solar Array Regulator (SAR) is instead investigated through the dynamic analysis, where a load is connected to the solar array. Based on the wave-forms obtained, the correct implementation of the solar array regulator may be verified and the sizing of other elements of the Electrical Power Subsystem (EPS) may be derived.

The reliability analysis, besides providing an accurate estimation of the system reliability, is also used to calculate the probability of occurrence of failures, from which a probability classification is determined. From the combination of the latter with the severity classification, it is possible to perform a criticality assessment of the failure modes for the selected Photovoltaic Array (PVA) configuration. This allows highlighting weaknesses in the system and acting accordingly with the implementation of mitigation measures. Furthermore, through the sensitivity analysis, recommendations for reliability improvement may be derived. The machine learning (ML)-based analysis is inconclusive with respect to importance ranking, nevertheless, it identifies the first 17 more relevant factors out of a list of 47.

The classification of the effects of the failure modes provides relevant insights about the synthesis of a reliable system, drawing attention to those components whose failure induces the most concerning performance degradation. Furthermore, the outcome of the research is a robust starting point for the development and analysis of a full EPS.

Preface

With this research, I wrote the last chapter of my academic journey, which brought me to the attainment of the Master's Degree in Aerospace Engineering with a specialization in Space Engineering at TU Delft.

I would like to thank Dr. Mehmet Şevket Uludağ, my academic supervisor, for his advice and for guiding me through the steps required to carry out a high-quality research. Furthermore, I appreciate the time that Ms. Sezen Sümer has dedicated to me, managing the graduation conditions and the agreement between the university and the company. Moreover, guidance and professional expertise have been provided by Dr. Philipp Oettershagen and Dr. Miroslav Pantaleev from RUAG Space, to whom I express my gratitude.

Lastly, I thank my family and friends for their support.

Davide Martelli
Delft, January 2022

List of Symbols

T_c	cell operating temperature
T_J	junction temperature
a_d	diode ideality factor
α_I	current temperature coefficient
$\alpha_{I_{mp}}$	current temperature coefficient @ maximum power point
α_V	voltage temperature coefficient
$\alpha_{V_{mp}}$	voltage temperature coefficient @ maximum power point
A_p	proportional gain
C_{bus}	bus capacitance
$C_{section}$	section capacitance
D	duty cycle
G	section conductance
I_0	dark saturation current
I_D	diffusion current in single-diode model
I_{mp}	current at maximum power
I_{ph}	photo-generated current
I_{sc}	short-circuit current
$I_{section}$	section output current
k	Boltzmann's constant
λ	wavelength
λ_b	base failure rate
λ	constant failure rate
$\lambda(t)$	failure rate as a function of time
n_c	number of crimping points in series
N_p	number of parallel-connected strings
N_s	number of series-connected solar cells
n_w	number of welding points in series
π_C	contact construction factor
π_E	environment factor
π_K	mating/unmating factor
π_P	power factor
π_Q	quality factor
π_S	electrical stress factor
π_T	temperature factor
q	electron charge
R_s	series resistance
R_{sh}	parallel (shunt) resistance
θ_e	apparent radius of the Earth
θ_{es}	apparent separation between the Earth and the Sun
θ_s	apparent radius of the Sun
V_{mp}	voltage at maximum power
V_{oc}	open-circuit voltage
ΔV_{ripple}	voltage ripple
$\Delta V_{ripple} _0$	voltage ripple with no switching delays
V_{th}	thermal voltage

List of Abbreviations

AWG	American Wire Gauge
BCR	Battery Charge Regulator
BDR	Battery Discharge Regulator
DET	Direct Energy Transfer
EEE	Electrical, Electronic, Electromechanical
EPS	Electrical Power Subsystem
FIT	Failure in time
FMEA	Failure Modes and Effects Analysis
FMECA	Failure Modes, Effects and Criticality Analysis
GEO	Geosynchronous Equatorial Orbit
HDRM	Hold Down & Release Mechanisms
ICE	Individual conditional expectation
LEO	Low Earth Orbit
MEA	Main Error Amplifier
ML	machine learning
MPP	Maximum Power Point
MPPT	Maximum Power Point Tracker
P&O	Perturb & Observe
PCDU	Power Control and Distribution Unit
PDP	Partial dependence plots
PI	Proportional-Integral
PV	photovoltaic
PVA	Photovoltaic Array
PWM	Pulse-Width Modulation
RMS	root mean square
S/C	spacecraft
S3MPR	Switching Shunt Maximum Power Regulation
S3R	Sequential Switching Shunt Regulator
S4R	Serial Sequential Switching Shunt Regulator
SA	Solar Array

SAR Solar Array Regulator

SHAP SHapley Additive exPlanations

STC Standard Test Condition

p.p. percentage points

List of Figures

2.1	Block diagram of an electrical power subsystem [28].	5
2.2	Energy Transfer Methods [11].	6
3.1	Solar cell software panel.	9
3.2	Single-diode model of a solar cell.	10
3.3	IV curve superposition [35].	10
3.4	Comparison between KC200GT from reference and from simulation (@ Standard Test Condition (STC): 25°C, 1000Wm ⁻²).	11
3.5	Comparison between xSi12922 from reference and from simulation (@ STC: 25°C, 1000Wm ⁻²).	12
3.6	Double-diode model of a solar cell.	13
3.7	Comparison between MSX60 from reference and from simulation (@ STC: 25°C, 1000Wm ⁻²).	14
3.8	Temperature dependency: algorithm comparison. Solar Cell: SolAero Z4J @ 1353Wm ⁻²	14
3.9	Irradiance dependency: algorithm comparison. Solar Cell: SolAero Z4J @ 28°C.	15
3.10	Customized Simscape Electrical Solar Cell Block.	16
3.11	Solar Cell Simulink Subsystem.	16
3.12	photovoltaic (PV) Array Layout Panel.	17
3.13	Diodes Redundancy.	18
3.14	Simulink Model of the Photovoltaic Array.	19
3.15	IV Curve comparison between the solution of the modified characteristic equation and the Simulink model output.	19
3.16	Solar Array IV Curve and operating points at different temperatures (@ G = 1353Wm ⁻²).	20
3.17	S3R model [40].	21
3.18	Sequential Switching Shunt Regulator [40]	22
3.19	S3R elements.	22
3.20	Electrical power system output performance.	23
3.21	EPS currents.	24
3.22	Bus voltage response to a positive step of the load current.	24
3.23	Sections output current.	25
3.24	Flowchart of the Perturb&Observe algorithm.	26
3.25	MPPT performance: source side.	26
3.27	Duty cycle variation.	27
3.26	IV curve of <i>DemoSat</i> @ T = 60°C and G = 1353Wm ⁻²	27
4.1	Shadow model theory.	30
4.2	Operating conditions profiles for a sample spacecraft.	31
4.3	Shadow cone surfaces parameters [25].	31
4.4	Sample PVA layout.	32
4.5	Characteristic curves of <i>DemoSat</i> solar array @ T = 28°C, G = 1353Wm ⁻²	32
4.6	Bypass diode: short-circuit fault.	33
4.7	Shorted bypass-diode effects at string level on <i>DemoSat</i> solar array characteristic curves @ T = 28°C, G = 1353Wm ⁻²	33
4.8	Applied voltage seen from the single solar cells within the healthy and faulty string.	34
4.9	Current through the short-circuited connection.	34
4.10	Shorted bypass-diode effects at PVA level on <i>DemoSat</i> solar array characteristic curves @ T = 28°C, G = 1353Wm ⁻²	34
4.11	Bypass Diode: impedance fault.	34
4.12	Impedance fault of one bypass diode. Effects on <i>DemoSat</i> solar array characteristic curve at string level @ T = 28°C, G = 1353Wm ⁻²	35
4.13	Current flowing through the faulty bypass diode.	35

4.14 Impedance fault of one bypass diode ($R = 50\Omega$). Effects on <i>DemoSat</i> solar array at solar cell level @ $T = 28^\circ\text{C}$, $G = 1353\text{Wm}^{-2}$	36
4.15 Impedance fault of one bypass diode. Effects on <i>DemoSat</i> solar array characteristic curve at PVA level @ $T = 28^\circ\text{C}$, $G = 1353\text{Wm}^{-2}$	36
4.16 Bypass diode: open-circuit fault.	37
4.19 Open-circuit of one bypass diode. Effects on <i>DemoSat</i> solar array characteristic curve at PVA level @ $T = 28^\circ\text{C}$, $G = 1353\text{Wm}^{-2}$	37
4.20 Blocking diode: short-circuit fault.	37
4.21 Short-circuit of one blocking diode. Effects on <i>DemoSat</i> solar array characteristic curve at string level @ $T = 28^\circ\text{C}$, $G = 1353\text{Wm}^{-2}$	37
4.22 Power dissipated in the blocking diode.	38
4.23 Short-circuit of one blocking diode. Effects on <i>DemoSat</i> solar array characteristic curve at PVA level @ $T = 28^\circ\text{C}$, $G = 1353\text{Wm}^{-2}$	38
4.24 Blocking diode: impedance fault.	39
4.25 Blocking diode impedance fault ($R = 50\Omega$). Voltage measurements.	39
4.26 Impedance fault of one blocking diode. Effects on <i>DemoSat</i> solar array characteristic curve at string level @ $T = 28^\circ\text{C}$, $G = 1353\text{Wm}^{-2}$	39
4.27 Power dissipated through the faulty diode ($R = 50\Omega$).	40
4.28 Impedance fault of one blocking diode. Effects on <i>DemoSat</i> solar array characteristic curve at PVA level @ $T = 28^\circ\text{C}$, $G = 1353\text{Wm}^{-2}$	40
4.29 Blocking diode: open-circuit fault.	41
4.30 Open-circuit of one blocking diode. Effects on <i>DemoSat</i> solar array characteristic curve at PVA level @ $T = 28^\circ\text{C}$, $G = 1353\text{Wm}^{-2}$	41
4.31 Line-to-line fault.	41
4.32 Line-to-line fault between the 6 th and the 7 th solar cell and between the 1 st and 2 nd solar cells of two different strings. Effects on <i>DemoSat</i> solar array characteristic curve at string level @ $T = 28^\circ\text{C}$, $G = 1353\text{Wm}^{-2}$	42
4.33 Simulated line-to-line fault.	42
4.34 Line-to-line fault between the 6 th and the 7 th solar cell and between the 1 st and 2 nd solar cells of two different strings. Wave-forms.	42
4.35 Line-to-line fault between the 6 th and the 7 th solar cell and between the 1 st and 2 nd solar cells of two different strings. Effects on <i>DemoSat</i> solar array characteristic curve at PVA level @ $T = 28^\circ\text{C}$, $G = 1353\text{Wm}^{-2}$	43
4.36 Ground Fault.	44
4.37 Ground fault at different string positions. Between the 3 rd and 4 th cell and between 6 th and 7 th cell. Effects on <i>DemoSat</i> solar array characteristic curve at string level @ $T = 28^\circ\text{C}$, $G = 1353\text{Wm}^{-2}$	44
4.38 Ground fault at different string positions. Between the 3 rd and 4 th cell and between 6 th and 7 th cell. Effects on <i>DemoSat</i> solar array characteristic curve at PVA level @ $T = 28^\circ\text{C}$, $G = 1353\text{Wm}^{-2}$	44
4.39 Connection Faults.	45
4.40 Impedance fault of a connection within a string. Effects on <i>DemoSat</i> solar array characteristic curve at string level @ $T = 28^\circ\text{C}$, $G = 1353\text{Wm}^{-2}$	46
4.41 Impedance fault of a connection within a string. Effects on <i>DemoSat</i> solar array characteristic curve at string level @ $T = 28^\circ\text{C}$, $G = 1353\text{Wm}^{-2}$	46
4.42 Shading of one solar cell for $G = 1200\text{Wm}^{-2}$, $G = 1000\text{Wm}^{-2}$, $G = 500\text{Wm}^{-2}$, and $G = 0\text{Wm}^{-2}$. Effects on <i>DemoSat</i> solar array characteristic curve at string level @ $T = 28^\circ\text{C}$, $G = 1353\text{Wm}^{-2}$	47
4.43 Shading of 1 solar cell ($G = 500\text{Wm}^{-2}$). Currents and voltages.	48
4.44 Analysis of the characteristic curves under shading condition.	48
4.45 Shading of one solar cell for $G = 1000\text{Wm}^{-2}$, $G = 500\text{Wm}^{-2}$, and $G = 0\text{Wm}^{-2}$. Effects on <i>DemoSat</i> solar array characteristic curve at PVA level @ $T = 28^\circ\text{C}$, $G = 1353\text{Wm}^{-2}$	49
4.46 Shading of two solar cells for different solar irradiances. Effects on <i>DemoSat</i> solar array characteristic curve at string level @ $T = 28^\circ\text{C}$, $G = 1353\text{Wm}^{-2}$	50
4.47 Shading of two solar cells for different solar irradiances. Effects on <i>DemoSat</i> solar array characteristic curve at PVA level @ $T = 28^\circ\text{C}$, $G = 1353\text{Wm}^{-2}$	50
4.48 Potential open-circuit conditions of a solar cell.	51

4.49	Open-circuit fault of one solar cell. Effects on <i>DemoSat</i> solar array characteristic curve at string level @ $T = 28^\circ\text{C}$, $G = 1353\text{Wm}^{-2}$	51
4.50	Open-circuit fault of one solar cell. Effects on <i>DemoSat</i> solar array characteristic curve at PVA level @ $T = 28^\circ\text{C}$, $G = 1353\text{Wm}^{-2}$	52
4.51	Reduced active area of solar cells. Effects on <i>DemoSat</i> solar array characteristic curve at string level @ $T = 28^\circ\text{C}$, $G = 1353\text{Wm}^{-2}$	52
4.52	Reduced active area of 2 solar cells ($A_{\text{active}} = 70\%$ and $A_{\text{active}} = 50\%$). Currents and voltages.	53
4.53	Reduced active area of solar cells. Effects on <i>DemoSat</i> solar array characteristic curve at PVA level @ $T = 28^\circ\text{C}$, $G = 1353\text{Wm}^{-2}$	53
4.54	Effects of a shorted bypass diode and a connection impedance fault ($R = 30\Omega$) involving 2 different strings.	54
4.55	Effects of the combination of one shorted bypass diode and one connection fault ($R = 30\Omega$).	55
4.56	Effects of the combination of one shorted bypass diode and one shaded solar cell ($G = 500\text{Wm}^{-2}$). Two different solar cells involved.	55
4.57	Effects of the combination of one shaded solar cell ($G = 500\text{Wm}^{-2}$) and the open-circuit of its parallel-connected bypass diode.	55
4.58	Effects of the combination of one shaded solar cell ($G = 500\text{Wm}^{-2}$) and the short-circuit of its parallel-connected bypass diode.	56
4.59	Effects of the combination of shorted bypass diode and shorted blocking diode within the same string.	56
4.60	Effects of the combination of shorted bypass diode and shorted blocking diode within the same string.	57
4.61	Analysis of the characteristic curves under a combination of faults: shorted bypass diode and shorted blocking diode within the same string.	57
4.62	Analysis of the implemented EPS, considering the <i>DemoSat</i> PVA layout and a resistive load of 10Ω ($T = 28^\circ\text{C}$ and $G = 1353\text{Wm}^{-2}$). SolAero Z4J are considered for the solar cells.	58
4.63	EPS analysis for a resistive load whose profile is characterized by a positive step from 10Ω to 25Ω at $t = 0.2\text{s}$	59
4.64	IV curves of the healthy and faulty PVA. Different load lines are also plotted together with a vertical line at $V = V_{\text{bus}}$	59
4.65	Analysis of the implemented EPS, considering the <i>DemoSat</i> PVA layout and a power load of 51W ($T = 28^\circ\text{C}$ and $G = 1353\text{Wm}^{-2}$). SolAero Z4J are considered for the solar cells.	60
4.66	EPS analysis for a power load whose profile is characterized by a negative step from 50.5W to 25W at $t = 0.2\text{s}$	61
4.67	System successful response to a shorted bypass-diode ($T = 28^\circ\text{C}$ and $G = 1353\text{Wm}^{-2}$).	61
4.68	IV curve of the PVA subjected to failure mechanisms that reduce that reduce the active area of two different cells to 20%	62
4.69	System unsuccessful response to two solar cells with reduced active area ($A_{\text{active}} = 20\%$) within the same string ($R_{\text{load}} = 10\Omega$).	62
4.70	System unsuccessful response to two solar cells with reduced active area ($A = 20\%$) within the same string ($R_{\text{load}} = 10\Omega$).	62
4.71	System successful response to two solar cells with reduced active area ($A = 20\%$) within the same string ($R_{\text{load}} = 25\Omega$).	63
4.72	System unsuccessful response to a open-circuit failure of a solar cell.	63
5.1	Typical bathtub curve for Electrical, Electronic, Electromechanical (EEE) components [15].	65
5.2	PVA Reliability Block Diagram: functions.	69
5.3	Series-connected elements.	70
5.4	Parallel-connected elements.	70
5.5	Example of a reliability block diagram of a string.	71
5.6	Effects of the number of cells per string on the reliability under different assumptions.	79
5.7	Number of acceptable string failures given different numbers of total strings.	80
5.8	Effects on system reliability of the number of parallel-connected bypass diodes.	80
5.9	Effects on system reliability of the number of series-connected bypass diodes.	81
5.10	Effects on the reliability of possible bypass diode arrangements.	81
5.11	Effects on system reliability of the number of parallel-connected blocking diodes.	82

5.12	Effects on system reliability of the number of series-connected blocking diodes.	82
5.13	Effects on the reliability of possible blocking diode arrangements.	83
5.14	Effects on system reliability of the bypass diodes and solar cells failure modes distribution (0 acceptable solar cells in short).	84
5.15	Effects on system reliability of the bypass diodes and solar cells failure modes distribution (1 acceptable solar cells in short).	84
5.16	Effects on system reliability of the blocking diode failure modes distribution.	84
5.17	Effects of number of grounding points and connections redundancy.	85
5.18	Effects of number of grounding points and grounding points redundancy.	85
5.19	Effects of the blocking diode characteristics on the system reliability.	86
5.20	Effects of the connector characteristic on the system reliability.	86
6.1	Features correlation.	90
6.2	Permutation features importance: box plot.	91
6.3	Features importance using column drop method.	92
6.4	SHAP Analysis.	93
6.5	PVA reliability dependence with the connector ambient temperature.	94
6.6	PVA reliability dependence on number of sections.	94
6.7	2D Partial dependence plots (PDP) for connector ambient temperature and number of sections.	94
6.8	PVA reliability dependence on number of parallel-connected blocking diode.	95
6.9	Effects of the number of parallel-connected diodes given different failure modes distributions.	95
6.10	2D PDP for number of parallel-connected blocking diodes and failure modes distribution.	96
6.11	2D PDP for number of parallel-connected blocking diodes and maximum number of acceptable string failures.	96
6.12	2D PDP for the blocking diode reverse voltage and the junction temperature.	97

List of Tables

3.1	KC200GT solar array.	11
3.2	xSi12922 photovoltaic module.	12
3.3	MSX60 photovoltaic module	13
3.4	Z4J Solar Cell @ 28°C and 1353 Wm ⁻²	15
3.5	Z4J operating points for different operating temperatures.	15
3.6	Z4J operating points for different operating irradiances.	16
3.7	<i>DemoSat</i> PVA configuration.	23
3.8	S3R user-defined parameters.	23
3.9	Calculated parameter for the S3R.	23
3.10	Boost converter operating ranges.	25
3.11	MPPT parameters.	26
3.12	Operating points of <i>DemoSat</i> @ $T = 60^\circ\text{C}$ and $G = 1353\text{ Wm}^{-2}$	27
4.1	Input parameters for the analytical method for calculating the penumbra transition period.	31
4.2	Umbra and penumbra geometry.	31
4.5	Performance of the <i>DemoSat</i> solar array @ $T = 28^\circ\text{C}$, $G = 1353\text{ Wm}^{-2}$	32
4.6	Shorted bypass-diode effects on <i>DemoSat</i> solar array performance @ $T = 28^\circ\text{C}$, $G = 1353\text{ Wm}^{-2}$	33
4.7	Effects of the impedance fault of the bypass-diode on <i>DemoSat</i> solar array performance at string level @ $T = 28^\circ\text{C}$, $G = 1353\text{ Wm}^{-2}$	35
4.8	Effects of the impedance fault of the bypass-diode on <i>DemoSat</i> solar array performance at PVA level @ $T = 28^\circ\text{C}$, $G = 1353\text{ Wm}^{-2}$	36
4.9	Shorted blocking-diode effects on <i>DemoSat</i> solar array performance @ $T = 28^\circ\text{C}$, $G = 1353\text{ Wm}^{-2}$	38
4.10	Effects of the impedance fault of the blocking-diode on <i>DemoSat</i> solar array performance at string level @ $T = 28^\circ\text{C}$, $G = 1353\text{ Wm}^{-2}$	39
4.11	Effects of the impedance fault of the blocking-diode on <i>DemoSat</i> solar array performance at PVA level @ $T = 28^\circ\text{C}$, $G = 1353\text{ Wm}^{-2}$	40
4.12	Open blocking-diode effects on <i>DemoSat</i> solar array performance at PVA level @ $T = 28^\circ\text{C}$, $G = 1353\text{ Wm}^{-2}$	41
4.13	Line-to-line fault between the 6 th and the 7 th solar cell and between the 1 st and 2 nd solar cells of two different strings. Effects on <i>DemoSat</i> solar array performance at string level @ $T = 28^\circ\text{C}$, $G = 1353\text{ Wm}^{-2}$	42
4.14	Line-to-line fault between the 6 th and the 7 th solar cell and between the 1 st and 2 nd solar cells of two different strings. Effects on <i>DemoSat</i> solar array performance at PVA level @ $T = 28^\circ\text{C}$, $G = 1353\text{ Wm}^{-2}$	43
4.15	Ground fault at different string positions. Between the 3 rd and 4 th cell and between 6 th and 7 th cell. Effects on <i>DemoSat</i> solar array characteristic curve at string level @ $T = 28^\circ\text{C}$, $G = 1353\text{ Wm}^{-2}$	44
4.16	Ground fault at different string positions. Between the 3 rd and 4 th cell and between 6 th and 7 th cell. Effects on <i>DemoSat</i> solar array characteristic curve at PVA level @ $T = 28^\circ\text{C}$, $G = 1353\text{ Wm}^{-2}$	45
4.17	Impedance fault of a connection within a string. Effects on <i>DemoSat</i> solar array characteristic curve at string level @ $T = 28^\circ\text{C}$, $G = 1353\text{ Wm}^{-2}$	46
4.18	Impedance fault of a connection within a string. Effects on <i>DemoSat</i> solar array characteristic curve at PVA level @ $T = 28^\circ\text{C}$, $G = 1353\text{ Wm}^{-2}$	47
4.19	Shading of one solar cell for $G = 1200\text{ Wm}^{-2}$, $G = 1000\text{ Wm}^{-2}$, $G = 500\text{ Wm}^{-2}$, and $G = 0\text{ Wm}^{-2}$. Effects on <i>DemoSat</i> solar array performance at string level @ $T = 28^\circ\text{C}$, $G = 1353\text{ Wm}^{-2}$	47
4.20	Shading of one solar cell for $G = 1200\text{ Wm}^{-2}$, $G = 1000\text{ Wm}^{-2}$, $G = 500\text{ Wm}^{-2}$, and $G = 0\text{ Wm}^{-2}$. Effects on <i>DemoSat</i> solar array performance at PVA level @ $T = 28^\circ\text{C}$, $G = 1353\text{ Wm}^{-2}$	49
4.21	Shading of two solar cells. Effects on <i>DemoSat</i> solar array performance at string level @ $T = 28^\circ\text{C}$, $G = 1353\text{ Wm}^{-2}$	50

4.22	Shading of two solar cells. Effects on <i>DemoSat</i> solar array performance at PVA level @ $T = 28^{\circ}\text{C}$, $G = 1353\text{Wm}^{-2}$	50
4.23	Open-circuit of one solar cell. Effects on <i>DemoSat</i> solar array characteristic curve at string level @ $T = 28^{\circ}\text{C}$, $G = 1353\text{Wm}^{-2}$	52
4.24	Open-circuit of one solar cell. Effects on <i>DemoSat</i> solar array characteristic curve at PVA level @ $T = 28^{\circ}\text{C}$, $G = 1353\text{Wm}^{-2}$	52
4.25	Reduced active area of solar cells. Effects on <i>DemoSat</i> solar array performance at string level @ $T = 28^{\circ}\text{C}$, $G = 1353\text{Wm}^{-2}$	53
4.26	Reduced active area of solar cells. Effects on <i>DemoSat</i> solar array performance at PVA level @ $T = 28^{\circ}\text{C}$, $G = 1353\text{Wm}^{-2}$	54
5.1	Failure rate models and obtained reliability values for single components (mission lifetime: 5 years).	69
5.2	<i>DemoSat</i> connection points.	71
5.3	Discrepancy between the system reliability predicted by the developed software and the available results of a reliability analysis report of a RUAG Space project (1).	77
5.4	Discrepancy between the system reliability predicted by the developed software and the available results of a reliability analysis report of a RUAG Space project (2).	77
5.5	Discrepancy between the system reliability predicted by the developed software and the values obtained from a qualified software for two RUAG Space projects.	77
5.6	Features considered in the sensitivity analysis.	78
5.7	Assumptions considered in the reliability prediction and sensitivity analysis.	78
5.8	Sensitivity Analysis Results	87
6.1	Features ranges for the retrieved dataset.	89
6.2	Bayesian optimization output for considered ML models.	90
6.3	ML models score.	90
6.4	Comparison between permutation and column drop methods.	92
7.1	Probability classification parameters [31].	99
7.2	Failure probabilities.	100
7.3	Severity classification guidelines[31].	100
7.4	Assigned severity criteria.	101
7.5	Severity classification.	101
7.6	Criticality Matrix [31].	101
7.7	Criticality classification.	101
8.1	Failure modes effects.	103
8.2	Solar array regulators response to failures.	104
8.3	Most relevant factors for the reliability of the sample satellite.	104
8.4	Feature Importance Analysis Results.	105

Contents

List of Symbols	vii
List of Abbreviations	ix
List of Figures	xi
List of Tables	xv
1 Introduction	1
1.1 Research Questions and Objectives	1
1.1.1 Research Questions	1
1.1.2 Research Objectives	2
1.2 Thesis Structure.	2
2 Satellite Electrical Power Subsystem	5
2.1 Space Solar Array	5
2.2 Energy Transfer Methods	5
2.3 Bus Voltage Regulation	6
2.4 Solar Array Power Regulation	6
3 System Modeling	9
3.1 Solar Cells Modeling	9
3.1.1 Single-diode Model	10
3.1.2 Double-diode Model.	13
3.1.3 Operating Conditions	13
3.1.4 Simulink Block Implementation	16
3.2 Solar Array Modeling	17
3.2.1 Strings and Sections	17
3.2.2 Diodes	17
3.2.3 Bleeding Function	18
3.2.4 Wiring, Cabling and Connections	18
3.2.5 Solar Array Model Validation.	18
3.3 Solar Array Power Regulation Modeling.	20
3.3.1 Sequential Shunt Switching Regulator (S3R)	21
3.3.2 Maximum Power Point Tracker (MPPT)	24
4 Failure Modes and Effects Analysis	29
4.1 Analysis Definition	29
4.1.1 Time-dependent Operating Conditions	29
4.2 Static Analysis.	32
4.2.1 Bypass Diode Faults	33
4.2.2 Blocking Diode Faults	37
4.2.3 Line-to-Line Fault	41
4.2.4 Ground Fault.	43
4.2.5 Connection Faults	45
4.2.6 Shading	47
4.2.7 Solar Cells Faults	51
4.2.8 Combination of Failures	54
4.3 Dynamic analysis	57
4.3.1 S3R Response to Failures.	57
4.3.2 MPPT Response to Failures	60

5	Reliability Analysis	65
5.1	System Reliability	66
5.1.1	Components Failure Rate	66
5.1.2	Reliability Model and Approach	69
5.1.3	Assumptions	70
5.2	Reliability Prediction	71
5.2.1	Power Generation	71
5.2.2	Power Transfer	76
5.2.3	Bleeding Function	76
5.2.4	PVA Reliability	77
5.2.5	Validation	77
5.3	Sensitivity Analysis	78
5.3.1	PVA Layout	78
5.3.2	Bypass Diodes Assembly Configuration	80
5.3.3	Blocking Diodes Assembly Configuration	82
5.3.4	Failure Modes Distribution	83
5.3.5	Connections	85
5.3.6	Grounding Points	85
5.3.7	Blocking Diode Characteristics	86
5.3.8	Bleeding Resistor Characteristics	86
5.3.9	Connector	86
5.3.10	Results of the Sensitivity Analysis	87
6	Machine Learning-based Feature Importance Analysis	89
6.1	Dataset	89
6.2	Machine Learning Model	90
6.3	Feature Importance Analysis	91
6.4	Features Effects on System Reliability	93
7	Criticality Assessment	99
7.1	Probability Classification	99
7.2	Severity Classification	100
7.3	Criticality Classification	101
8	Conclusions	103
8.1	Limitations	105
8.2	Future Work	106
	Bibliography	109

1

Introduction

Photovoltaic Array (PVA) is the primary power generation source in the satellite Electrical Power Subsystem (EPS) [38] and, combined with a secondary energy storage system, is the preferred choice for Earth-orbiting satellites and space exploration missions targeting solar system planets not farther than Jupiter [11]. These systems are able to provide up to several kilowatts of power throughout a satellite lifetime that may exceed 15 years [28]. Besides the energy generation and storage purposes, the power system is also responsible for power conditioning, distribution, and conversion, and dedicated analyses need to be carried out to design the most reliable and suitable architecture for the intended mission of the satellite. In addition to the traditional mechanical and power performance design, the increased cost, complexity, and lifetime requirements of modern space missions have put a strong focus on system-level reliability. As a consequence, a Failure Modes and Effects Analysis (FMEA), as well as a reliability analysis, is crucial for the design and production of a compliant and fault-tolerant system, and the development of software in support of the aforementioned activities becomes of primary interest.

1.1. Research Questions and Objectives

Considering the laborious, intensive, and iterative procedures that lead to the development of a reliable system, the lack of accurate automated tools supporting these operations drives the interest in the development of a software that aims to answer the research questions in Section 1.1.1. The solution to the research questions will be found by fulfilling the research objectives in Section 1.1.2.

1.1.1. Research Questions

The project focuses on the failure and reliability analysis of satellite solar arrays and the research questions involve the assessment of the system behavior subjected to different failure modes and the investigation of efficient techniques for reliability improvement. The first research question is formulated as follows:

RQ1 What are the effects of potential foreseen failures on solar arrays performance?

A solar array can work within a specific operating range, limited by its short-circuit and open-circuit condition. The above question puts the focus of the research on the analysis of the effects of failure modes on the static characteristic curve of the system. Nevertheless, since the specific operating point of the PVA is controlled by the solar array regulator, the following research question is proposed:

RQ2 How does the solar array regulator react to the failures?

Lastly, as far as the reliability is concerned, the scope of the project is not narrowed to the prediction of its value. Rather, the investigation of the impact of identified factors on the reliability is pursued, as highlighted by the third research question:

RQ3 What are the most relevant factors that influence the reliability of a solar array?

Eventually, the answer to the above question will allow deriving a classification of strategies for reliability improvement based on effectiveness and feasibility.

1.1.2. Research Objectives

The previous section of the report constitutes a solid framework for the formulation of the research objectives:

RO1 To simulate the electrical performance of the selected solar array, under both healthy and faulty conditions, by implementing a suitable modeling software.

The achievement of the aforementioned objective provides the results needed to answer **RQ1** and **RQ2**. The software shall be able to model the Solar Array (SA) configuration, offering a high degree of flexibility, and to simulate its behavior given specified boundary conditions. The boundary conditions define the nature of the analysis to be performed, which, according to the research questions, shall be either static or dynamic. Moreover, the software shall possess the capability of triggering specified failure modes, whose analysis shall allow deriving their degradation effects.

The electrical model does not support the prediction of the system reliability, for this purpose the software shall translate it into a reliability model, leading to the following research objective:

RO2 To estimate the system reliability by integrating the software with an algorithm that is able to translate the implemented electrical model into a reliability model.

However, even though its fulfillment lies the foundation to answer **RQ3**, an additional objective is required for the purpose of the research:

RO3 To assess the impact of identified factors on the system reliability and provide recommendations for reliability improvement by performing an automated sensitivity analysis run by the software.

This concludes the project, whose outcome will contribute to deepening the knowledge of space solar arrays and their potential improvements.

1.2. Thesis Structure

The thesis begins with a brief introduction to the satellite electrical power subsystem in Chapter 2. The focus is put on the elements that are directly involved in the research, namely the energy conversion, achieved by solar arrays (Section 2.1), and the power regulation and control. Three main factors characterize the latter: the energy transfer method, described in Section 2.2, the bus regulation, treated in Section 2.3, and the solar array power regulation, presented in Section 2.4. The selection of the EPS topology depends on the intended mission.

Chapter 3 covers in detail the modeling approach implemented in the software, whose development is imposed by the research objectives. It begins, in Section 3.1, with the fundamental component of the solar array: the solar cell. The two most commonly used models are presented, with a dedicated section relative to the influence of operating conditions, i.e. temperature and irradiance. Verification is also successfully carried out. It follows the explanation of the implementation of the models in the programming environment selected. Section 3.2 outlines the components that the software handles to build up the solar array model, validated by comparison with analytical results. Then, the modeling approach followed to implement the solar array regulator is explained in Section 3.3. The software only supports the implementation of the Maximum Power Point Tracker (MPPT)-based unregulated bus and of the Sequential Switching Shunt Regulator (S3R). This choice is mainly driven by the Company's needs, nevertheless, the aforementioned solar array regulators are two of the most common architectures for LEO (MPPT) and GEO missions (S3R), and therefore the result of the research offers the possibility to characterize several projects.

The electrical model built by the software is exploited in Chapter 4 to perform a Failure Modes and Effects Analysis. A definition of the two different approaches followed to perform the analysis is given in Section 4.1, where additional information are also provided regarding the capability of the software to manage time-dependent operating conditions. Section 4.2 deals with the static analysis: the effects of the failure modes are evaluated with respect to the performance degradation induced on the characteristic curve of the PVA. A detailed investigation of failures involving solar arrays is carried out and presented. The analysis is extended, in Section 4.3, to the dynamic behavior of the system. The objective is to evaluate the response of the selected Solar Array Regulator (SAR) to the considered faults.

In Chapter 5 the focus is put on the reliability analysis of the solar array. An introduction to the system reliability is offered in Section 5.1, where the failure rates of the components are calculated, and the reliability model from which the software retrieves the associated mathematical model is presented. A separate section is reserved for the assumptions considered, of primary importance for the interpretation of the results.

The reliability prediction of the PVA is performed in Section 5.2, divided into the main SA functionalities. The validation process is also provided, carry out with the support of existing reliability analysis reports. The sensitivity analysis, as per **RO3**, is described in Section 5.3. The software is able to iterate over different user-defined modifications and to calculate the deriving variation in the reliability.

Since the results of the sensitivity analysis are representative of the PVA modeled, they cannot be used for the categorization of a general solar array. Therefore, an attempt of broadening the meaning of the research results is made in Chapter 6 by performing a machine learning-based analysis. The goal is to retrieve an importance classification of the different features based on their impact on the system reliability. Section 6.1 explains how the data over which the machine learning (ML) model is trained are collected, while the selected ML model is introduced in Section 6.2. The feature importance is evaluated in Section 6.3 by implementing three different algorithms. The analysis extends further towards the investigation of the dependence of the system reliability on some of the most important features and on their combinations (Section 6.4).

The research ends with a criticality assessment of the simulated failure modes in Chapter 7. This is possible thanks to the combination of the probability classification, obtained in Section 7.1, and the severity classification (Section 7.2) derived from the static FMEA. The criticality of the failure modes is given in Section 7.3. The conclusions of the thesis are provided in Chapter 8, where the answers to the research questions may be found. Furthermore, Section 8.1 outlines the limitations of the research and of the developed software, while Section 8.2 suggests future research topics that may use the thesis as a starting point.

2

Satellite Electrical Power Subsystem

The EPS satisfies what arguably is the most critical requirement involving the payload of the satellite, i.e. the electrical power demand. Besides the onboard instrumentation, the EPS enables all the other spacecraft subsystems, which further highlights its essential role throughout the entire space mission.

As illustrated in Figure 2.1, the EPS converts the energy from a primary source into electrical power, which is regulated, controlled, and distributed by the Power Control and Distribution Unit (PCDU). The generated power is also stored in rechargeable energy storage, typically secondary batteries, and the overall system employs over-current and over-voltage protection.

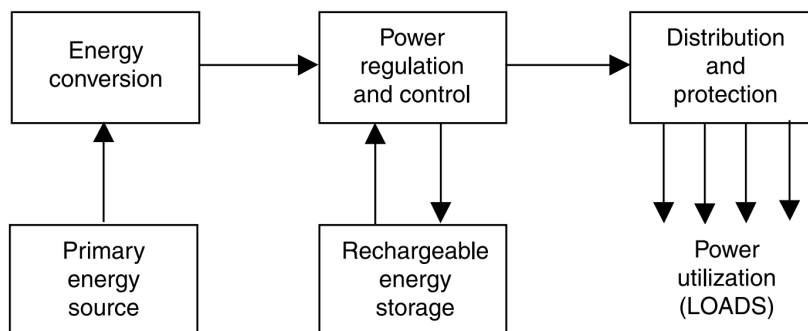


Figure 2.1: Block diagram of an electrical power subsystem [28].

The research focuses on the PVA and power regulation and control unit of photovoltaic (PV)-battery systems.

2.1. Space Solar Array

The fundamental components of photovoltaic arrays are solar cells, semiconductor devices that perform a direct energy conversion process, namely the photovoltaic process, to generate electrical energy from the sunlight. Every cell is parallel-connected to a bypass diode, which offers current mismatch protection, providing an alternative current path should the cell be reversed biased. Solar cells are connected in series to form strings, which are then assembled in parallel to build the solar array. Assuming no losses, the solar array voltage is the summation of the voltage of the single solar cells in series, while the strings in parallel build up the solar array current. Another protection strategy is implemented by connecting blocking diodes at the positive terminal of the strings. This avoids current flowing from the bus to the strings in the event of voltage mismatches. The power generated by the SAs feeds one or multiple buses, depending on the EPS topology implemented, which also strongly affects the power regulation, as explained in Section 2.3.

2.2. Energy Transfer Methods

The EPS topology may be classified by the energy transfer method implemented following either a Direct Energy Transfer (DET) or a MPPT approach. The former supplies the load directly from the PVA, while the latter places a conversion unit in series downstream the solar array to de-couple the PVA from the loads and the battery. In this case, maximum power is always extracted from the photovoltaic array. Thanks to the

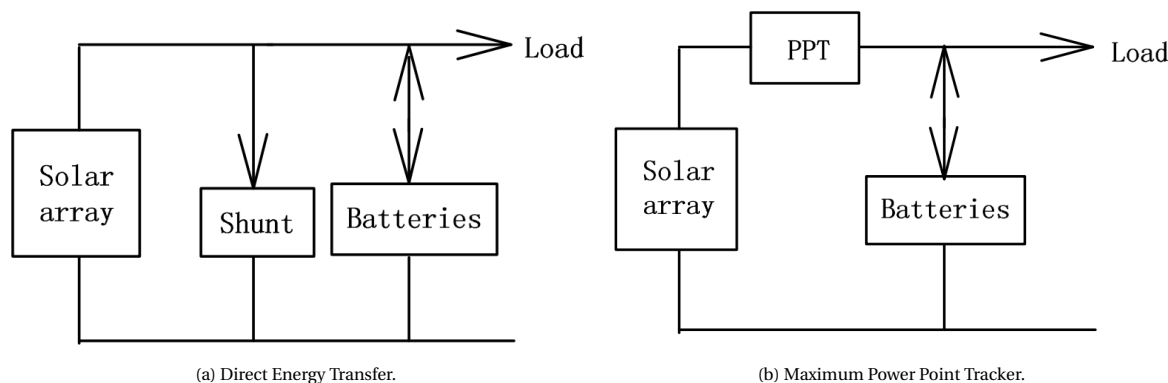


Figure 2.2: Energy Transfer Methods [11].

lower number of converters, the DET topology is more reliable and efficient, and it is particularly suitable for Geosynchronous Equatorial Orbit (GEO) missions, where the SA inputs are not subjected to significant variations. On the other hand, the systems implemented with an MPPT architecture achieve a greater power availability, and for this reason, higher flexibility is allowed for the design of the PVA layout. This topology is preferred when large variations in temperature and irradiance are experienced, mainly for Low Earth Orbit (LEO) missions [36].

2.3. Bus Voltage Regulation

The method to achieve bus voltage regulation is another fundamental factor that defines the EPS topology. Five different regulation techniques may be implemented according to [36]: unregulated bus, regulated bus, semi-regulated bus, quasi-regulated bus, and hybrid bus. These techniques are compatible with both DET and MPPT, leading to ten different EPS architectures, that extend the ones proposed by [20] and [19]. The unregulated bus regulates the SA output voltage during sunlight, when the SA excess power is either shunted (for DET architectures) or reduced (for MPPT architectures) if the battery is fully charged, and it is completely unregulated during the eclipse. The bus voltage is always clamped to the battery voltage, however, thanks to the presence of the DC/DC converter, MPPT architectures achieve the highest possible SA utilization rate. The bus output is characterized by a low impedance that renders it suitable to sustain peak and pulse loads, and it is mainly implemented for LEO missions. A major drawback is represented by the need for point-of-load converters due to the high voltage variations experienced by the bus. The regulated bus keeps the voltage regulated during both sunlight and eclipse by introducing two additional converters: Battery Charge Regulator (BCR) and Battery Discharge Regulator (BDR). The high regulation accuracy is achieved at the expense of lower reliability and efficiency. For the DET topology, two main architectures exist, namely the S3R and the Serial Sequential Switching Shunt Regulator (S4R). The former adopts a three-domain control (SA, BCR, BDR), while the latter introduces a direct connection between the SA and the battery, managed by an independent feedback loop [16]. As far as the MPPT is concerned, a three-domain control is implemented and it may be combined with the S3R to form the Switching Shunt Maximum Power Regulation (S3MPR). The regulated bus has high output impedance and does not properly manage peak and pulse loads, but it achieves a tight and accurate regulation that may be preferred when dealing with instruments that have low input voltage tolerance. The regulated bus may be a valid choice for GEO missions and when large variations in SA output are experienced. Both semi- and quasi-regulated buses offer voltage regulation during sunlight, while the bus voltage is clamped to the battery during the eclipse. These architectures achieve higher efficiency and reliability than the regulated bus but require point-of-load converters. Their implementation may be suitable for GEO missions that require little power during the eclipse. Lastly, the hybrid bus combines the advantages from both the regulated and unregulated bus providing a convenient system for satellites that supply a balanced combination of static and pulse/peak loads [20].

2.4. Solar Array Power Regulation

The definition of the EPS topology also goes through the selection of the solar array power regulation, whose methods may be divided into parallel and series regulation, as stated in [11]. Parallel regulation is imple-

mented in DET architectures, and the excess output power from the solar array is either dissipated by means of resistors (linear shunts) or shunted to the ground by transistors (switch shunt regulators). Switch shunt regulators are adopted in S3R, whose functioning principle is thoroughly presented in [40], S4R and Pulse-Width Modulation (PWM), which are used for regulated bus architectures. The most common S3Rs and PWMs operate sequentially, where a specific number of transistors, defined by a Main Error Amplifier (MEA), work in the saturated region, while one section of the SA is fine regulated by the transistor in switching state. The main difference between the two lies in the complexity of the structure, S3R being characterized by a simpler one. Both S3R and PWM may be used for GEO satellites requiring limited charging current. The latter is a constraint that is not imposed by the S4R, whose functioning principle is similar to the S3R but with a direct series connection for battery charging, and therefore large charging current can be easily handled in both LEO and GEO.

Series regulation is achieved by MPPT architectures, and is mainly implemented in LEO with high variations in SA inputs. A wider range of applications may be covered by the S3MPR, which combines S3R and MPPT, as described by [24].

3

System Modeling

The first step towards the fulfillment of **ROI** is the development of the modeling software that is able to generate a functioning system model. The approach followed for the implementation is explained in this chapter, starting with the fundamental components of the PVA in Section 3.1: the solar cells. Then, their integration with the other elements to build the solar array, as well as the inputs required by the software to properly build the model, is described in Section 3.2. Lastly, Section 3.3 deals with the solar array regulators, needed to perform one of the analyses in Chapter 4.

3.1. Solar Cells Modeling

The non-linear nature of a PV system makes it challenging to perform an accurate performance estimation. Several different methods to retrieve the IV curve of such systems have been developed for years, with the goal of achieving high evaluation accuracy within a restricted computational time.

The most widely adopted models for simulating solar cell performance are the single-diode model and the double-diode model. A three-diode model has also been studied to increase the simulation accuracy [13], however, its complexity puts a considerable effort on the implementation and it is not commonly used. Figure 3.1 shows the user interface that has been developed for the definition of the solar cells considered to build up the PVA electrical model. As will be further explained in the next sections, a drop-down menu allows selecting the desired model for the implementation. For this project, whose purpose is not the study of techniques for increasing the accuracy of the performance prediction of single solar cells, the choice can be made between the single-diode and the double-diode model, both supported by the software, as requested by the Company. Thanks to the detailed research performed over the years on these two models, this decision lays solid foundations for the whole electrical model, being the solar cells its fundamental components. Furthermore, since a large amount of validated data are available for the models considered, it eases the verification processes, critical to ensure meaningful results.

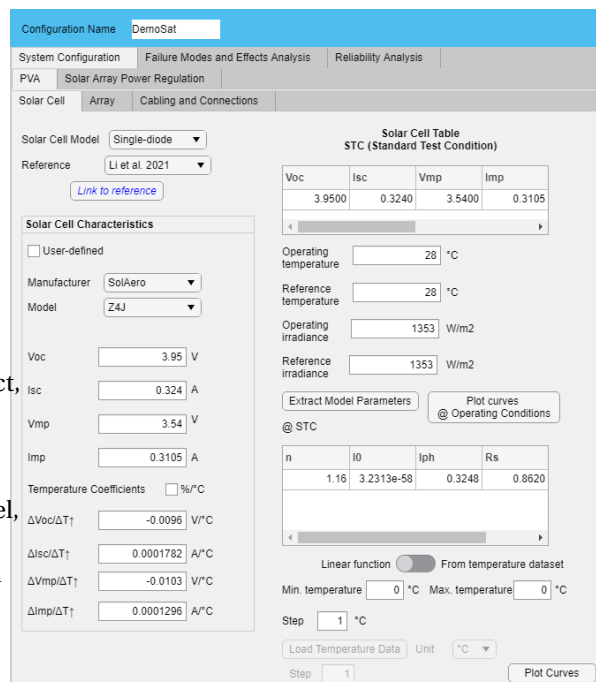


Figure 3.1: Solar cell software panel.

3.1.1. Single-diode Model

The single-diode model is shown in Figure 3.2, and its characteristic equation is given in equation 3.1.

$$I = I_{ph} - I_0 \left(\exp \left(\frac{V + IR_s}{a_d V_{th}} \right) - 1 \right) - \frac{V + IR_s}{R_{sh}} \quad (3.1)$$

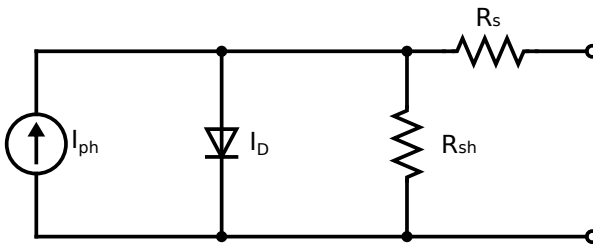


Figure 3.2: Single-diode model of a solar cell.

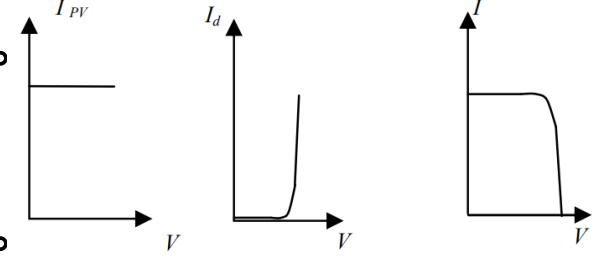


Figure 3.3: IV curve superposition [35].

Here I_{ph} or I_{pv} is the photo-generated current, I_0 is the dark saturation current, R_s is the series resistance, R_{sh} is the parallel resistance, a_d is the diode ideality factor, and $V_{th} = \frac{kT_c}{q}$ is the thermal voltage, being k the Boltzmann's constant, T_c the cell operating temperature, and q the electron charge. Every parameter is given at Standard Test Condition (STC). In the model, the parasitic resistors R_{sh} and R_s are representative of the leakage current across the PN-junction and of the losses due to the ohmic contact between metal and semiconductor respectively, and they influence two distinct regions of the IV curve. The series resistance mostly affects the performance of the solar cell when operating as a voltage source (to the right of the maximum power point), decreasing the slope of the curve. The same impact on the slope is induced by the parallel resistance, however in this case the current source region is involved. This is coherent with the modeling approach since R_{sh} is introduced to account for the leakage current through the layers of the solar cell. As far as the diode is concerned, it accounts for the diffusion mechanism and the generated current is indicated by I_D , calculated by the Shockley diode equation [18]. As can be seen from Figure 3.3, assuming $R_{sh} = \infty$, the model is based on the assumption that the output current of a solar cell is given by the superposition of the drifting current, dominated by the impinging light, and the diffusion current. The validity of such assumption has been studied in [10].

The characteristic equation 3.1 shows that 5 parameters are needed to evaluate the performance of the solar cell: I_{ph} , I_0 , a_d , R_s , R_{sh} . There exist several techniques to extract these parameters, either by fitting experimental data or by applying boundary conditions at known operating points. With the purpose of increasing the applicability of the analysis, it has been decided to implement techniques that are based exclusively on data that can be found in the solar cells manufacturer's data-sheet. In this way, the analysis is not limited to PVAs for which solar cells measurement data are available. For what concerns the algorithm of the aforementioned techniques, two different references have been used. [37] is one of the most valuable papers when dealing with solar cell modeling, while [21] has been implemented given its proved higher accuracy.

Parameters Extraction Technique by Villalva et al., 2009 [37] The algorithm starts with the calculation of the dark saturation current by applying open-circuit conditions ($I = 0$, $V = V_{oc}$) to the single-diode characteristic equation in 3.1. Two assumptions are made that allow writing equation 3.2: $I_{ph} = I_{sc}$, $I_{sc} \gg \frac{V_{oc}}{R_{sh}}$.

$$I_0 = \frac{I_{sc}}{\exp \left(\frac{V_{oc}}{a_d V_{th}} \right) - 1} \quad (3.2)$$

The ideality factor is arbitrarily chosen and lies within the range [1, 1.5]. Moreover, by setting the maximum power calculated by the IV model ($P_{max,m}$) equal to the value provided in the data-sheet ($P_{max,e}$), the equation 3.3 may be found.

$$R_{sh} = \frac{V_{mp} (V_{mp} + I_{mp} R_s)}{V_{mp} I_{ph} - V_{mp} I_0 \exp \left(\frac{V_{mp} + I_{mp} R_s}{a_d V_{th}} \right) + V_{mp} I_0 - P_{max,e}} \quad (3.3)$$

An iterative process is implemented to find the unique solution for which the pair of parasitic resistances satisfies $P_{max,m} = P_{max,e}$, starting from the following initial conditions: $R_s = 0$, $R_{sh,min} = \frac{V_{mp}}{I_{sc} - I_{mp}} - \frac{V_{oc} - V_{mp}}{I_{mp}}$.

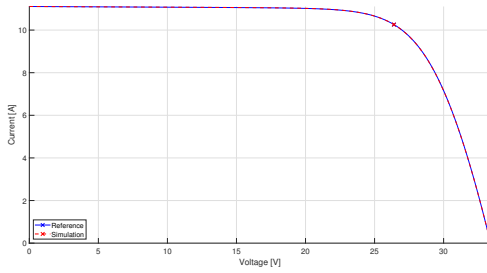
I_{mp}	7.61 A
V_{mp}	26.3 V
$P_{max,e}$	200.143 W
I_{sc}	8.21 A
V_{oc}	32.9 V
α_V	$-0.1230 \text{ V}^\circ\text{C}^{-1}$
α_I	$0.0032 \text{ A}^\circ\text{C}^{-1}$
N_s	54

(a) KC200GT Solar Array @ 25 °C and 1000 Wm⁻².

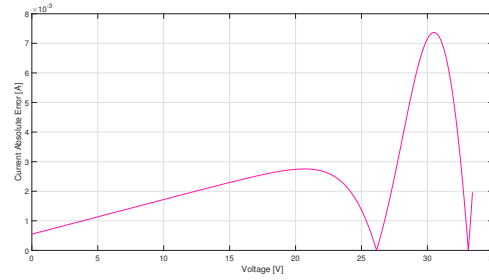
Parameters	Villalva et al. 2009	Simulation
$I_{0,STC}$	$9.825 \times 10^{-8} \text{ A}$	$9.825 \times 10^{-8} \text{ A}$
$I_{ph,STC}$	8.214 A	8.214 A
a	1.3	1.3
$R_{sh,STC}$	415.405 Ω	430.92 Ω
$R_{s,STC}$	0.221 Ω	0.222 Ω

(b) Comparison of KC200GT solar array parameters.

Table 3.1: KC200GT solar array.



(a) IV curves obtained from the solar cell characteristic equation for the set of parameters in [37] and for those retrieved from the simulation.



(b) Current absolute error between reference and simulation.

Figure 3.4: Comparison between KC200GT from reference and from simulation (@ STC: 25 °C, 1000 Wm⁻²).

The photo-generated current is given by equation 3.4.

$$I_{ph} = \frac{R_s + R_{sh}}{R_{sh}} \cdot I_{sc} \quad (3.4)$$

The single-diode characteristic equation is numerically solved within the range $V \in [0, V_{oc}]$ for each iteration until the power equality is satisfied.

The accuracy of the results highly depends on three different parameters: the error tolerance $\text{err} = P_{\max,m} - P_{\max,e}$ and both the step-sizes of the series resistance, taken as the free variable in the iterative process, and the one of the operating voltage in the range $[0, V_{oc}]$. The implementation of the algorithm has been verified against the results of the KC200GT solar array provided in [37], whose characteristics are given in Table 3.1. Because the parameters refer to a whole solar array composed by $N_s = 54$ series-connected solar cells, the thermal voltage V_{th} needs to be multiplied by the factor N_s . A comparison between the values provided in [37] and the ones retrieved from the implemented algorithm is shown in Table 3.1b. The step-sizes used in the iterative process are $\Delta R_s = 0.0001 \Omega$ for the series resistance and $\Delta V = 0.0001 \text{ V}$ for the operating voltage. From the table, it can be concluded that the algorithm achieves a high degree of accuracy, providing a unit level verification of the tool. To support this, the IV curves obtained from the two set of parameters are plotted in Figure 3.4. Furthermore, the current absolute error of the simulation with respect to [37] is also shown. The curves are built by solving the solar cell characteristic equation, exploiting the MATLAB function `fzero`. A small discrepancy can be noted in the parallel resistance, for which the implemented tool calculates a slightly higher value. Although this leads to a lower parasitic current flowing through the cell's layers, thus to an increase in solar cell performance, the absolute error is at most 3 order of magnitude lower than the solar cell current for the whole operating voltage range. Therefore, it can be considered negligible for the purpose of the research.

Parameters Extraction by Li et al., 2021 [21] The parameters of the single-diode model are extracted by using a dual-iteration algorithm, based on the three operational points provided in the solar cell data-sheet:

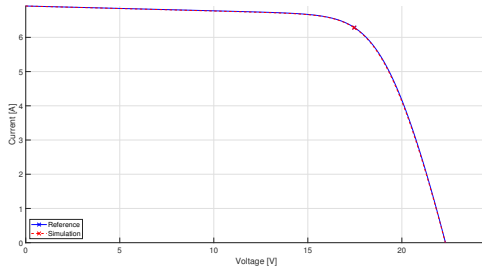
I_{mp}	4.66A
V_{mp}	17.63V
I_{sc}	5.166A
V_{oc}	22.05V
α_V	$-0.34\% \text{ } ^\circ\text{C}^{-1}$
α_I	$0.05\% \text{ } ^\circ\text{C}^{-1}$
N_s	36

(a) xSi12922 Module @ 25°C and 1000 Wm⁻².

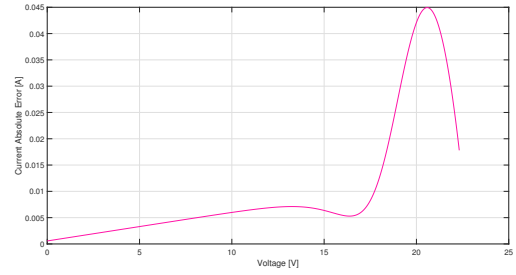
Parameters	Li et al. 2021	Simulation
$I_{0,STC}$	8.38×10^{-10} A	4.38×10^{-10} A
$I_{ph,STC}$	5.1342A	5.1355A
a	1.06	1.03
$R_{sh,STC}$	96.40Ω	92.74Ω
$R_{s,STC}$	0.3421Ω	0.3540Ω

(b) Comparison of xSi12922 photovoltaic module.

Table 3.2: xSi12922 photovoltaic module.



(a) IV curves obtained from the solar cell characteristic equation for the set of parameters in [23] and for those retrieved from the simulation.



(b) Current absolute error between reference and simulation.

Figure 3.5: Comparison between xSi12922 from reference and from simulation (@ STC: 25°C, 1000 Wm⁻²).

open-circuit, short-circuit, and maximum power. The model has been proved to be more accurate than the one in [37] under different environmental conditions. The algorithm objective is to find the pair of a_d and R_s , whose ranges are arbitrarily chosen, that minimizes the error between two different equations retrieved for R_{sh} by applying the three aforementioned operational conditions to the characteristic equation. The inner loop varies the value of the series resistance while the outer one spans the range of the ideality factor. Once these two parameters have been determined, the following equations are used to fully characterize the solar cell model:

$$I_0 = \frac{(R_s + R_{sh})I_{sc} - V_{oc}}{R_{sh}} \frac{\exp\left(\frac{V_{oc}}{a_d V_{th}}\right) - \exp\left(\frac{R_s I_{sc}}{a_d V_{th}}\right)}{\exp\left(\frac{V_{oc}}{a_d V_{th}}\right) - \exp\left(\frac{R_s I_{sc}}{a_d V_{th}}\right)} \quad (3.5)$$

$$I_{ph} = I_0 \left(\exp\left(\frac{V_{oc}}{a_d V_{th}}\right) - 1 \right) + \frac{V_{oc}}{R_{sh}} \quad (3.6)$$

$$R_{sh} = \frac{(R_s I_{sc}) \frac{\exp\left(\frac{V_{oc}}{a_d V_{th}}\right) - \exp\left(\frac{V_{mp} + R_s I_{mp}}{a_d V_{th}}\right)}{\exp\left(\frac{V_{oc}}{a_d V_{th}}\right) - \exp\left(\frac{R_s I_{sc}}{a_d V_{th}}\right)} + V_{oc} - V_{mp} - R_s I_{mp}}{I_{mp} - I_{sc} \frac{\exp\left(\frac{V_{oc}}{a_d V_{th}}\right) - \exp\left(\frac{V_{mp} + R_s I_{mp}}{a_d V_{th}}\right)}{\exp\left(\frac{V_{oc}}{a_d V_{th}}\right) - \exp\left(\frac{R_s I_{sc}}{a_d V_{th}}\right)}} \quad (3.7)$$

The accuracy of the retrieved parameters highly depends on the step-sizes considered to iterate over the ideality factor and the series resistance. For the simulation $\Delta a_d = 0.01$ and $\Delta R_s = 0.0001 \Omega$ are used. As for the previously described algorithm, the results have been verified against the values provided in [23] for the photovoltaic module xSi12922 in Table 3.2, while the IV curves and the absolute error are plotted in Figure 3.5. The implementation of the algorithm results to be slightly less accurate than what has been achieved for [37], being the order of magnitude of the current absolute error equal to -2. Nonetheless, the error is still sufficiently low to be neglected, assumption that allows considering the algorithm verified.

3.1.2. Double-diode Model

The double-diode model introduces the losses due to the recombination phenomenon I_{D_2} , i.e. an electron-hole pair recombination resulting in a loss of charge carrier.

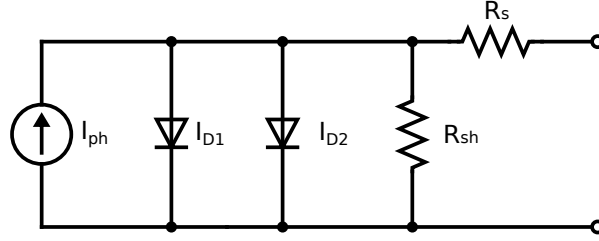


Figure 3.6: Double-diode model of a solar cell.

$$I = I_{ph} - I_{01} \left(\exp \left(\frac{V + IR_s}{a_{d1} V_{th}} \right) - 1 \right) - I_{02} \left(\exp \left(\frac{V + IR_s}{a_{d2} V_{th}} \right) - 1 \right) - \frac{V + IR_s}{R_{sh}} \quad (3.8)$$

The characteristic equation 3.8 shows that the number of unknown parameters is increased from 5 to 7 with the introduction of the saturation current (I_{02}) and of the ideality factor (a_{d2}) of the second diode. For what concerns the parameters extraction technique, the implemented algorithm may be found in [27].

Parameters Extraction by Meng et al. 2020 [27]: In this model, an iterative process is implemented to find the value of the series resistance, which allows calculating the other missing parameters. Two assumptions hold: first, the ideality factors a_{d1} and a_{d2} are set to 1 and 2 respectively, second, due to the small entity of the dark saturation currents and the difficulty in retrieving their actual values, the same value is considered for both saturation currents, i.e. $I_{01} = I_{02}$. Once again, the correctness of the implementation is verified by using a PV module provided in [27]. The module characteristics, as well as the comparison between the given parameters and those retrieved from the implemented algorithm, are presented in Table 3.3 (step-size: $\Delta R_s = 0.001 \Omega$). As can be seen from the graphs in Figure 3.7, the simulation reaches a satisfactory level of

I_{mp}	3.5A
V_{mp}	17.1V
I_{sc}	3.8A
V_{oc}	21.1V
α_V	$-0.08 \text{ V}^\circ\text{C}^{-1}$
α_I	$0.003 \text{ A}^\circ\text{C}^{-1}$
N_s	36

(a) MSX60 photovoltaic module @ 25°C and 1000Wm⁻².

Parameters	Meng et al. 2020	Simulation
$I_{01,STC}$	$4.598 \times 10^{-10} \text{ A}$	$4.558 \times 10^{-10} \text{ A}$
$I_{02,STC}$	$4.598 \times 10^{-10} \text{ A}$	$4.558 \times 10^{-10} \text{ A}$
$I_{ph,STC}$	3.808A	3.808A
a_1	1	1
a_2	2	2
$R_{sh,STC}$	169.081 Ω	167.308 Ω
$R_{s,STC}$	0.372 Ω	0.371 Ω

(b) Comparison of MSX60 photovoltaic module.

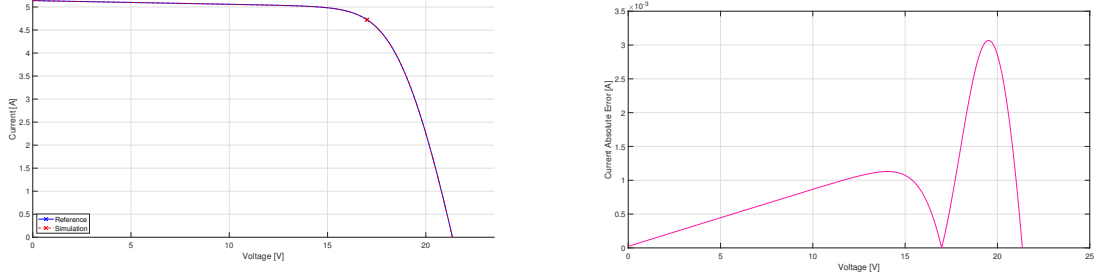
Table 3.3: MSX60 photovoltaic module

accuracy for the purpose of this project and the implementation of the algorithm is verified.

3.1.3. Operating Conditions

Solar cells are highly influenced by environmental factors, i.e. temperature and irradiance. Radiations are also a big concern for solar arrays, which cannot be properly shielded due to their functioning principle. Displacement damage is what mainly impacts the system, degrading its performance. Keeping this in mind, radiation effects are beyond the scope of this research and will not be treated here. Therefore, when operating/working conditions are mentioned, they refer to the temperature and solar irradiance which the system is subjected to.

The equations describing the relationship between the estimated parameters and the working conditions are



(a) IV curves obtained from the solar cell characteristic equation for the set of parameters in [27] and for those retrieved from the simulation.

(b) Current absolute error between reference and simulation.

Figure 3.7: Comparison between MSX60 from reference and from simulation (@ STC: 25 °C, 1000 Wm⁻²).

retrieved from [27], where no assumptions of constant parameters are made. Nonetheless, the paper indicates a linear relationship between the ideality factor and the temperature ($a_d(T) = a_{d,ref} \cdot \frac{T}{T_{ref}}$), which cannot be extended to the temperature ranges considered experienced in space. For this reason, the ideality factors are kept constant, as is the case in [37] and [23].

$$I_{ph}(T, G) = (I_{ph,STC} + \alpha_I \Delta T) \frac{G}{G_{STC}} \quad (3.9)$$

$$I_{sc}(T, G) = (I_{sc,STC} + \alpha_I \Delta T) \frac{G}{G_{STC}} \quad (3.10)$$

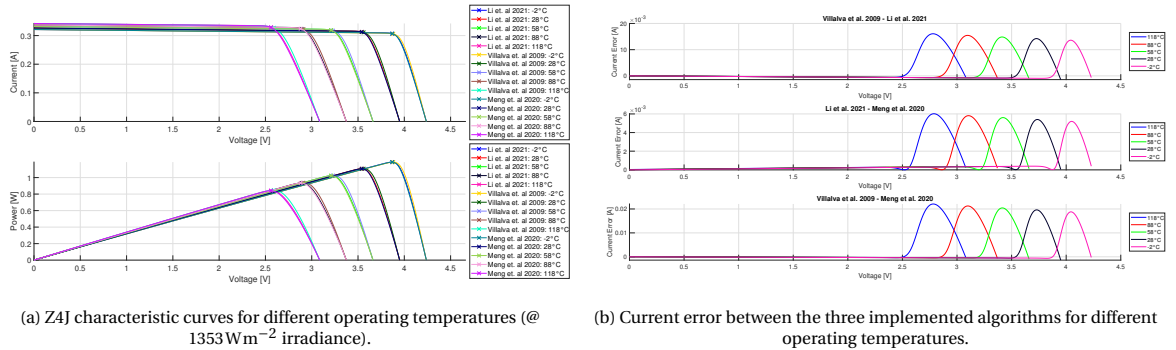
$$V_{oc}(T, G) = V_{oc,STC} + a_{d1} V_{th} \ln\left(\frac{G}{G_{STC}}\right) + \alpha_V \Delta T \quad (3.11)$$

$$R_s(T, G) = R_{s,STC} \frac{T}{T_{STC}} \left(1 - 0.217 \ln\left(\frac{G}{G_{STC}}\right)\right) \quad (3.12)$$

$$R_{sh}(T, G) = R_{sh,STC} \frac{G}{G_{STC}} \quad (3.13)$$

where α_I is the temperature coefficient of the short-circuit current, α_V is the temperature coefficient of the open-circuit voltage, and $\Delta T = T - T_{STC}$. The subscript STC refers to the standard test conditions. The value of I_0 is then calculated by substituting the parameters at operating conditions in the equation provided by the algorithm implemented.

Temperature Dependence Figure 3.8a illustrates how the solar cell performance varies for different operating temperatures. The solar cell considered for the analysis is the Z4J (27 cm²), a 4-junction solar cell developed by SolAero. Its characteristics are provided in Table 3.4. It may be seen the significant impact on the open-circuit voltage which decreases while increasing the temperature. The IV curves obtained from all the three algorithms implemented are plotted. For better visualization of the discrepancies between them, Figure 3.8b is provided. The lack of experimental data does not allow evaluating an absolute accuracy of the



(a) Z4J characteristic curves for different operating temperatures (@ 1353 Wm⁻² irradiance).

(b) Current error between the three implemented algorithms for different operating temperatures.

Figure 3.8: Temperature dependency: algorithm comparison. Solar Cell: SolAero Z4J @ 1353 Wm⁻².

algorithms, which, for this reason, are analyzed with respect to each other. The graph highlights a high level of

agreement between the IV curves output by [27] and [23]. The comparison with the results from [37], instead, exhibits a maximum error of one order of magnitude higher (-2). It appears that the discrepancies between the parameters extraction techniques are constrained to the voltage source region of the solar cell. This is reasonable if one considers that the solar cell model is built on the assumption of superposition between the dark current and the photogenerated current and that the former is the only parameter that is calculated by an equation that is specific to the implemented algorithm, whose input variables are derived from eqs. (3.9) to (3.13).

As already mentioned, this analysis provides a comparison between the different algorithms rather than a verification of the function implemented, for which reference data would be needed. The performance of the solar cell at the three main operating points are provided in Table 3.5 for the different simulated temperatures.

I_{mp}	0.3105 A
V_{mp}	3.54 V
P_{mp}	1.10 W
I_{sc}	0.324 A
V_{oc}	3.95 V
α_V	$-9.6 \text{ mV}^\circ\text{C}^{-1}$
α_I	$0.1782 \text{ mA}^\circ\text{C}^{-1}$

Table 3.4: Z4J Solar Cell @ 28°C and 1353 Wm⁻².

		V_{oc}	I_{sc}	V_{mp}	I_{mp}
$T = 118^\circ\text{C}$	Villalva et al. 2009	3.086	0.342	2.590	0.327
	Li et al. 2021	3.086	0.342	2.560	0.329
	Meng et al. 2020	3.086	0.342	2.560	0.328
$T = 88^\circ\text{C}$	Villalva et al. 2009	3.374	0.337	2.910	0.322
	Li et al. 2021	3.374	0.337	2.890	0.323
	Meng et al. 2020	3.374	0.337	2.880	0.324
$T = 58^\circ\text{C}$	Villalva et al. 2009	3.662	0.332	3.230	0.317
	Li et al. 2021	3.662	0.332	3.210	0.318
	Meng et al. 2020	3.662	0.332	3.210	0.318
$T = 28^\circ\text{C}$	Villalva et al. 2009	3.950	0.326	3.560	0.311
	Li et al. 2021	3.950	0.326	3.540	0.313
	Meng et al. 2020	3.950	0.326	3.540	0.313
$T = -2^\circ\text{C}$	Villalva et al. 2009	4.238	0.321	3.880	0.306
	Li et al. 2021	4.238	0.321	3.870	0.307
	Meng et al. 2020	4.238	0.321	3.870	0.307

Table 3.5: Z4J operating points for different operating temperatures.

No significant discrepancies between the algorithms may be seen from the table for the current and the voltage at the operating points considered. This result is interesting for the research because, as far as the static analysis is concerned, the effects of the failure modes will be evaluated at these points, as they usually shall comply with defined requirements. From this, it may be concluded that the choice of the parameters extraction technique has a negligible impact on this kind of analysis. The discrepancies between the implemented algorithms may have a greater influence when the dynamic analysis is performed, where the solar array operating point is determined by either the connected load or the SAR. As previously mentioned, Figure 3.8b highlights that the higher discrepancy is reached when the PVA is working within the voltage source region.

Irradiance Dependence The same analysis described above has been performed for different operating irradiance values, as shown in Figure 3.9a. Overall, the error between the algorithms is lower than the one induced by the temperature variation. The higher discrepancies are once again found by comparing [27] and [23] with respect to [37].

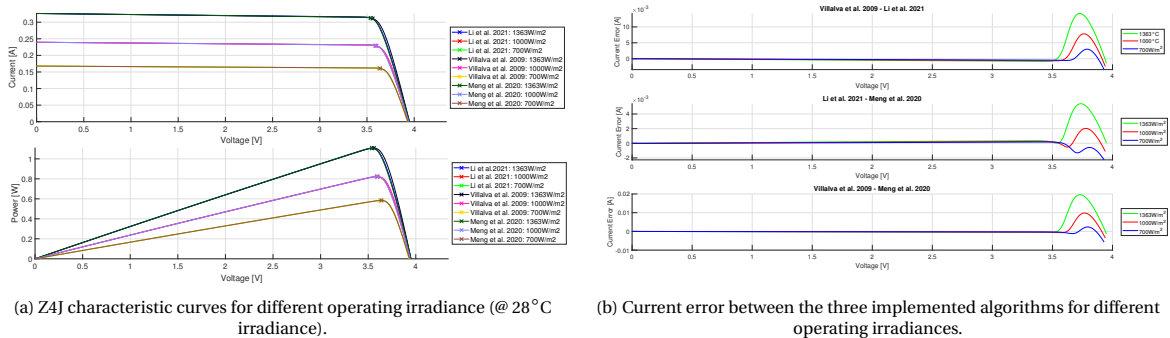


Figure 3.9: Irradiance dependency: algorithm comparison. Solar Cell: SoAero Z4J @ 28°C.

The same considerations expressed for the temperature dependency of the solar cell parameters apply. The discrepancies are limited to the voltage source region of the solar cell for the reasons previously described.

		V_{oc}	I_{sc}	V_{mp}	I_{mp}
$G = 1363 \text{ W m}^{-2}$	Villalva et al. 2009	3.950	0.326	3.560	0.311
	Li et al. 2021	3.950	0.326	3.540	0.313
	Meng et al. 2020	3.950	0.326	3.540	0.313
$G = 1000 \text{ W m}^{-2}$	Villalva et al. 2009	3.940	0.240	3.600	0.228
	Li et al. 2021	3.941	0.240	3.590	0.229
	Meng et al. 2020	3.942	0.240	3.590	0.230
$G = 700 \text{ W m}^{-2}$	Villalva et al. 2009	3.928	0.168	3.630	0.160
	Li et al. 2021	3.930	0.168	3.630	0.161
	Meng et al. 2020	3.933	0.168	3.640	0.161

Table 3.6: Z4J operating points for different operating irradiances.

The error between the algorithms tends to decrease with decreasing solar irradiance.

3.1.4. Simulink Block Implementation

The definition of the solar cell parameters allows proper modeling of the output power of the solar cell when connected to a load. Everything presented so far is implemented in MATLAB and aims to retrieve the parameters needed as input for a Simulink block that is used to build the electrical model of the PVA. The toolbox adopted for the implementation of the model, i.e. `Simscape Electrical`, offers two different blocks that are representative of solar cells and PV modules. The `PV Array` block is implemented in a specialized electrical domain and it is mainly used for ground applications. It provides two input ports for defining the environmental conditions, however, the solar irradiance is constrained within the range $0 - 1000 \text{ W m}^{-2}$. This excludes the possibility of selecting this block for building the PVA model. Moreover, the `PV Array` block is based exclusively on the single-diode model. Another possible choice for the solar cell modeling would be the `Solar Cell` block of the `Simscape Electrical Foundation` library. However, the temperature dependence is taken into account by applying equations that slightly differ from the ones introduced in Section 3.1.3, involving parameters that are not always provided in the manufacturer's data-sheet, e.g. the energy band-gap and temperature exponents for both the saturation currents and the parasitic resistances. Furthermore, while performing software testing involving `Solar Cell` block, stability issues and high computational time have been recorded. The aforementioned considerations justify the choice of implementing a customized `Simscape Electrical` block for the solar cell.

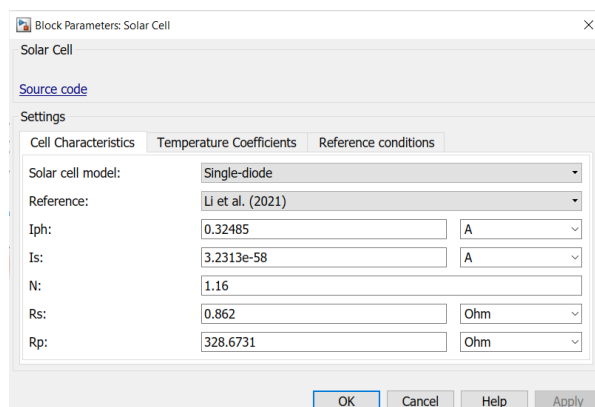
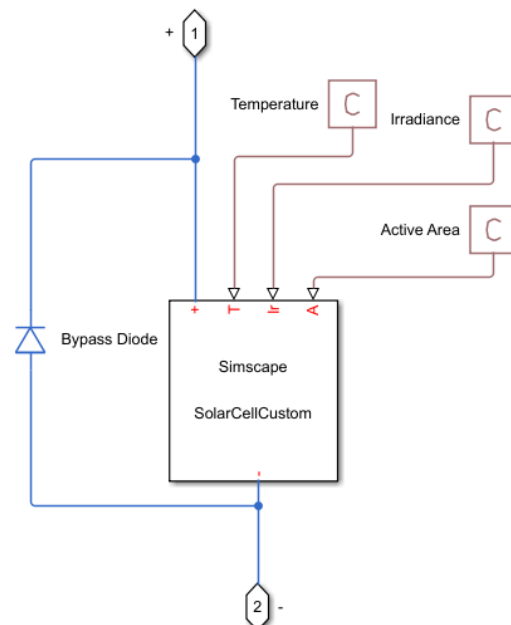
Figure 3.10: Customized `Simscape Electrical` Solar Cell Block.

Figure 3.11: Solar Cell Simulink Subsystem.

Figure 3.10 shows the block parameters of the customized solar cell. In agreement with the modeling approach described previously in this chapter, a drop-down list is present for allowing the choice between the single-diode and the double-diode model, which manages the visibility of the 5 or 7 solar cells parameters, respectively. The values are considered applicable to the cell at STC conditions, defined in the *Reference con-*

ditions panel. Another panel is present for defining the current and voltage temperature coefficients of the three main operating points: short-circuit, open-circuit, and maximum power. Please note that, although they are not involved in any equations of the implemented algorithms, specific values may be set for $\alpha_{V_{mp}}$ and $\alpha_{I_{mp}}$. These have been included in the block to facilitate future updates of the software that may consider different temperature dependence relationships. In addition to the positive and negative terminals, the block also has three input ports for defining the operating conditions, i.e. operating temperature and irradiance, and the active area of the solar cell. The latter is needed for the proper simulation of micrometeorites impacts, as will become clear in Chapter 4. As explained in Chapter 1, in solar arrays for space applications, the solar cell is connected in parallel with a bypass diode for reverse voltage protection. In the Simulink model, solar cell, input parameters, and the bypass diode are grouped together into a subsystem, as shown in Figure 3.11.

3.2. Solar Array Modeling

Having defined the fundamental components of the PVA, the next step is to interconnect the solar cells to build the system under analysis.

First, the terminology used in the projects needs to be clarified to avoid ambiguity. A *string* is defined as a number of series-connected solar cells. Depending on the panel geometry and other geometry requirements (number of Hold Down & Release Mechanisms (HDRM), spacing between cells, etc.), the length of the string may not entirely fit on the substrate. Therefore, some additional wiring, like jumpers, may be needed to connect different string segments. A *segment* consists of a number of solar cells that are connected in series directly through their interconnectors, with no wires in between. The strings are then connected in parallel to build a *section*.

3.2.1. Strings and Sections

Figure 3.12 shows the graphical user interface of the software that allows defining the PVA layout. The number of series-connected solar cells is assumed to be the same for every string in the solar array. It would be unreasonable to implement this feature as customizable for different strings since, depending on the operating points, it would create a voltage mismatch between them, which is not desirable. Furthermore, the total number of sections as well as the number of strings per section can be defined.

3.2.2. Diodes

The implementation of diodes redundancy is supported by the software. Although, in reality, bypass diodes are rarely redundant, both blocking and bypass diode redundancy may be implemented in the model. The low feasibility of redundant bypass diodes is due to geometry constraints as well as to the fact that many state-of-the-art space solar cells are already made available with an integrated bypass diode. Nonetheless, it may be interesting, especially for what concerns the reliability analysis, to investigate how this kind of redundancy would affect the estimated reliability of the system. Based on the arrangement of the diodes, high or level redundancy may be achieved (Figure 3.13). The implications of the different arrangements will be explained later in the thesis.

To achieve a higher degree of flexibility of the software, each solar cell may have a different number of redundant bypass diodes connected either in parallel or in series and the same applies for the blocking diodes at the positive terminal of the strings.

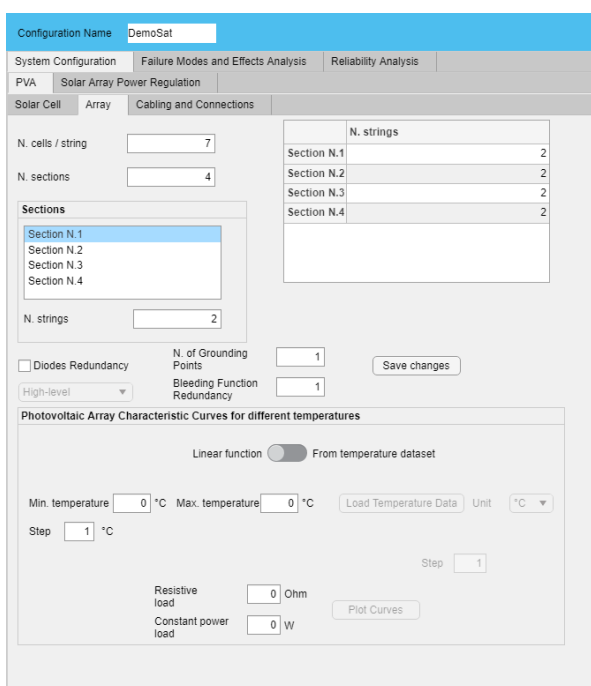


Figure 3.12: PV Array Layout Panel.

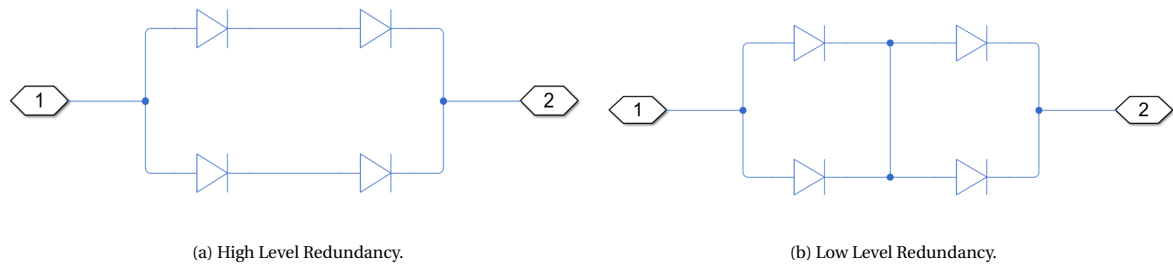


Figure 3.13: Diodes Redundancy.

3.2.3. Bleeding Function

The software offers the possibility to take into account the bleeding function of the PVA. The entry *N. of Grounding Points* in Figure 3.12 indicates the number of elements that are grounded. Usually, this corresponds to the number of solar panels, whose substrate is connected to the satellite ground to avoid charge accumulation and to limit leakage current in response to different failure modes. Each substrate may be grounded at one location, or it may have redundant grounding points, defined by *Bleeding Function Redundancy*. Please note that it is assumed that each grounded element has the same redundancy.

The bleeding function is not involved in the electrical analysis of the PVA since it concerns the substrate and failure modes that are not treated in this research. However, it will affect to a certain extent the reliability calculations, as will be explained later.

3.2.4. Wiring, Cabling and Connections

A dedicated section of the software is developed for wiring, cabling, and connections, where it is also possible to define the number of segments per string. The features involved are implemented to achieve a high level of flexibility of the tool. The number of segments is customizable for every different string and the same applies to the number of series-connected solar cells that constitute each segment. Besides the significant degrees of freedom for defining the PVA layout, to facilitate the user operations and avoid the need for an excessive number of inputs, check-boxes are added to the tool for allowing common configuration for all the different strings and/or segments.

As far as the connections are involved, they are considered at string and section level. Moreover, connections that are used for the realization of the grounding points may be defined as well. The connections' type and configuration are assumed to be the same for the whole PVA, i.e. the connections defined at string level are shared by all the strings. The editable features related to the connections are the number of connections in series between two primary connection points, the connection type, and the redundancy of each connection (if applicable¹). The user may choose between two types of connections: welds and crimps. This choice will then influence the reliability analysis.

For what concerns wires and cables, the user can select whether redundancy is implemented. Please note that the resistance value of all the resistors introduced into the model for redundancy purposes is negligible, i.e. it is equivalent to the lowest value (eps) accepted by a Simulink block. As a consequence, no harness losses are considered in the model.

3.2.5. Solar Array Model Validation

Once the PVA configuration is fully defined, the software is able to automatically build a Simulink model representative of the system (Figure 3.14). To simulate the IV curve of the solar array, a variable voltage source is connected to it, spanning the voltage range $[0V - V_{oc}]$. At this point, another test may be performed to validate the model. This can be done by comparison with the IV curve obtained by scaling the solar cell characteristic equation to account for the number of series-connected solar cells and the number of strings

¹The connections scheme is system-specific and it is not an easy task to allow modeling all the different configurations. Therefore, assumptions have to be made. For instance, two *primary* connection points are the string negative terminal and the negative termination of the first segment within the string. Based on geometry constraints and other factors, several additional connection points may be needed to connect them, hence, the user shall be able to select the number of connection points in series, the type of these connections as well as their respective redundancies. A different assumption is made for the string jumpers and other components terminations, for which a single welding connection point is considered, allowing the user to exclusively modify the redundancy.

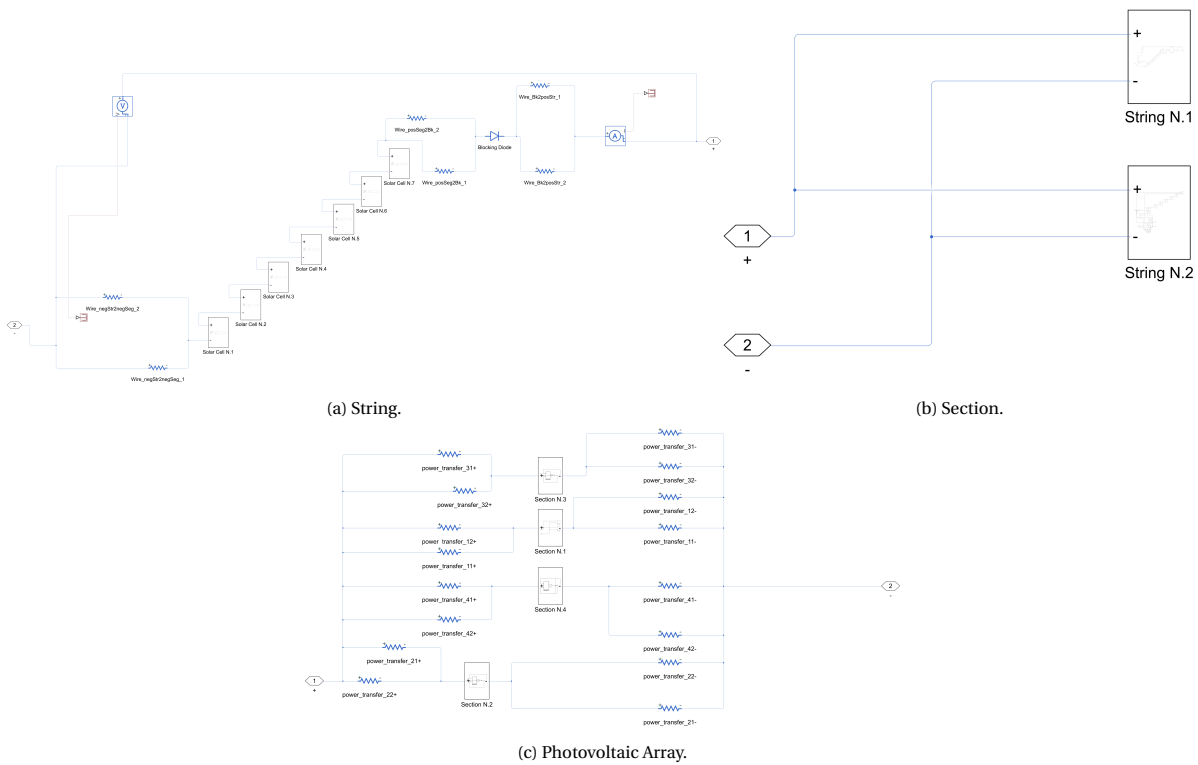


Figure 3.14: Simulink Model of the Photovoltaic Array.

that build up the array. The modified characteristic equation is equation 3.14 [27].

$$I = N_p \cdot I_{ph} - N_p \cdot I_0 \left(\exp \left(\frac{N_p \cdot V + N_s \cdot IR_s}{a_d \cdot N_s \cdot N_p \cdot V_{th}} \right) - 1 \right) - \frac{N_p \cdot V + N_s \cdot IR_s}{N_s \cdot R_{sh}} \tag{3.14}$$

where N_s is the number of cells per string and N_p is the total number of strings. The relative IV curve can be obtained from the tool by selecting **Linear** function and constraining the temperature range to the operating temperature in the Photovoltaic Array Characteristic Curves for different temperatures in the box in Figure 3.12. The comparison is provided in Figure 3.15. As can be seen from the graph, the

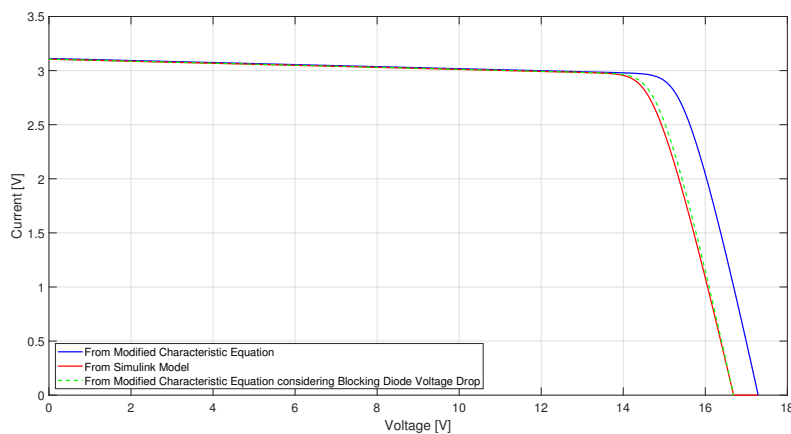


Figure 3.15: IV Curve comparison between the solution of the modified characteristic equation and the Simulink model output.

curves share the same shape but they are shifted along the x-axis by a certain voltage value. Nonetheless, one must consider that the voltage and current measurements in the Simulink model are taken at PVA level. For this reason, a voltage drop is experienced due to the presence of the blocking diodes placed at the positive

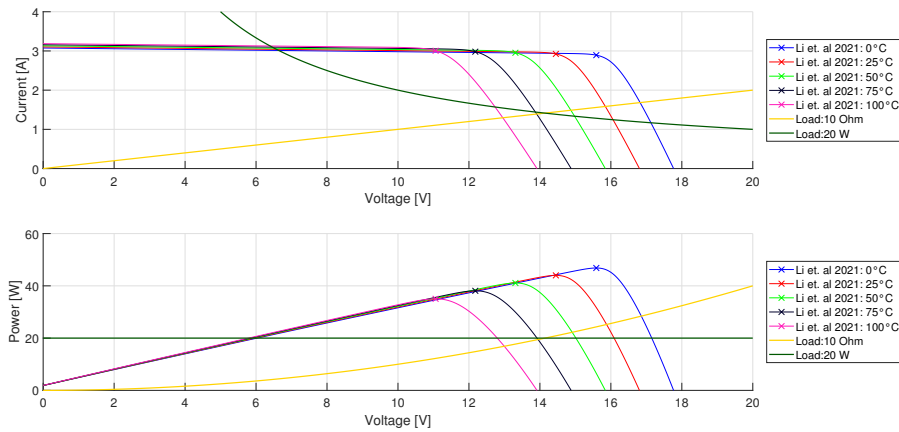


Figure 3.16: Solar Array IV Curve and operating points at different temperatures (@ $G = 1353 \text{ Wm}^{-2}$).

terminal of each string. In this case, the forward voltage is equal to the default value of 0.6V. By accounting for this voltage drop, the green line in the graph is drawn, which almost overlaps with the Simulink model output. The remaining discrepancy arises from the voltage drop due to the diode's resistance, which has a default value of 0.3Ω . Upon this consideration, since the requirement baseline function and performance are correctly and completely implemented in the final Simulink model, the algorithm of the software managing the solar array modeling can be considered validated.

The characteristic curve obtained from the solution of equation 3.14 may be useful to perform another preliminary analysis. In fact, it may be plotted together with the load curve to understand the operating point of the solar array. An example is provided in Figure 3.16 for different temperatures. The two loads considered are a constant resistive load ($R = 10\Omega$) and a constant power load ($P = 20\text{W}$). Focusing on the constant power line, it can be seen that it crosses the IV curve of the solar array in two different locations, one in the current source region and the other in the voltage source region. As explained in [28], only the latter is a stable operating point. When operating in the current source region, a small source or load disturbance would trigger a runaway effect. Assuming, for instance, that a small voltage drop was experienced in the solar array, it would follow an output current lower than the one required by the load, inducing a further decrease of the voltage. Similar behavior is expected for a positive voltage variation. In this case, the excessive output current from the solar array would cause an additional increment in the PVA potential, driving the system away from the correct operating point. This does not happen in the voltage-source region when a potential shift would be followed by a system's response that would properly restore the original conditions. The condition for stability is provided in equation 3.15 [28].

$$\left[\frac{\Delta V}{\Delta I} \right]_{source} > \left[\frac{\Delta V}{\Delta I} \right]_{load} \quad (3.15)$$

This condition suggests that the system is always stable when the solar array is feeding a resistive load. At this point, it is important to highlight a model limitation that prevents recognizing the stable operating point of the system when attached to a power load. Indeed, at $t = 0\text{s}$, Simulink lets the system work at the operating point closest to the initial conditions determined by the defined bus voltage². Nevertheless, it is worth saying that this does not always affect the overall performance of the electrical model, since a solar array regulator will be implemented when performing dynamic analyses, which may drive the output impedance seen by the PVA, thus avoiding the risk of multiple operating points. For flexibility purposes, the user has also the possibility to build the electrical model with no regulators between the source and the load, in which case the aforementioned limitation must be taken into account.

3.3. Solar Array Power Regulation Modeling

The PVA is connected to the load through a SAR. The software, based on Company's needs, offers the possibility to model either the S3R or the MPPT, already introduced in Section 2.4. As these architectures are

²Please note that such behavior is not limited to the customized Solar Cell model. Tests have verified that it extends to the PV models available from the Simscape Electrical library.

extensively adopted for GEO and LEO missions respectively, the software has the capability to study a wide range of satellites.

3.3.1. Sequential Shunt Switching Regulator (S3R)

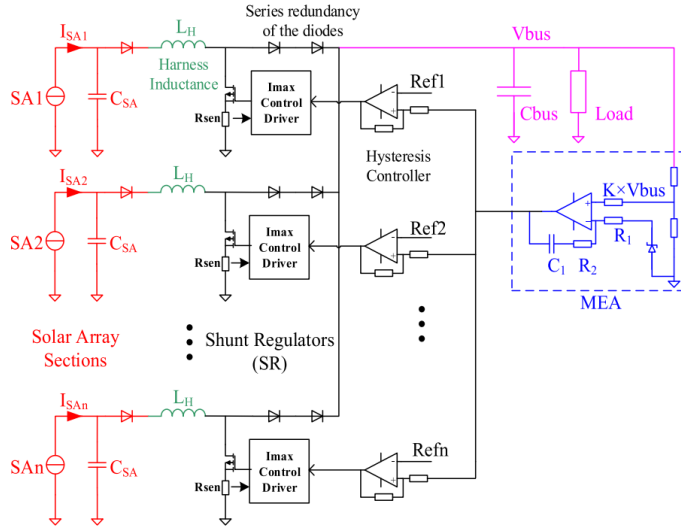


Figure 3.17: S3R model [40].

The S3R circuit is shown in Figure 3.17. The solar array sections are connected to a dedicated shunt regulator. The bus voltage is regulated by the MEA, which controls the switching state of the regulators. The latter may operate in three different modes, determined by the output voltage of the MEA, fed to n hysteresis comparators, one for each section. The shunt regulator may operate either in

- feeding mode: the solar array section delivers power to the bus;
- shunting mode: the switch is *on* and the regulator shunts the solar array output current;
- switching mode: the switch operates alternatively in *on* and *off* condition to provide fine regulation for the bus voltage.

By controlling the commutation of the SA sections, the MEA imposes a step-wise current to the bus, from which the load current is subtracted and the difference builds up the bus voltage on the capacitor C_{bus} . All SA sections are parallel connected to the bus capacitor C_{bus} . The bus voltage is sampled through a resistive divider $K = \frac{V_{ref}}{V_{bus}}$ and is regulated by the MEA Proportional-Integral (PI) compensator, whose output control signal is fed to the hysteresis comparators, characterized by different reference voltages. Since the latter are distributed on different levels, the MEA hysteresis bands increase sequentially, leading to a steady-state condition where only one regulator operates in switching mode, while the others are either fully *on* or *off* [22, 40].

A guideline for the sizing of the S3R is provided in [12] and it is implemented in the software to model the solar array regulator. Several inputs are required from the user, indicated in Table 3.8 with the assigned sample values. The dynamic analysis also requires integration of time-dependent electronic components, such as the section parasitic capacitance³, also involved in the S3R sizing. The capacitance per unit area of a Z4J⁴ within the frequency range [2, 10] kHz is $C_{Z4J} = 107.4 \text{ nF cm}^{-2}$, while the one of the blocking diode is 24.5 nF. For the modeled PVA of a sample satellite (*DemoSat*), whose configuration is given in Table 3.7, the calculated section capacitance is $C_{section} = 4.6313 \times 10^{-8} \text{ F}$.

The sizing of the S3R starts from the definition of the resistances of the voltage divider:

$$R_1 = V_{bus} \cdot (1 - K) \cdot 10^3 \quad (3.16)$$

$$R_2 = V_{bus} \cdot K \cdot 10^3 \quad (3.17)$$

³Section inductance is not considered in the model.

⁴With integrated bypass diode.

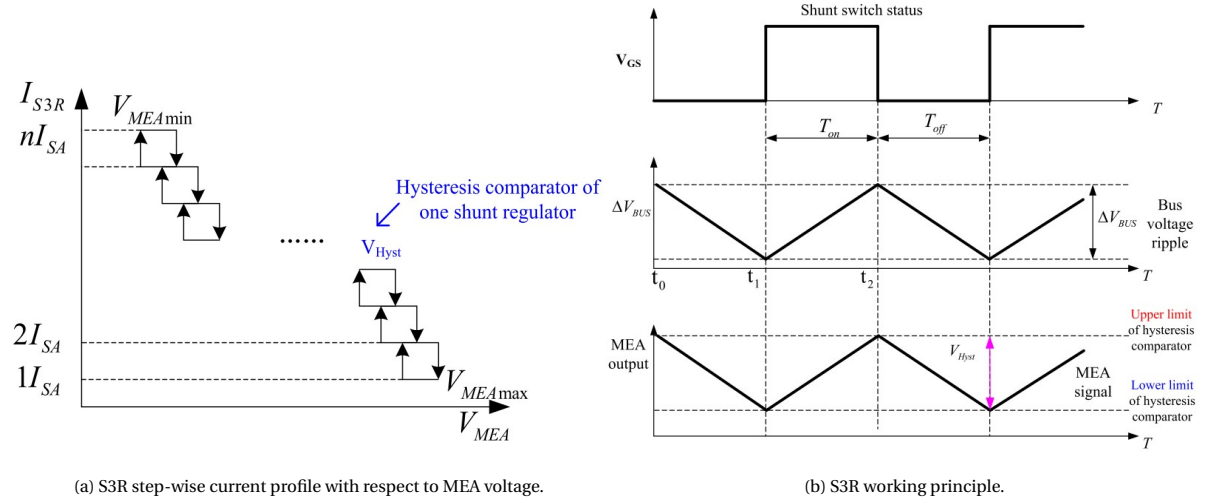


Figure 3.18: Sequential Switching Shunt Regulator [40]

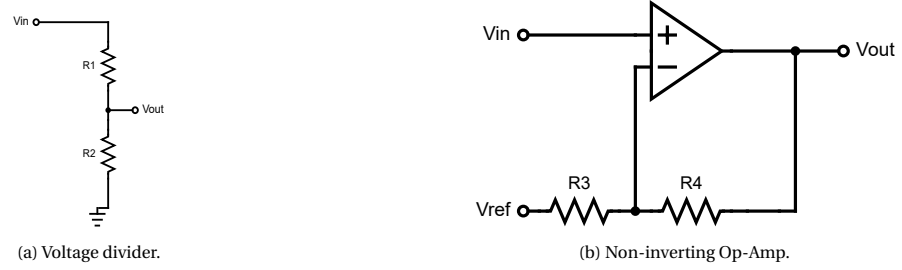


Figure 3.19: S3R elements.

Then, by indicating as I_{section} the output current of a single SA section, the turn *off* delay of the switches may be computed as follows:

$$\tau_{\text{off}} = \tau_{\text{on}} + \frac{C_{\text{section}} V_{\text{bus}}}{I_{\text{section}}} \quad (3.18)$$

Equation 3.19 gives the bus capacitance, determined such to comply with the voltage ripple requirement.

$$C_{\text{bus}} = \frac{I_{\text{section}}}{4\Delta V_{\text{ripple}} f_{\text{max}}} \quad (3.19)$$

From equation 3.19, the voltage ripple with no switching delays may be computed.

$$\Delta V_{\text{ripple}}|_0 = \Delta V_{\text{ripple}} - \frac{I_{\text{section}}}{2C_{\text{bus}}} (\tau_{\text{on}} + \tau_{\text{off}}) \quad (3.20)$$

Moreover, the sections conductance is given in equation 3.21, where n is the total number of sections in the array.

$$G = \frac{nI_{\text{sections}}}{V_{\text{MEA,max}} - V_{\text{MEA,min}}} \quad (3.21)$$

The proportional gain has to be calculated next. In this study, to facilitate the sizing process, it is assumed that the MEA does not contain any integrator, which would anyway have negligible impact, as explained in [12]. The gain is determined as follows:

$$\frac{1}{KZ_{\text{max}}G} \leq A_p \leq \frac{V_{\text{MEA,max}} - V_{\text{MEA,min}}}{K \left(\Delta V_{\text{ripple}}|_0 + (n-1) \frac{I_{\text{section}}}{C_{\text{bus}}} \tau_{\text{off}} \right)} \quad (3.22)$$

Here Z_{max} is the maximum output impedance, constrained by the mask provided in [34], and it is calculated as in equation 3.23, where P_{max} is the maximum delivered power.

$$Z_{\text{max}} = 0.02 \frac{V_{\text{bus}}^2}{P_{\text{max}}} \quad (3.23)$$

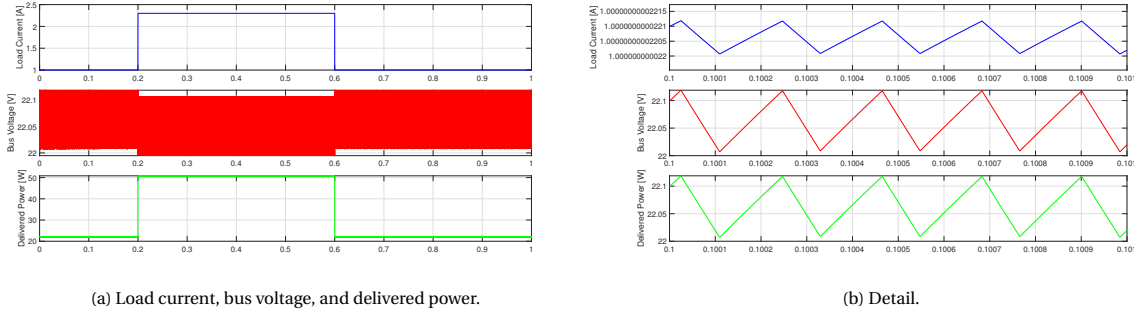


Figure 3.20: Electrical power system output performance.

As suggested in [12], the proportional gain is here chosen equal to the upper extreme of the validity range. To achieve the obtained A_p gain, the assigned values of the Op-Amp resistances are $R_3 = 1 \times 10^3 \Omega$ and $R_4 = A_p \cdot 10^3$. Lastly, the hysteresis voltage V_{hyst} , as well as the voltage gap ΔV_{hyst} between the voltage boundaries of two consecutive switches, is calculated.

$$V_{\text{hyst}} = K A_p \Delta V_{\text{ripple}}|_0 \quad (3.24)$$

$$\Delta V_{\text{hyst}} = \frac{(V_{\text{MEA,max}} - V_{\text{MEA,min}}) - V_{\text{hyst}}}{n - 1} \quad (3.25)$$

The obtained parameters, dependent on the user inputs, are given in Table 3.9.

			Parameter	Unit	Value
			Bus voltage	V	22
			Maximum voltage ripple	% bus voltage	0.5
			Turn on switch delay	s	1
			Maximum delivered power	W	52.9
			Maximum switching frequency	Hz	5000
			MEA maximum voltage	V	10
			MEA minimum voltage	V	2
			MEA reference voltage	V	2
Solar cell	Z4J				
Number of cells / string	7				
Number of strings / section	2				
Number of sections	4				
Number of bypass diodes / cell	1				
Number of blocking diodes / string	1				

Table 3.7: DemoSat PVA configuration.

Table 3.8: S3R user-defined parameters.

Parameter	Unit	Value
K	-	0.091
R_1	k Ω	20
R_2	k Ω	2
C_{section}	F	4.631×10^{-8}
I_{section}	A	0.638
τ_{off}	ms	2.597
C_{bus}	F	2.900×10^{-4}
$\Delta V_{\text{ripple}} _0$	V	0.106
G	AV^{-1}	0.319
A_p	-	714.384
$Z_{\text{max,ECSS}}$	Ω	0.183
$Z_{\text{max,S3R}}$	Ω	0.048
R_3	k Ω	1
R_4	k Ω	714.384
V_{hyst}	V	6.887
ΔV_{hyst}	V	0.371

Table 3.9: Calculated parameter for the S3R.

The table also highlights that the output impedance of the system, calculated as $Z_{\text{max,S3R}} = \frac{1}{A_p G K}$ lies within the ideal impedance mask indicated in [34].

To verify the implementation of the S3R, a simulation is run by connecting a pulse load to the power source and the consistency of the results is checked with respect to the inputs. Such load is modeled as a current generator that drains current from the PVA. The pulse has a period of 1 s, equal to the simulation time, and starts from an initial value of 1 A and reaches a pulsed value of 2.3 A after 0.2 s of delay, which is kept constant for 0.4 s before dropping back to the initial value. The performance of the electrical power system is plotted in Figure 3.20. The upper graph is representative of the load current. As expected, it follows the load profile modeled with negligible impact from the switching condition of the S3R. As far as the bus voltage is concerned, it experiences ripples whose amplitude is constrained below the user input in Table 3.8 ($\Delta V_{\text{ripple}} = 0.11$ V). The lower limit, equal to the indicated bus voltage in this case, as well as the root mean square (RMS) value, depends on the selected proportional gain. The delivered power is obtained by multiplying the bus voltage with the load current. Another relevant analysis involves the different currents flowing through the EPS circuit. In Figure 3.21, the profiles are plotted over the simulation time. In the detail in Figure 3.21b, it is visible that the S3R current, measured upstream the shunting system, is pulse-width modulated according to the voltage ripple

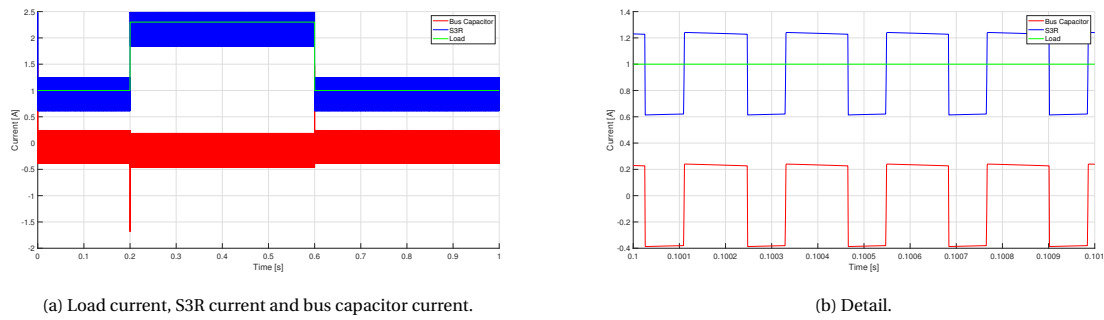


Figure 3.21: EPS currents.

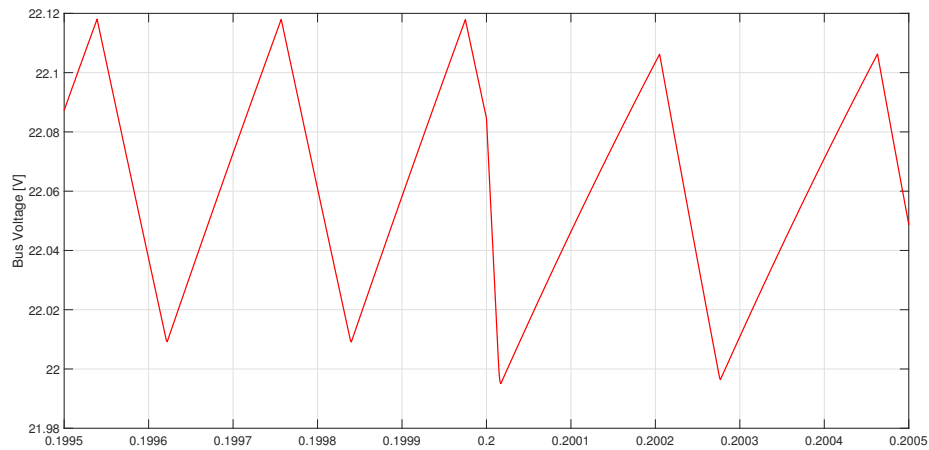


Figure 3.22: Bus voltage response to a positive step of the load current.

requirement. The upper and lower values of the pulse determine the amount of current that flows in and out of the bus capacitor. When the S3R current is higher than the load current, the excess current charges the bus capacitor, increasing the bus voltage. When the upper limit of the latter is reached, constrained by the voltage ripple requirements, the S3R output current is reduced below the required value from the load. Therefore, the bus capacitor starts feeding the load by providing the needed amount of current. As a consequence, the bus voltage decreases until the lower limit is reached and the section path to the ground is opened. The dependence between the current and the bus voltage becomes visible by comparing Figure 3.20b and Figure 3.21b. Moreover, by looking at the positive load current step, a spike in the discharging current of the bus capacitor is measured. This behavior may be explained by the graph in Figure 3.22. It shows that the bus voltage does not drop instantaneously to its lower limit when the load current is stepped up, instead it takes some additional time. During this amount of time, the number of shunted sections remains constant and the load drains a higher amount of current from the bus capacitor.

Lastly, to fully understand the functioning of the S3R, the sections output current is plotted in Figure 3.23. From the graphs, it appears that Section 4 always feeds the bus, as its hysteresis comparator is characterized by the highest voltage reference, while Section 3 is pulse-width modulated when the load current is equal to $I_{load} = 1$ A. Under these conditions, the remaining sections are shunted and do not provide any power. When a positive current step is requested by the load, Section 3 is brought from switching mode to feeding mode together with Section 2, also needed to satisfy the load profile. For $I_{load} = 2.3$ A, Section 1, in switching mode, has the function of keeping the bus voltage constant.

3.3.2. Maximum Power Point Tracker (MPPT)

The MPPT is implemented to achieve the maximum power availability from the PVA, by forcing it to operate at the point where the maximum power is delivered to the system. Despite the development in photovoltaic systems accomplished throughout the years, the energy conversion efficiency of such systems is still relatively low. Therefore, considering that solar energy serves as the main energy source for satellite operations, the

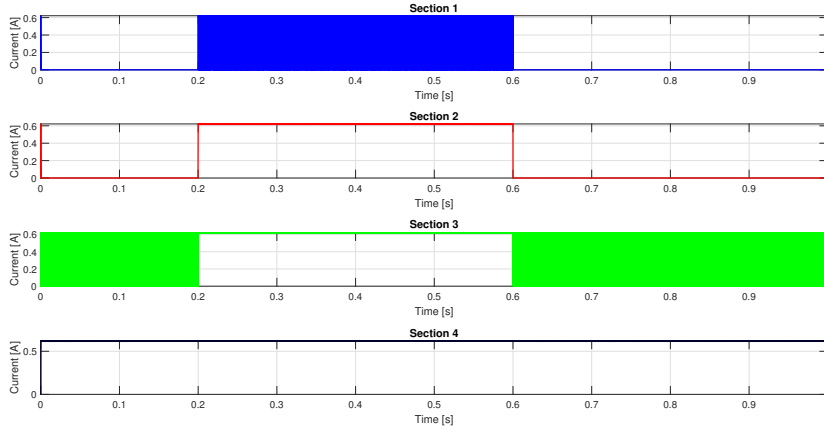


Figure 3.23: Sections output current.

Converter	$M(D)$	Operational Range	
		Constant Output Voltage (V_0)	Resistive Load (R_{load})
Boost	$\frac{1}{1-D}$	$[V_0, \text{open-circuit}]$	$[\text{short-circuit}, \frac{1}{R_{load}}]$

Table 3.10: Boost converter operating ranges.

ability to extract maximum power from the solar array is sometimes crucial for the success of the missions. An MPPT consists of a MPPT controller that interfaces with a conversion stage, a DC/DC converter, which decouples the PVA from the other EPS elements. The MPPT acts on the input voltage or impedance seen by the PVA by dynamically adjusting the duty cycle of the DC/DC converter. By indicating with $M(D) = \frac{V_o}{V_i}$ the voltage conversion ratio achieved by the converter, input voltage, and impedance may be obtained as follows [14]:

$$R_{in}(d) = \frac{R_{load}}{M(D)^2} \quad (3.26)$$

$$V_i(d) = \frac{V_o}{M(D)} \quad (3.27)$$

To date, according to the Company's request, the current version of the software is limited to the implementation of a boost converter, characterized by $M(D) = \frac{1}{1-D}$ ⁵. By substituting the boundary values of the duty cycle, i.e. 1 and 0, the operating range of the MPPT may be obtained based on the connected load (Table 3.10). It is important to note that due to the limitation of the model relative to the power load, explained in Section 3.2.5, the MPPT is not able to operate when connected to such kind of load. Indeed, since the detected PVA operating point lies within the current source region⁶ and the load seen from the solar array behaves like a resistive load, the maximum power point would never be included in the applicability range of the boost converter.

An open-loop controller is implemented, where the output of the MPPT algorithm is the duty cycle of the converter. The Perturb & Observe (P&O) algorithm has been selected and the respective flowchart is shown in Figure 3.24. To accurately model the MPPT, some user defined parameters are needed, grouped in Table 3.11.

⁵ D indicates the duty cycle.

⁶The initial bus voltage is 0V.

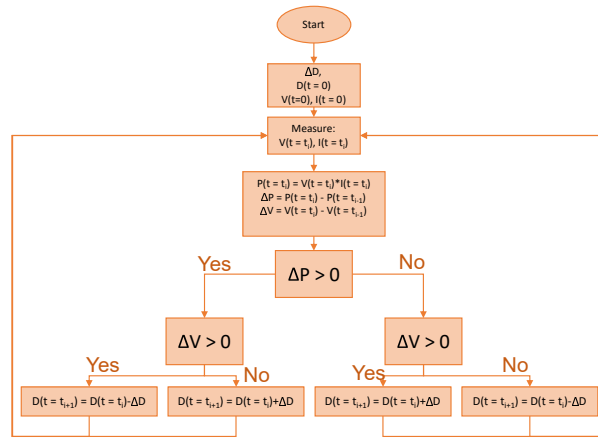


Figure 3.24: Flowchart of the Perturb&Observe algorithm.

Parameter	Unit	Value
Sample&Hold Frequency	Hz	5000
Switching Frequency	Hz	10000
Initial Duty Cycle	-	0.5
Duty Cycle Step-Size	-	0.001
Converter Inductance	H	0.05
Converter Capacitance	F	8×10^{-6}

Table 3.11: MPPT parameters.

Minimum critical values exist for the converter inductance and capacitance to ensure that the respective components operate in continuous conduction mode. For a resistive load, the following formulas hold:

$$L_c = \frac{D(1-D)R_{load}}{2f} \quad (3.28)$$

$$C_c = \frac{D}{2fR_{load}} \quad (3.29)$$

Conditions have to be satisfied for the integration of a stable open-loop controller, however, the control analysis goes beyond the scope of this research. Because of the satisfactory behavior of the system, the parameters in Table 3.11 are chosen. Particular attention must be put on the selection of the Sample&Hold frequency, i.e. the frequency at which the duty cycle is updated by the controller, and the duty cycle step-size, essential to limit the oscillatory behavior of the system around the maximum power point.

For a sample simulation, a resistive load is attached to the EPS of *DemoSat* ($T = 60^\circ\text{C}$), whose value is pulsed from 10Ω to 35Ω at $t = 0.2\text{s}$. The pulse lasts 0.4s while its period is 1s , equal to the simulation time. The simulation output is shown in Figure 3.25. At $t = 0\text{s}$, the PVA voltage is clamped to the operating point deter-

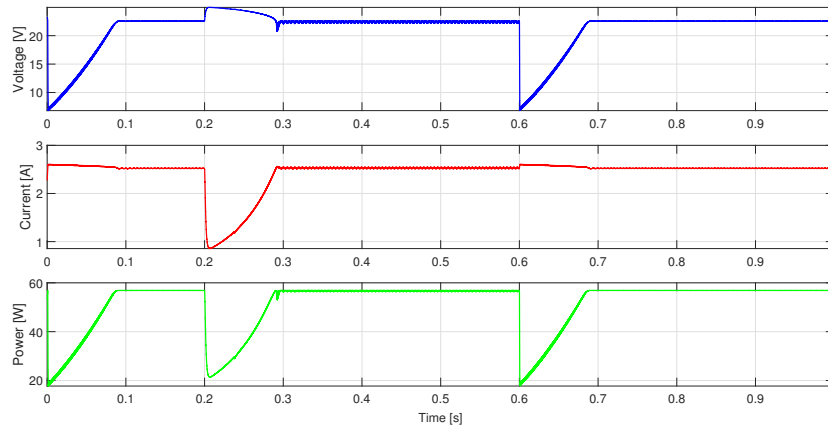


Figure 3.25: MPPT performance: source side.

mined by the intersection of the IV curve with the load line, whose slope is $\frac{1}{R_{load}}$. Then, the voltage suddenly drops according to the value assigned to the initial duty cycle. In this case, since $D|_{t=0} = 0.5$, the load seen by the PVA is equal to $R_{in} = 2.5\Omega$, which brings the operating voltage to $\approx 6.8\text{V}$ ⁷. After that, the PVA voltage starts increasing following a duty cycle decrease imposed by the controller until it stabilizes around its maximum power point at $\approx 22.5\text{V}$ (Figure 3.26 and Table 3.12).

⁷Please note that the voltage value does not drop exactly to the value corresponding to the operating point determined by the initial duty cycle since the latter has been already gone through some controller iterations before the voltage reaches its maximum value.

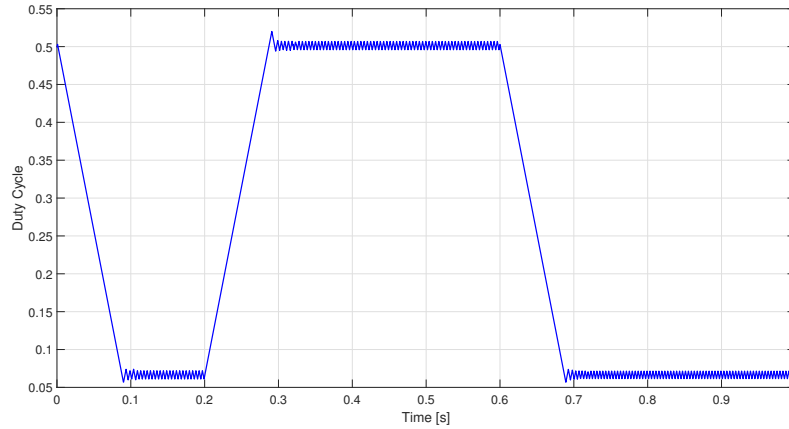
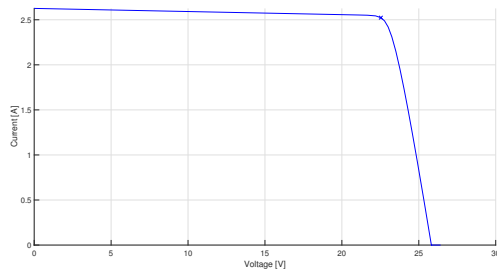


Figure 3.27: Duty cycle variation.

Figure 3.26: IV curve of *DemoSat* @ $T = 60^\circ\text{C}$ and $G = 1353\text{Wm}^{-2}$.

I_{mp}	2.52 A
V_{mp}	22.54 V
P_{mp}	56.87 W
I_{sc}	2.63 A
V_{oc}	25.82 V

Table 3.12: Operating points of *DemoSat* @ $T = 60^\circ\text{C}$ and $G = 1353\text{Wm}^{-2}$.

As soon as the positive resistance step is induced by the load, the solar array voltage experiences a sudden increase, whose magnitude depends on the duty cycle and on the resistance value. The system is brought back to its maximum power point with a settling time that depends on the Sample&Hold frequency and on the duty cycle step-size. When the resistance value falls back to 10Ω , the voltage is decreases before being settled again to deliver maximum power. It is interesting to note that the input voltage after the negative step of the load resistance assumes the same value as the one under initial conditions. This is because the duty cycle at which the boost converter operate for $R_{load} = 35\Omega$ is really close to the initial value of $D = 0.5$, as it may be seen from Figure 3.27. Nevertheless, this may not always be the case, rather it may be considered a coincidence.

4

Failure Modes and Effects Analysis

In this chapter, failure modes affecting the PVA are simulated by means of the developed software and their effects on the output performance are analyzed. It is important to highlight that failure effects are highly dependent on the system configuration. For instance, a short-circuit of one bypass diode would have a different impact based on the number of cells and strings. For this reason, it is not possible to generalize the results obtained by performing FMEA. The *DemoSat*, presented in Section 3.3.1, is taken as reference.

Two different analyses, defined in Section 4.1, may be run to investigate the effects of the failure modes. A static analysis, that focuses on the degradation induced on the characteristic curves of the modeled PVA, is presented in Section 4.2, while Section 4.3 studies the dynamic response of the SAR to the failures considered.

4.1. Analysis Definition

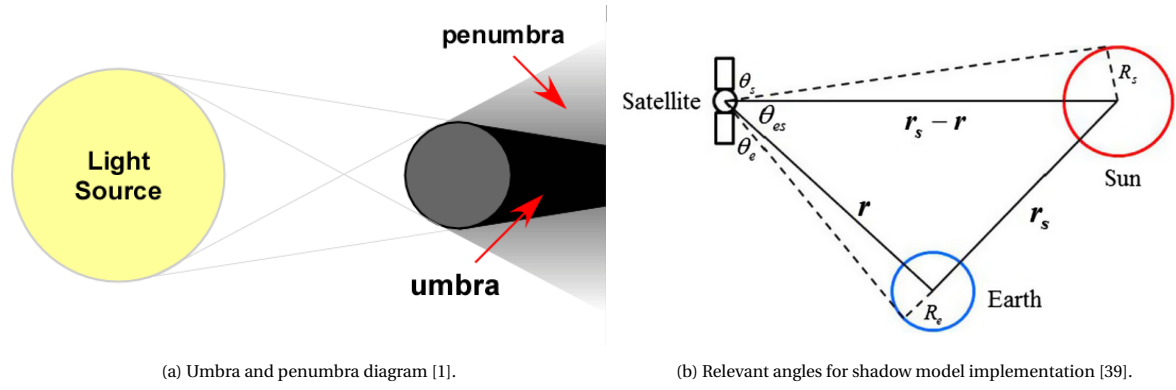
Employing the developed software, two different types of analysis may be performed to investigate different effects on solar array performance. The *static* analysis studies the IV and PV curves of the PVA, and it is carried out by connecting a controlled-voltage source directly to the solar array. As the controlled-voltage source spans a range that goes from short-circuit conditions to V_{oc} , the characteristic curves of the solar array are drawn. The selected simulation time drives the slope of the linear function of the voltage. Given the static nature of the analysis, the capacitance of the solar array is neglected, and the failure modes are modeled by modifying the involved components in the electrical model of the healthy system, i.e. no temporal triggers are implemented.

As far as the dynamic analysis is concerned, the goal is to simulate the behavior of the system during operations and to obtain the relevant wave-forms (voltage, current, and power). This is achieved by replacing the controlled-voltage source with a load. The software offers the possibility to model three types of loads: resistive load, power load, and current load. The latter is implemented with a controlled-current source that drains current from the solar array. Each of these loads may be implemented with three different profiles: constant, step, and pulsed. Even though the limitations explained in Section 3.2.5 must be taken into account, a direct connection is possible between the load and the PVA. To simulate a more realistic behavior of the system, a solar array power regulator may be modeled as described in Section 3.3. The failure modes are in this case triggered at a specific instant in time within the simulation period.

4.1.1. Time-dependent Operating Conditions

When dealing with dynamic analysis, the load profile is not the only factor that influences the behavior of the system. As highlighted in Section 3.1, the PVA output power is highly influenced by temperature and solar irradiance. A major concern for EPS is the transition between sunlight and eclipse, which induces significant temperature variations and high discontinuities in the PVA output power. As a consequence, the implemented electrical model shall be able to accept input temperature and irradiance profiles. These input ports are available in the `Solar Cell` block, making the model suitable for any environmental condition.

As far as the temperature and irradiance profiles are concerned, they are retrieved from a thermal simulation software implemented by RUAG Space. By considering all the relevant thermal radiation sources, the software is able to calculate the temperature profile of the solar panels of a spacecraft, upon definition of its geometry and orbital parameters. A modification has been needed for taking into account the transition of the space-



(a) Umbra and penumbra diagram [1].

(b) Relevant angles for shadow model implementation [39].

Figure 4.1: Shadow model theory.

craft (S/C) within the penumbra region, neglected in the original version of the software. The shadowing effect is considered by introducing a scaling factor for the solar irradiance. The shadow model implemented is described in [39], neglecting the presence of the Moon. To calculate the aforementioned scaling factor, three relevant angles are needed, shown in Figure 4.1b. Please note that the position vectors are relative to the geocentric equatorial coordinate system. θ_e is the apparent radius of the Earth, θ_s is the apparent radius of the Sun and θ_{es} is the apparent separation between the two bodies. The equations for the angles are:

$$\theta_e = \arcsin \frac{R_e}{|\mathbf{r}|} \quad (4.1)$$

$$\theta_s = \arcsin \frac{R_s}{|\mathbf{r}_s - \mathbf{r}|} \quad (4.2)$$

$$\theta_{es} = \arccos \frac{-\mathbf{r}^\top (\mathbf{r}_s - \mathbf{r})}{|\mathbf{r}| |\mathbf{r}_s - \mathbf{r}|} \quad (4.3)$$

By projecting the Sun and the Earth in the direction of the satellite sight, an occulting area may be drawn for the penumbra condition, whose equation is shown in 4.4.

$$S = 2(\blacksquare - \blacktriangle) + 2(\blacklozenge - \blackstar) \quad (4.4)$$

where

$$\blacksquare = \frac{1}{2} \cdot \arccos \frac{\theta_s^2 + \theta_{es}^2 - \theta_e^2}{2\theta_s\theta_{es}} \cdot \theta_s^2$$

$$\blacktriangle = \frac{1}{2} \cdot (\theta_s \cdot \sin \left(\arccos \frac{\theta_s^2 + \theta_{es}^2 - \theta_e^2}{2\theta_s\theta_{es}} \right)) \cdot (\theta_s \cdot \cos \left(\arccos \frac{\theta_s^2 + \theta_{es}^2 - \theta_e^2}{2\theta_s\theta_{es}} \right))$$

$$\blacklozenge = \frac{1}{2} \cdot \arccos \frac{\theta_e^2 + \theta_{es}^2 - \theta_s^2}{2\theta_e\theta_{es}} \cdot \theta_e^2$$

$$\blackstar = \frac{1}{2} \cdot (\theta_e \cdot \sin \left(\arccos \frac{\theta_e^2 + \theta_{es}^2 - \theta_s^2}{2\theta_e\theta_{es}} \right)) \cdot (\theta_e \cdot \cos \left(\arccos \frac{\theta_e^2 + \theta_{es}^2 - \theta_s^2}{2\theta_e\theta_{es}} \right))$$

The spacecraft is in penumbra when $|\theta_e - \theta_s| < \theta_{es} < \theta_e + \theta_s$. Partial occultation is experienced when $\theta_s - \theta_e > \theta_{es}$, for which the area assumes the value of $S = \pi\theta_e^2$. When the S/C crosses the umbra region, then $S = \pi\theta_s^2$. Lastly, in sunlight $S = 0$. From the value of S , the scaling factor for the solar irradiance may be calculated by using equation 4.5.

$$F = 1 - \frac{S}{\pi\theta_s^2} \quad (4.5)$$

Figure 4.2 shows the software output profiles for a sample spacecraft. A unit test is performed to verify the correct implementation of the shadow model. For this purpose, the transition period within the penumbra region given by the software and the one retrieved by analytical calculation are compared. The analytical method follows the guideline provided by a NASA technical report [25]. Figure 4.3 clarifies the parameters involved. The assumed inputs are given in Table 4.1. The penumbra and umbra cone geometries are calculated

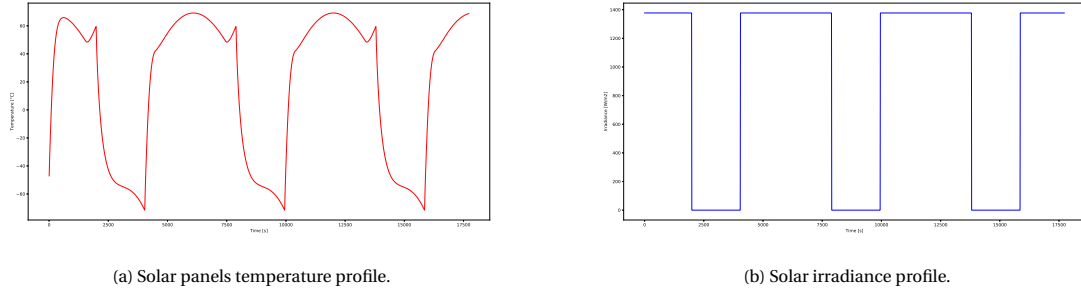


Figure 4.2: Operating conditions profiles for a sample spacecraft.

Orbit	circular
Orbit Altitude	685 km
Earth Radius	6378 km
Earth Mass	5.97×10^{24} kg
Sun Radius	696 340 km
Distance Earth-Sun	1.48×10^8 km
Gravitational constant G	6.67×10^{-11} N m ² kg ⁻²

Table 4.1: Input parameters for the analytical method for calculating the penumbra transition period.

as follows:

$$X_u = \frac{D_p \delta_{p-s}}{D_s - D_p} \tag{4.6}$$

$$\alpha_u = \arcsin \frac{D_p}{2X_u} \tag{4.7}$$

$$X_p = \frac{D_p \delta_{p-s}}{D_s + D_p} \tag{4.8}$$

$$\alpha_p = \arcsin \frac{D_p}{2X_p} \tag{4.9}$$

The points of intersections of the satellite orbit with the umbra and penumbra cones are the so-called terminator points. A pair of points identifies a different transition between sunlight and shadow. By focusing on a single pair of points, two triangles may be drawn by tracing the lines that connect the center of the Earth with the intersection points, as shown in Figure 4.2.

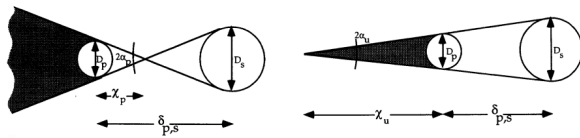


Figure 4.3: Shadow cone surfaces parameters [25].

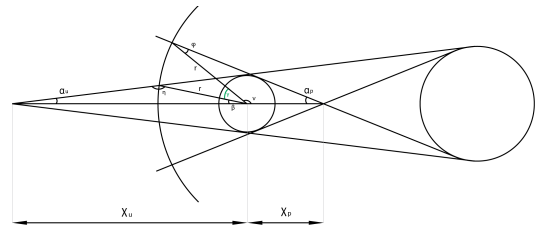


Table 4.2: Umbra and penumbra geometry.

One triangle is delimited by X_p , r^1 and one side of the penumbra cone, while the sides of the other are X_u , r

¹The orbit radius.

and one side of the umbra cone.

$$\eta = \pi - \text{asin}\left(\frac{X_u}{r} \sin \alpha_u\right) \quad (4.10)$$

$$\phi = \text{asin}\left(\frac{X_p}{r} \sin \alpha_p\right) \quad (4.11)$$

$$\beta = \pi - \alpha_u - \eta \quad (4.12)$$

$$\nu = \pi - \alpha_p - \phi \quad (4.13)$$

Then, the angle subtended to the orbit arc within the penumbra region may be calculated as $\gamma = \pi - \beta - \nu$. The angular velocity of the satellite is $\omega_{sc} = \sqrt{\frac{G \cdot M_e}{r^3}}$, from which it follows a penumbra transition period of $T_{\text{penumbra}} = \frac{\gamma}{\omega_{sc}}$, which equals 8.88s for the sample orbit. This is in line with the result retrieved from the RUAG Space software, whose value lies within the range [8 – 10s].

4.2. Static Analysis

In this section the failure modes of the PVA are simulated and their effects investigated in terms of performance reduction. This process will eventually lead to a severity classification of the latter, presented in Chapter 7. The system under analysis is the solar array of *DemoSat*, whose characteristic curves are given in Figure 4.5. The performance are summarized in Table 4.3a. Please note that Figure 4.4 is meant for explanatory purposes and does not refer to the particular PVA layout of *DemoSat*. As the purpose of the research does not relate to the identification of the failure modes but to the investigation of their effects, the faults listed and explained in [29] and [26] are simulated.

I_{mp}	2.48 A
V_{mp}	24.09 V
P_{mp}	59.83 W
I_{sc}	2.59 A
V_{oc}	27.05 V

(a) PVA level.

I_{mp}	0.31 A
V_{mp}	24.09 V
P_{mp}	7.48 W
I_{sc}	0.32 A
V_{oc}	27.05 V

(a) String level.

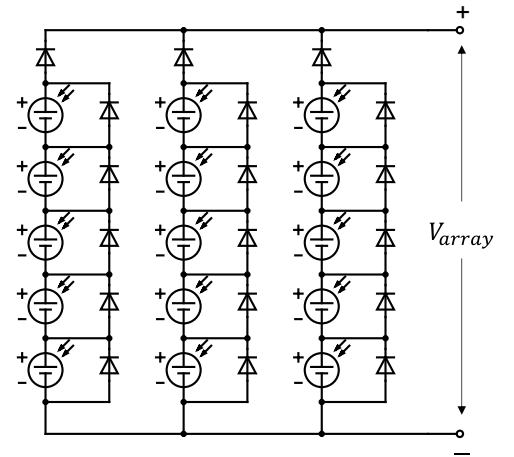
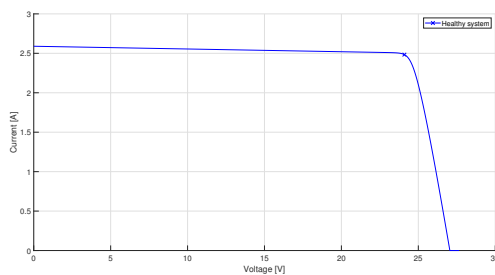
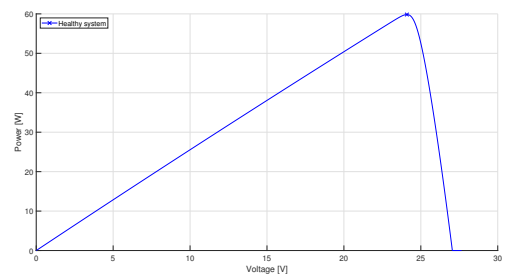


Figure 4.4: Sample PVA layout.

Table 4.5: Performance of the *DemoSat* solar array @ $T = 28^\circ\text{C}$, $G = 1353\text{Wm}^{-2}$.



(a) IV curve.



(b) PV curve

Figure 4.5: Characteristic curves of *DemoSat* solar array @ $T = 28^\circ\text{C}$, $G = 1353\text{Wm}^{-2}$.

4.2.1. Bypass Diode Faults

Three failure modes are considered for the bypass diodes: short-circuit, which may be the consequence of overcurrent and overvoltage, open-circuit, which may be caused by bond wire lift-off, and impedance², whose occurrence may be induced by defects and other failure mechanisms.

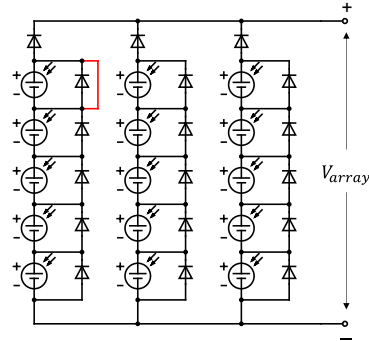


Figure 4.6: Bypass diode: short-circuit fault.

Short-circuit fault The effects of a short-circuit in the bypass diode at string level are shown in Figure 4.7 and Table 4.6. The voltage-source region of the string is strongly affected by the fault as the IV curve is

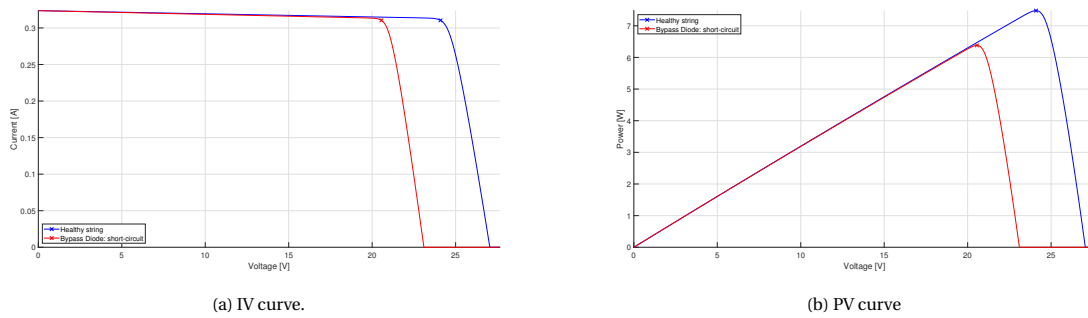


Figure 4.7: Shorted bypass-diode effects at string level on *DemoSat* solar array characteristic curves @ $T = 28^\circ\text{C}$, $G = 1353\text{Wm}^{-2}$.

Bypass Diode: short-circuit fault														
I_{mp}	ΔI_{mp}		V_{mp}	ΔV_{mp}		P_{mp}	ΔP_{mp}		I_{sc}	ΔI_{sc}		V_{oc}	ΔV_{oc}	
0.31A	-0.00A	$-8.95 \times 10^{-3} \%$	20.56V	-3.54V	-14.69%	6.38W	-1.10W	-14.70%	0.32A	-0.00A	-0.01%	23.10V	-3.95V	-14.60%

(a) String level.

Bypass Diode: short-circuit fault														
I_{mp}	ΔI_{mp}		V_{mp}	ΔV_{mp}		P_{mp}	ΔP_{mp}		I_{sc}	ΔI_{sc}		V_{oc}	ΔV_{oc}	
2.46A	-0.02A	-0.86%	21.35V	-2.74V	-11.38%	52.56W	-7.27W	-12.15%	2.59A	-0.00A	-0.00%	27.05V	-0.00V	-0.00%

(b) PVA level.

Table 4.6: Shorted bypass-diode effects on *DemoSat* solar array performance @ $T = 28^\circ\text{C}$, $G = 1353\text{Wm}^{-2}$.

horizontally shifted to the left by the operating voltage of the faulty solar cell. This is justified by the fact that, since the applied voltage remains unchanged, the short-circuit of one cell leads to an increase in the input voltage seen from the remaining cells within the faulty string. This behavior is shown in Figure 4.8.

²Here considered as if the diode behaves like a resistor.

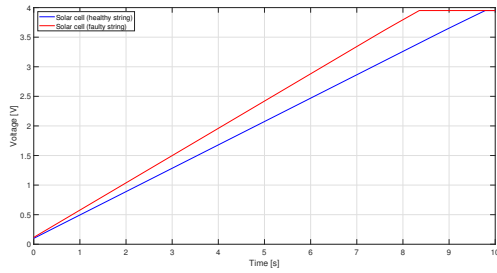


Figure 4.8: Applied voltage seen from the single solar cells within the healthy and faulty string.

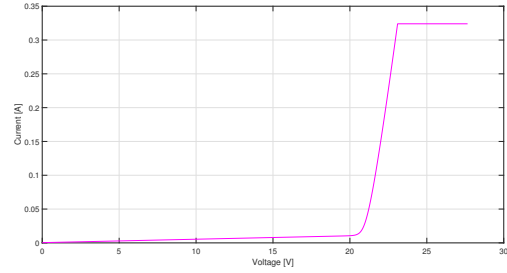
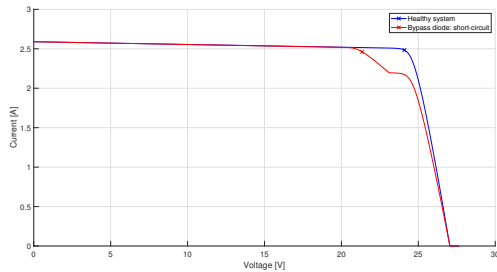
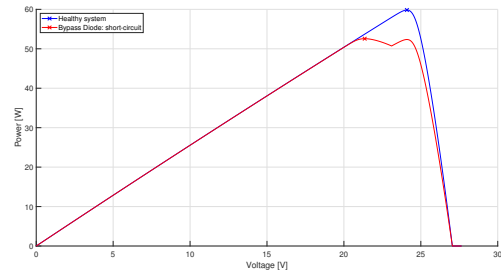


Figure 4.9: Current through the short-circuited connection.

The solar cell connected to the faulty diode always operates at its short-circuit condition. As the current flowing through the string decreases due to the increasing voltage, the excessive output current from the solar cell flows through the short-circuited connection (Figure 4.9). The overall effect at string level is the decrease of the output power by the equivalent output power produced by the faulty cell if it was healthy. In fact, since it operates at short-circuit conditions, its output power is 0W. The graphs in Figure 4.10 show the effects at PVA level. The characteristic curves of the solar array present an inflection point at the open-circuit



(a) IV curve.



(b) PV curve

Figure 4.10: Shorted bypass-diode effects at PVA level on *DemoSat* solar array characteristic curves @ $T = 28^{\circ}\text{C}$, $G = 1353\text{Wm}^{-2}$.

voltage of the string that contains the faulty bypass diode. As long as the voltage of the array is higher than V_{oc} of the involved string, the latter is able to generate current, consistently with the curve in Figure 4.7a. If the voltage increased further, the string would start behaving like a load, draining current from the healthy strings. However, this is prevented by the presence of the blocking diode, which denies a reverse current flow from the bus to the string. Hence, the faulty string keeps operating at its open-circuit condition. Since the blocking diode decouples the string from the bus, the open-circuit voltage of the PVA is not affected by the fault. On the contrary, the voltage at maximum power experiences a significant decrease, leading to a maximum power loss equal to a value that is slightly below the maximum output power of a complete string.

Impedance fault This failure mode is modeled as in Figure 4.11. The output parameters of the system are

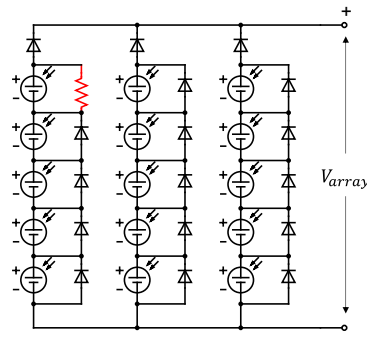


Figure 4.11: Bypass Diode: impedance fault.

dependent on the resistance value that characterizes the fault. Figure 4.12 shows the effects on the character-

Bypass Diode: impedance fault														
$R = 20\Omega$														
I_{mp}	ΔI_{mp}		V_{mp}	ΔV_{mp}		P_{mp}	ΔP_{mp}		I_{sc}	ΔI_{sc}		V_{oc}	ΔV_{oc}	
0.31A	-0.00A	-0.40%	20.90V	-3.19V	-13.24%	6.46W	-1.02W	-13.59%	0.32A	-0.00A	-0.01%	26.86V	-0.19V	-0.70%
$R = 50\Omega$														
0.31A	-0.01A	-1.74%	21.60V	-2.50V	-10.36%	6.59W	-0.89W	-11.92%	0.32A	-0.00A	-0.01%	26.98V	-0.07V	-0.28%

Table 4.7: Effects of the impedance fault of the bypass-diode on *DemoSat* solar array performance at string level @ $T = 28^\circ\text{C}$, $G = 1353\text{Wm}^{-2}$.

istic curves at string level, while Table 4.7 summarizes the impacts on the performance. It can be seen that

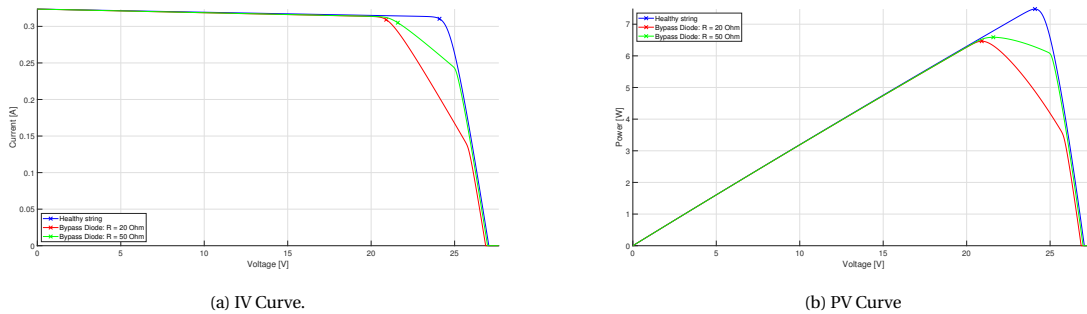


Figure 4.12: Impedance fault of one bypass diode. Effects on *DemoSat* solar array characteristic curve at string level @ $T = 28^\circ\text{C}$, $G = 1353\text{Wm}^{-2}$.

the power loss increases while decreasing the resistance value. By decreases the voltage difference across the solar cells, a lower value of the resistance brings the bypass diode closer to its shorted condition, reducing the output power of the involved solar cell. The graph in Figure 4.13, where the current flowing through the faulty bypass diode is shown, highlights this effect. As the input voltage increases, the solar cell continues to produce a higher amount of current than required. Thus, the excessive current is shunted through the diode. As far as the applied voltage seen from the solar cells is concerned, the considerations are similar to the ones for the previous failure mode. Due to the presence of the resistance, a voltage drop across the faulty solar cell assembly is experienced, which is dependent on the resistance value. As a consequence, the applied voltage seen from the solar cells within the faulty string is subjected to a variation (Figure 4.14a). A significant difference from the short-circuit fault is that, in this case, the affected solar cell is not clamped to work at its short-circuit condition, but the output current has a wave-form similar to the original IV curve, as may be observed in Figure 4.14b. However, due to the presence of the fault, which allows an additional current path, the solar cell does not reach its open-circuit condition but it is eventually clamped to the operating point determined by the fault when the string reaches its V_{oc} .

The effects of the failure mode at PVA level are investigated in Figure 4.15. Since the PVA current output is the sum of the output current from each string, the shape of the characteristic curves follows the one of the faulty string in Figure 4.12. The open-circuit voltage is preserved by the presence of the blocking diode. The impact that the fault has on the PVA performance are summarized in Table 4.8. When no other failure modes

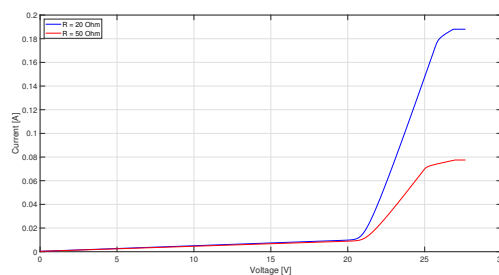
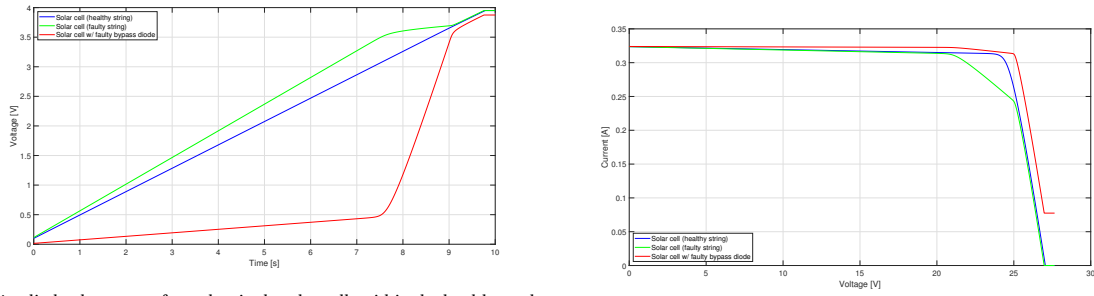


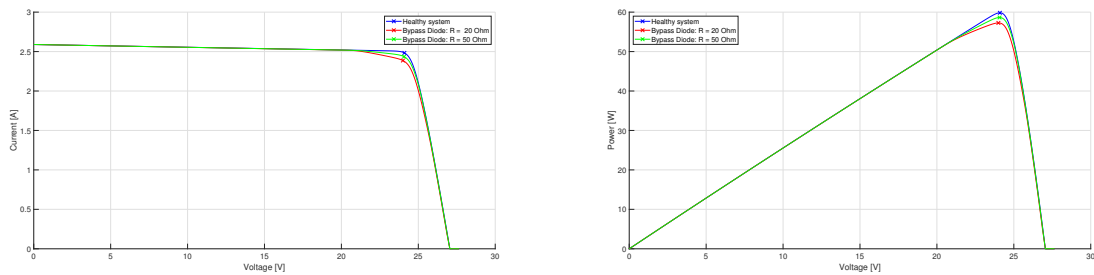
Figure 4.13: Current flowing through the faulty bypass diode.



(a) Applied voltage seen from the single solar cells within the healthy and faulty string.

(b) Output current of the solar cells within the healthy and faulty strings.

Figure 4.14: Impedance fault of one bypass diode ($R = 50\Omega$). Effects on *DemoSat* solar array at solar cell level @ $T = 28^\circ\text{C}$, $G = 1353\text{Wm}^{-2}$.



(a) IV curve.

(b) PV curve.

Figure 4.15: Impedance fault of one bypass diode. Effects on *DemoSat* solar array characteristic curve at PVA level @ $T = 28^\circ\text{C}$, $G = 1353\text{Wm}^{-2}$.

Bypass Diode: impedance fault														
$R = 20\Omega$														
I_{mp}	ΔI_{mp}		V_{mp}	ΔV_{mp}		P_{mp}	ΔP_{mp}		I_{sc}	ΔI_{sc}		V_{oc}	ΔV_{oc}	
2.39A	-0.10A	-3.90%	24.00V	-0.10V	-0.40%	57.27W	-2.57W	-4.29%	2.59A	-0.00A	-0.00%	27.05V	-0.00V	-0.00%
$R = 50\Omega$														
2.44A	-0.05A	-1.90%	24.07V	-0.02V	-0.09%	58.64W	-1.19W	-1.99%	2.59A	-0.00A	-0.00%	27.05V	-0.00V	-0.00%

Table 4.8: Effects of the impedance fault of the bypass-diode on *DemoSat* solar array performance at PVA level @ $T = 28^\circ\text{C}$, $G = 1353\text{Wm}^{-2}$.

are experienced, the impedance fault of the bypass diode may be described as an intermediate condition between nominal operations and the short-circuited state of the same component. From this consideration, it is clear that the worst condition is experienced when the voltage across the cell is equal to zero, i.e. the bypass diode is shorted. As a consequence, the power loss due to an impedance fault may range between $[0, 7.27\text{W}]$ dependently on the impedance value assumed by the bypass diode.

Open-circuit fault In nominal conditions, i.e. when no other failures occur, the bypass diodes are reversed biased, therefore no effects are visible if a bypass diode fails open. This is confirmed by the graphs in Figure 4.19, where no differences may be detected between the characteristic curves of the healthy and faulty system.

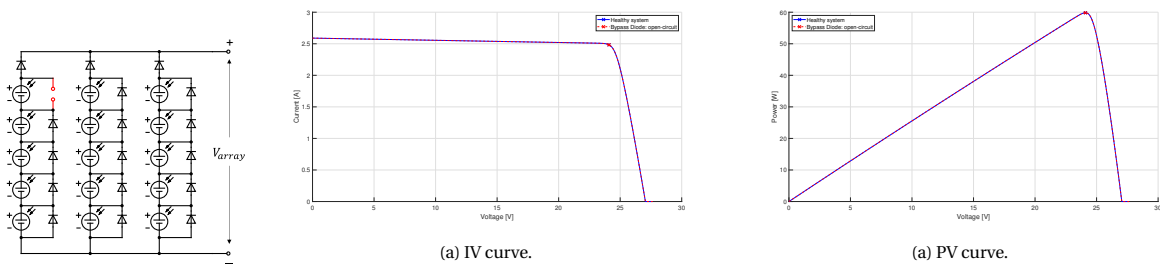


Figure 4.16: Bypass diode: open-circuit fault. Figure 4.19: Open-circuit of one bypass diode. Effects on *DemoSat* solar array characteristic curve at PVA level @ $T = 28^\circ\text{C}$, $G = 1353\text{Wm}^{-2}$.

4.2.2. Blocking Diode Faults

Like for the bypass diodes, the failure modes investigated are short-circuit, open-circuit and impedance.

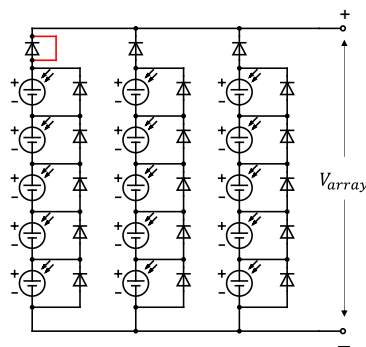


Figure 4.20: Blocking diode: short-circuit fault.

Short-circuit fault The function of the blocking diodes is to decouple the strings from the bus, avoiding the risk of reverse currents should a voltage mismatch be experienced between the different strings. When no mismatch occurs, however, a short-circuit of a blocking diode does not lead to any relevant variation of the PVA performance. As a matter of fact, if the characteristic curves at string level are analyzed, a slight increase in the output power may be detected. The graphs in Figure 4.21 show this behavior. The IV curve is subjected

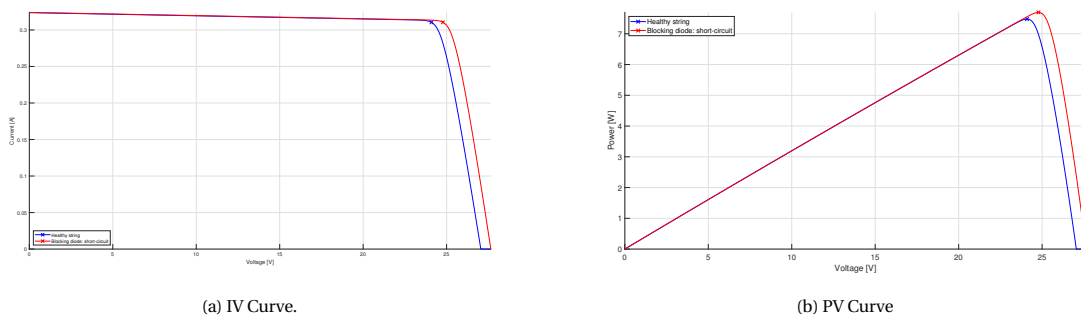


Figure 4.21: Short-circuit of one blocking diode. Effects on *DemoSat* solar array characteristic curve at string level @ $T = 28^\circ\text{C}$, $G = 1353\text{Wm}^{-2}$.

to a horizontal shift towards the right whose magnitude is equal to the voltage drop across the blocking diode. In the simulation, a default value of 0.6V is kept for the forward voltage while the on-resistance is set to 0.3Ω . It is worth saying that this voltage increase is somehow fictitious, i.e. it does not shift the operating points of the string, it is rather dependent on the location where the potential is measured. The voltage measurement is taken at the PVA terminals, downstream of the blocking diodes. This means that in nominal conditions, the strings operate at a voltage that is equal to $V_{\text{string}} = V_{\text{array}} + V_{\text{diode}}$. Therefore, if the string voltage was measured before the blocking diode, the obtained IV curve of the healthy string would match the red curve in

Blocking Diode: short-circuit fault																
I_{mp}	ΔI_{mp}		V_{mp}	ΔV_{mp}			P_{mp}	ΔP_{mp}			I_{sc}	ΔI_{sc}		V_{oc}	ΔV_{oc}	
0.31 A	0.00 A	0.03 %	24.78 V	0.69 V	2.85 %		7.69 W	0.22 W	2.88 %		0.32 A	0.00 A	0.09 %	27.65 V	0.60 V	2.22 %

(a) String level.

Blocking Diode: short-circuit fault																
I_{mp}	ΔI_{mp}		V_{mp}	ΔV_{mp}			P_{mp}	ΔP_{mp}			I_{sc}	ΔI_{sc}		V_{oc}	ΔV_{oc}	
2.48 A	-0.00 A	-0.00 %	24.13 V	0.03 V	0.14 %		59.91 W	0.08 W	0.13 %		2.59 A	0.00 A	0.01 %	27.65 V	0.60 V	2.22 %

(b) PVA level.

Table 4.9: Shorted blocking-diode effects on *DemoSat* solar array performance @ $T = 28^\circ\text{C}$, $G = 1353\text{Wm}^{-2}$.

Figure 4.21a. Nonetheless, it is important to plot the graphs with respect to the voltage of the PVA array since performance requirements are given at system level. For instance, the increase in the open-circuit voltage shall be checked against the relative requirements, which are usually driven by the technical specifications of the electronics found downstream the PVA. For what concerns the increase in the output power, as can be seen from the comparison of Table 4.9a with the graph in Figure 4.22, it corresponds to the power dissipated in the blocking diode. Furthermore, investigating Table 4.9b and Figure 4.23, one may conclude that, if not

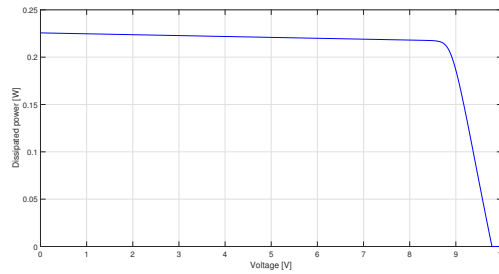


Figure 4.22: Power dissipated in the blocking diode.

combined with other types of failures inducing voltage mismatch between the strings, the short-circuit of one blocking diode does not have a significant impact on the PVA performance. Nonetheless, such a conclusion

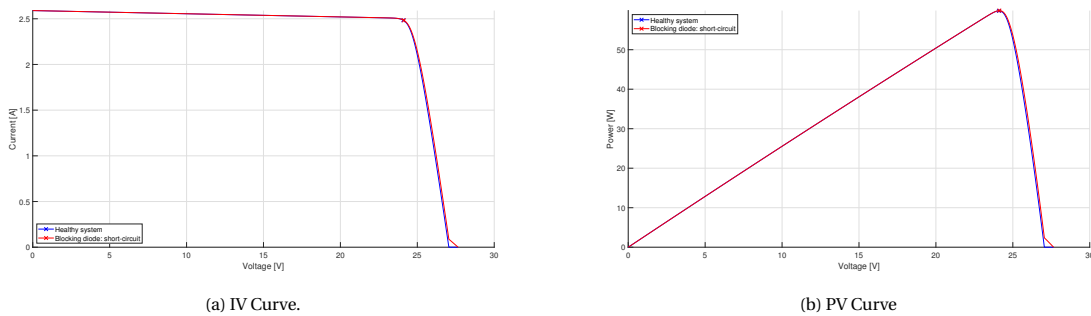


Figure 4.23: Short-circuit of one blocking diode. Effects on *DemoSat* solar array characteristic curve at PVA level @ $T = 28^\circ\text{C}$, $G = 1353\text{Wm}^{-2}$.

must be treated very carefully. As the PVA is a highly dynamic system, it may be affected by disturbances that can lead to the aforementioned voltage mismatch. Therefore a detailed analysis of all the possible scenarios must be performed when assessing the severity of the described failure mode.

Impedance fault When a failure mechanism is triggered such that it brings the blocking diode to behave like a resistor, a voltage drop is experienced across the diode, whose magnitude depends on the resistance value. As a consequence, the voltage seen by the string, i.e. upstream the blocking diode, is also subjected to a variation. For a better understanding of this behavior, the graph in Figure 4.25 is provided.

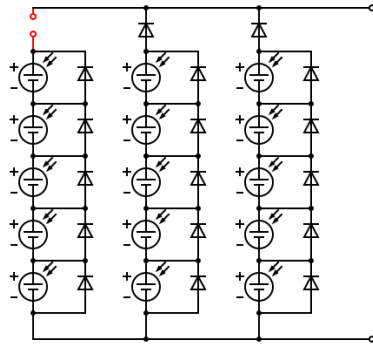


Figure 4.24: Blocking diode: impedance fault.

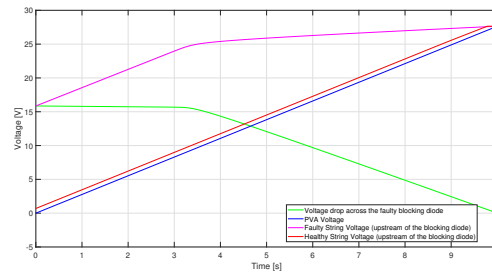
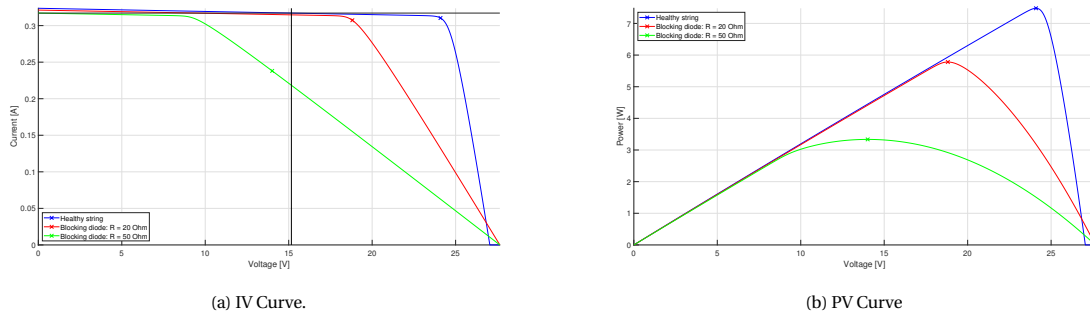


Figure 4.25: Blocking diode impedance fault ($R = 50 \Omega$). Voltage measurements.

The red curve is representative of the voltage seen from a healthy string, upstream of the blocking diode, which determines the output current. Due to the presence of the resistor, the voltage applied to the faulty string (pink curve) is higher, shifted upwards by a value equivalent to the voltage drop across the resistive diode (green curve). The latter is not linear, since it depends on the amount of current flowing through the electrical component. Figure 4.26 shows the effects on the IV and PV curve at string level. Please note that, as for the previous graphs presented in this section, the x-axis refers to the PVA voltage. To further verify the



(a) IV Curve.

(b) PV Curve

Figure 4.26: Impedance fault of one blocking diode. Effects on *DemoSat* solar array characteristic curve at string level @ $T = 28^\circ\text{C}$, $G = 1353\text{Wm}^{-2}$.

considerations made above, a horizontal line may be drawn from the I_{sc} of the IV curve of the system that experiences the fault of the blocking diode with an equivalent resistance of $R = 50 \Omega$. It is found that this line intersects the IV curve of the healthy string at a voltage value which is equal to the voltage seen from the faulty string when the PVA is operating at short-circuit conditions³, i.e. the y-intercept of the pink curve in Figure 4.25. Table 4.10 shows the effects of the impedance fault on the performance at string level, where

Blocking Diode: impedance fault														
$R = 20 \Omega$														
I_{mp}	ΔI_{mp}		V_{mp}	ΔV_{mp}		P_{mp}	ΔP_{mp}		I_{sc}	ΔI_{sc}		V_{oc}	ΔV_{oc}	
0.31A	-0.00A	-1.00%	18.81V	-5.28V	-21.92%	5.78W	-1.70W	-22.70%	0.32A	-0.00A	-0.77%	27.65V	0.60V	2.22%
$R = 50 \Omega$														
0.24A	-0.07A	-23.31%	14.01V	-10.08V	-41.85%	3.34W	-4.14W	-55.41%	0.32A	-0.01A	-2.03%	27.65V	0.60V	2.22%

Table 4.10: Effects of the impedance fault of the blocking-diode on *DemoSat* solar array performance at string level @ $T = 28^\circ\text{C}$, $G = 1353\text{Wm}^{-2}$.

the significant impact of the equivalent resistance value assumed by the diode can be noted. In particular, the latter affects the slope of the IV curve at open-circuit condition, equal to $-\frac{1}{R_s}$, as it increases the series resistance of the string.

³More precisely, it is equal to $V_{PVA} + V_{diode}$.

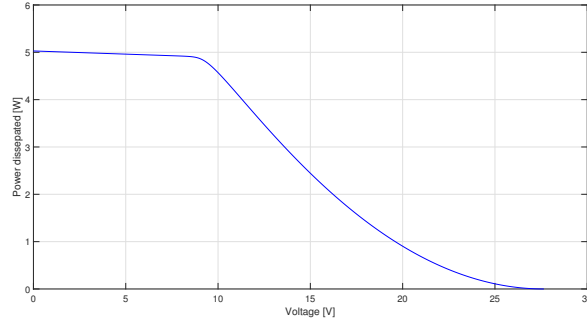


Figure 4.27: Power dissipated through the faulty diode ($R = 50 \Omega$).

A consideration similar to the one discussed for the impedance fault involving a bypass diode may be done, with opposite results. In nominal conditions, the blocking diode is forward biased and allows the string to feed the bus and satisfy the load request. Under such circumstances, the power loss through the diode is relatively low and depends on its forward voltage and on-resistance. As the failure occurs, the diode increases its resistance, leading to an increase in the power dissipated. This may be investigated by comparing the power dissipated through the faulty and healthy diode, Figure 4.27 and 4.22 respectively. It is worth noting that, in this case, since the output current at the maximum output power differs significantly from the one of the healthy string, the maximum power loss registered is not solely traceable to the blocking diode but it also depends on the operating conditions of the string. At PVA level, the same considerations made for the

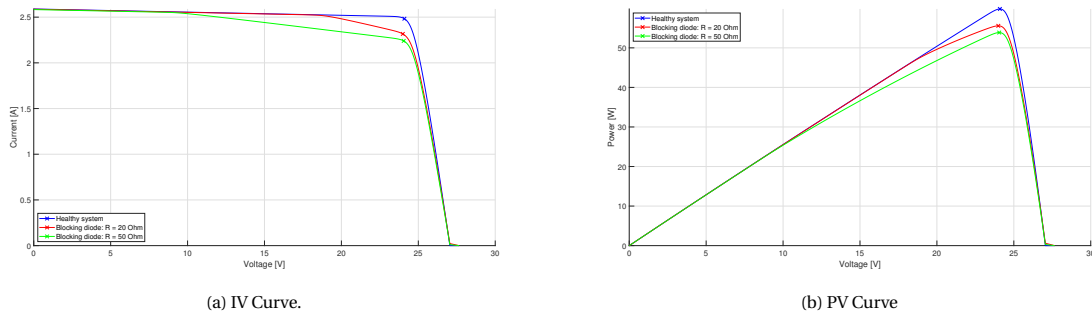


Figure 4.28: Impedance fault of one blocking diode. Effects on *DemoSat* solar array characteristic curve at PVA level @ $T = 28^\circ\text{C}$, $G = 1353 \text{ Wm}^{-2}$.

impedance fault of the bypass diode apply, with the difference that a small increase in the V_{oc} is experienced, whose magnitude is equal to the forward voltage of the blocking diode.

Blocking Diode: impedance fault														
$R = 20 \Omega$														
I_{mp}	ΔI_{mp}		V_{mp}	ΔV_{mp}		P_{mp}	ΔP_{mp}		I_{sc}	ΔI_{sc}		V_{oc}	ΔV_{oc}	
2.31A	-0.17A	-6.72%	23.99V	-0.10V	-0.42%	55.57W	-4.26W	-7.12%	2.59A	-0.00A	-0.10%	27.65V	0.60V	2.22%
$R = 50 \Omega$														
2.24A	-0.24A	-9.80%	24.05V	-0.04V	-0.18%	53.87W	-5.96W	-9.97%	2.58A	-0.01A	-0.25%	27.65V	0.60V	2.22%

Table 4.11: Effects of the impedance fault of the blocking-diode on *DemoSat* solar array performance at PVA level @ $T = 28^\circ\text{C}$, $G = 1353 \text{ Wm}^{-2}$.

Open-circuit fault The open-circuit of a blocking diode leads to the loss of a whole string since it denies the current to flow and feed the bus. The effects at PVA level may be investigated from Figure 4.30 and Table 4.12. As expected, the current loss equals one string current, leading to a decrease in the PVA output power of $P_{pva,loss} = P_{string}$. Since the number of series-connected cells is not subjected to any modification, no effects in terms of voltage are experienced. The open-circuit of a blocking diode may be considered as one of the most severe failures that may occur at PVA level. For this reason, a requirement is usually formulated to ensure that the system can sustain one string failure.

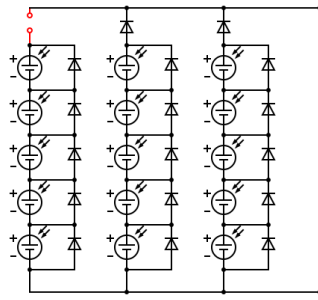


Figure 4.29: Blocking diode: open-circuit fault.

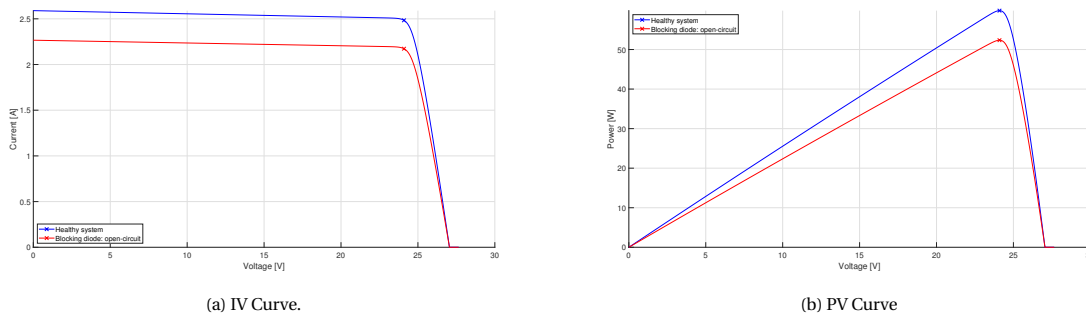


Figure 4.30: Open-circuit of one blocking diode. Effects on *DemoSat* solar array characteristic curve at PVA level @ $T = 28^{\circ}\text{C}$, $G = 1353\text{Wm}^{-2}$.

Blocking Diode: open-circuit fault														
I_{mp}	ΔI_{mp}	V_{mp}	ΔV_{mp}	P_{mp}	ΔP_{mp}	I_{sc}	ΔI_{sc}	V_{oc}	ΔV_{oc}					
2.17A	-0.31A	-12.50%	24.09V	-0.00V	-0.00%	52.35W	-7.48W	-12.50%	2.27A	-0.32A	-12.50%	27.05V	-0.00V	-0.00%

Table 4.12: Open blocking-diode effects on *DemoSat* solar array performance at PVA level @ $T = 28^{\circ}\text{C}$, $G = 1353\text{Wm}^{-2}$.

4.2.3. Line-to-Line Fault

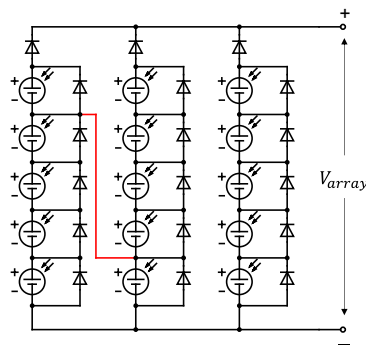


Figure 4.31: Line-to-line fault.

A line-to-line fault is the short-circuit or a low impedance current path that connects two PVA points. It may occur within the same string (intra-string fault) or between two different strings (cross-string fault). To describe the effects on the performance, a cross-string line-to-line fault is modeled, where the short-circuited points of the PVA are located between the 6th and the 7th solar cell and between the 1st and 2nd solar cells of two different strings. A comparison between the characteristic curves of a faulty and healthy string is presented in Figure 4.32. Please note that the faulty string is the one whose shorted point has the highest potential in nominal conditions. For a better visualization of the electrical behavior of the system,

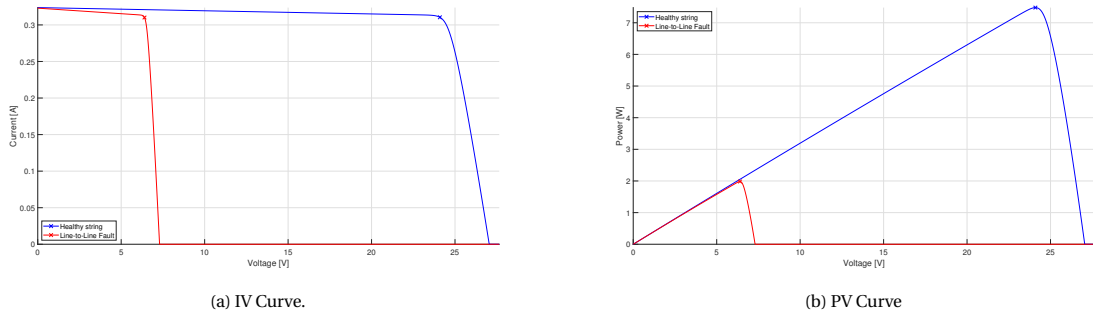


Figure 4.32: Line-to-line fault between the 6th and the 7th solar cell and between the 1st and 2nd solar cells of two different strings. Effects on *DemoSat* solar array characteristic curve at string level @ $T = 28^\circ\text{C}$, $G = 1353\text{ W m}^{-2}$.

Line-to-Line fault														
I_{mp}	ΔI_{mp}		V_{mp}	ΔV_{mp}		P_{mp}	ΔP_{mp}		I_{sc}	ΔI_{sc}		V_{oc}	ΔV_{oc}	
0.31A	-0.00A	-0.10%	6.40V	-17.70V	-73.46%	1.98W	-5.50W	-73.48%	0.32A	-0.00A	-0.23%	7.30V	-19.75V	-73.00%

Table 4.13: Line-to-line fault between the 6th and the 7th solar cell and between the 1st and 2nd solar cells of two different strings. Effects on *DemoSat* solar array performance at string level @ $T = 28^\circ\text{C}$, $G = 1353\text{ W m}^{-2}$.

Figure 4.33 is provided. It may be seen that the first six cells of the faulty string are clamped to the first cell

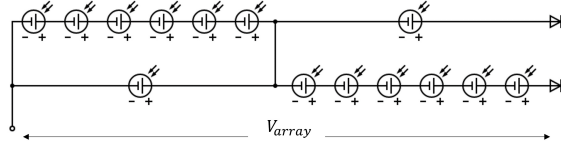


Figure 4.33: Simulated line-to-line fault.

of the healthy string. As a consequence, the characteristic curves of the faulty string are equivalent to those of two series-connected solar cells. This is proved by the values in Table 4.13, where the voltage and power reduction corresponds to the voltage and power of 5 series-connected cells. A more detailed analysis can be performed by investigating the current and voltage wave-forms in Figure 4.34⁴. As the array voltage increases,

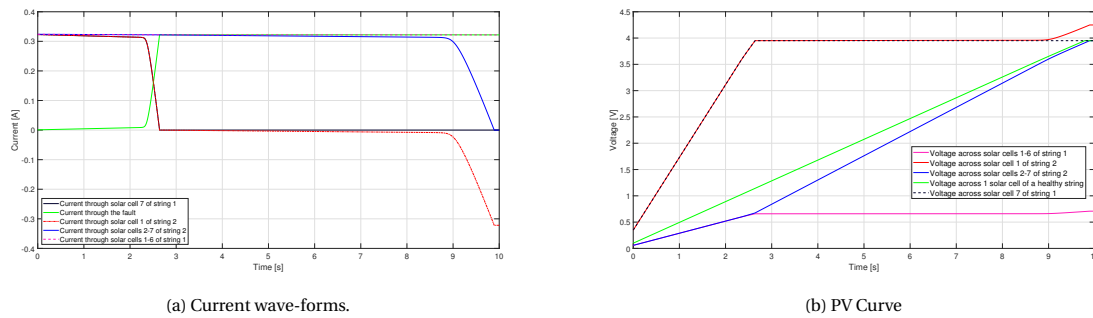


Figure 4.34: Line-to-line fault between the 6th and the 7th solar cell and between the 1st and 2nd solar cells of two different strings. Wave-forms.

so does the voltage applied to the 7th and 1st solar cell of the faulty and healthy string, respectively. Due to the configuration created by the fault, these two cells reach their open-circuit voltage when $V_{PVA} \approx 2 \cdot V_{oc,cell}$. On the other hand, the other cells of the two strings experienced a relatively low increase in voltage, equal to $V_{oc,cell}/5$. At this point, the presence of the blocking diode avoids a further increase of the voltage of the 7th

⁴Please recall that the curves are drawn by connecting a variable voltage source to the PVA that spans a voltage range between 0 and the open-circuit voltage of the solar array in nominal conditions.

cell of the faulty string, which would otherwise drain current from the bus, and an increasing voltage difference is built across the diode. However, the other 6 cells are still clamped to the 1st cell of the healthy string and keep delivering high current, which flows through the fault. Nonetheless, this current does not follow the IV curve of the 6 cells of the healthy string downstream the line-to-line fault, since its value is determined by the voltage difference across the first one. For this reason, the excessive current starts flowing through the latter in the opposite direction. Looking at the IV curve, this means that the voltage difference across the 1st cell of the healthy string grows greater than the open-circuit voltage. This effect becomes significantly visible when the 6 series-connected cells of the healthy string reach their voltage-source region and their output current decreases drastically, and the current through the fault entirely feeds the 1st cell that is behaving like a load. Because of the high slope of the IV curve beyond the open-circuit condition, the aforementioned phenomenon does not increase the voltage across the cells enough to let the 6 series-connected solar cells of the faulty string enter their voltage-source region and decrease their output current. As a consequence, a self-sustained current always flows through the fault even when no power is fed to the bus. The effects at PVA level are shown in Figure 4.35. The impacts on the output parameters are similar to the

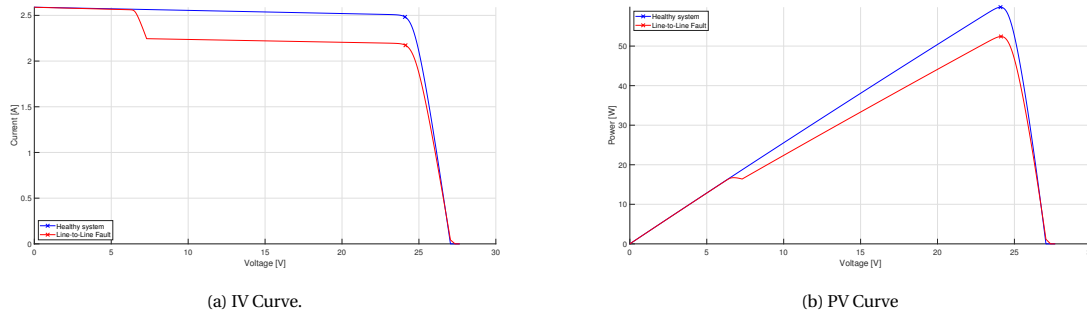


Figure 4.35: Line-to-line fault between the 6th and the 7th solar cell and between the 1st and 2nd solar cells of two different strings. Effects on *DemoSat* solar array characteristic curve at PVA level @ $T = 28^\circ\text{C}$, $G = 1353\text{ W m}^{-2}$.

Line-to-Line fault														
I_{mp}	ΔI_{mp}	V_{mp}	ΔV_{mp}	P_{mp}	ΔP_{mp}	I_{sc}	ΔI_{sc}	V_{oc}	ΔV_{oc}					
2.17A	-0.31A	-12.5%	24.13V	-0.03V	-0.14%	52.42W	-7.41W	-12.38%	2.59A	-0.00A	-0.02%	27.35V	0.30V	1.11%

Table 4.14: Line-to-line fault between the 6th and the 7th solar cell and between the 1st and 2nd solar cells of two different strings. Effects on *DemoSat* solar array performance at PVA level @ $T = 28^\circ\text{C}$, $G = 1353\text{ W m}^{-2}$.

ones caused by the short-circuit of bypass diodes. An inflection point is visible at the open-circuit voltage of the faulty string. Furthermore, a slight increase in the open-circuit voltage of the PVA is experienced, due to the higher voltage across the 1st cell of the healthy string involved in the fault. This leads to a small decrease in the voltage difference applied to the remaining cells, horizontally shifting their IV curve to the right. Furthermore, it is worth saying that the power loss due to a line-to-line fault is highly dependent on the location of the shorted point within the PVA. The greater their voltage difference under nominal conditions, the more severe is the degradation of the output performance. However, although this is always true at string level, when analyzing the PVA performance the relevance of the fault location may have a negligible impact depending on the system configuration and bare cells performance. This will be further explained in Section 4.2.4, where ground faults are investigated.

4.2.4. Ground Fault

Similar to the line-to-line fault, a ground fault is the short-circuit or a low impedance current path between the ground and a current-carrying conductor. The effects at string level are shown in Figure 4.37. All the solar cells upstream of the fault are brought to operate at their short-circuit conditions⁵. As a consequence, a self-sustained current path is generated and the solar cells are not able to provide any power to the load. Therefore, the faulty string is equivalent to a string composed of a number of series-connected solar cells

⁵More precisely, the operating point of the solar cells is determined by the voltage difference between the negative terminal of the string and the ground. In this simulation, $\Delta V = 0$.

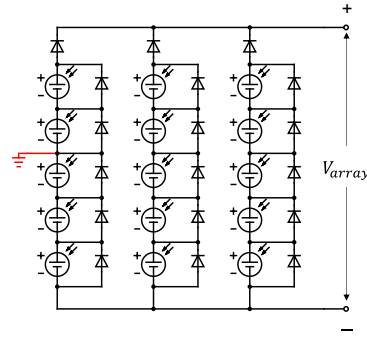


Figure 4.36: Ground Fault.

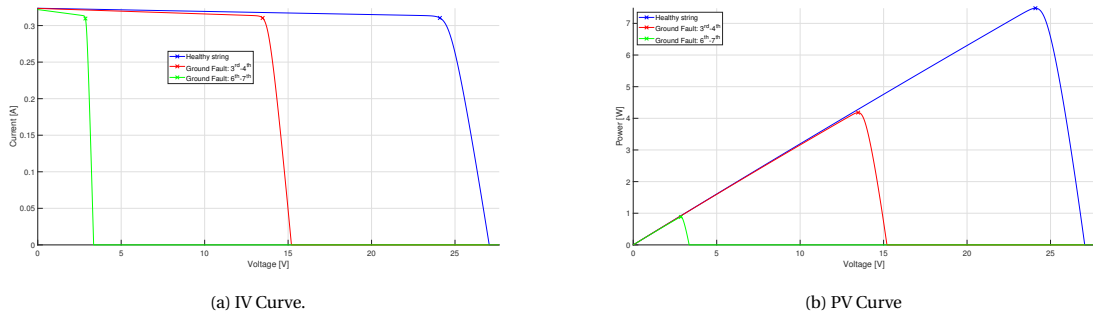


Figure 4.37: Ground fault at different string positions. Between the 3rd and 4th cell and between 6th and 7th cell. Effects on *DemoSat* solar array characteristic curve at string level @ $T = 28^{\circ}\text{C}$, $G = 1353\text{Wm}^{-2}$.

equal to the number of cells downstream of the ground fault. This can be verified by looking at the values in Table 4.15. At PVA level, an inflection point is present at the open-circuit voltage of the faulty string. It

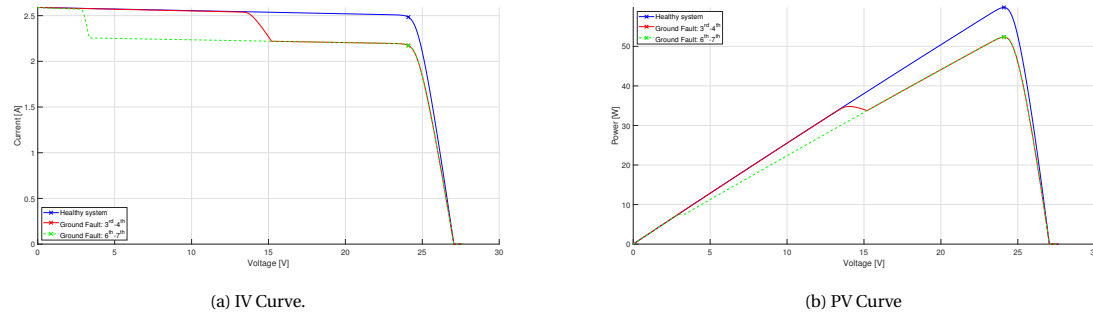


Figure 4.38: Ground fault at different string positions. Between the 3rd and 4th cell and between 6th and 7th cell. Effects on *DemoSat* solar array characteristic curve at PVA level @ $T = 28^{\circ}\text{C}$, $G = 1353\text{Wm}^{-2}$.

can be noted that, even though at string level the location of the ground fault has a significant impact, this does not happen when considering the maximum power point at PVA level, for which such a factor does not

Ground Fault														
Between the 3 rd and 4 th cell														
I_{mp}	ΔI_{mp}	V_{mp}	ΔV_{mp}	P_{mp}	ΔP_{mp}	I_{sc}	ΔI_{sc}	V_{oc}	ΔV_{oc}					
0.31A	-0.00A	-0.02%	13.47V	-10.62V	-44.08%	4.18W	-3.30W	-44.09%	0.32A	-0.00A	-0.07%	15.20V	-11.85V	-43.80%
Between the 6 th and 7 th cell														
0.31A	-0.00A	-0.26%	2.86V	-21.24V	-88.15%	0.88W	-6.59W	-88.18%	0.32A	-0.00A	-0.56%	3.35V	-23.70V	-87.6%

Table 4.15: Ground fault at different string positions. Between the 3rd and 4th cell and between 6th and 7th cell. Effects on *DemoSat* solar array characteristic curve at string level @ $T = 28^{\circ}\text{C}$, $G = 1353\text{Wm}^{-2}$.

Ground Fault														
Between the 3 rd and 4 th cell														
I_{mp}	ΔI_{mp}		V_{mp}	ΔV_{mp}		P_{mp}	ΔP_{mp}		I_{sc}	ΔI_{sc}		V_{oc}	ΔV_{oc}	
2.17A	-0.31A	-12.50%	24.09V	-0.00V	-0.00%	52.35W	-7.48W	-12.50%	2.59A	-0.00A	-0.09%	27.05V	-0.00V	-0.00%
Between the 6 th and 7 th cell														
2.17A	-0.31A	-12.50%	24.09V	-0.00V	-0.00%	52.35W	-7.48W	-12.50%	2.59A	-0.00A	-0.07%	27.05V	-0.00V	-0.00%

Table 4.16: Ground fault at different string positions. Between the 3rd and 4th cell and between 6th and 7th cell. Effects on *DemoSat* solar array characteristic curve at PVA level @ $T = 28^\circ\text{C}$, $G = 1353\text{Wm}^{-2}$.

lead to any variation. This is due to the fact that the maximum power point is always beyond the inflection point, where the faulty string does not provide power. However, such consideration cannot be generalized to all kinds of systems because it depends on the specific layout and solar cells used. Furthermore, the fact that the fault location does not affect the maximum power point alone is not indicative of whether or not any performance degradation is experienced with respect to the load request. Indeed, being the implemented solar array regulator what drives the operating point of the PVA, the unchanged conditions for achieving maximum power point guarantee no performance variations only if a maximum power point tracker is integrated. For all the other solar array regulators, a more detailed analysis is needed to assess whether or not the location of the ground fault is relevant. As mentioned, the same consideration applies to the line-to-line fault. It is important to highlight that the power loss due to the ground fault is usually mitigated by the presence of the bleeding resistors, which limit the leakage current. The latter is calculated as in equation 4.14.

$$I_{\text{leak}} = \frac{V}{R_{\text{bleed}}} \tag{4.14}$$

where V refers to the potential of the PVA point where the failure takes place. It may be inferred from equation 4.14 that, as the voltage increases, so does the leakage current. As soon as the voltage reaches a level such that the output current from the solar cells equals the leakage current, all the cells upstream of the fault start discharging completely through the ground. This is indeed consistent with what was explained before in this section, when no bleeding resistor was present, allowing the fault to drain all the current from the upstream cells. For this reason, the bleeding resistor usually has high resistance, between $2\text{k}\Omega$ and $20\text{k}\Omega$, as stated in [34], decreasing the leakage current and thus limiting the power loss.

4.2.5. Connection Faults

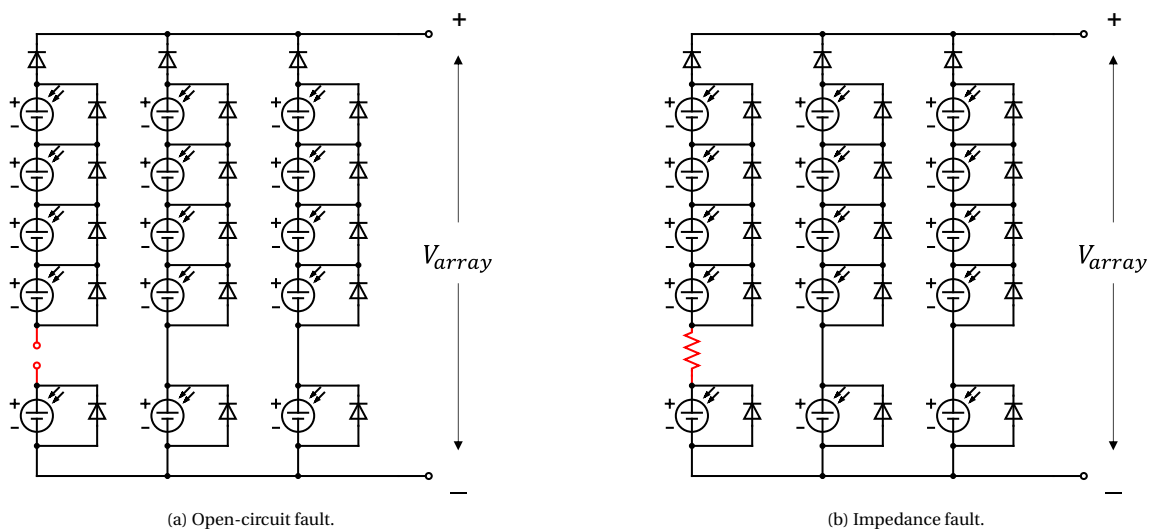


Figure 4.39: Connection Faults.

As far as interconnectors and wires are concerned, two failure modes are analyzed: open-circuit and the increase in resistance value, which can be both caused by thermal cycling.

Open-circuit fault An open-circuit fault of a connection at string level leads to the same effects as a blocking diode in open, i.e. the loss of the complete faulty string. It is worth saying that the open fault modeled involves the interconnector and its implemented redundancies. This is done to clearly show the failure effects, that otherwise would be mitigated by the redundancy. This kind of fault may also occur at section level, leading to the loss of the section.

Impedance Fault An impedance fault involving a connection at string level causes a voltage drop within the string, increasing the voltage difference seen by the solar cells. If no other failures occur, the solar cells work at the same operating point and thus the voltage difference is equally distributed across them, horizontally shifting the string IV curve to the left. Furthermore, the presence of the fault corresponds to an increase in the series resistance of the string. As a consequence, the slope of the curve at open-circuit condition is decreased dependently on the value of the resistance⁶. The effects at string level are documented in Figure 4.40 and Table 4.17. From the curves in Figure 4.40a, the impact of the value of the resistance on the slope of the

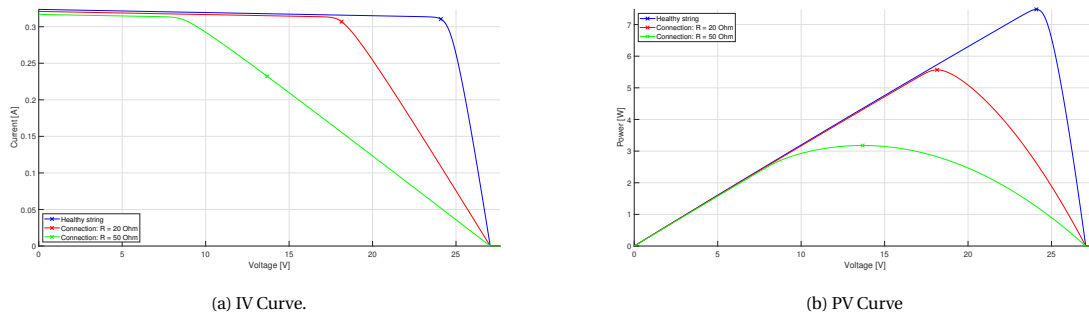


Figure 4.40: Impedance fault of a connection within a string. Effects on *DemoSat* solar array characteristic curve at string level @ $T = 28^\circ\text{C}$, $G = 1353\text{Wm}^{-2}$.

Connection: Impedance Fault														
$R = 20\Omega$														
I_{mp}	ΔI_{mp}		V_{mp}	ΔV_{mp}		P_{mp}	ΔP_{mp}		I_{sc}	ΔI_{sc}		V_{oc}	ΔV_{oc}	
0.31A	-0.00A	-1.14%	18.15V	-5.95V	-24.68%	5.57W	-1.91W	-25.54%	0.32A	-0.00A	-0.86%	27.05V	-0.00V	-0.00%
$R = 50\Omega$														
0.23A	-0.08A	-25.20%	13.68V	-10.41V	-43.21%	53.18W	-4.30W	-57.52%	0.32A	-0.01A	-2.12%	27.05V	-0.00V	-0.00%

Table 4.17: Impedance fault of a connection within a string. Effects on *DemoSat* solar array characteristic curve at string level @ $T = 28^\circ\text{C}$, $G = 1353\text{Wm}^{-2}$.

voltage-source region may be seen. The characteristic curves at PVA level follow the shape respective string curves. If the fault involves a current-carrying conductor at section level, a more significant power loss is

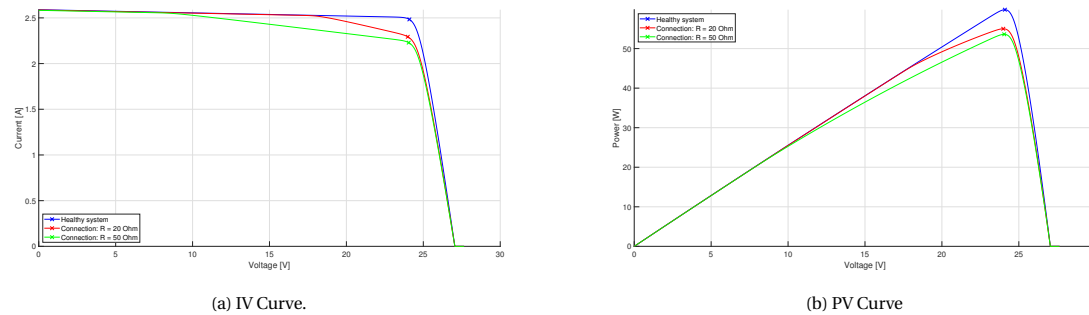


Figure 4.41: Impedance fault of a connection within a string. Effects on *DemoSat* solar array characteristic curve at string level @ $T = 28^\circ\text{C}$, $G = 1353\text{Wm}^{-2}$.

⁶Recall that the slope of the IV curve at V_{oc} is equal to $-\frac{1}{R_s}$.

Connection: Impedance Fault														
$R = 20\Omega$														
I_{mp}	ΔI_{mp}	V_{mp}	ΔV_{mp}		P_{mp}	ΔP_{mp}		I_{sc}	ΔI_{sc}		V_{oc}	ΔV_{oc}		
2.29A	-0.19A	-7.65%	23.99V	-0.11V	-0.44%	55.01W	-4.82W	-8.05%	2.59A	-0.00A	-0.11%	27.05V	-0.00V	-0.00%
$R = 50\Omega$														
2.23A	-0.25A	-10.24%	24.05V	-0.04V	-0.18%	53.61W	-6.22W	-10.40%	2.58A	-0.01A	-0.27%	27.05V	-0.00V	-0.00%

Table 4.18: Impedance fault of a connection within a string. Effects on *DemoSat* solar array characteristic curve at PVA level @ $T = 28^\circ\text{C}$, $G = 1353\text{Wm}^{-2}$.

expected. As a section is composed of a number of parallel-connected strings, the current flowing through the fault is higher, increasing the voltage drop across it. As a consequence, the voltage applied to the string of the faulty section is also considerably higher, depending on the value of the equivalent resistance. This horizontally shifts to the left the IV curve of the strings, with the risk of eliminating completely the current-source region. Furthermore, as already explained, the fault behaves like an additional series resistance of the equivalent section circuit, decreasing the slope of the curve at the open-circuit conditions. These two factors combined generate high power losses.

4.2.6. Shading

The shade is modeled by reducing the solar irradiance input to the selected cells. The effects at string level of one shaded cell are shown in Figure 4.42 for different solar irradiances. As the decrease in the solar irradiance

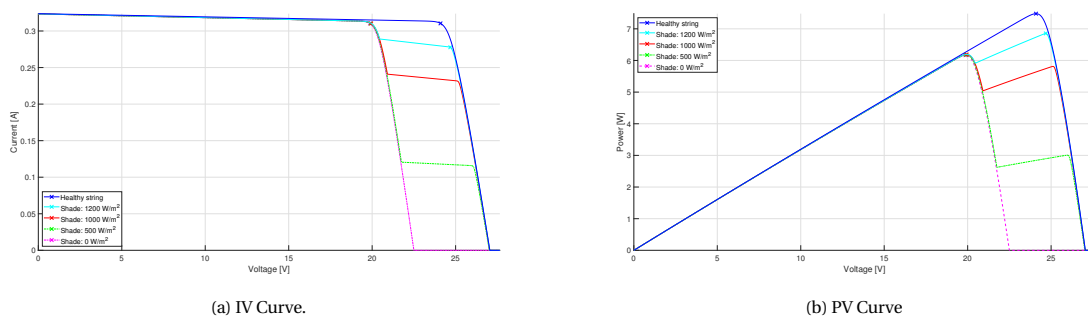


Figure 4.42: Shading of one solar cell for $G = 1200\text{Wm}^{-2}$, $G = 1000\text{Wm}^{-2}$, $G = 500\text{Wm}^{-2}$, and $G = 0\text{Wm}^{-2}$. Effects on *DemoSat* solar array characteristic curve at string level @ $T = 28^\circ\text{C}$, $G = 1353\text{Wm}^{-2}$.

Shading														
$G = 1200\text{Wm}^{-2}$														
I_{mp}	ΔI_{mp}	V_{mp}	ΔV_{mp}		P_{mp}	ΔP_{mp}		I_{sc}	ΔI_{sc}		V_{oc}	ΔV_{oc}		
0.31A	-0.03A	-10.54%	24.68V	0.59V	2.44%	6.85W	-0.62W	-8.35%	0.32A	-0.00A	-0.11%	27.05V	-0.00V	-0.01%
$G = 1000\text{Wm}^{-2}$														
0.31A	-0.00A	-0.04%	19.94V	-4.15V	-17.24%	6.19W	-1.29W	-17.27%	0.32A	-0.00A	-0.11%	27.04V	-0.01V	-0.03%
$G = 500\text{Wm}^{-2}$														
0.31A	-0.00A	-0.04%	19.91V	-4.19V	-17.39%	6.18W	-1.30W	-17.42%	0.32A	-0.00A	-0.12%	27.02V	-0.03V	-0.10%
$G = 0\text{Wm}^{-2}$														
0.31A	-0.00A	-0.05%	19.87V	-4.22V	-17.54%	6.16W	-1.31W	-17.57%	0.32A	-0.00A	-0.12%	22.50V	-4.55V	-16.81%

Table 4.19: Shading of one solar cell for $G = 1200\text{Wm}^{-2}$, $G = 1000\text{Wm}^{-2}$, $G = 500\text{Wm}^{-2}$, and $G = 0\text{Wm}^{-2}$. Effects on *DemoSat* solar array performance at string level @ $T = 28^\circ\text{C}$, $G = 1353\text{Wm}^{-2}$.

reduces the output current capability of the shaded solar cell, the overall effect at string level is the presence of an inflection point within the voltage-source region of the IV curve of the system composed of the illuminated solar cells. After this point, the output current reduces to the one provided by the shaded cell. The graphs in Figure 4.43 are provided for a more detailed analysis of the impact of the shade. Initially, the shaded cell is reverse biased and, consistently with its IV curve, it drains an amount of current that is close to its short-circuit

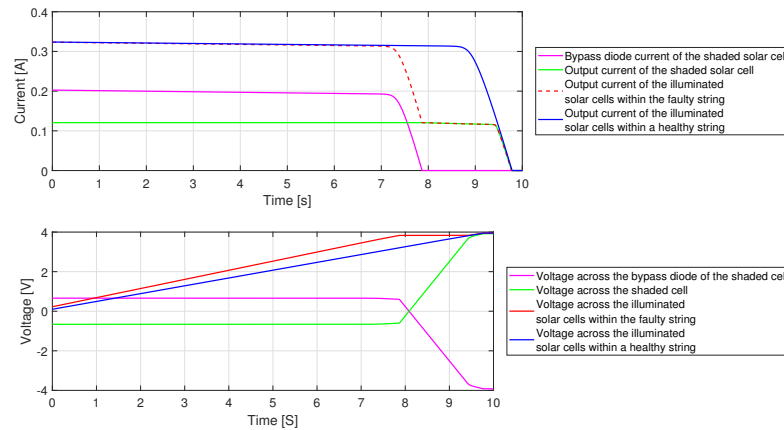


Figure 4.43: Shading of 1 solar cell ($G = 500 \text{ Wm}^{-2}$). Currents and voltages.

current. As mentioned, due to the shade, such an amount of current is lower than the output current from the illuminated solar cells and the excessive current flows through the bypass diode, which is forward biased. This condition remains stable until the voltage-source region of the illuminated solar cells is reached. At this point, the output current decreases while a bias switching is triggered between the shaded solar cell and its bypass diode. Once the level of current falls to the achievable output current of the shaded solar cell, the IV curve experiences the aforementioned inflection point. Moreover, slight variations are also experienced in the open-circuit voltage and in the short-circuit current. The small decrease in the former is due to the weak dependence of the open-circuit voltage on the irradiance, while the limited reduction of the short-circuit current is determined by the operating point of the assembly of the shaded cell with its bypass diode. The latter may be determined by analyzing the graph in Figure 4.44. The characteristic curve of the assembly is

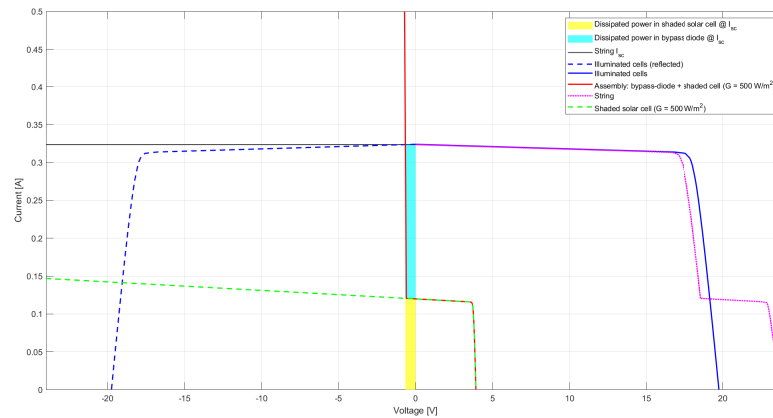


Figure 4.44: Analysis of the characteristic curves under shading condition.

shown in red, while the IV curve of all the series-connected illuminated solar cells is drawn in blue. When the string is operating at short-circuit the following relationship must be satisfied:

$$V_{\text{string}} = \sum_{i=1}^n V_i + V_{\text{shaded cell}} = 0 \quad (4.15)$$

where n is the number of illuminated cells. The solution of this equation may be retrieved by reflecting the blue line with respect to the y-axis. The point of intersection between the reflected curve and the operating curve of the shaded solar cell assembly gives the I_{sc} of the string. Furthermore, the graph also shows the current flowing through the bypass diode and the current flowing through the shaded cell, highlighting the power dissipated by the two components (yellow and light-blue areas). Lastly, by plotting the IV curve of the

shaded solar cell alone, it becomes clear the high impact that the bypass diode has on the reduction of the power loss due to the current mismatch for series-connected cells. If no diode was integrated, the I_{sc} would drastically decrease to the intersection between the blue and green line, with a significant power dissipated by the shaded solar cell.

As can be seen from Figure 4.45b, as far as the shape of the curve is concerned, the impact of the simulated

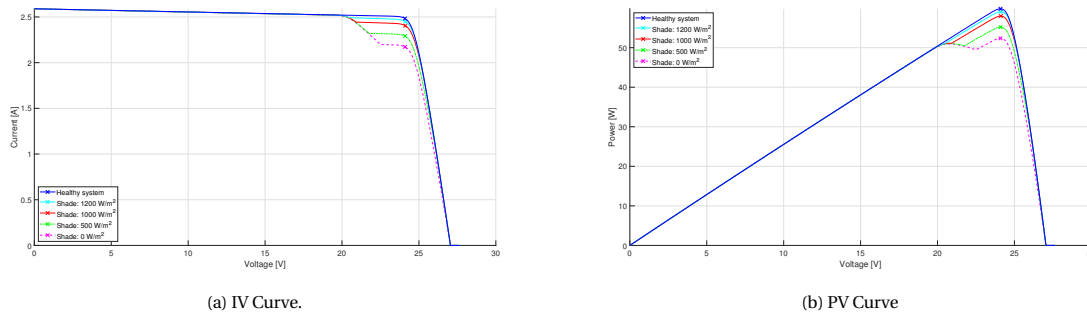


Figure 4.45: Shading of one solar cell for $G = 1000 \text{ W m}^{-2}$, $G = 500 \text{ W m}^{-2}$, and $G = 0 \text{ W m}^{-2}$. Effects on *DemoSat* solar array characteristic curve at PVA level @ $T = 28^\circ\text{C}$, $G = 1353 \text{ W m}^{-2}$.

shade is reflected similarly at PVA level, i.e. the inflection points are experienced at the same voltage levels of the string. However, if the focus is put on the maximum power point, a significant difference may be noted between the effects at string level and the ones at PVA level. Figure 4.42a and Table 4.19 highlight that the value assumed by the solar irradiance of the shaded cell may set the maximum power condition either on the reverse biased or in the forward-biased region of the shaded solar cell. The lower the solar intensity that reaches the shaded solar cell, the lower the output current of the latter region, which likely would not include the maximum power point. Therefore, under a certain solar irradiance threshold, the shade intensity has no impact on the location of the Maximum Power Point (MPP), as it constantly lies in the reverse biased region of the shaded cell. As a consequence, below the aforementioned threshold value, the power loss at string level is more or less constant regardless of the light intensity. Nevertheless, this behavior is not reflected when the performance at PVA level are investigated. Table 4.20 shows that the value of the solar intensity always affects

Shading														
$G = 1200 \text{ W m}^{-2}$														
I_{mp}	ΔI_{mp}	V_{mp}	ΔV_{mp}	P_{mp}	ΔP_{mp}	I_{sc}	ΔI_{sc}	V_{oc}	ΔV_{oc}					
2.45A	-0.03A	-1.34%	24.12V	0.02V	0.10%	59.09W	-0.74W	-1.24%	2.59A	-0.00A	-0.01%	27.05V	-0.00V	-0.00%
$G = 1000 \text{ W m}^{-2}$														
2.40A	-0.08A	-3.16%	24.12V	0.02V	0.09%	57.99W	-1.84W	-3.08%	2.59A	-0.00A	-0.01%	27.05V	-0.00V	-0.00%
$G = 500 \text{ W m}^{-2}$														
2.29A	-0.19A	-7.79%	24.10V	0.01V	0.06%	55.20W	-4.64W	-7.75%	2.59A	-0.00A	-0.02%	27.05V	-0.00V	-0.00%
$G = 0 \text{ W m}^{-2}$														
2.17A	-0.31A	-12.50%	24.09V	0.00V	0.00%	52.35W	-7.48W	-12.50%	2.59A	-0.00A	-0.03%	27.05V	-0.00V	-0.00%

Table 4.20: Shading of one solar cell for $G = 1200 \text{ W m}^{-2}$, $G = 1000 \text{ W m}^{-2}$, $G = 500 \text{ W m}^{-2}$, and $G = 0 \text{ W m}^{-2}$. Effects on *DemoSat* solar array performance at PVA level @ $T = 28^\circ\text{C}$, $G = 1353 \text{ W m}^{-2}$.

the MPP at PVA level. This, however, is dependent on the PVA layout. For the modeled configuration, the IV curve is such that the maximum power point is reached within the region where the output current of the string that includes the shaded solar cell is constrained to the output power of the latter. If, for instance, a lower number of strings was present, the MPP might be achieved where the shaded cell is reverse biased. In that case, the degree of shade would not affect the maximum power point of the PVA.

It is important to stress that the results presented above are specifically representative of the shading of a single solar cell. Nevertheless, shade has different impacts depending on the pattern and intensity of the solar irradiance. For this reason, another analysis is carried out where two solar cells are shaded within the same string with a pattern that induces different intensities of the light impinging on them. The difference with respect to a uniform shadow is visible from the graphs in Figure 4.46. The presence of multiple inflection points is indicative of different shading conditions involving multiple solar cells. For the simulated cases, the

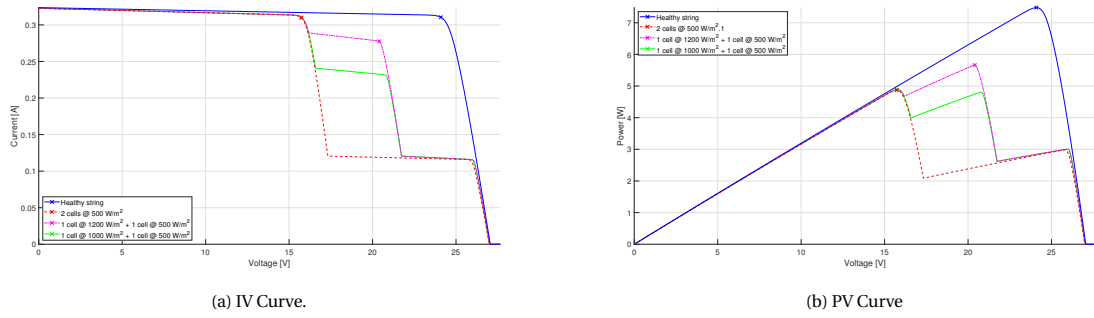


Figure 4.46: Shading of two solar cells for different solar irradiances. Effects on *DemoSat* solar array characteristic curve at string level @ $T = 28^\circ\text{C}$, $G = 1353\text{ Wm}^{-2}$.

Shading														
2 solar cells @ $G = 500\text{ Wm}^{-2}$														
I_{mp}	ΔI_{mp}	V_{mp}	ΔV_{mp}	P_{mp}	ΔP_{mp}	I_{sc}	ΔI_{sc}	V_{oc}	ΔV_{oc}					
0.31A	-0.00A	-0.13%	15.72V	-8.38V	-34.76%	4.87W	-2.61W	-34.84%	0.32A	-0.00A	-0.29%	27.00V	-0.06V	-0.21%
1 solar cell @ $G = 1200\text{ Wm}^{-2}$ and 1 solar cell @ $G = 500\text{ Wm}^{-2}$														
0.28A	-0.03A	-10.56%	20.40V	-3.70V	-15.34%	4.87W	-1.82W	-24.28%	0.32A	-0.00A	-0.28%	27.02V	-0.03V	-0.12%
1 solar cell @ $G = 1000\text{ Wm}^{-2}$ and 1 solar cell @ $G = 500\text{ Wm}^{-2}$														
0.31A	-0.00A	-0.12%	15.76V	-8.34V	-34.61%	4.88W	-2.59W	-34.69%	0.32A	-0.00A	-0.28%	27.01V	-0.04V	-0.14%

Table 4.21: Shading of two solar cells. Effects on *DemoSat* solar array performance at string level @ $T = 28^\circ\text{C}$, $G = 1353\text{ Wm}^{-2}$.

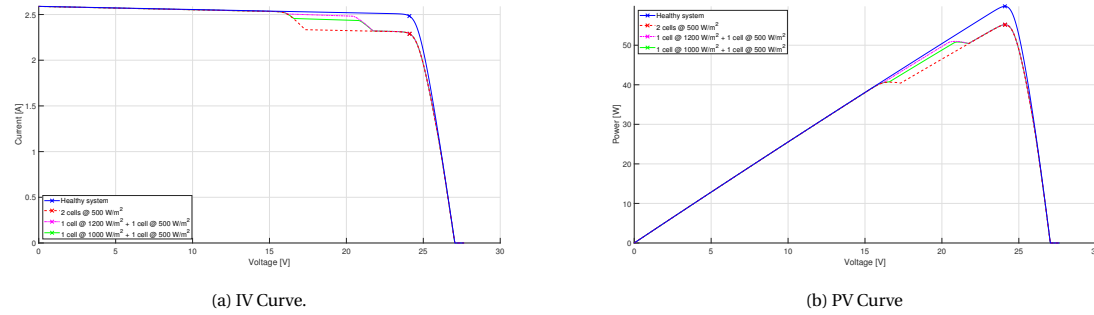


Figure 4.47: Shading of two solar cells for different solar irradiances. Effects on *DemoSat* solar array characteristic curve at PVA level @ $T = 28^\circ\text{C}$, $G = 1353\text{ Wm}^{-2}$.

Shading														
2 solar cells @ $G = 500\text{ Wm}^{-2}$														
I_{mp}	ΔI_{mp}	V_{mp}	ΔV_{mp}	P_{mp}	ΔP_{mp}	I_{sc}	ΔI_{sc}	V_{oc}	ΔV_{oc}					
2.29A	-0.19A	-7.84%	24.11V	0.01V	0.05%	55.17W	-4.66W	-7.80%	2.59A	-0.00A	-0.04%	27.05V	-0.00V	-0.00%
1 solar cell @ $G = 1200\text{ Wm}^{-2}$ and 1 solar cell @ $G = 500\text{ Wm}^{-2}$														
2.29A	-0.19A	-7.79%	24.11V	0.01V	0.05%	55.20W	-4.64W	-7.75%	2.59A	-0.00A	-0.03%	27.05V	-0.00V	-0.00%
1 solar cell @ $G = 1000\text{ Wm}^{-2}$ and 1 solar cell @ $G = 500\text{ Wm}^{-2}$														
2.29A	-0.19A	-7.79%	24.11V	0.01V	0.05%	55.20W	-4.64W	-7.75%	2.59A	-0.00A	-0.03%	27.05V	-0.00V	-0.00%

Table 4.22: Shading of two solar cells. Effects on *DemoSat* solar array performance at PVA level @ $T = 28^\circ\text{C}$, $G = 1353\text{ Wm}^{-2}$.

maximum power point at string level changes between the different shade patterns, while it remains constant at PVA level. It is once again highlighted that the results are highly dependent on the system configuration and on the shading considered, therefore it is not possible to generalize them in terms of power losses. On the other hand, the electrical behavior of the solar cell-bypass diode assembly subjected to shading is characteristic of this condition.

4.2.7. Solar Cells Faults

The failure modes considered for the solar cells are short-circuit, open-circuit and reduced active area.

Short-circuit fault The short-circuit of a solar cell mainly occurs at the interconnections. The effects are equivalent to the ones of a shorted bypass-diode and the fault is modeled as in Figure 4.6. The faulty cell always operates at short-circuit conditions and the excessive current flows through the fault. Therefore, the higher the applied voltage the greater is the amount of excessive current since the healthy solar cells follow their characteristic IV curve. At open-circuit conditions, the string voltage is reduced by the V_{oc} of one cell, and the faulty cell keeps delivering current, sustained by the presence of the shorted connection.

Open-circuit The open-circuit condition of a solar cell may be induced by different failure mechanisms, which are mainly triggered by thermal cycles. The most common, even though quite rare due to the implementation of redundancy, is the rupture of interconnectors and welding points. Then, very unlikely yet to be considered, is the physical fracture of the solar cell, that, should it be experienced along the interconnector line as in Figure 4.48b, would deny the mitigation action of the bypass diode. This failure leads to the loss of the complete string.

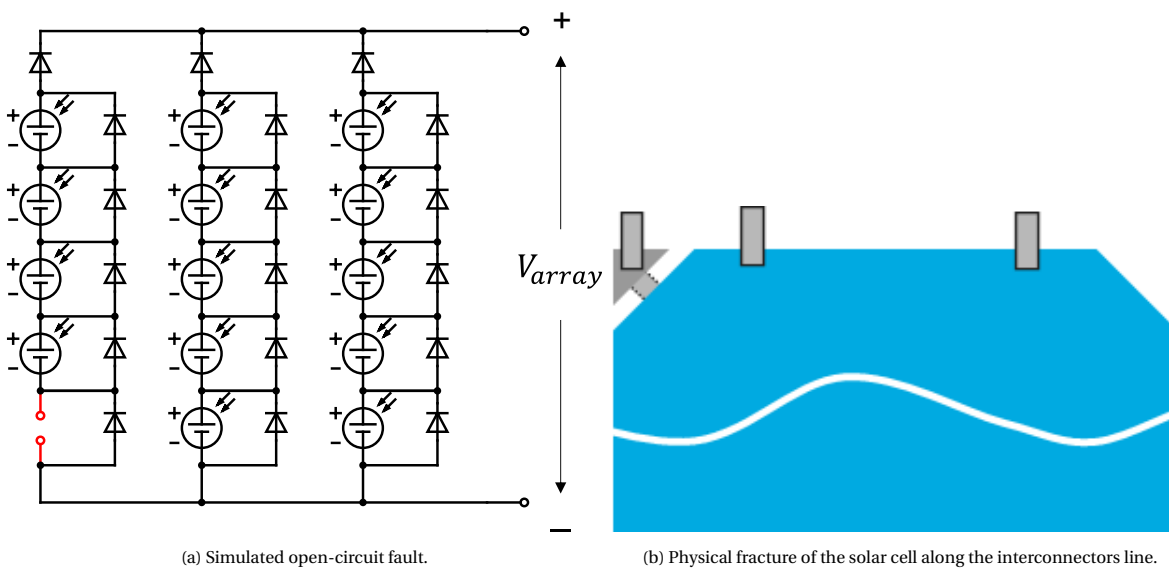


Figure 4.48: Potential open-circuit conditions of a solar cell.

As far as the simulation is concerned, it is now important to clarify the difference between the connection open fault and the solar cell open fault. For the latter, it is considered as if the current has no alternative path. This is equivalent to the aforementioned physical fracture or the open-circuit of all the interconnectors, including those of the bypass diode. A solar cell in open, instead, is modeled as in Figure 4.48a, where the bypass diode allows the current to flow and mitigates the power loss. As may be expected, the obtained character-

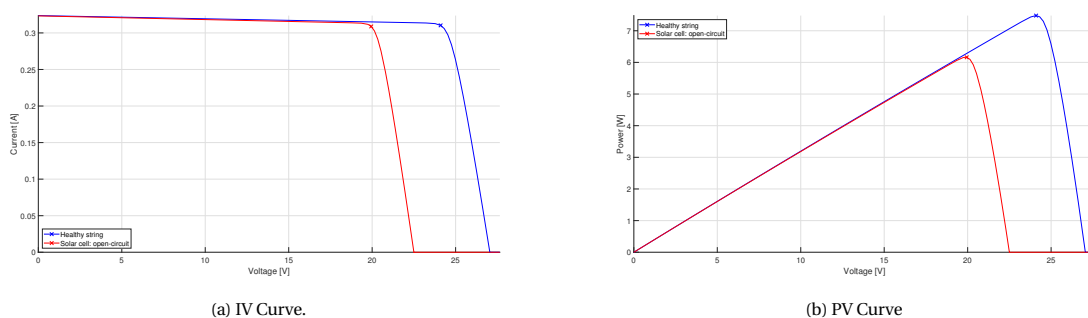


Figure 4.49: Open-circuit fault of one solar cell. Effects on *DemoSat* solar array characteristic curve at string level @ $T = 28^{\circ}\text{C}$, $G = 1353\text{Wm}^{-2}$.

Solar cell: Open-circuit Fault														
I_{mp}	ΔI_{mp}		V_{mp}	ΔV_{mp}		P_{mp}	ΔP_{mp}		I_{sc}	ΔI_{sc}		V_{oc}	ΔV_{oc}	
0.31A	-0.00A	-0.47%	19.95V	-4.16V	-17.24%	6.16W	-1.32W	-17.63%	0.32A	-0.00A	-0.12%	22.50V	-4.55V	-16.82%

Table 4.23: Open-circuit of one solar cell. Effects on *DemoSat* solar array characteristic curve at string level @ $T = 28^\circ\text{C}$, $G = 1353\text{Wm}^{-2}$.

istic curves, both at string and PVA level, show similarities with those influenced by a shorted bypass diode. The absence of an operating solar cell, bypassed thanks to the presence of the diode, justifies the reduction of the open-circuit voltage of the faulty string. However, the maximum power point is registered under different conditions if compared with the aforementioned failure mode that induces a comparable electrical behavior. This is due to the voltage drop across the bypass diode, which increases the voltage difference seen from the string, horizontally shifting the IV curve to the left by a value of V_{diode} . As a consequence, the inflection point occurs at a lower voltage, resulting in a different location of the maximum power point. From Table 4.24 and 4.6b, the difference between the discussed faults may be investigated. Once again, the results presented as quantitative parameters can be hardly generalized as they are dependent on the system layout.

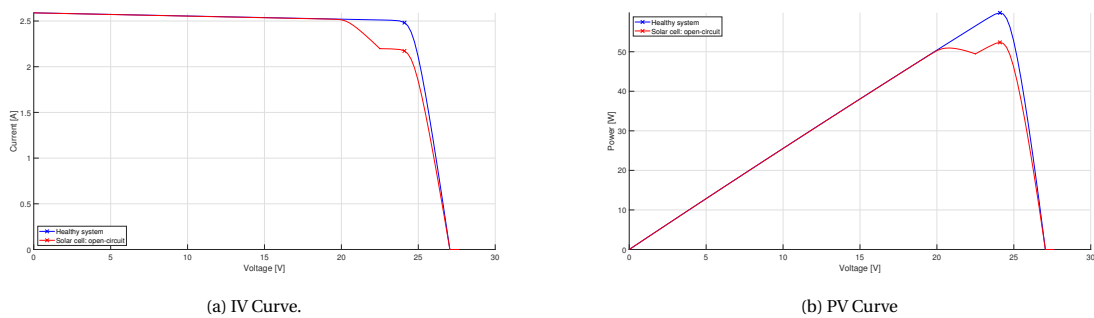


Figure 4.50: Open-circuit fault of one solar cell. Effects on *DemoSat* solar array characteristic curve at PVA level @ $T = 28^\circ\text{C}$, $G = 1353\text{Wm}^{-2}$.

Solar cell: Open-circuit Fault														
I_{mp}	ΔI_{mp}		V_{mp}	ΔV_{mp}		P_{mp}	ΔP_{mp}		I_{sc}	ΔI_{sc}		V_{oc}	ΔV_{oc}	
2.17A	-0.31A	-12.49%	24.10V	-0.00V	-0.01%	52.35W	-7.48W	-12.50%	2.59A	-0.00A	-0.02%	27.05V	-0.00V	-0.00%

Table 4.24: Open-circuit of one solar cell. Effects on *DemoSat* solar array characteristic curve at PVA level @ $T = 28^\circ\text{C}$, $G = 1353\text{Wm}^{-2}$.

Reduced Active Area A reduced active area can be mainly experienced due to micrometeorites impacts, and it is modeled by scaling the photogenerated current by the factor $\frac{A_{active,damaged}}{A_{active,new}}$. Since the induced effect is the reduction of the output current, this kind of fault influences the system in a way that is closely comparable with the electrical behavior produced by shading conditions. As may be seen in Figure 4.51a, the IV curve

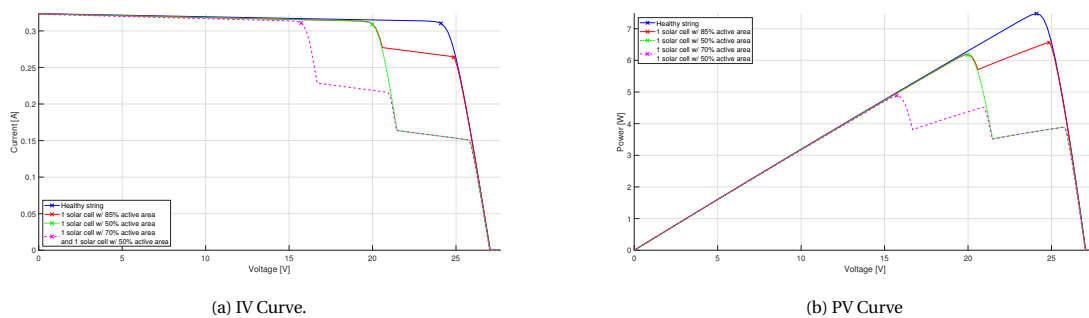


Figure 4.51: Reduced active area of solar cells. Effects on *DemoSat* solar array characteristic curve at string level @ $T = 28^\circ\text{C}$, $G = 1353\text{Wm}^{-2}$.

Reduced Active Area														
1 faulty solar cell ($A_{active} = 85\%$)														
I_{mp}	ΔI_{mp}		V_{mp}	ΔV_{mp}		P_{mp}	ΔP_{mp}		I_{sc}	ΔI_{sc}		V_{oc}	ΔV_{oc}	
0.26A	-0.05A	-14.93%	24.86V	0.76V	3.14%	6.56W	-0.92W	-12.26%	0.32A	-0.00A	-0.11%	27.05V	-0.06V	-0.02%
1 faulty solar cell ($A_{active} = 50\%$)														
0.31A	-0.00A	-0.41%	19.99V	-4.12V	-17.07%	6.18W	-1.30W	-17.41%	0.32A	-0.00A	-0.12%	27.03V	-0.02V	-0.08%
2 faulty solar cells ($A_{active} = 70\%$ and $A_{active} = 50\%$)														
0.31A	0.00A	0.15%	15.72V	-8.38V	-34.77%	4.89W	-2.59W	-34.67%	0.32A	-0.00A	-0.28%	27.02V	-0.03V	-0.12%

Table 4.25: Reduced active area of solar cells. Effects on *DemoSat* solar array performance at string level @ $T = 28^\circ\text{C}$, $G = 1353\text{Wm}^{-2}$.

of the string follows the curve of the healthy cell up to the voltage level where their output current is equal to the one of the faulty cell. The number of inflection points is representative of the number of solar cells with a unique value of the reduced active area, in terms of percentage. The current and voltage wave-forms of the relevant electronic components are provided in Figure 4.52, where a close similarity may be noted with those in Figure 4.43. It is interesting to note that, while the faulty cell is operating in forward biased conditions,

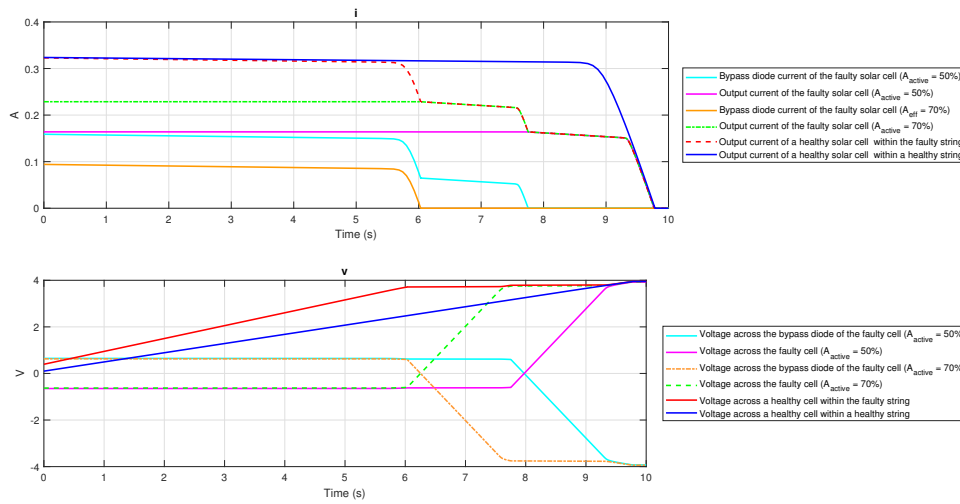
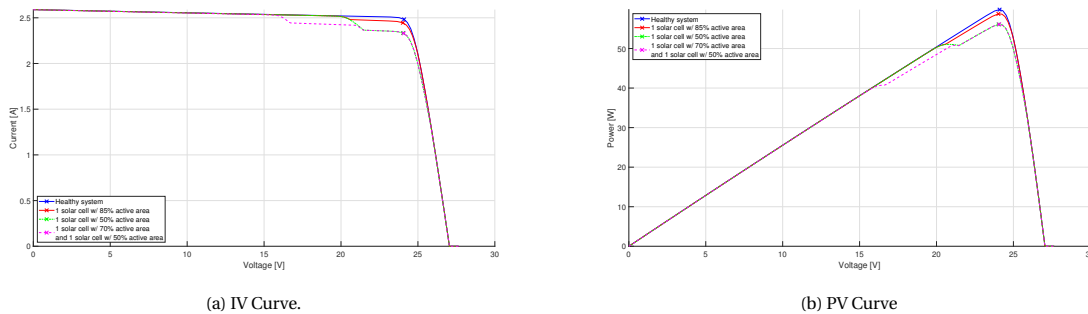


Figure 4.52: Reduced active area of 2 solar cells ($A_{active} = 70\%$ and $A_{active} = 50\%$). Currents and voltages.

experiencing a steep increase of the voltage, the voltage across the healthy cells is almost constant. This is because these cells are working within their voltage-source region, where little voltage increase leads to significant current variations.



(a) IV Curve.

(b) PV Curve

Figure 4.53: Reduced active area of solar cells. Effects on *DemoSat* solar array characteristic curve at PVA level @ $T = 28^\circ\text{C}$, $G = 1353\text{Wm}^{-2}$.

Reduced Effective Area														
1 faulty solar cell ($A_{\text{active}} = 85\%$)														
I_{mp}	ΔI_{mp}		V_{mp}	ΔV_{mp}		P_{mp}	ΔP_{mp}		I_{sc}	ΔI_{sc}		V_{oc}	ΔV_{oc}	
2.45A	-0.04A	-1.49%	24.02V	-0.08V	-0.32%	58.75W	-1.08W	-1.81%	2.59A	-0.00A	-0.01%	27.05V	-0.00V	-0.00%
1 faulty solar cell ($A_{\text{active}} = 50\%$)														
2.33A	-0.15A	-6.00%	24.04V	-0.06V	-0.26%	56.09W	-3.74W	-6.25%	2.59A	-0.00A	-0.01%	27.05V	-0.00V	-0.00%
2 faulty solar cells ($A_{\text{active}} = 70\%$ and $A_{\text{active}} = 50\%$)														
2.33A	-0.15A	-6.14%	24.08V	-0.02V	-0.09%	56.11W	-3.72W	-6.22%	2.59A	-0.00A	-0.03%	27.05V	-0.00V	-0.00%

Table 4.26: Reduced active area of solar cells. Effects on *DemoSat* solar array performance at PVA level @ $T = 28^\circ\text{C}$, $G = 1353\text{Wm}^{-2}$.

4.2.8. Combination of Failures

Up to this point, the failure modes have been analyzed separately with respect to each other for the purpose of investigating their specific effects. On the other hand, multiple failures may occur in the PVA. As long as the failures involve different strings, the overall impact at PVA level may be obtained by investigating the single fault effects at string level and considering the following relationship:

$$I_{\text{PVA}}|_{V \in [0, V_{oc}]} = \sum_{i=1}^n I_i|_{V \in [0, V_{oc}]} \quad (4.16)$$

where n is the total number of strings. An example is provided for better visualization. A short-circuit of one bypass diode is modeled in one string while an impedance fault of a connection, whose resistance value is $R = 30\Omega$, characterizes a second string. Both IV curves at string and PVA level are plotted in Figure 4.54. As previously discussed, the short-circuit of a bypass diode leads to a loss of one cell, while the increased

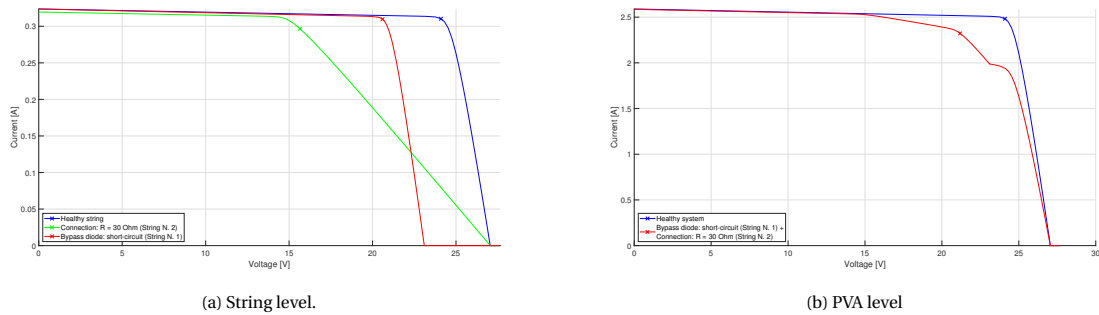


Figure 4.54: Effects of a shorted bypass diode and a connection impedance fault ($R = 30\Omega$) involving 2 different strings.

resistance of a current-carrying conductor decreases the slope of the IV curve at the V_{oc} . These effects are separately plotted in Figure 4.54a. Recalling that the system under analysis contains 8 parallel-connected strings, by investigating the IV curve at PVA level, it can be noted that the relationship in equation 4.16 is satisfied. Consistently with this, the inflection point is registered at the V_{oc} of the string including the shorted bypass diode and the impact of the faulty connection is visible from the slope of the curve.

When multiple failures occur within the same string, the superposition of the single effects may be applied in most cases. Two examples are proposed: a combination of a shorted bypass diode and a connection fault with an increased resistance equal to $R = 30\Omega$, and a shaded cell ($G = 500\text{Wm}^{-2}$) combined with a shorted bypass diode connected in parallel with another cell within the same string. The obtained IV curves for both combinations of faults are given in Figure 4.55 and 4.56. From the graphs, it can be noted how the effects of the combination of faults at string level are equivalent to the superposition of the effect of the single faults on the string IV curve. Figure 4.55 highlights that the IV curve of the string is horizontally shifted to the left due to the presence of the shorted bypass diode, while a decrease in the slope at V_{oc} is caused by the impedance fault, as previously discussed. The red curve is representative of the IV curve of the string subjected to both failures. The impact of the faulty components is visible as it shares the slope at V_{oc} of the green line and it is also characterized by the V_{oc} imposed by the shorted bypass diode. Therefore, the IV curve of the faulty string may be retrieved by applying superposition of the effects. A similar result may be obtained for the conditions simulated in Figure 4.56, i.e. a shaded solar cell, whose equivalent solar irradiance is $G = 500\text{Wm}^{-2}$ and a

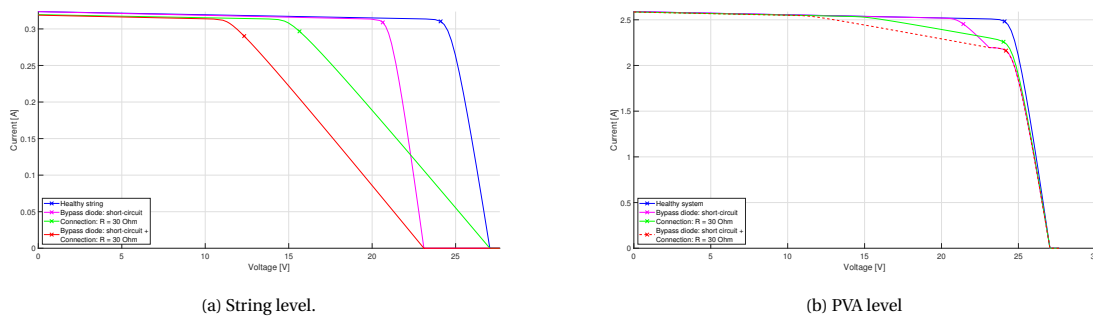


Figure 4.55: Effects of the combination of one shorted bypass diode and one connection fault ($R = 30 \Omega$).

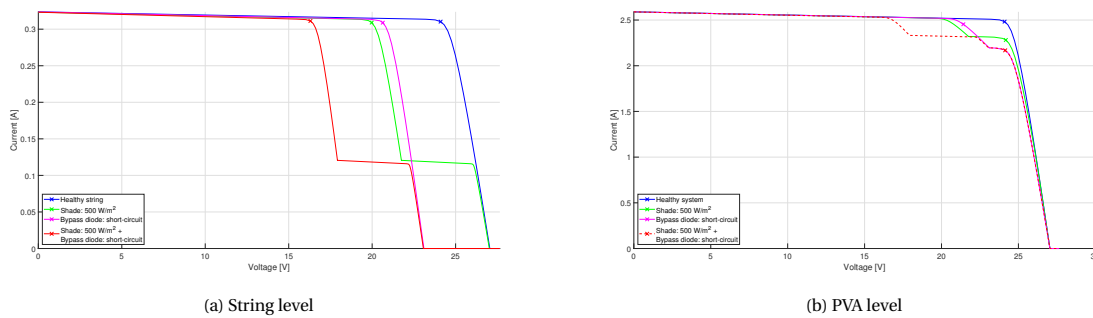


Figure 4.56: Effects of the combination of one shorted bypass diode and one shaded solar cell ($G = 500 \text{ W m}^{-2}$). Two different solar cells involved.

shorted bypass diode of another cell. In this case, the shading is responsible for the appearance of the inflection point, while the faulty bypass diode limits the open-circuit voltage. Then, the relationship in equation 4.16 holds for building the characteristic curve at PVA level.

Nevertheless, there exist cases for which the superposition method cannot be applied for drawing the IV curve of the string affected by multiple faults. These cases are those that occur when a current or voltage mismatch is triggered by a first failure or condition, and the component that is supposed to mitigate its effects is also subjected to a specific kind of failure. The shaded condition of a solar cell, for instance, leads to a current mismatch between the faulty cell and the healthy cells within the same string. The effects of shading have been already analyzed in Section 4.2.6, where a healthy bypass diode is parallel-connected to the shaded cell. Under the latter assumption, the electrical behavior of the string is well represented by the graph in Figure 4.44. However, if the bypass diode fails open, denying the flow of the excessive current from the healthy cells, a significant amount of power is dissipated through the shaded cell and the string is clamped to work at the operating conditions of the latter. This behavior is shown in Figure 4.57. In this case, the I_{sc} of the string

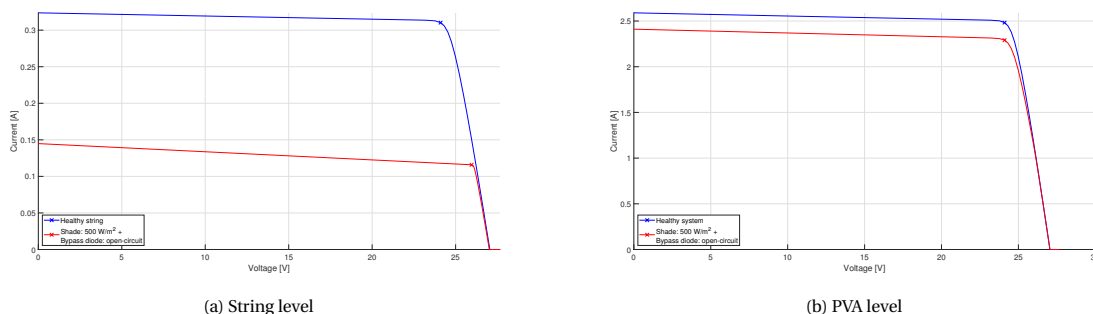


Figure 4.57: Effects of the combination of one shaded solar cell ($G = 500 \text{ W m}^{-2}$) and the open-circuit of its parallel-connected bypass diode.

corresponds to the point of intersection between the blue and green dashed lines in Figure 4.44, and the re-

sulting IV curve follows the latter. A different impact is predicted for the short-circuit of the bypass diode that, providing an alternative current path, dominates the effects on the IV curve regardless of the shading. This is proved by the graphs in Figure 4.58.

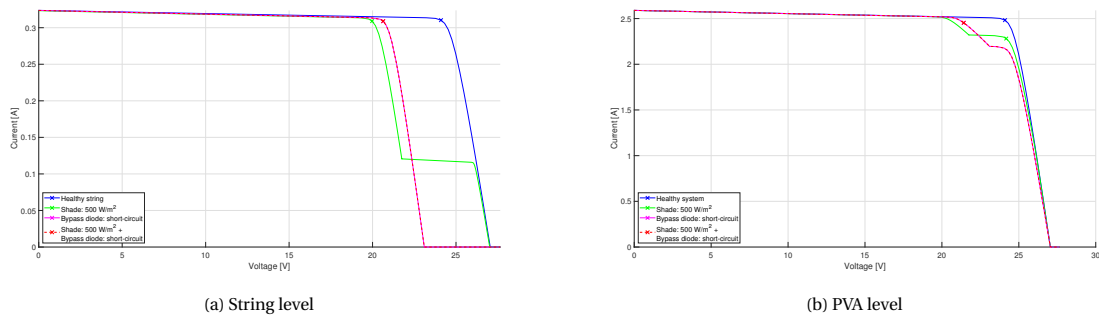


Figure 4.58: Effects of the combination of one shaded solar cell ($G = 500 \text{ Wm}^{-2}$) and the short-circuit of its parallel-connected bypass diode.

Another potential situation that requires attention is the voltage mismatch between parallel-connected strings when the faulty string, i.e. the string that has a lower voltage, is also affected by a short-circuit failure of the blocking diode. This is modeled and simulated, where the voltage mismatch is a consequence of a shorted bypass diode. The results at string level are plotted in Figure 4.59. At this point, it is known that the short-

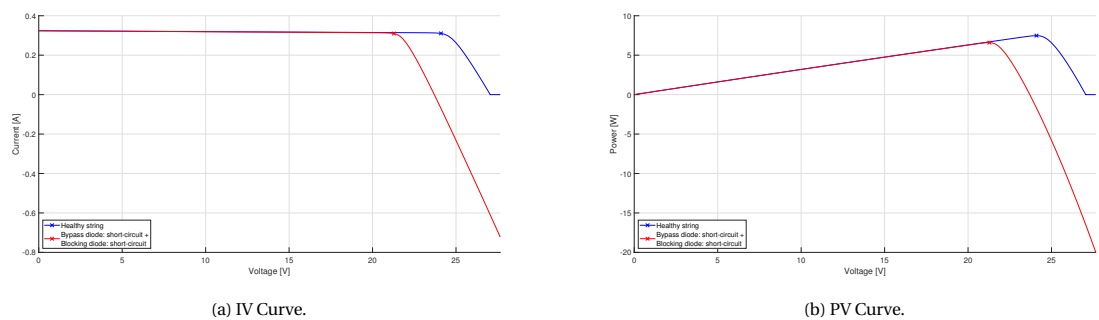


Figure 4.59: Effects of the combination of shorted bypass diode and shorted blocking diode within the same string.

circuit of a bypass diode reduces the open-circuit voltage of the string by the V_{oc} of one solar cell. Assuming a nominal behavior of the blocking diode, the resulting IV curve would be the one discussed in Section 4.2.1 and shown in Figure 4.7. No reverse current would flow through the faulty string, cut off by the blocking diode, avoiding the string to behave like a load. However, in this case, the shorted condition of the blocking diode nullifies its function, providing a current path. Therefore, the faulty string drains current from the other strings and, if the request of the former exceeds the capabilities of the latter, the load starts feeding the faulty string as well. This behavior is visible from the graph in Figure 4.60a, where the PVA current becomes negative. It is important to highlight that an operating point where the PVA behaves like a load is hardly reached. In this case, due to the presence of the voltage source connected to draw the characteristic curve, these points are visible. In reality, a similar situation can happen with an unregulated bus, directly connected to the battery, from which the PVA would drain current. Another analogous event may occur when the combination of the two faults under analysis brings the V_{oc} of the PVA below the voltage value of a regulated bus. However, a solar array regulator is connected between the solar array and the bus, into which another blocking diode is usually integrated, greatly decreasing the risks. It is impossible to reach the aforementioned PVA conditions when a resistive or power load is connected. Indeed, no intersection points between the load curve and the IV curve may be registered in the IV quadrant of the Cartesian coordinate system.

A more detailed analysis may be carried out by investigating the graph in Figure 4.61. The blue line represents the IV curve of the 7 combined healthy strings, while the performance of the faulty string is shown in red. At open-circuit conditions, the following relationship holds:

$$V_{oc,array} = \sum_{i=1}^n V_{oc,i} + V_{oc,faulty \text{ string}} \quad (4.17)$$

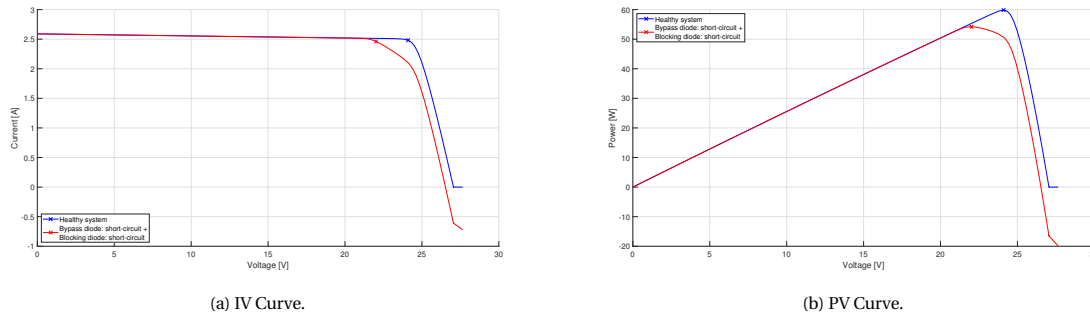


Figure 4.60: Effects of the combination of shorted bypass diode and shorted blocking diode within the same string.

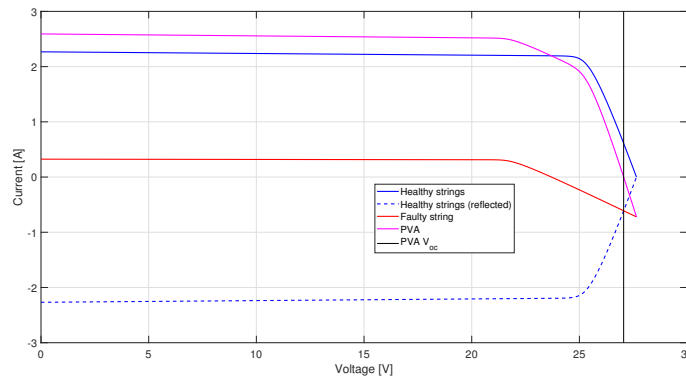


Figure 4.61: Analysis of the characteristic curves under a combination of faults: shorted bypass diode and shorted blocking diode within the same string.

where n is the total number of healthy strings. This point corresponds to the intersection of the faulty string IV curve and the reflection of the blue line with respect to the x-axis. Since equation 4.16 always apply, the IV curve of the PVA falls below the one relative to healthy strings as soon as the V_{oc} of the faulty string is exceeded and the latter starts behaving like a load. As previously discussed, beyond the V_{oc} of the PVA, the output current of the strings is no longer enough to satisfy the request of the faulty string and additional current is drained from the external voltage source.

4.3. Dynamic analysis

The FMEA presented in Section 4.2 allows evaluating the effects of the considered failure modes within the whole range of operating points of the PVA. However, this is not necessarily representative of the actual impacts on the system performance when the PVA is connected to a load. As seen in Section 3.2.5, the operating point of the solar array is determined by the intersection with its IV curve and the characteristic curve of the load, in Figure 3.16. As a consequence, the occurrence of a failure alters the behavior of the system only if the operating point lies within the modified region of the IV curve. Furthermore, it is important to point out that, for real applications, the power source is not directly connected to the load, but a solar array regulator is placed between them. The S3R and the MPPT, whose modeling approaches have been described in Section 3.3, and their response to different temporal-triggered failures are discussed here.

4.3.1. S3R Response to Failures

The modeled S3R is the one presented in Section 3.3.1, with a slight deviation in the bus voltage, $V_{bus} = 23V$ in this case, and an operating temperature of $T = 28^{\circ}C$. The system response to failures is dependent on the type of load connected to the EPS. A first analysis is proposed to investigate the behavior of the S3R, feeding a 10Ω resistive load, when facing a short-circuit failure of a bypass diode triggered at $t = 0.15$ s. Figure 4.62b

⁷Please note that the IV curves have been horizontally shifted to the left by a value of 0.6V with respect to the curves provided in Section 4.2. This corresponds to the voltage drop across the additional blocking diodes integrated into the S3R configuration. Additional losses

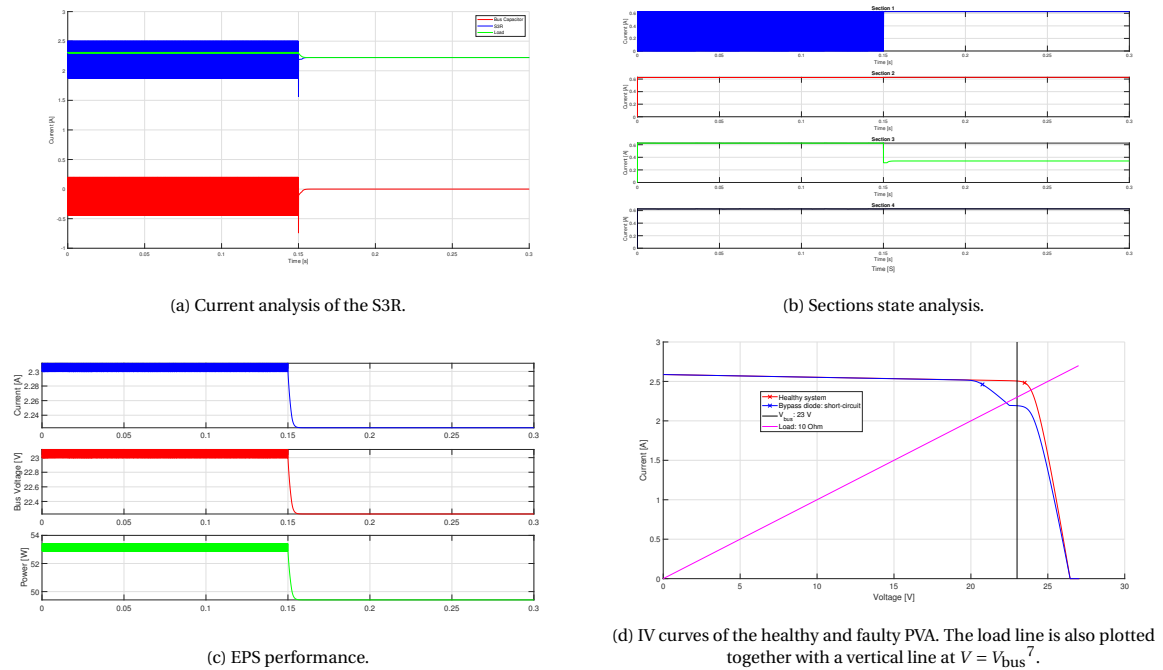


Figure 4.62: Analysis of the implemented EPS, considering the *DemoSat* PVA layout and a resistive load of 10Ω ($T = 28^\circ\text{C}$ and $G = 1353\text{Wm}^{-2}$). SolAero Z4J are considered for the solar cells.

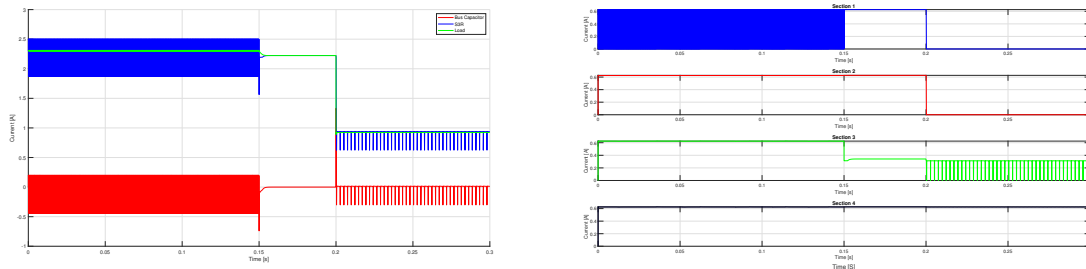
and 4.62c show that the S3R is able to control the healthy PVA and to feed the load while keeping the desired constant bus voltage. This is achieved by driving Section 1 in its switching state. In healthy condition, the current drained by the load is given by $I_{load} = \frac{V_{bus}}{R_{load}}$, which corresponds to the intersection of the magenta and black line in Figure 4.62d. Since the PVA is clamped to the bus voltage, its output current is in excess and it requires to be properly modulated and shunted. If the load line was such that it crossed the IV curve of the healthy PVA exactly at $V = V_{bus}$, then all sections would continuously feed the bus and the duty cycle of the switching devices would be 0.

As soon as the short-circuit of the bypass diode occurs, the IV curve is modified into the blue line in Figure 4.62d and the operating point of the solar array suddenly changes, falling below the load line. Under this condition, the output current is not sufficient to satisfy the load request and the load starts draining current from the bus capacitor, decreasing the voltage. The voltage stabilizes at the point of intersection between the load line and the IV curve of the faulty PVA, where the output current equals the load current. Figure 4.62d suggests that, even though the S3R may lose its main function, i.e. decoupling the source from the load by maintaining a constant bus voltage, the system is always able to feed a resistive load regardless of the failure experienced. Furthermore, as demonstrated by the graphs in Figure 4.63, the system has the capability of restoring its nominal operating conditions should the load demand decrease below the performance of the PVA at $V = V_{bus}$. Figure 4.63 shows the results obtained from a simulation where load profile is modeled such to undergo a positive step from 10V to 25V at $t = 0.2\text{s}$.

Another analysis is carried out by connecting a power load to the solar array. Different load lines are plotted together with the IV curves in the graph in Figure 4.64. It may be seen that for a relatively high power request, after the occurrence of the failure, the solar array fails to fulfill the power requirement as the IV curve falls below the load line at $V = V_{bus}$.

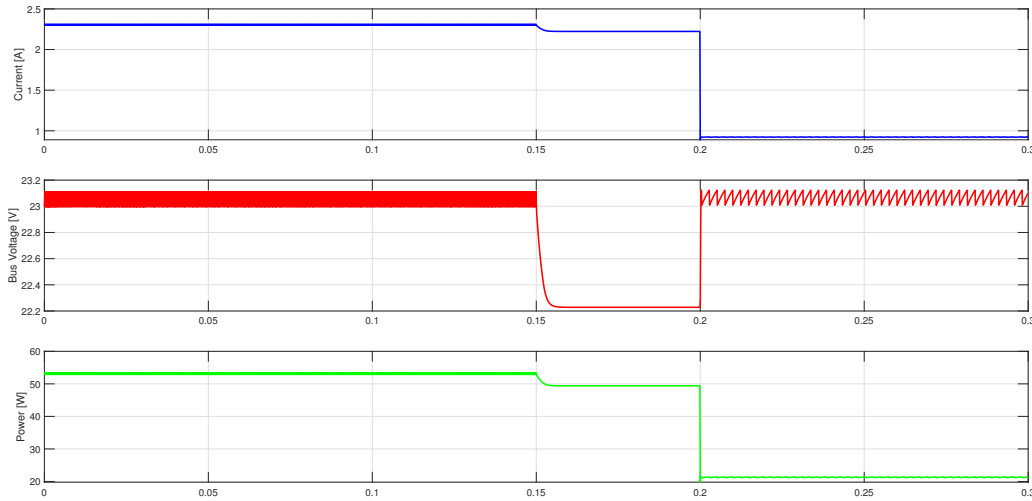
The results obtained by simulating the EPS behavior while supplying a 51 W load are provided in Figure 4.65. As soon as the failure is triggered, the load, that does not receive enough power from the PVA, starts draining current from the bus capacitor, decreasing the bus voltage. The rate of such decrease is determined by the difference between the power requested by the load and the power supplied by the source, or, in other terms, by the difference between the load current demand and the output current of the solar array operating at the instantaneous input voltage. This is represented by the vertical distance between the blue and magenta lines in Figure 4.64. Since in the region $[0, 23\text{V}]$ does not exist any condition such that the PVA is able to

due to the internal resistance of the diode are neglected.



(a) Current analysis of the S3R.

(b) Sections state analysis.



(c) EPS performance.

Figure 4.63: EPS analysis for a resistive load whose profile is characterized by a positive step from 10Ω to 25Ω at $t = 0.2s$.

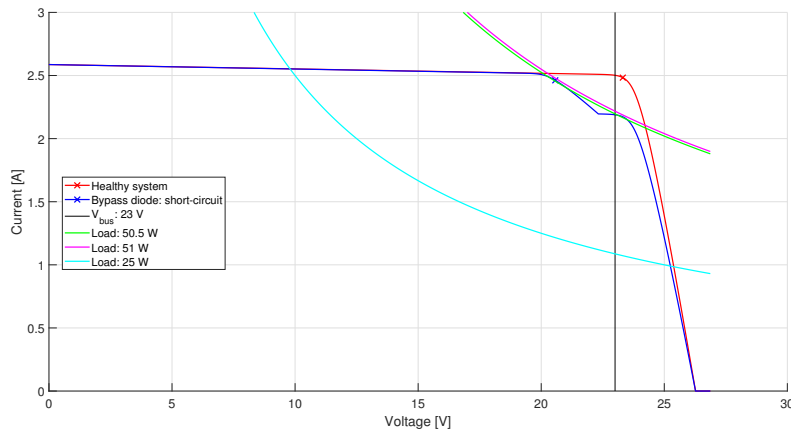
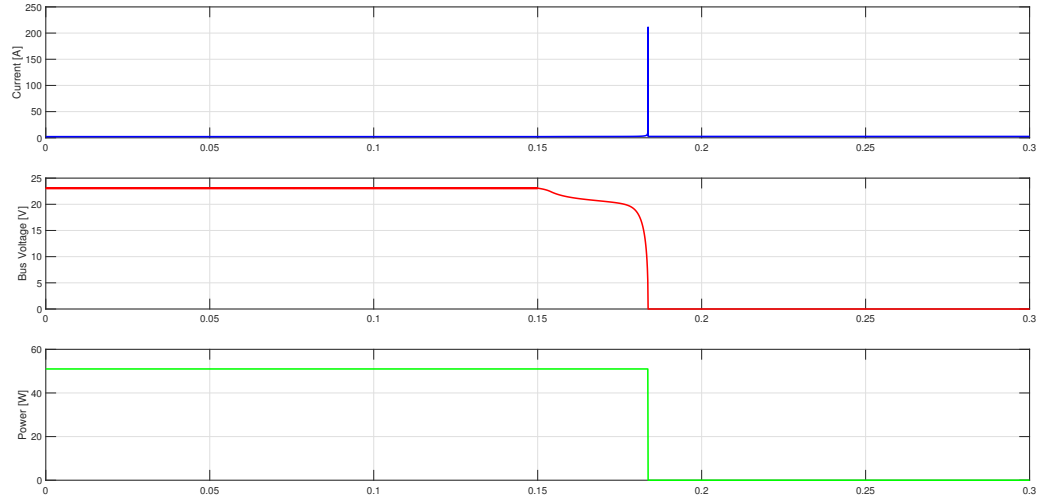
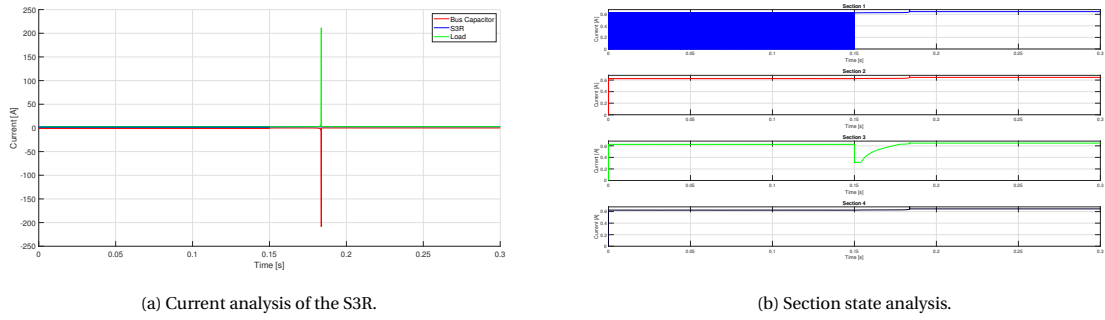


Figure 4.64: IV curves of the healthy and faulty PVA. Different load lines are also plotted together with a vertical line at $V = V_{bus}$

satisfy the load demand, the increasing power difference leads to a rapid increase of the rate of discharge of the bus capacitor, causing a current spike (Figure 4.65a). Eventually, the bus capacitor becomes completely discharged, clamping the PVA to its short-circuit condition and reducing to 0W the delivered power. For a different simulation, the load demand is set to 50.5W. Figure 4.64 shows that even though at $V = V_{bus}$ the power supplied by the PVA is deficient, the load line crosses the IV curve at a lower voltage, allowing the system to reach stability. The behavior is then similar to what has been described for a resistive load.



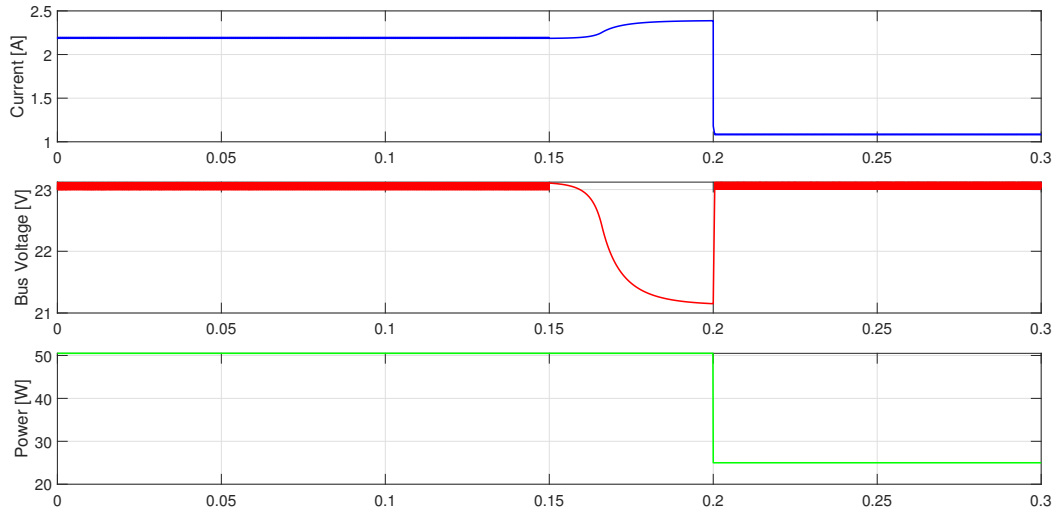
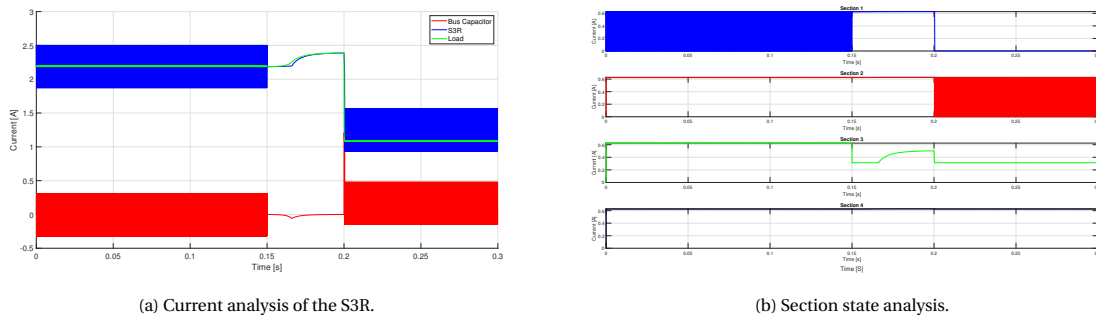
(c) EPS performance.

Figure 4.65: Analysis of the implemented EPS, considering the *DemoSat* PVA layout and a power load of 51 W ($T = 28^\circ\text{C}$ and $G = 1353\text{Wm}^{-2}$). SolAero Z4J are considered for the solar cells.

Despite the S3R loses its function of maintaining a constant bus voltage, the solar array is able to comply with the power requirement. Contrary to the critical condition reached when the bus capacitor gets completely discharged, in this case, the operating point of the PVA is shifted following a decrease in the power demand. If this happens, the bus voltage, which increases due to the excess supplied power, may either remain clamped to the load, or it may be restored to its reference value. The nominal operating state of the S3R may be re-attained in case the power load is lower than the output power of the PVA at $V = V_{\text{bus}}$. An example is provided in Figure 4.66, where the load profile is characterized with a negative step, from 50.5W to 25W, at $t = 0.2$ s. An important aspect to take into account is that the modeled EPS does not contain any secondary battery, which could significantly modify the behavior of the system. For instance, if the 51 W is considered, the low output current of the PVA would be compensated by the battery, keeping the bus voltage constant. Please recall that the S3R is characterized by a regulated bus, thus the battery is decoupled from the bus via charge and discharge regulators. Then, the PVA would reach short-circuit condition only in the unlikely event of a fully discharged battery.

4.3.2. MPPT Response to Failures

The modeled MPPT is the one presented in Section 3.3.2, for an operating temperature of $T = 28^\circ\text{C}$. A first analysis is performed by simulating the short-circuit failure of one bypass diode at $t = 0.1$ s, where a constant resistive load of $R_{\text{load}} = 25\Omega$ is connected to the EPS. Input voltage, output current, and output power of the solar array are plotted in Figure 4.67. The initial conditions dominate the behavior of the system within the first instants in time. The time that elapses between the beginning of the simulation and the voltage drop



(c) EPS performance.

Figure 4.66: EPS analysis for a power load whose profile is characterized by a negative step from 50.5 W to 25 W at $t = 0.2$ s.

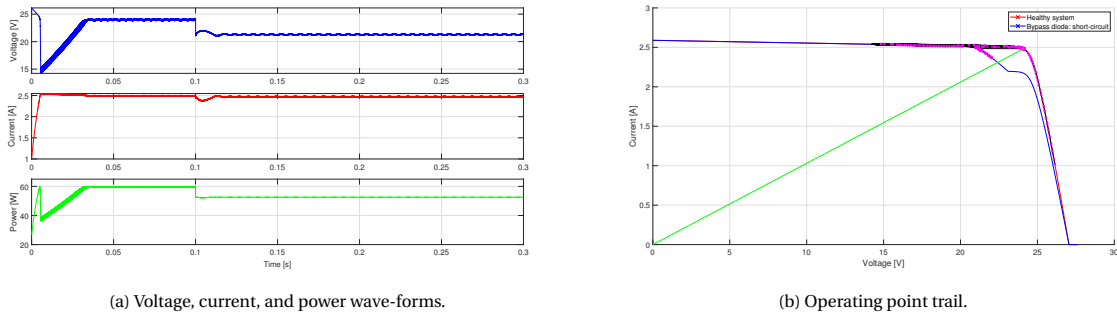


Figure 4.67: System successful response to a shorted bypass-diode ($T = 28^\circ\text{C}$ and $G = 1353\text{ W m}^{-2}$).

due to the initial duty cycle is the time needed for the converter inductor to charge⁸. For the healthy system, the maximum power point is tracked within a limited region around 24 V, consistently with the value in Table 4.3a. As soon as the short-circuit failure of the bypass diode occurs, due to the current stored in the inductor and the circuit configuration that imposes $I_{PVA} = I_{\text{inductor}}$, the operating point is instantly shifted to the voltage value on the faulty IV curve that is able to sustain the inductor current. However, since the solar array is still attached to the resistive load with an apparent resistance of $R_{\text{in}} = \frac{R_{\text{load}}}{M(D)^2}$, the actual operating point is rapidly restored. The latter is somewhere close to the intersection point between the load line at MPP of the

⁸Please note that within this region the voltage wave-form has the same shape as the one in Figure 3.25. Here the influence of the initial state of the inductor is more visible because of the different time scale.

healthy system and the new IV curve that characterizes the faulty system⁹. This behavior is shown in Figure 4.67b, where the black line represents the trail of the different operating points of the PVA, managed by the MPPT controller. The upper graph in Figure 4.67 demonstrates that the controller is able to track the new maximum power point by setting the input voltage to 21.3V. This is consistent with the result of FMEA in Table 4.6b.

Other simulations are performed, where failure mechanisms that reduce the active area of two different cells to 20% are triggered simultaneously at $t = 0.1$ s. A 10Ω and 25Ω resistive loads are connected to the EPS for two different simulations. The IV curves are provided in Figure 4.68. For the 10Ω resistive load, it may be seen

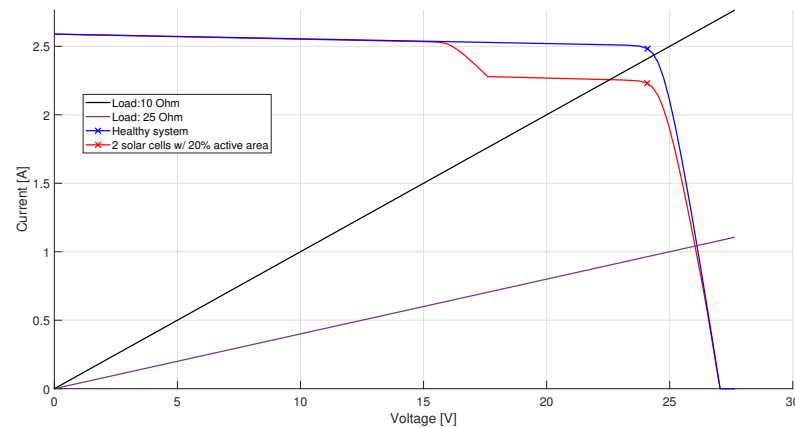


Figure 4.68: IV curve of the PVA subjected to failure mechanisms that reduce that reduce the active area of two different cells to 20%.

that the maximum power point of the faulty system lies within the region $\left[\frac{1}{R_{load}}, V_{oc}\right]$, not reachable by the boost converter. The EPS incapability of restoring the MPP conditions is visible from Figure 4.69 and 4.70.

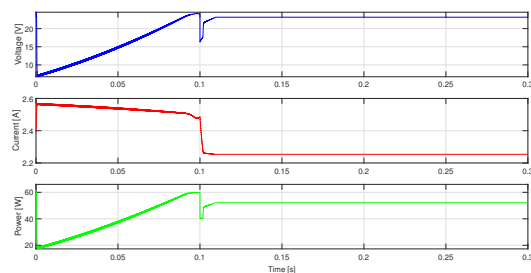


Figure 4.69: System unsuccessful response to two solar cells with reduced active area ($A_{active} = 20\%$) within the same string ($R_{load} = 10\Omega$).

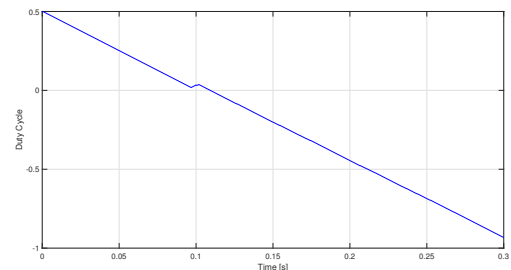


Figure 4.70: System unsuccessful response to two solar cells with reduced active area ($A = 20\%$) within the same string ($R_{load} = 10\Omega$).

Once the operating point reaches the load line with slope $\frac{1}{R_{load}}$, i.e. when the duty cycle is 0, the MPPT algorithm keeps trying to track the MPP by decreasing the duty cycle further¹⁰. A negative duty cycle leads to a permanent open condition of the converter switch, establishing a direct connection between the source and the load. This behavior is proved by the constant input voltage seen by the solar array when $d < 0$. Please note that the voltage value is greater than the one characterizing the intersection point in Figure 4.68 by a value equal to the voltage drop across the diode of the boost converter. A different result is obtained when the EPS feeds a 25Ω resistive load. In this case, the maximum power point belongs to the achievable IV curve region of the converter and it is correctly restored after the failures (Figure 4.71).

A third example covers the last situation that may be encountered following a PVA failure. An open-circuit failure of one solar cell is simulated, whose effect is mitigated by the presence of the bypass diode. As mentioned in Section 4.2.7, the effects are similar to those caused by a shorted bypass diode, however, the voltage drop across the diode shifts the maximum power point to a higher voltage. Figure 4.72b shows that the apparent load line at which the system operates under healthy conditions intersects the IV curve of the faulty

⁹Some deviations are expected because of the duty cycle variations imposed by the controller during settling time.

¹⁰To reach the MPP the slope has to decrease, thus $R_{load} \uparrow \Rightarrow D \downarrow$.

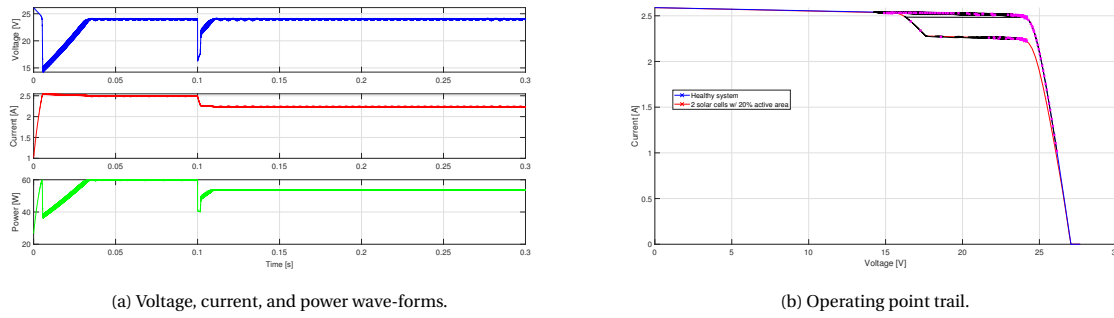


Figure 4.71: System successful response to two solar cells with reduced active area ($A = 20\%$) within the same string ($R_{load} = 25\Omega$).

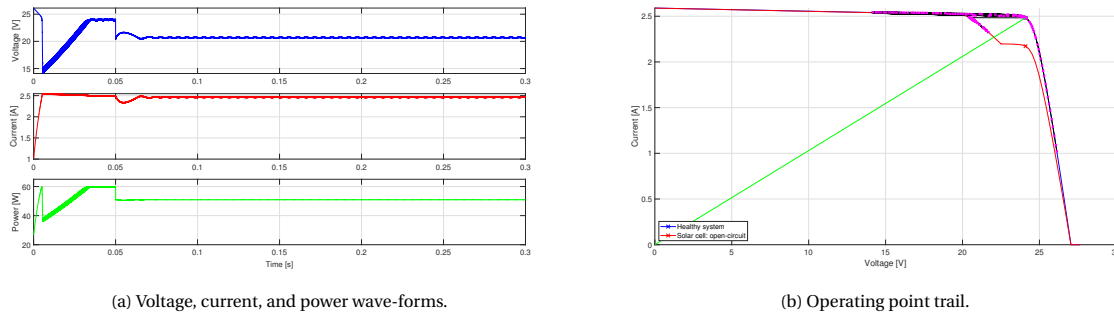


Figure 4.72: System unsuccessful response to an open-circuit failure of a solar cell.

PVA in a region that is characterized by a local maximum. To date, the implemented MPPT algorithm is not fault-tolerant against multiple local maxima, and, as a consequence, once the failure mechanism is triggered the operating point of the solar array is brought to the wrong power point. Please note that, by analyzing Figure 4.71b, it may be studied that for a short amount of time the solar array is clamped to a region with a local maximum, similarly to what has just been described. However, that is a temporary condition driven by the electrical inertia of the inductor, which is rapidly overcome by the connected load, allowing the PVA operating point to cross the inflection point.

5

Reliability Analysis

The *reliability*, according to [33], is the "the ability of an item to perform a required function under given conditions for a given time interval". Its mathematical expression is

$$R(t) = \exp\left(-\int_0^t \lambda(t) dt\right) \quad (5.1)$$

where $\lambda(t)$ is the failure rate as a function of time.

To perform a reliability analysis, four different steps have to be carried out properly. The first step is to investigate the type of elements involved, which can be grouped in three categories: Electrical, Electronic, Electromechanical (EEE), mechanical, and miscellaneous. As the analysis is focused on the PVA, the first category includes all the components involved in this study. Then, the types of failures to be considered have to be determined from the following classification:

- random failures: triggered by unknown residual defects;
- systematic failures: deriving from design and manufacturing;
- wear-out failures: due to the physical process of the component;
- extrinsic failures.

The latter are the consequence of the external space environment and they are usually taken into account as stress contributors for random failures. The examination of the aforementioned failures leads to the bathtub curve distribution of the failure rates of the components over their operational life (Figure 5.1). The relatively high failure rate that characterizes the early stages of the operational lifetime of the component is called infant mortality and is mainly due to systematic failures. This region is difficult to model and it is usually studied by

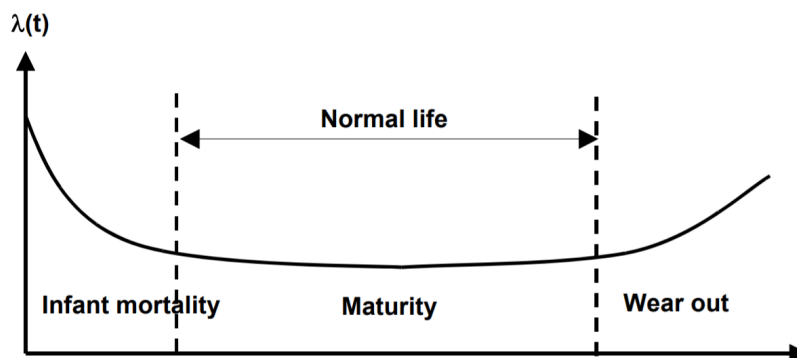


Figure 5.1: Typical bathtub curve for EEE components [15].

testing. Then, the component goes through a period of time, considered to be the useful life period, where its failure rate is more or less constant. Eventually, the component experiences an accelerated deterioration due to wear-out. The useful life is dominated by random failures and this allows for reliability predictions, upon the definition of a proper reliability model. It is important to highlight that the constant failure rate is an assumption that is done exclusively for EEE components and does not apply for miscellaneous and mechanical elements. Nonetheless, when dealing with EEE components, the aforementioned assumption ($\lambda(t) = \lambda$) reduces the reliability distribution to an exponential distribution:

$$R(t) = \exp(-\lambda \cdot t) \quad (5.2)$$

The following step is to retrieve the value of the failure rates of the components involved in the analysis. There exist different methods to accomplish this task: obtaining the failure rates from samples of heritage data, using manufacturer reliability data, exploitation of test data, relying on engineering judgment, and performing prediction based on existing databases. In this research, due to the lack of other sources of data, the latter approach is used. As explained later in this chapter, this will also allow carrying out a more detailed sensitivity analysis. The last step involves the selection of the reliability model. The reliability block diagram is the most common and it is the one implemented for this project. Such choice makes the validation process easier since it was shared between available reliability analyses of satellite PVAs.

The approach adopted for the software implementation of the reliability analysis is presented in Section 5.1, followed, in Section 5.2, by the explanation of the mathematical model built by the software to perform a system reliability prediction. The research proceeds with a sensitivity analysis, mentioned in RO3, treated in Section 5.3.

5.1. System Reliability

It has been defined that the reliability analysis carried out in this project exclusively involves the PVA, and therefore it only deals with EEE components. As a consequence, the reliability is expressed by the exponential distribution in equation 5.2. In this section, the method for calculating the failure rates and how they are allocated to the respective components is discussed. Furthermore, the reliability block diagram is presented, and the considered fundamental functions are described.

5.1.1. Components Failure Rate

As previously mentioned, the calculation of the failure rates of the involved components is based on existing data bases. For this research the military handbook "*Reliability Prediction of Electronic Equipment*" [4] and, in particular, its revision [6] are used. These handbooks are widely spread within the space community¹ and are adopted for those reliability analyses used for validating the software.

In the MIL handbooks the failure rate model of a component, for instance a semiconductor, takes the form of

$$\lambda = \lambda_b \pi_T \pi_A \pi_R \pi_S \pi_C \pi_Q \pi_E \quad (5.3)$$

where λ_b is the base failure rate, calculated by taking into account electrical and temperature stresses relevant to the part under analysis, and the π s take into account environmental effects and other parameters that influence the reliability. Please be aware that the unit of λ in equation 5.3 is $1 \times 10^{-6} \text{ h}^{-1}$, while the required unit to calculate the reliability in equation 5.3 is 1 h^{-1} . Moreover, another commonly used unit is $1 \times 10^{-9} \text{ h}^{-1}$, called Failure in time (FIT).

It is important to point out that this reliability prediction technique is constrained by several limitations. The base failure rates have been derived from existing available data, thus they are valid under the specific conditions to which the part or component was subjected. For instance, it is explicitly stated in [4] that none of the models takes into account the effects of ionizing radiation, of primary concern for space applications. Furthermore, some confusion involves the correct approach on how to treat the failure rates of different failure modes characteristic of the same components. The MIL handbooks do not provide any guidelines on this matter, that are instead treated in [3], the old version of the ECSS. In [3], the total failure rate is apportioned into contributions that relate to three failure modes, namely short-circuit, open-circuit, and drift, referring to a variation of the nominal rating values. Such failure rate allocation applies to most of the components treated in the document. Nevertheless, this is not consistent with the list of failure modes given in [31], where, for

¹Mentioned as a reliable source also in [32].

instance, open-circuit and short-circuit are the only faulty states considered for diodes and solar cells. For this reason, it is not an easy task to accurately predict the failure rate of the parts in play and, whenever the consultation of the handbooks and standards has raised ambiguities, parameters values used in the technical documentation of ongoing RUAG projects have been adopted.

A failure rate prediction of the following EEE components is needed to carry out the reliability analysis of the satellite PVA: solar cell, bypass diode, blocking diode, connections, resistor, and connector. All the parameters that will be presented in this section are user-defined to increase the flexibility of the software.

Solar Cells No failure rate model is provided for solar cells in [4, 6]. A value for the FIT of this component is given in [3] and it is equal to $FIT = 1$. Being a three-state device, as mentioned in Chapter 4, a solar cell may fail either open or short. However, no clear instructions have been found on the distribution of such failure modes. It has been discussed that the open fault of a cell is mainly due to the rupture of the interconnectors, as the probability of crack propagation in the cell structure is very low. Since the failure rates of the connections are considered separately in this reliability analysis, the contribution of an open-circuit failure to the part failure rate is limited. By comparison with different reliability analyses of on-going solar array wings projects, it has been decided to assume the following failure modes distribution: 20% for open-circuit failures and 80% for short-circuit failures.

Bypass Diodes [6] proposes a failure rate model for low-frequency diodes in Section 6.1. Nevertheless, when dealing with reliability analyses of solar panels for space applications, there is a tendency to consider the failure rate of the bypass diode equivalent to that of the solar cells. To support this assumption, there is the fact that many space solar cell suppliers², manufacture the bypass diodes by adopting the same technology used for the solar cells. For this reason, $FIT = 1$ is chosen for the simulation. The same consideration applies to the failure modes distribution, and 20% of open-circuit and 80% of short-circuit failures is assumed.

Blocking Diodes The model found in Section 6.1 of the MIL handbook is used for the calculation of the failure rate of the blocking diodes.

$$\lambda = \lambda_b \pi_T \pi_S \pi_C \pi_Q \pi_E \quad (5.4)$$

1N5809 diode is selected, an ultrafast recovery power rectifier diode whose corresponding base failure rate is $\lambda_b = 0.025 \times 10^{-6} \text{ h}^{-13}$. The temperature factor π_T is calculated as follows:

$$\pi_T = \exp\left(-3091 \cdot \left(\frac{1}{T_J + 273} - \frac{1}{298}\right)\right) \quad (5.5)$$

where T_J is the junction temperature in degree Celsius chosen equal to the solar panels' worst-case temperature of 101 °C according to [17]⁴. This results in a temperature factor of $\pi_T = 8.230$. Then, the electrical stress factor is given by the following equations:

$$\pi_S = 0.054 \quad \text{if } V_s \leq 0.3 \quad (5.6)$$

$$\pi_S = V_s^{2.43} \quad \text{if } 0.3 < V_s \leq 1 \quad (5.7)$$

where V_s is the voltage stress ratio defined as

$$V_s = \frac{\text{Voltage Applied}}{\text{Voltage Rated}} \quad (5.8)$$

Here the voltage refers to the diode reverse voltage. The maximum reverse voltage applied is the operating voltage of the PVA when the string is completely shaded. Considering worst-case conditions, i.e. -60°C according to [30], the applied voltage is $V_{mp} = 28.98 \text{ V}$. A 1N5809 diode has a breakdown voltage of 110 V, if derating is applied and 70 V is designed, then the voltage stress ratio is $V_s = 0.42$. Since it is higher than 0.3, the second equation for the stress factor applies, from which it follows $\pi_S = 0.117$. The diodes are categorized in different product assurance levels, whose requirements are specified in [5] and [7]. For this analysis, JANTXV is assumed which corresponds to $\pi_Q = 0.7$. 1N5809 diodes are metallurgical bonded, for which a contact construction factor of $\pi_C = 1$ is given. Moreover, the environment factor is $\pi_E = 0.5$ for space applications. As far as the failure modes distribution is concerned, 60% short-circuit and 40% open-circuit failures are assumed according to [3].

²AzurSpace is an example.

³The choice has been made based on an ongoing project.

⁴The technical report refers to *Delfi-n3Xt*, a CubeSat whose configuration is equal to the configuration of *DemoSat*.

Connections The failure rate model proposed for the connections is given in equation 5.9.

$$\lambda = \lambda_b \cdot \pi_E \quad (5.9)$$

The types of connection that are used in the manufacturing of a PVA are welds and crimps, whose base failure rates are $\lambda_b = 0.000015 \times 10^{-6} \text{ h}^{-1}$ and $\lambda_b = 0.0002 \times 10^{-6} \text{ h}^{-1}$, respectively. As for the environment factor π_E , 0.5 is used.

Connector The failure rate for the connector is calculated by using equation 5.10.

$$\lambda = \lambda_b \pi_T \pi_K \pi_Q \pi_E \quad (5.10)$$

Rectangular connectors are assumed, whose base failure rate is $\lambda_b = 0.023 \times 10^{-6} \text{ h}^{-1}$. The temperature factor π_T is given by equation 5.11, where $T_0 = \text{Connector Ambient Temperature} + \Delta T$.

$$\pi_T = \exp\left(\frac{-0.14}{8.617 \cdot 10^{-5}} \cdot \left(\frac{1}{T_0 + 273} - \frac{1}{298}\right)\right) \quad (5.11)$$

ΔT is the connector insert temperature rise, whose formula depends on the American Wire Gauge (AWG) number, here assumed to be 22. The obtained temperature rise is $\Delta T = 0.27^\circ\text{C}$. It will be proven later that the AWG number does not have a significant impact on the reliability. Considering an ambient temperature of 101°C ⁵, the resulting temperature factor is $\pi_T = 3.037$. As far as the quality factor π_Q is concerned, it is assumed that the connector is qualified and compliant with the MIL specification, thus a value of 1 is assigned. The same value is selected for the mating/unmating factor π_K , since the connector does not experience any cycles of this kind during its operational lifetime. Lastly, the environment factor related to space condition is used ($\pi_E = 0.5$).

Resistor

$$\lambda = \lambda_b \pi_T \pi_P \pi_S \pi_Q \pi_E \quad (5.12)$$

Equation 5.12 gives the failure rate for a resistor. In this analysis, resistors are assumed to be integrated only to perform the bleeding function, thus the base failure rate of wire wound resistors⁶ is considered: $\lambda_b = 0.0024 \times 10^{-6} \text{ h}^{-1}$. The temperature factor is calculated as in equation 5.13.

$$\pi_T = \exp\left(\frac{-E_a}{8.617 \cdot 10^{-5}} \cdot \left(\frac{1}{T + 273} - \frac{1}{298}\right)\right) \quad (5.13)$$

Here T is the resistor case temperature, assumed 101°C , and E_a is either 0.2 or 0.08 based on the type of resistor. In this case, RWR resistors are considered⁷ and $E_a = 0.08$ is used, giving $\pi_T = 1.883$. For what concerns the power factor π_P , the formula used is shown in equation 5.14.

$$\pi_P = (\text{Power Dissipation})^{0.39} \quad (5.14)$$

For bleeding resistors, the dissipated power is usually relatively low, $P_{\text{diss}} = 0.15 \text{ W}$ is taken. This means that if a ground fault occurs at the point at the highest potential, i.e. at the string/section positive terminal, while the PVA is operating at its MPP, the resistance value is:

$$R_{\text{bleed}} = \frac{V_{mp}^2}{P_{\text{diss}}} \Big|_{T=-60^\circ\text{C}} = \frac{28.98^2}{0.15} = 5.60 \text{ k}\Omega \quad (5.15)$$

The obtained value lies within the range indicated in [34]⁸. Then, $\pi_P = 0.477$. The power stress factor π_S also depends on the type of resistor, and its formula may be either

$$\pi_S = 0.71 \cdot \exp(1.1 \cdot S) \quad (5.16)$$

$$\text{or} \quad (5.17)$$

$$\pi_S = 0.54 \cdot \exp(2.4 \cdot S) \quad (5.18)$$

⁵Worst-case according to [17].

⁶Wire wound resistors limit the current, which is the goal of the bleeding resistors.

⁷Taken from an on-going RUAG Space project.

⁸Please note that the resistance is calculated at worst-case condition, i.e. at the minimum temperature of -60°C

Component	Reliability Reference	Appendix	Section	Model	Values								FIT	Failure Rate (λ)		Failure Modes [%]		Reliability		
					λ_b	π_T	π_S	π_C	π_Q	π_E	π_K	π_P		(Failures / hours)	Short	Open	Total	Short-circuit	Open-circuit	
Solar Cell	ESA PSS-01-302	-	-	-	-	-	-	-	-	-	-	-	-	1.000	1.000E-09	80	20	0.9999562	0.9999650	0.9999912
Bypass Diode	-	-	-	-	-	-	-	-	-	-	-	-	-	1.000	1.000E-09	80	20	0.9999562	0.9999650	0.9999912
Blocking Diode	MIL-HBK-217F	Notice 2	6.1	$\lambda = \lambda_b \pi_T \pi_S \pi_C \pi_Q \pi_E$ (Failures / 10^6 hours)	0.025	8.230	0.117	1.000	0.700	0.500	-	-	-	8.447	8.447E-09	60	40	0.9996301	0.9997780	0.9998520
Weld	MIL-HBK-217F	Notice 2	17.1	$\lambda = \lambda_b \pi_E$ (Failures / 10^6 hours)	0.000015	-	-	-	-	0.500	-	-	-	0.008	7.500E-12	-	-	0.9999997	-	-
Crimp	MIL-HBK-217F	Notice 2	17.1	$\lambda = \lambda_b \pi_E$ (Failures / 10^6 hours)	0.00026	-	-	-	-	0.500	-	-	-	0.130	1.300E-10	-	-	0.9999943	-	-
Connector	MIL-HBK-217F	Notice 2	15.1	$\lambda = \lambda_b \pi_T \pi_K \pi_Q \pi_E$ (Failures / 10^6 hours)	0.023	3.037	-	-	1.000	0.500	1.000	-	-	34.921	3.492E-08	-	-	0.9984716	-	-
Resistor	MIL-HBK-217F	Notice 2	9.1	$\lambda = \lambda_b \pi_T \pi_S \pi_Q \pi_E$ (Failures / 10^6 hours)	0.0024	1.883	0.996	-	0.100	0.500	-	0.477	-	0.107	1.074E-10	-	-	0.9999953	-	-

Table 5.1: Failure rate models and obtained reliability values for single components (mission lifetime: 5 years).

Considering the assumption made relative to the type of resistor, the second equation is used in this case. S refers to the ratio between the dissipated power and the rated power of the resistor, where $P_{\text{rated}} = 0.5\text{W}$ is chosen. This gives $\pi_S = 0.996$. The quality factor π_Q is assigned based on the established reliability styles that are assessed through testing and are defined in [8]. Quality R is assumed, corresponding to $\pi_Q = 0.1$. The environment factor is $\pi_E = 0.5$.

For a mission lifetime of 5 years, the calculated parameters and the obtained reliability values considered in the analysis for the single components are summarized in Table 5.1.

5.1.2. Reliability Model and Approach

As previously mentioned, the reliability model implemented for the analysis is the reliability block diagram, whose purpose is defined in [2]: "The purpose of the reliability block diagram is to show by concise visual shorthand the various series-parallel block combinations (paths) that result in item success. [...] The reliability block diagram shall be drawn so that each element or function employed in the item can be identified. Each block of the reliability block diagram shall represent one element or function contained in the item". For the solar array, three main functions are identified, which are series-connected from a reliability perspective: power generation, power transfer, and bleeding function. The power generation function involves all



Figure 5.2: PVA Reliability Block Diagram: functions.

the components that are integrated to build the strings such that they achieve the objective to feed the main bus: these include solar cells, bypass diodes, blocking diodes, and all the intra-string connections. Then, all the connection points that are needed to connect the terminals of the strings with the connectors, as well as the connectors themselves, are items that shall fulfill the function of power transfer. Moreover, the bleeding function is essential to mitigate the severe effects of ground faults, and, for this reason, is also considered in the reliability analysis. As it may be inferred from this consideration, every function may be considered as an interaction of items, that are connected in a specified configuration to fulfill the intended objective. Then, the reliability of every function may be calculated by applying the following general formula, taken from [2]:

$$R_S = R_S(\text{if } x \text{ works}) \cdot R_x + R_S(\text{if } x \text{ fails}) \cdot Q_x \quad (5.19)$$

where $R_S(\text{if } x \text{ works})$ is the reliability of the function if item X is properly working, R_x is the reliability of item X , $R_S(\text{if } x \text{ fails})$ is the reliability of the function if item X is faulty, and $Q_x = 1 - R_x$. Equation 5.19 is the fundamental equation for the conventional probability method. As will become clear later in this section, a function can also be divided into different subsystems, whose reliability is also calculated by applying equation 5.19. For instance, if n items work in series or in parallel, equation 5.19 reduces to equation 5.20 and 5.21, respectively.

$$R_S(t) = \prod_{i=1}^n R_i(t) = \prod_{i=1}^n \exp(-\lambda_i t) = \exp\left(-\sum_{i=1}^n \lambda_i t\right) = \exp(-\lambda_S t) \quad \text{serial configuration} \quad (5.20)$$

$$R_S(t) = 1 - \prod_{i=1}^n (1 - R_i) = 1 - \prod_{i=1}^n (1 - \exp(-\lambda_i t)) \quad \text{parallel configuration} \quad (5.21)$$

It is here specified that equipment connected in parallel represent "the existence of more than one means for performing the required function" [2], i.e. the implementation of redundancy. A proof of the above equations is briefly provided in the following. For series-elements:

$$R_s = R_A \cdot R_B + 0 \cdot (1 - R_B) = R_A \cdot R_B \quad (5.22)$$

The same result is obtained if the multiplication rule of probability is applied: since A and B are independent, the probability that both *events* occur, where *event* is defined as the ability of either A and B of properly functioning, is the product of their respective probabilities. In a similar way, for parallel-connected elements:

$$R_s = 1 \cdot R_A + R_B \cdot (1 - R_A) = R_A + R_B - R_A \cdot R_B = 1 - (1 - R_A) \cdot (1 - R_B) \quad (5.23)$$

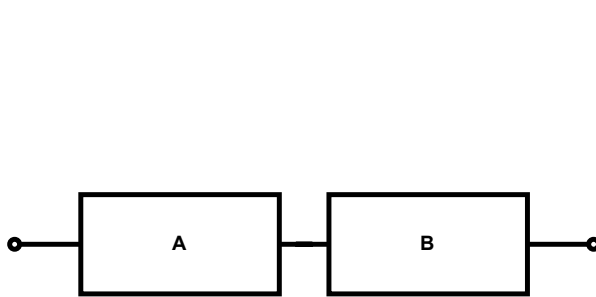


Figure 5.3: Series-connected elements.

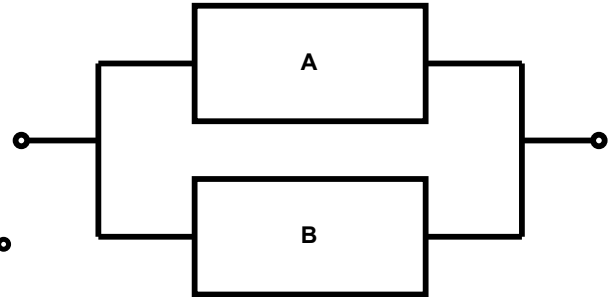


Figure 5.4: Parallel-connected elements.

Also in this case, the same result may be obtained by applying the addition rule for non-exclusive cases. Equations 5.20 and 5.21 are valid under the assumption that all the elements within the system are independent with respect to each other, i.e. a component failure does not influence the behavior of the other components. In addition to this, it is assumed that the system is new at time $t = 0$. Furthermore, equation 5.21 is only applicable when the equipment is in a state of hot redundancy, i.e. all equipment is active continuously and a single item is sufficient to achieve the required objective.

The introduced formulas are implemented in the software algorithm, explained in Section 5.2, to predict the reliability of the functions considered and eventually retrieve the reliability of the whole PVA.

5.1.3. Assumptions

Some assumptions are needed to perform the reliability analysis that have impact on the predicted value.

The first assumption involves the blocking diodes. As explained in Chapter 4, a short-circuit failure of the component does not affect the output performance of the PVA if no voltage mismatch is experienced between the bus and the faulty string. In such a case, it may be reasonable to assume that no string loss occurs whenever a short-circuit of the blocking diode occurs. On the other hand, it has been studied that if the voltage mismatch arises, the power loss may be significant. Therefore, the choice is left to the user on whether a string failure has to be considered for a shorted blocking diode. However, it is important to understand the impact of this assumption. Indeed, if a string failure is considered following a short-circuit of the blocking diode, adding redundancy by parallel-connecting additional diodes would result in a decreased reliability. This effect will be further analyzed later in this chapter.

A second assumption includes considerations on the bypass diode. It has been demonstrated that the open-circuit failure of a bypass diode does not induce any power loss if not combined with a current mismatch of its respective cell with the other cells within the same string. In the latter case, the current is limited by the faulty or shaded unprotected cell. This behavior is difficult to take into account while performing a reliability analysis. It has been decided, consistently with the reliability analyses of the ongoing RUAG Space projects, to let the possibility of assuming a short-circuit failure of the cell following an open fault of the bypass diode. Whether or not the assumption is valid for the reliability analysis can make a big difference if combined with another parameter that is left to the user to define, i.e. the maximum number of solar cells in short that are acceptable beyond which the string is considered lost.

Lastly, the open-circuit failure of the solar cells considered for the analysis has to be defined. As said in Section 4.2.7, the mechanism that triggers this kind of fault may or may not prevent the bypass diode to provide an alternative current path. Therefore, it may have a significant impact on the reliability prediction and

a choice has to be made on whether or not the bypass diode is able to mitigate an open solar cell.

Closely related to all the aforementioned assumptions, the definition of the maximum allowable string failures is also crucial. This determines the number of failures that the system can sustain and still be able to fulfill its mission.

For the proposed analysis, the following assumptions are made:

- the string is not lost if the blocking diode fails short;
- if the bypass diode experiences an open-circuit failure, the respective solar cells is still considered healthy;
- the bypass diode mitigates an open-circuit failure of the solar cell;
- maximum number of allowable solar cell in short: 0;
- maximum number of string failures: 0.

5.2. Reliability Prediction

In this section the calculations carried out to estimate the reliability of the PVA are presented. The reliability block diagram that is representative of the mathematical model used for the prediction is based on the PVA configuration, defined by the user through the different panels presented in Section 3.2. *DemoSat* is used as case study, where assumptions are made on the connections and wiring of the solar array. The details may be found in Table 5.2.

Number of segments / string	1
Number of intra-string welds	35
Number of intra-string crimps	2
Number of welds at section level	4
Number of crimps at section level	0
Number of welds / grounding point	1
Number of crimps / grounding point	2

Table 5.2: *DemoSat* connection points.

5.2.1. Power Generation

A sample reliability block diagram of a small string consisting of two series-connected solar cells is shown in Figure 5.5. Within the string, different subsystems are identified to facilitate the calculations: connections, solar cell assembly, bypass diode assembly, and blocking diode assembly. Diodes assemblies consist of all the items considered in the reliability analysis whose function is identified in that of the bypass or blocking diode. These items include redundant components and connections⁹.

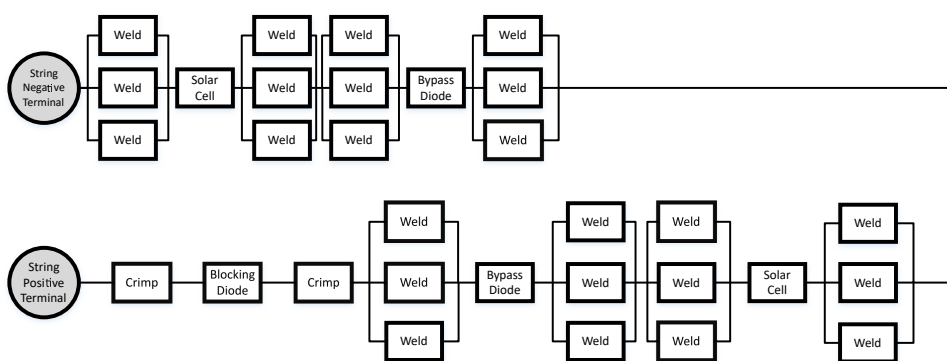


Figure 5.5: Example of a reliability block diagram of a string.

solar cell assembly, bypass diode assembly, and blocking diode assembly. Diodes assemblies consist of all the items considered in the reliability analysis whose function is identified in that of the bypass or blocking diode. These items include redundant components and connections⁹.

⁹Please recall that, for increasing the software flexibility and performing a more detailed reliability analysis, bypass diodes redundancy is provided as an option for the user even though it is hardly implemented in real applications.

Connections All the connections of the string, except those of the diodes that are used as a corrective factor of the failure modes of the latter, are grouped to calculate the overall reliability of the harness. For a single string, the applicable formulas are the following:

$$R_{\text{welds}} = \prod_{i=1}^{n_w} 1 - (1 - R_{w,i})^{\text{redundancy}_{w,i}} \quad (5.24)$$

$$R_{\text{crimps}} = \prod_{i=1}^{n_c} 1 - (1 - R_{c,i})^{\text{redundancy}_{c,i}} \quad (5.25)$$

n_w and n_c are the number of welding points and crimping points in series within a string, respectively, and depend on the PVA layout. A higher number of segments, for instance, would increase the number of connections needed. The values of R_w and R_c are taken from Table 5.1. The redundancy of the single connection points, if implemented, is also considered in the calculation. Then, to obtain the overall reliability of the intra-string connections:

$$R_{\text{intra-string connections}} = R_{\text{welds}} \cdot R_{\text{crimps}} \quad (5.26)$$

As mentioned, the software offers the flexibility to model a different number of segments for each string, thus the result of equation 5.26 is an array of reliability values whose length is equal to the number of strings in the PVA. *DemoSat* has a common configuration for all the strings, and the predicted reliability value is $R_{\text{intra-string connections}} = 0.99999376$. Furthermore, another interesting outcome that can be provided at this point is the probability of failure of a connection. Due to the need of limiting the computational time for such calculation, only the probability of occurrence of a single connection rupture within the PVA is calculated. Moreover, for such analysis, the lowest reliability contained in the resulting array from equation 5.26 is assigned to every string. Please be aware that every connection point may have a different reliability based on the degree of redundancy implemented. The failure probability is given by the sum of all the probabilities for which one connection point fails while all the others are intact, which is translated in the following formula:

$$P = \sum_{i=1}^N \left((1 - R_i) \cdot \prod_{k \in \{j\}_{j=1}^N - \{i\}} R_k \right) \quad (5.27)$$

where $N = n_w + n_c$, and $R = 1 - (1 - R_{w/c})^{\text{redundancy}_{w/c}}$ is the reliability of a single connection point considering its redundancy. It can be verified that the probability of multiple failures is negligible by calculating the highest probability of a connection failure, which, for the modeled configuration, is obtained for a crimp with no redundancy $P_c = 1 - R_c = 5.69 \times 10^{-6}$. This value has to be raised by a power equal to the number of failures that have to be considered. It is clear that for only two failures the probability has an order of magnitude of -11.

By multiplying P from equation 5.27 by the number of strings, the probability of an intra-string connection failure in the whole PVA is found. The obtained probability is $P_{\text{intra-string connection failure,PVA}} = 4.99 \times 10^{-5}$.

Blocking Diode Assembly A blocking diode assembly is considered as the assembly of all the blocking diodes and their respective connections that are used in a single string to fulfill the function explained in Chapter 4. As far as the connections are concerned, their reliability is calculated by using equations 5.24, 5.25 and 5.26 per single diode, assuming that all the redundancies are implemented with the same wiring configuration. Then, a reliability $R_{\text{conn,bk}}$ is retrieved for the connection point of a single blocking diode. This affects the probability of the assembly being subjected to an open-circuit failure. Thus, an equivalent open-circuit reliability¹⁰ may be calculated as

$$R_{\text{oc,bk,eq}} = R_{\text{oc,bk}} \cdot R_{\text{conn,bk}} \quad (5.28)$$

Here the subscripts *oc*, *bk* and *conn* refer to *open-circuit*, *blocking diode* and *connections*, respectively. $R_{\text{oc,bk}}$ is the value from Table 5.1. The above equation is consistent with the multiplication rule of probability since for the diode to not fail open both the connection points and the component itself must not fail open to avoid an overall open-circuit failure. Then, the total reliability of the assembly depends on the redundancy level as well as on the assumption made. If a string failure follows a short-circuit failure of the blocking diode, the reliability values of both failure modes play a role in the analysis. In case this assumption is not considered valid, only the probability of occurrence of an open fault influences the system reliability. This means that, if the

¹⁰i.e. the probability that a blocking diode does not fail open.

shorted diode is considered detrimental for the string, the diode has to be analyzed as a three-state device, i.e. it can be either in open, short, or operating state. These states are mutually exclusive. Under these circumstances, considerations have to be made regarding the assembly configuration. For a series-connected diode, the reliability of the assembly is the probability that there are no open-circuit failures, from which is subtracted the probability that all components are shorted. On the other hand, if diodes are connected in parallel, the total reliability is given by the probability that no short-circuit failures occur minus the probability that all diodes fail open. These probabilities are translated into two different equations based on the redundancy level. For high-level redundancy, shown in Figure 3.13a:

$$R_{\text{bk,assy}} = (1 - (1 - R_{\text{sc,bk}})^{n_s})^{n_p} - (1 - R_{\text{oc,bk,eq}}^{n_s})^{n_p} \quad (5.29)$$

while for a low-level redundancy (Figure 3.13b):

$$R_{\text{bk,assy}} = (1 - (1 - R_{\text{oc,bk,eq}}^{n_p})^{n_s} - (1 - R_{\text{sc,bk}}^{n_p})^{n_s}) \quad (5.30)$$

where n_p is the number of parallel-connected diode, n_s is the number of series-connected diode, $R_{\text{sc,bk}}$ is taken from Table 5.1. The subscript *sc* means *short-circuit* while *assy* refers to the *assembly*.

However, if the aforementioned assumption is not made, then a short-circuit failure of the blocking diode is not seen as a degraded state of the component from a reliability perspective. Taking into account that a parallel connection from an electrical point of view is also a parallel connection when translated into a reliability block diagram, the two equations for the different redundancy levels are:

$$R_{\text{bk,assy}} = 1 - (1 - R_{\text{oc,bk,eq}}^{n_s})^{n_p} \quad \text{High-level redundancy} \quad (5.31)$$

$$R_{\text{bk,assy}} = (1 - (1 - R_{\text{oc,bk,eq}})^{n_p})^{n_s} \quad \text{Low-level redundancy} \quad (5.32)$$

Similar to the reliability values for the intra-string connections, since the blocking diode assembly configuration of each string may be user-defined, $R_{\text{bk,assy}}$ is an array of length equal to the number of strings. For the simulated CubeSat, one blocking diode is integrated with each string, thus a unique reliability of $R_{\text{bk,assy}} = 0.99984062901657$ is calculated.

Furthermore, the probability of failure in either open or short condition can be calculated for the blocking diode assembly. To do this, the short-circuit reliability, meant as the probability of the assembly of not experiencing a short-circuit failure, has to be calculated. When analyzing a short failure mode, it is important to highlight that a parallel physical connection is modeled as a series connection from a reliability perspective. It follows:

$$R_{\text{sc,bk,assy}} = 1 - (1 - R_{\text{sc,bk}}^{n_p})^{n_s} \quad \text{High-level redundancy} \quad (5.33)$$

$$R_{\text{sc,bk,assy}} = (1 - (1 - R_{\text{sc,bk}})^{n_s})^{n_p} \quad \text{Low-level redundancy} \quad (5.34)$$

Indicating $P_{\text{Fmode,bk}}$ as the probability of failure in either open or short conditions, the general formula for k faulty assemblies is given by equation 5.35.

$$P_{\text{Fmode,bk,assy}} = \binom{N}{N-k} R_{\text{Fmode,bk,assy}}^{N-k} \cdot (1 - R_{\text{Fmode,bk,assy}})^k \quad (5.35)$$

where N is the total number of strings. The binomial coefficient indicates the number of possible failure combinations of the assemblies. Equation 5.35 can only be used if a single value of $R_{\text{mode,bk,assy}}$ is selected and assigned to all the blocking diode assemblies. When this is the case, the minimum value of the respective array is chosen, assuming worst conditions¹¹. The predicted probabilities for *DemoSat*, considering a failure of a single assembly, are $P_{\text{oc,bk}} = 1.274 \times 10^{-3}$ and $P_{\text{sc,bk}} = 1.773 \times 10^{-3}$.

Bypass Diode Assembly For the bypass diode assembly, the same considerations made relative to the blocking diode apply, however, different assumptions have to be taken into account. Equations 5.29 and 5.30 are used when an open-circuit failure of the bypass diode is assumed detrimental for the unprotected solar cell. As a consequence, both failure modes of the bypass diode have a negative impact on the reliability. If this is not the case, only a short-circuit failure induces performance losses on the PVA. Once again, it is stressed

¹¹This does not apply for the modeled PVA, since the assemblies with the same configuration are integrated into the strings.

that when short faults are analyzed, an electrical parallel connection is translated into a series connection in a reliability block diagram. Therefore, equation 5.33 and 5.34 apply when this the open-circuit failure does not influence the behavior of the respective cell.

For the modeled CubeSat, a single bypass diode is considered, and according to the assumption made, the reliability of the assembly reduces to the short-circuit reliability of the bypass diode from Table 5.1. To be able to calculate the probabilities of occurrence of the failure modes, the open-circuit reliability is needed, calculated by using equation 5.31 or 5.32, which both reduce to $R_{oc,by,eq} = R_{oc,by} \cdot R_{conn,by}$ due to the integration of a single component. Then, the probabilities of failure are calculated by using equation 5.35, where N is, in this case, the total number of solar cells in the PVA. Considering a single failure, the probabilities of occurrence are $P_{oc,by} = 5.271 \times 10^{-4}$ and $P_{sc,by} = 1.958 \times 10^{-3}$.

Solar Cell Assembly The solar cell assembly is the integration of the bypass diode assembly, which for simplicity will be referred to as bypass diode, and the solar cell. Like its components, also the assembly has to be treated as a three-state device, and, as such, both its open-circuit and short-circuit reliability values have to be calculated. To retrieve the needed formulas, the probability of failures is used as starting point. If the bypass diode is able to mitigate an open fault of the solar cell, the probability of a short-circuit failure of the assembly is the sum of the probabilities of two mutually exclusive events, calculated in equation 5.36.

$$P_{sc,SC,assy} = \underbrace{P_{sc,SC} + P_{by,assy} - P_{sc,SC} \cdot P_{by,assy}}_{\text{solar cell fails short and/or the bypass diode fails}^{12}} + \underbrace{P_{oc,SC} \cdot (1 - P_{oc,by,assy})}_{\text{solar cell fails open and bypass diode does not fail open}} \quad (5.36)$$

where the subscript *SC* means *solar cell*. $P_{by,assy}$ is the probability of failure of the bypass diode considering the involved assumptions. By rearranging equation 5.36 and replacing the probabilities of failure with the respective reliability ($P = 1 - R$), the following expression for the short-circuit reliability of the solar cell assembly is obtained:

$$R_{sc,SC,assy} = R_{by,assy} \cdot R_{sc,SC} - R_{oc,by,assy} + R_{oc,by,assy} \cdot R_{oc,SC} \quad (5.37)$$

Then, as far as the open-circuit mode is concerned, it occurs when both the solar cell and the bypass diode fail open:

$$P_{oc,SC,assy} = P_{oc,SC} \cdot P_{oc,by,assy} \quad (5.38)$$

↓

$$R_{oc,SC,assy} = R_{oc,SC} + R_{oc,by,assy} - R_{oc,SC} \cdot R_{oc,by,assy} \quad (5.40)$$

Once again, it is highlighted that the above equations are valid under the assumption that the bypass diode is able to mitigate an open-circuit failure of a solar cell. If this assumption is not valid, the formulas for calculating the reliability reduces to:

$$R_{sc,SC,assy} = R_{by,assy} \cdot R_{sc,SC} \quad \text{for the short-circuit reliability} \quad (5.41)$$

$$R_{oc,SC,assy} = R_{oc,SC} \quad \text{for the open-circuit reliability} \quad (5.42)$$

For *DemoSat*, the results are $R_{sc,SC,assy} = 0.999921162576407$ and $R_{oc,SC,assy} = 0.99999999917508$.

The equations above allow calculating the reliability of a single solar cell assembly, nonetheless, a string is built by a series connection of several of N assemblies. Therefore, it is needed to calculate the overall reliability for an entire string. As before, short-circuit and open-circuit failures have to be treated differently. For the analysis of the former, the series connection of the solar cell assemblies may be seen as the implementation of a k -out-of- n redundancy, where k is the number of solar cells within a string minus the number of acceptable solar cells in short, defined by the assumption. If the assemblies are identical, the overall reliability is given by equation 5.43.

$$R_{sc,SC,assy,@\text{ string level}} = \sum_{i=k}^N \binom{N}{i} R_{sc,SC,assy}^i \cdot (1 - R_{sc,SC,assy})^{N-i} \quad (5.43)$$

where the binomial coefficient gives the possible combinations of failures of the assemblies. However, the above equation applies exclusively when the assemblies involved are identical. Given the flexibility of the

¹²Short/open or exclusively short depending on the assumption.

software, it may be possible to model solar cell assemblies that differ with respect to each other even within the same string. This can be due to different parameters: number of connections or redundancy implemented, and number of bypass diodes. For this reason, another algorithm has to be implemented to take into account the different combinations of failures for a system that involves non-homogeneous components. An example is provided to better understand the function of this software feature. It is here considered a sample string that consists of 4 different solar cell assemblies, 2 of which must operate to fulfill the power requirement. In this case, the 2-out-of-4 reliability is calculated as:

$$R_{\text{tot}} = R_1 R_2 R_3 (1 - R_4) + R_1 R_2 (1 - R_3) R_4 + R_1 (1 - R_2) R_3 R_4 + (1 - R_1) R_2 R_3 R_4 + \\ + R_1 R_2 (1 - R_3) (1 - R_4) + R_1 (1 - R_2) R_3 (1 - R_4) + (1 - R_1) R_2 R_3 (1 - R_4) + R_1 (1 - R_2) (1 - R_3) R_4 + \\ + (1 - R_1) R_2 (1 - R_3) R_4 + (1 - R_1) (1 - R_2) R_3 R_4 \quad (5.44)$$

The terms on the right-hand side of equation 5.44 corresponds to all the mutually exclusive cases under whose state the system is not in a fault condition. The implemented algorithm may be found in [9]. According to the reference, the overall reliability of the k-out-of-n configuration of non-identical components may be calculated by building the event matrix \mathbf{C} and the probability vector \mathbf{p} . The matrix \mathbf{C} represents the component events, i.e. *healthy* or *faulty*.

$$\mathbf{C}_1 = [1 \ 0]^\top \quad (5.45)$$

$$\mathbf{C}_i = \begin{bmatrix} \mathbf{C}_{i-1} & 1 \\ \mathbf{C}_{i-1} & 0 \end{bmatrix} \quad \text{for } i \in [2, N] \quad (5.46)$$

$$\mathbf{p}_1 = [R_1 \ (1 - R_1)]^\top \quad (5.47)$$

$$\mathbf{p}_i = \begin{bmatrix} \mathbf{p}_{i-1} \cdot R_i \\ \mathbf{p}_{i-1} \cdot (1 - R_i) \end{bmatrix} \quad \text{for } i \in [2, N] \quad (5.48)$$

Then, from the matrix \mathbf{C} , the event vector \mathbf{c}_{sys} is obtained for the k-out-of-n system:

$$\mathbf{c}_{\text{sys}} = \mathbf{I}(\mathbf{C}_n \cdot \mathbf{1} \geq k) \quad (5.49)$$

Here, $\mathbf{I}(\cdot)$ is a function which gives 1 or 0 if the statement in bracket is *true* or *false*, respectively. Lastly, the system reliability is given by equation 5.50.

$$R_{\text{sc,SC,assy,@ string level}} = \mathbf{c}_{\text{sys}}^\top \cdot \mathbf{p}_n \quad (5.50)$$

For solar arrays whose strings are built by series-connecting a high number of non-identical solar cell assemblies, the indicated matrix and vector may exceed the memory capability of MATLAB, resulting in a computational error. If this happens, the software is able to detect the flaw and to calculate the reliability by using equation 5.43, considering the worst-case scenario where all the assemblies within the string take the lowest reliability value in the array $R_{\text{sc,SC,assy}}$.

The solar array of *DemoSat* is built by homogeneous strings, whose short-circuit reliability is calculated to be $R_{\text{sc,SC,assy}} = 0.999448268539824$. Note that, given the assumption made for the CubeSat under analysis, where no shorted solar cell assemblies are tolerated, the formula for calculating the reliability reduces to $R_{\text{sc,SC,assy,@ string level}} = R_{\text{sc,SC,assy}}^N$ being N the total number of cells within a string.

As far as the open-circuit failure of a string due to the solar cell assemblies is concerned, the string does not experience such failure mode if and only if none of the assemblies fails open. Please note that the potential mitigation effect provided by the presence of the bypass diode has already been taken into account since the discussion here involves the complete solar cell assembly. As a consequence, the open-circuit reliability is always calculated as in equation 5.51.

$$R_{\text{oc,SC,assy,@ string level}} = R_{\text{oc,SC,assy}}^N \quad (5.51)$$

For *DemoSat*, $R_{\text{oc,SC,assy,@ string level}} = 0.999999999422556$.

It is now possible to calculate the overall reliability of the solar cell assemblies at string level. As mentioned before, open- and short-circuit failures are mutually exclusive events, thus the probability that either one of the two occurs is the sum of the respective probabilities. It follows:

$$R_{\text{SC,assy,@ string level}} = 1 - ((1 - R_{\text{oc,SC,assy,@ string level}}) + (1 - R_{\text{sc,SC,assy,@ string level}})) \quad (5.52)$$

This results in a value of $R_{\text{SC,assy,@ string level}} = 0.99944826796238$ for *DemoSat*.

String At this point, it is possible to calculate the total reliability of a string. Connections, solar cell assemblies and blocking diode assembly are connected in series from a reliability perspective, and the reliability is retrieved by using equation 5.53.

$$R_{\text{string}} = R_{\text{SC,assy,@ string level}} \cdot R_{\text{bk,assy}} \cdot R_{\text{intra-string connections}} \quad (5.53)$$

The obtained value for the satellite under analysis is $R_{\text{string}} = 0.999282747866288$, that is common for all strings given the shared configuration. Then, the reliability of the power generation function may be computed by considering the assumption made on the number of acceptable string failures. Once again, this consideration makes the parallel-connected strings a k-out-of-n system, whose characteristic reliability formula has been described previously in this section. Also in this case, should the strings have different reliability values, the matrix \mathbf{C} and the vector \mathbf{p} shall be constructed and the explained algorithm executed. In the simulation considered, all the strings must operate in a healthy state in order to be able to fulfill the requirements, thus the power generation reliability can be calculated as in equation 5.54.

$$R_{\text{power generation}} = (R_{\text{strings}})^N \quad (5.54)$$

Here N indicates the total number of strings in the PVA.

It follows for *DemoSat*: $R_{\text{power generation}} = 0.994276366902787$.

5.2.2. Power Transfer

The power transfer function includes all the connections and components whose objective is to feed the satellite power bus. This means that everything between the connector(s) and the string terminals is considered in the analysis. Two connectors per section are assumed. The reliability relative to the connections is computed by applying the formulas in equation 5.24, 5.25 and 5.26. Then, the reliability of a single section is given by equation 5.55.

$$R_{\text{section}} = R_{\text{section connections}} \cdot (R_{\text{connector}})^2 \quad (5.55)$$

where $R_{\text{connector}}$ is taken from Table 5.1. The parallel-connected sections are in series from a reliability point of view. As a consequence, the formula to obtain the reliability of the power transfer function is given in equation 5.56, where N is the total number of sections.

$$R_{\text{power transfer}} = (R_{\text{section}})^N \quad (5.56)$$

The predicted value for *DemoSat* is $R_{\text{power transfer}} = 0.987833151505885$.

The reliability values calculated in this section allow to estimate the failure probability of the transfer function. The failure mode considered for the involved components, i.e. connection point and connectors, is the open-circuit failure. It follows:

$$P_{\text{power transfer}} = N \cdot \left[\sum_{i=1}^n \left((1 - R_i) \cdot \prod_{k \in \{j\}_{j=1}^N - \{i\}} R_k \right) \right] \quad (5.57)$$

where N is the total number of sections and n is the total number of elements integrated into a single section to perform the power transfer function (connection points and connectors)¹³. The result is $P_{\text{power transfer}} = 0.012213398$.

5.2.3. Bleeding Function

The bleeding function mitigates the negative impact of potential short-circuit between a current-carrying conductor and the panel substrate. Every grounding point is considered to be constituted by a single bleeding resistor, for which hot redundancy may be implemented. The reliability of a single grounding point with no redundancy is given by equation 5.58.

$$R_{\text{GND}} = R_{\text{connector}} \cdot R_{\text{connections}} \cdot R_{\text{resistor}} \quad (5.58)$$

Then, by considering the hot redundant branches (r), assumed to be the same for all the grounding points, and the total number of the latter, the overall bleeding function reliability is predicted by using equation 5.59.

$$R_{\text{bleeding function}} = (1 - (1 - R_{\text{GND}})^r)^N \quad (5.59)$$

¹³Please note that it is possible to estimate the overall failure probability of the function by multiplying the probability of a single section only if the power transfer is implemented for every section in the same way.

Here N is the total number of grounding points.
For *DemoSat*: $R_{\text{bleeding function}} = 0.998455247164272$.

5.2.4. PVA Reliability

The reliability values of all the three functions identified for the PVA have been estimated, and the reliability of the whole PVA may be calculated.

$$R_{\text{PVA}} = R_{\text{power generation}} \cdot R_{\text{power transfer}} \cdot R_{\text{bleeding function}} \quad (5.60)$$

Equation 5.60 is used for the calculation, leading to $R_{\text{pva}} = 0.980661932947456$ for *DemoSat*.

5.2.5. Validation

The validation process of the reliability analysis is carried out by exploiting the available data of two ongoing RUAG Space projects. Two approaches are followed: a first approach consists of comparing the reliability value predicted by the developed software with the result from the reliability analysis report of the respective project. For the second activity, the system reliability is calculated by using an existing qualified software, that is compared with the ones retrieved from the tool.

As far as the first approach is concerned, 4 different reliability values are available for one of the two projects, corresponding to the reliability for 0, 1, 2, and 3 acceptable string failures. The discrepancies found with respect to the predicted reliability by the developed software are summarized in Table 5.3.

	Acceptable String Failures			
	0	1	2	3
ΔReliability	0.008387659868525 p.p.	0.001165712625972 p.p.	0.000083544735385 p.p.	0.000000345301943 p.p.

Table 5.3: Discrepancy between the system reliability predicted by the developed software and the available results of a reliability analysis report of a RUAG Space project (1).

The table highlights that the error decreases with increasing number of acceptable string failures. Overall, the error is negligible.

The difference between the calculated reliability and the value provided by the second project report is significantly higher, as shown in Table 5.4, where the reliability discrepancy with respect to two different PVA sections is provided. Nonetheless, the information provided on the methodology followed by the supplier to

	Section N. 1	Section N. 2
ΔReliability	1.117137338 p.p.	0.322822019 p.p.

Table 5.4: Discrepancy between the system reliability predicted by the developed software and the available results of a reliability analysis report of a RUAG Space project (2).

perform the reliability analysis lacks of relevant details needed to correctly recreate the system configuration in the software. As a consequence, a lower degree of accuracy is expected.

For what concerns the comparison of the results with the qualified software, Table 5.5 shows that small errors are registered for both projects. Please be aware that the value compared is the probability of N string loss rather than the actual reliability.

		Probability of N String Failures	
		N = 0	N = 1
ΔReliability	Project 1	0.031902549 p.p.	-0.027453836 p.p.
	Project 2	-0.360387427 p.p.	0.307948619 p.p.
	Section N. 1	-0.093860087 p.p.	0.090736324 p.p.
	Section N. 2	-0.093860087 p.p.	0.090736324 p.p.

Table 5.5: Discrepancy between the system reliability predicted by the developed software and the values obtained from a qualified software for two RUAG Space projects.

In conclusion, given the small discrepancies registered for both approaches, the implemented algorithm for the reliability prediction may be considered validated.

<ul style="list-style-type: none"> • # Solar Cells / string • # Total Strings • # Sections • # Segments / string • # Blocking Diodes (series-connected) • # Blocking Diodes (parallel-connected) • # Bypass Diodes (series-connected) • # Bypass Diodes (parallel-connected) • # Welds (string level) • Welds Redundancy (string level) • # Crimps (string level) • Crimps Redundancy (string level) • # Welds (section level) • Welds Redundancy (section level) • # Crimps (section level) • Crimps Redundancy (section level) 	<ul style="list-style-type: none"> • # Welds (bleeding function) • Welds Redundancy (bleeding function) • # Crimps (bleeding function) • Crimps Redundancy (bleeding function) • # Welds (blocking diodes) • Welds Redundancy (blocking diodes) • # Crimps (blocking diodes) • Crimps Redundancy (blocking diodes) • # Welds (bypass diodes) • Welds Redundancy (bypass diodes) • # Crimps (bypass diodes) • Crimps Redundancy (bypass diodes) • Welds Redundancy (segment level) • Bleeding Function Redundancy • # GND Points • Diodes Redundancy Level 	<ul style="list-style-type: none"> • Failure modes distribution: Solar Cells • Failure modes distribution: Bypass Diodes • Failure modes distribution: Blocking Diodes • Bleeding Resistor Type • Resistor Case Temperature • Resistor Rated Power • Resistor Dissipated Power • Blocking Diode Junction Temperature • Blocking Diode Reverse Voltage • AWG (connector) • Connector Ambient Temperature • String Lost if Blocking Diode fails Short • Cell in Short if Bypass Diode fails Open • Bypass Diode mitigates Solar Cell in Open • Max. Acceptable Solar Cell in Short • Max. Acceptable String Failures
--	---	--

Table 5.6: Features considered in the sensitivity analysis.

5.3. Sensitivity Analysis

Once the PVA reliability has been retrieved, the research objective requires analyzing which *features* have a strong impact on it and which modifications may lead to a reliability improvement. A *feature* is here intended as every parameter that somehow affects the predicted value, i.e. all the parameters related to the PVA layout, the implemented redundancy of the different components as well as those factors that are directly involved in the failure rate models of the single components. The analysis is not performed over the π factors that are user-defined nor on the base failure rates λ_b , unless they are calculated by using a specific formula given in [4, 6]. This means that, for instance, the variation of the environment factor π_E is not investigated, while the temperature factor π_T is indirectly investigated in the sensitivity analysis, where the component's temperature is included. Table 5.6 provides a list of all the features considered for the sensitivity analysis.

In practice, it might not always be possible to apply changes to every listed feature. For instance, as previously mentioned in this report, redundancy is rarely implemented for bypass diodes. Consequently, a tool option allows the user to keep some of the features constant, decreasing the computational time and avoiding unnecessary output files. In this case, for research purposes, all the features are included in the sensitivity analysis.

The objective of such analysis is to investigate the reliability response to the variation of the features by applying changes to a single feature at a time. In this way, the ΔR relative to the reliability of the benchmark design can be analyzed.

The assumptions introduced in Section 5.1.3 are included in the sensitivity analysis and are referred as *Assumption 1*, *Assumption 2*, *Assumption 3* according to Table 5.7.

Assumption 1	Assumption 2	Assumption 3
<ul style="list-style-type: none"> • String loss if the blocking diode fails short. 	<ul style="list-style-type: none"> • Shorted solar cell if the bypass diodes experiences an open-circuit failure. 	<ul style="list-style-type: none"> • The bypass diode mitigates the open-circuit failure of the solar cell.

0 = FALSE , 1 = TRUE

Table 5.7: Assumptions considered in the reliability prediction and sensitivity analysis.

5.3.1. PVA Layout

It is here analyzed the impact on the system reliability of the parameters that concern the PVA layout. In Figure 5.6, the influence of the number of solar cells under different assumptions may be investigated. The graphs on the left show the reliability obtained by applying the feature modification, while on the right the ΔR with respect to the reliability of the benchmark design, in this case, $R_{PVA} = 0.980677288762557$, is given. The unit of the latter is *percentage points*, meaning that, for instance, a deviation of 0.2 *percentage points* (*p.p.*) affects the third decimal digit of the reliability. Different graphs are drawn for allowing the analysis of the multiple assumptions available to the user, whose associated binary value, 1 or 0, indicates whether the respective assumption is considered true or false. The graphs in Figure 5.6 also show the results for several values of acceptable short-circuit failures of the solar cells.

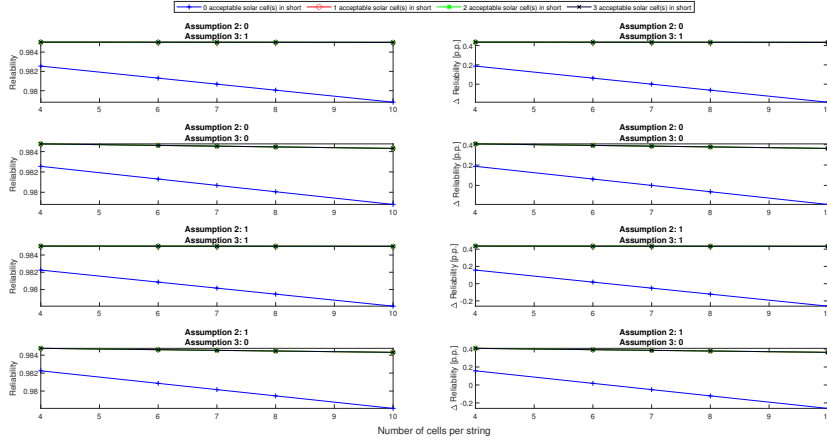


Figure 5.6: Effects of the number of cells per string on the reliability under different assumptions.

The trend, clearly visible when considering 0 acceptable solar cells in short, is that the higher the number of series-connected cells the lower the system reliability. This is reasonable since the probability of failure is increased when there are more components that must operate in a healthy state to fulfill the requirements. Please be aware that for 0 acceptable short-circuit failures of the solar cell assemblies, the overall reliability of the latter becomes $R_{SC,assy,@\text{string level}} = (R_{SC,assy})^N$, where N is the total number of solar cells per string. It can be noted that the number of solar cells lost that the system can sustain within a string has a significant impact on the reliability. Indeed, other than a reliability increase, it also induces a decrease (in absolute value) of the slope, mitigating the impact of a higher number of series-connected cells. It is important to highlight, however, that the rate of return of the reliability improvement decreases rapidly while increasing the number of admissible faults. This is proved by the fact that the red, green, and black lines lie within a limited range of reliability values. Furthermore, it is interesting to point out that for the solar array of *DemoSat*, *Assumption 2* does not have relevant effects on the reliability, resulting in a small decrease when a bypass diode in open leads to a solar cell in short, with ΔR that slightly increase for an increasing number of cells. This is true when 0 short faults are allowed, otherwise, the impact on the reliability is completely negligible. The mitigation capability of the bypass diode when facing an open-circuit failure of the solar cell also has small effects on the reliability, with a decrease experienced when the mitigation is not applicable. Similar to the other assumption, the impact of *Assumption 3* increases with the number of series-connected cells, however, it is only visible for admissible short faults higher than 1. This is reasonable since the mitigation techniques convert an open-circuit failure of the solar cell into a short-circuit one.

A few more considerations have to be done in order to avoid misunderstanding in the results. As mentioned before, it is not possible to generalize the prediction for the characterization of the impact of the analyzed features on the reliability of satellites, not even by reducing the range of applicability to CubeSats. The obtained reliability values are exclusively indicative of the modeled configuration and they are closely dependent on other parameters. For instance, the considerations made on the three investigated assumptions may not hold for different failure modes distribution, which, as explained in Section 5.2, are also assumptions themselves. An attempt to generalize the results from the reliability analysis will be done and explained in Section 6. Another due consideration is that the number of acceptable solar cells in short is not a feature whose modification can physically be implemented in the PVA design. The increase of such value practically means that the strings contain an additional solar cell whose output power is not essential for the fulfillment of the power requirements. Therefore, if this modification is chosen to improve the reliability, one must take into account that its implementation requires an additional solar cell to be series-connected to the existing strings. As a consequence, the reliability gain would be the ΔR between the benchmark design and the design that has an additional solar cell per string and that can sustain one short fault.

The impact of another feature that modifies the PVA layout is investigated in Figure 5.7. On the x-axes, the total number of acceptable string failures is displayed, and curves are plotted that are representative of the reliability for different numbers of strings. As could have been expected, increasing the number of strings of the PVA decreases the system reliability. However, the impact of this feature is drastically contained when at least one string operates in hot redundancy. This brings the reliability of the systems with different numbers

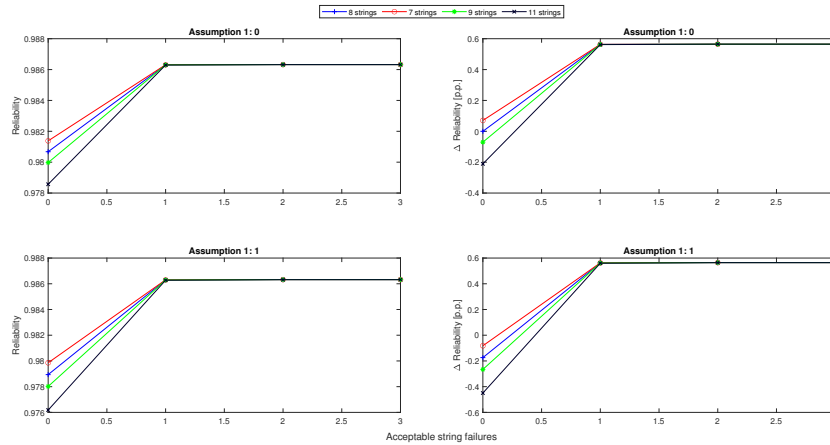


Figure 5.7: Number of acceptable string failures given different numbers of total strings.

of strings to increase and converge to a very limited region of values. Furthermore, the graphs highlight that a number of acceptable string failures above 1 does not lead to significant reliability improvements, therefore it is convenient to design for a single redundant string.

A similar analysis is performed to investigate the impact on the reliability of the number of sections per string. No relevant results are retrieved for the current configuration, therefore no graphs are reported here.

5.3.2. Bypass Diodes Assembly Configuration

The effects on the PVA reliability of the number of parallel-connected bypass diode are plotted in Figure 5.8. The results are given for different numbers of cells per string as well as different numbers of acceptable short

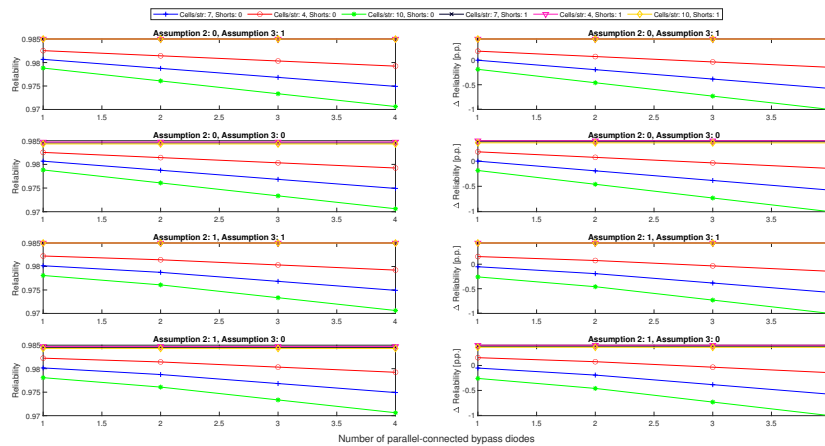


Figure 5.8: Effects on system reliability of the number of parallel-connected bypass diodes.

faults. Multiple components connected in parallel increase the probability of experiencing a short-circuit failure of the bypass diode assembly, leading to the loss of the respective solar cell. This has a negative impact on the system reliability, as proved by the negative slope of the curves in the graphs in Figure 5.8. Similar to the consideration made for the number of solar cells per string, the number of parallel-connected bypass diodes becomes irrelevant as soon as the number of acceptable short-circuit failures is increased from 0 to 1, with no further improvements if more failures are allowed. Even though the impact of *Assumption 2* and *Assumption 3* is negligible with respect to the features under analysis, some considerations can be made for *Assumption 3*: a higher number of parallel-connected bypass diode adds confidence about the fact that an open solar cell would be properly mitigated since it decreases the probability that the bypass diode assembly fails open. On the other hand, this would also increase the probability of the assembly of experiencing a short-circuit failure, with a consequent decrease in the reliability. These two effects counteract each other

and the result is hardly detectable by the proposed graphs, especially since the effects of the assumptions are mainly overcome by those of the other features. The impact of the integration of multiple bypass diode in series is analyzed in Figure 5.9. The most visi-

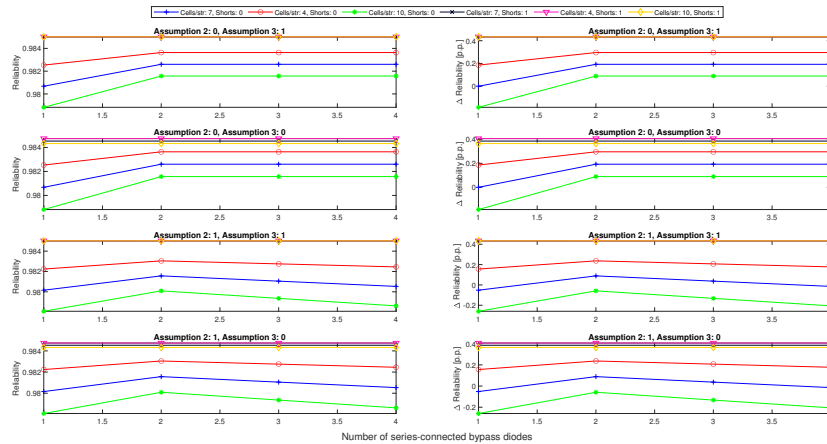


Figure 5.9: Effects on system reliability of the number of series-connected bypass diodes.

ble result is the trend difference imposed by *Assumption 2*. If no effects on the unprotected solar cell are considered after the occurrence of an open-circuit failure of the bypass diode (*Assumption 2 = 0*), a series connection of multiple components decreases the probability of a short-circuit failure of the bypass diode assembly. The rate of return of improvement, however, decreases rapidly, and the reliability gain is constant for ≥ 2 series-connected bypass-diode. On the other hand, if *Assumption 2 = 1*, the series connection also increases the probability of open faults, leading to the presence of an optimal number of bypass diode, 2 in this case, beyond which the reliability is negatively affected. *Assumption 3* is also involved in the analysis and the increased number of series-connected diodes lowers the probability of mitigation success in the case of a solar cell in open. However, the impact of such an assumption is negligible.

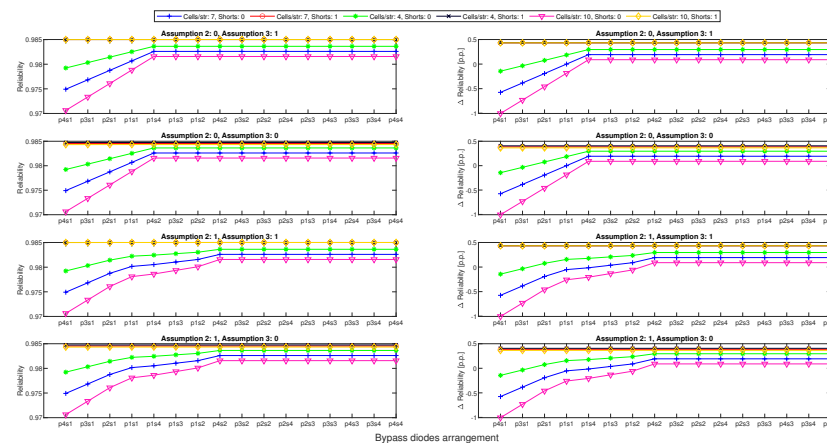


Figure 5.10: Effects on the reliability of possible bypass diode arrangements.

Figure 5.10 combines the above analyses by plotting the reliability against possible arrangements of the bypass diode assembly. It can be seen that, when *Assumption 2* is false, the reliability gain induced by series-connected diodes dominates over the negative effects of the parallel-connected components. Indeed, for every number of diodes in series > 1 the reliability is constant. An interesting behavior is instead registered when the aforementioned assumption is considered valid. In this case, the implementation of a redundant configuration with both parallel and series-connected diode helps increase the overall reliability. Even if from the previous consideration would seem that the optimal configuration is the assembly with 2 series-connected diodes and no redundant component in parallel, that is not the case as the maximum reliability

is reached when both components in series and parallel are > 1 . However, it is important to highlight that adding more components does not improve the reliability further. For this reason, the optimal configuration would be $p2s2$, limiting the number of components and the complexity of the implementation. Please note that, as mentioned, the redundancy of the bypass diode is hardly implemented in real applications. A qualitative classification of the feasibility of the modifications proposed will be treated later in this report.

5.3.3. Blocking Diodes Assembly Configuration

It is here analyzed the impact of blocking diodes on the PVA reliability. The effects of their parallel connection are shown in Figure 5.11, where a clear influence of the first assumption is highlighted. If a short-circuit

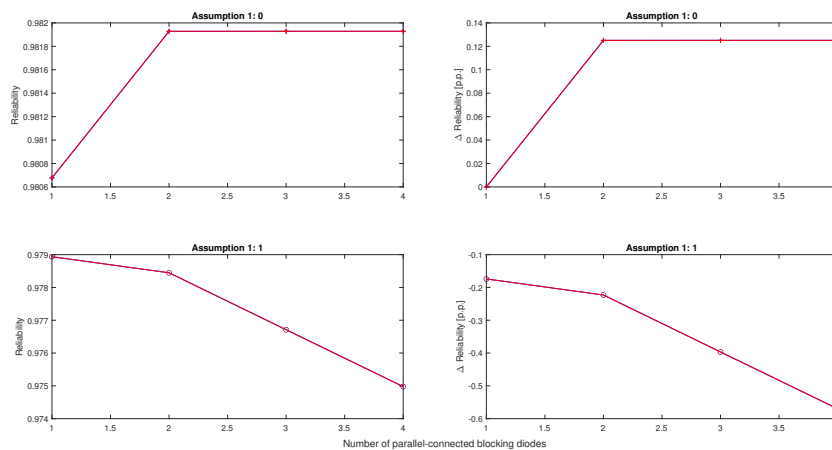


Figure 5.11: Effects on system reliability of the number of parallel-connected blocking diodes.

failure of the blocking diode assembly is not judged as detrimental for the correct functioning of the involved string, a parallel connection decreases the probability of string loss due to an open-circuit failure. Similar to the configuration modifications analyzed so far, the rate of return of the reliability improvements decreases rapidly with adding redundancy, and the value stays more or less constant for ≥ 2 parallel-connected blocking diodes. On the other hand, if a string loss is considered following a shorted blocking diode assembly, then the curve acquires a negative slope and becomes nearly linear for ≥ 2 components. This means that the gain obtained for diminishing the probability of occurrence of an open-circuit failure is completely overcome by the probability of losing a string due to a short-circuit failure. Such a result is reasonable considering the failure modes distribution assigned to the blocking diodes, according to which the 60% of the overall failure rate of the component has to be allocated to the short-circuit failures.

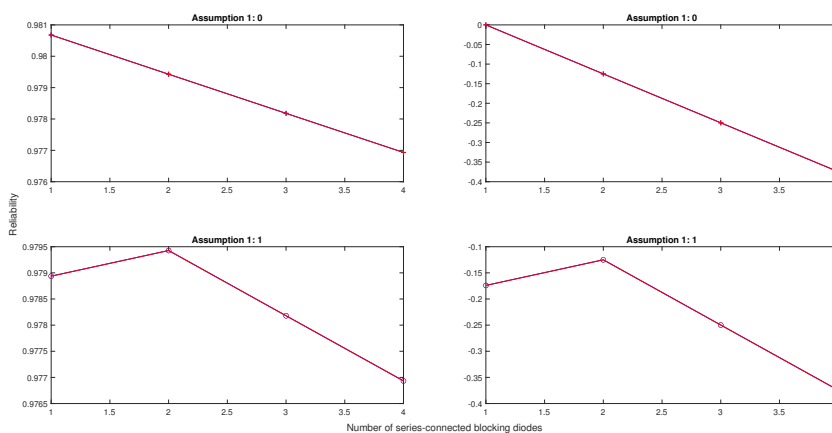


Figure 5.12: Effects on system reliability of the number of series-connected blocking diodes.

As far as the series connection is concerned, in Figure 5.12, a negative correlation exists between the system reliability and the number of blocking diodes if *Assumption 1* = 0. As the number of blocking diodes increases, so does the probability of occurrence of an open-circuit failure. A different curve is drawn if *Assumption 1* = 1, under which condition an optimal configuration exists. The goal is indeed to find the layout that minimizes both the risk of open- and short-circuit failures. This is found for 2 parallel-connected blocking diodes. Please note that the reliability gain ΔR is in this case always negative since the benchmark design was modeled assuming no consequences for a short-circuit failure of the blocking diode assembly.

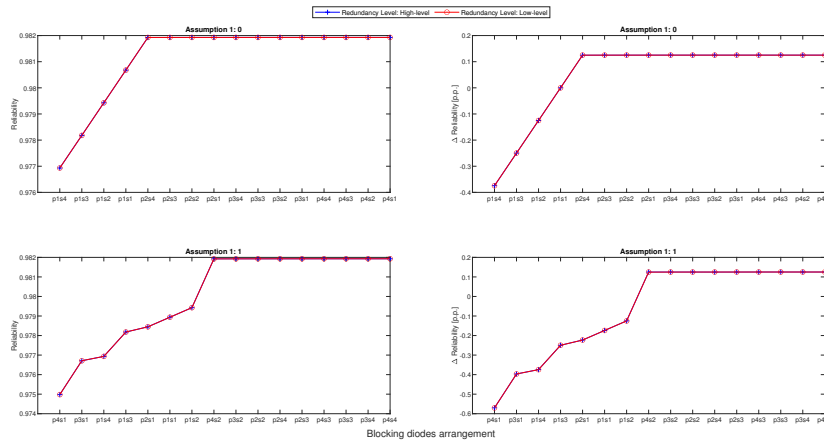


Figure 5.13: Effects on the reliability of possible blocking diode arrangements.

The reliability values for different blocking diodes arrangements are plotted in Figure 5.13. From the top-left graph, it can be seen that the parallel connection of the components completely mitigates the negative impact of the series connection, and ΔR increases as soon as a parallel-connected diode is added to the configuration. The integration of additional parallel-connected components does not improve the reliability further. When *Assumption 1* = 1, a complex configuration, where complex here refers to the presence of both parallel- and series-connected components, mitigates the negative effects of both connections when singularly implemented. It is also possible to obtain a positive reliability gain with respect to the benchmark design despite the less conservative assumption made for the latter.

The curves are plotted for both high-level and low-level redundancy, however, no significant difference is registered. As expected, low-level redundancy always gives a higher reliability value, but the redundancy level may be considered irrelevant for the purpose of reliability improvements, at least for the modeled configuration.

5.3.4. Failure Modes Distribution

A sensitivity analysis is also performed to investigate the impact of the assumed failure modes distribution on the PVA reliability. Figure 5.14 combines the effects of the failure modes of both the solar cells and the bypass diodes. As long as *Assumption 2* = 0, the distribution of the failures of the solar cell does not influence the reliability, regardless of the third assumption. Please note that this is true because the number of acceptable cells in short is set to 0, therefore a faulty solar cell leads to the loss of the whole string, independently of the failure mode experienced. A different relationship exists when considering a higher number of acceptable short faults, as proved by the graphs in Figure 5.15. In the latter, a significant reliability increase is registered towards a higher percentage of short-circuit failures involving the solar cell when *Assumption 3* = 0.

Under *Assumption 2* = 0, a positive correlation exists between the reliability and the percentage relative to the failure rate of the open-circuit failure of the bypass diode. On the contrary, if the second assumption is true and no short faults are allowed, the influence of both distributions decreases significantly. A weak positive correlation is registered between the reliability and the open-circuit failure probability of the solar cells, but the overall impact is negligible.

Figure 5.16 focuses on the failure modes distribution of the blocking diodes. Reasonably, when no concerns are raised for the short-circuit failure of the components, the reliability increases with a greater failure rate allocated to the short-circuit failure. The introduction of 1 acceptable string failure mitigates the effects of a high percentage of open-circuit failures, increasing the reliability and keeping its value within a limited range.

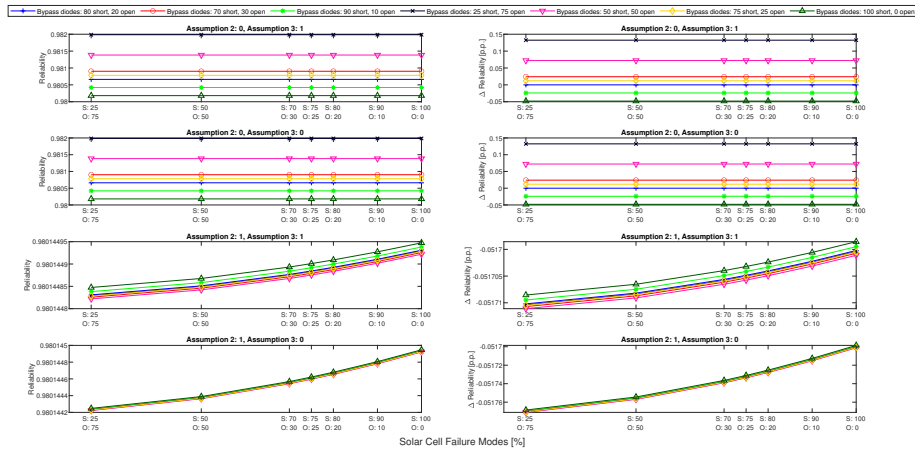


Figure 5.14: Effects on system reliability of the bypass diodes and solar cells failure modes distribution (0 acceptable solar cells in short).

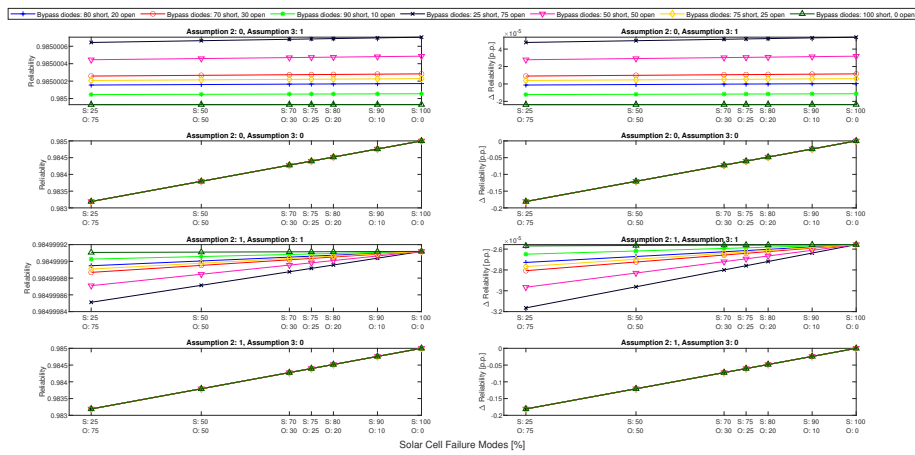


Figure 5.15: Effects on system reliability of the bypass diodes and solar cells failure modes distribution (1 acceptable solar cells in short).

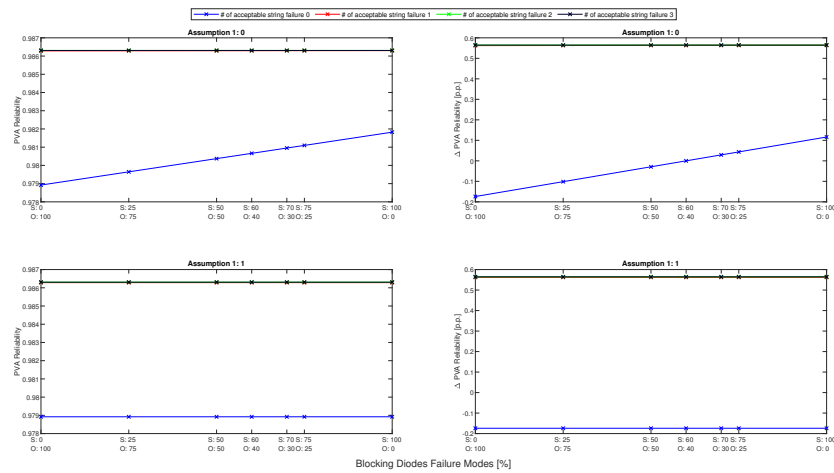


Figure 5.16: Effects on system reliability of the blocking diode failure modes distribution.

On the other hand, if both failure modes have to be considered in the reliability analysis, then their respective impacts balance each other, and the failure modes distribution becomes almost irrelevant, as can be seen from the bottom graphs.

5.3.5. Connections

For the failure rates associated with the connections considered, welds and crimps, their effects on the reliability are found to be negligible. This is true for both their number and their respective implemented redundancy.

5.3.6. Grounding Points

It is here analyzed the effects of the bleeding function on the reliability, where different features are taken into consideration: number of grounding points, redundancy of the grounding points, and redundancy of the connections included in the grounding points.

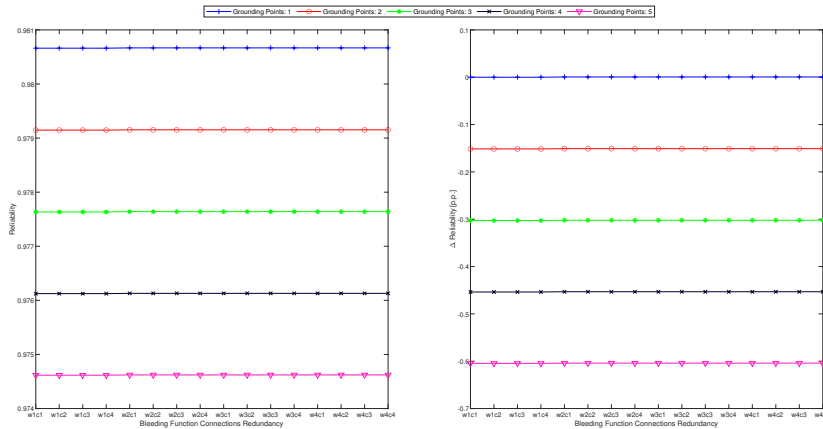


Figure 5.17: Effects of number of grounding points and connections redundancy.

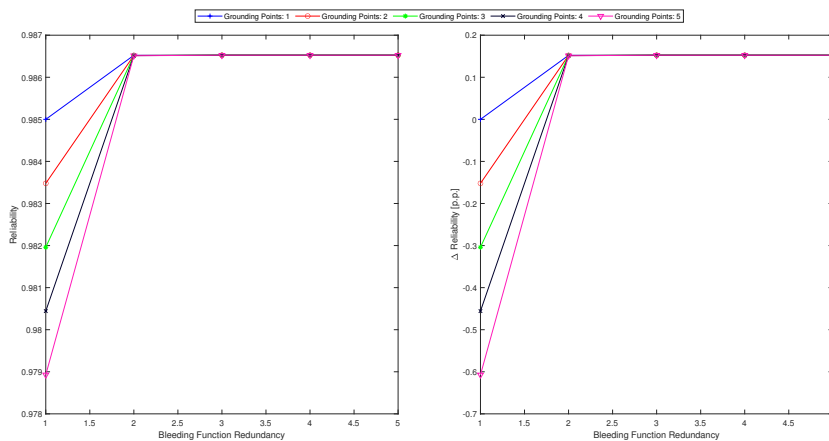


Figure 5.18: Effects of number of grounding points and grounding points redundancy.

The reliability of the system as a function of the connections redundancy is plotted in the graph in Figure 5.17 for different numbers of grounding points. To clarify, assuming that a grounding point consists of a single bleeding resistor, the connections may be two crimps, used for the resistor leads, and a third crimp for the connection of the cable to the ground. Each of these connections may be redundant¹⁴. Such redundancy must not be confused with the redundancy of the bleeding function itself, which indicates the existence of multiple grounding points that protect the same element (panel). From the figure, it appears that the number of redundant connections is not relevant for the reliability, at least considering the failure rates taken from [6] for crimps and welds. This proves what has been said before regarding the PVA connection points. A significant impact may be instead attributed to the number of grounding points, whose increase leads to a reliability reduction. The number of grounding points is indicative of the number of panels of the solar array since their purpose is to mitigate a short-circuit of the PVA with the panel substrate.

¹⁴Please note that from a practical perspective, a redundant crimp is hardly implementable when the connection involves a resistor lead. However, for research purposes the connections considered for the bleeding function are given in Table ??, and each of them can be redundant. This allows performing the sensitivity analysis on every feature.

Figure 5.18, however, shows that it is sufficient the integration of a redundant point to mitigate the negative impact of multiple panels, bringing all the configurations to a higher and constrained reliability value. The difference between the configurations is more limited with increasing redundant points.

5.3.7. Blocking Diode Characteristics

The blocking diode characteristics that, according to [6], are relevant for the calculation of the failure rate of the component, are features involved in the sensibility analysis. Their effects on the reliability are shown in Figure 5.19. The curves are plotted for diverse values of reverse voltage, while the x-axis is representative

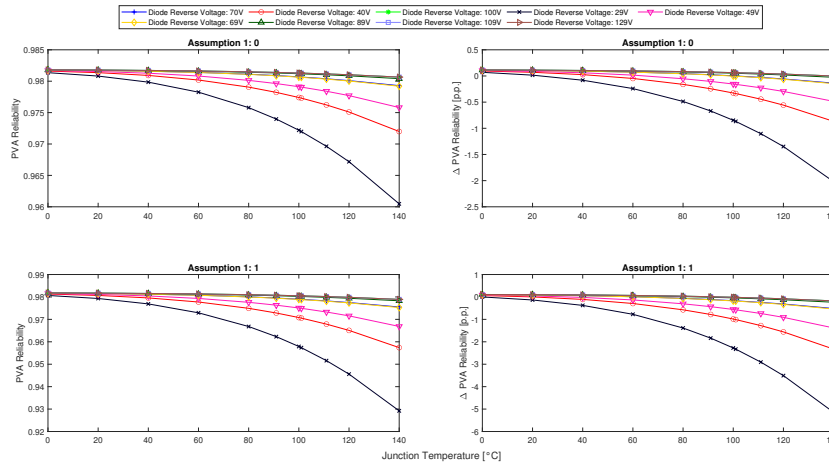


Figure 5.19: Effects of the blocking diode characteristics on the system reliability.

of the junction temperature. It appears that the reliability increases with increasing reverse voltage. This is consistent with the formula provided in the handbook for the electrical stress factor π_S . A negative correlation also exists between the junction temperature and the system reliability. Furthermore, the graphs highlight that the effects of the temperature are more significant for blocking diodes with a lower reverse voltage.

5.3.8. Bleeding Resistor Characteristics

The parameters involved in the failure rate model provided by [6] are studied in the sensibility analysis. However, negligible effects are obtained on the system reliability, whose ΔR has an order of magnitude of -4.

5.3.9. Connector

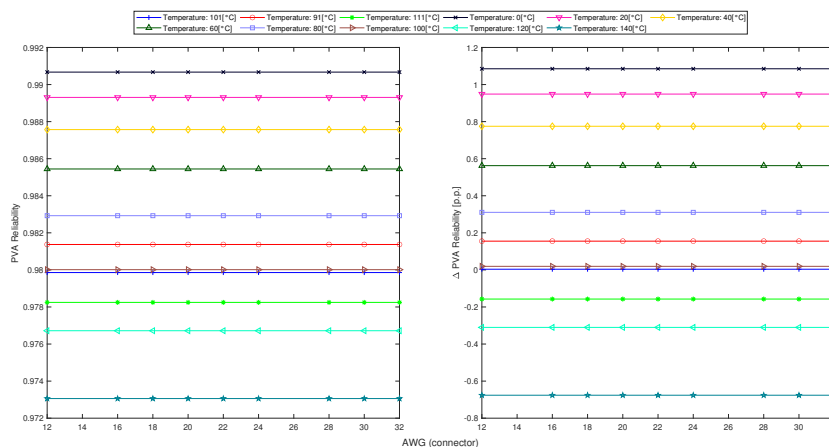


Figure 5.20: Effects of the connector characteristic on the system reliability.

From Figure 5.20 it appears that the AWG number of the wire has negligible impact on the reliability, while

the same cannot be said for the connector ambient temperature. Indeed, as the latter increases, the reliability experiences a significant reduction. Once again, this result is consistent with the formulas provided in the MIL handbook for the calculation of the failure rate of the connector.

5.3.10. Results of the Sensitivity Analysis

The results obtained from the sensitivity analysis are used to investigate possible modifications that allow improving the reliability. Table 5.8 shows, for every feature, the ΔR predicted by applying modification within a reasonable range with respect to the design value. The highest increase in the reliability is achieved by increasing the number of acceptable string failures. However, such a feature does not involve any practical implementation, and its meaning is limited to the assumption of the existence of a redundant string. If not driven by a requirement, this may not be the case for the designed layout. Therefore, in order to implement such modification, an additional string has to be added to the solar array. Such action would decrease the reliability of about 0.07 p.p., as reported in Table 5.8. However, the combination of these two features, as proved by the graph in Figure 5.7, results in the reliability gain of the first feature in the table, which mitigates the impact of the increased number of strings. Although such modification achieves the highest reliability gain, its feasibility is also an important factor to investigate.

Feature	Delta	Reliability benchmark	- [p.p.]	+ [p.p.]	Reliability (-)	Reliability (+)	Feasibility
Max. acceptable string failures	+/- 1	0.980661933		0.563109382	0.980661933	0.986293027	1
Max. acceptable solar cells in short	+/- 1	0.980661933		0.433823463	0.980661933	0.985000168	2
# Bypass Diodes (series-connected)	+/- 1	0.980661933		0.19261326	0.980661933	0.982588066	1
Bleeding Function Redundancy	+/- 1	0.980661933		0.15148803	0.980661933	0.982176813	4
# Blocking Diodes (parallel-connected)	+/- 1	0.980661933		0.12510101	0.980661933	0.981912943	4
Blocking Diode reverse voltage [V]	+/- 30V	0.980661933	-0.335632164	0.062677799	0.977305611	0.981288711	5
Percentage blocking diode in short	+/- 10%	0.980661933	-0.029022451	0.029031043	0.980371708	0.980952243	-
Crimps Redundancy (blocking diodes)	+/- 1	0.980661933		0.004467188	0.980661933	0.980706605	1
Welds Redundancy (string level)	+/- 1	0.980661933		0.004123573	0.980661933	0.980703169	4
AWG	+/- size	0.980661933	0.003662972	0.003662972	0.980698563	0.980698563	5
Welds Redundancy (section level)	+/- 1	0.980661933		0.000515437	0.980661933	0.980667087	4
Welds Redundancy (bleeding function)	+/- 1	0.980661933		0.000515437	0.980661933	0.980667087	4
Resistor rated power [W]	+/- 0.25W	0.980661933	-0.000389383	8.51258E-05	0.980658039	0.980662784	5
Percentage solar cell in short	+/- 10%	0.980661933	-1.36978E-06	1.5805E-06	0.980661919	0.980661949	-
Welds Redundancy (bypass diodes)	+/- 1	0.980661933		6.27276E-12	0.980661933	0.980661933	3
Crimps Redundancy (bleeding function)	+/- 1	0.980661933		0	0.980661933	0.980661933	4
Resistor case temperature [°C]	+/- 10°C	0.980661933	3.04097E-05	-3.08049E-05	0.980662237	0.980661625	3
# Segments / string	+/- 1	0.980661933		-0.001030866	0.980661933	0.980651624	3
Percentage bypass diode in short	+/- 10%	0.980661933	0.024056837	-0.024050937	0.980902501	0.980421424	-
Junction Temperature [°C]	+/- 10°C	0.980661933	0.023586597	-0.02787832	0.980897799	0.98038315	3
# Solar Cells / string	+/- 1	0.980661933	0.062388064	-0.062348399	0.981285814	0.980038449	2
# Total Strings	+/- 1	0.980661933	0.070388673	-0.070338186	0.98136582	0.979958551	1
# Blocking Diodes (series-connected)	+/- 1	0.980661933		-0.124961525	0.980661933	0.979412318	4
Grounding Points	+/- 1	0.980661933		-0.15148803	0.980661933	0.979147053	4
Connector ambient temperature [°C]	+/- 10°C	0.980661933	0.155231336	-0.157452965	0.982214246	0.979087403	3
# Bypass Diodes (parallel-connected)	+/- 1	0.980661933		-0.192242417	0.980661933	0.978739509	1

Table 5.8: Sensitivity Analysis Results

A feasibility column is included in Table 5.8, where a value from 1 to 5 is assigned to every feature. The features characterized by a feasibility factor of 1 are considered to be unfeasible or constrained by other requirements, while a value of 5 indicates an easy implementation, like a change of component. The integration of an additional string is constrained by the geometry requirements of the panel and it is hardly achievable. A similar consideration applies to the maximum number of shorted solar cells, which would require the series connection of an additional solar cell to every string. A feasibility factor of 2 is assigned due to the lower panel area required with respect to a whole string. Another modification that may increase the reliability, even though with a limited gain in comparison with the aforementioned features, involves the series connection of an additional bypass diode. However, this is not an option that may be taken into consideration. Indeed, many of the state-of-the-art solar cells are manufactured as an assembly with their integrated bypass diode, and even though that was not the case, the spacing between the cells would likely be insufficient to accommodate multiple bypass diodes. This is not an issue that involves the blocking diode assembly, which offers a significant reliability gain together with the implementation of the bleeding function redundancy and the decrease of the connector ambient temperature. The integration of a redundant configuration on the blocking diode board is relatively easy and not severely constrained by geometry requirements considering its location in the back of the panel. As far as the bleeding function redundancy is concerned, its implementation does not require relevant effort and would hardly impact other requirements. A bit more complex may be the thermal control of the connector, whose temperature is dependent on its location as well as on the attitude of the satellite.

Table 5.8 reveals that all the other features do not have a significant impact on the system reliability. Worth mentioning is the blocking diode reverse voltage, whose decrease leads to the highest reliability drop. On the other hand, the designed value is conservative enough such that a potential increase would bring minor benefits from a reliability perspective.

6

Machine Learning-based Feature Importance Analysis

The results obtained from the sensitivity analysis cannot be generalized and used for the characterization of every PVA as they are intimately dependent on the system configuration. An attempt to broaden the purpose of the research to an analysis that may lead to a general importance ranking of the considered features from a reliability perspective is described in this chapter. In order to achieve this objective, a feature importance analysis is performed by implementing a ML model.

Section 6.1 introduces the dataset used to train the ML model presented in Section 6.2. The feature importance analysis is carried out in Section 6.3, while the dependence of the system reliability on different combination of features is investigated in Section 6.4.

6.1. Dataset

To perform the analysis, a dataset is required over which the selected machine learning model has to be trained. Due to the high number of features involved and the existing dependence between their effects on the reliability and their combination¹, a large dataset is retrieved, consisting of 50000 samples. These are obtained by running multiple times the reliability analysis for different values of the features and collecting the predicted PVA reliability. The values are uniformly distributed within an arbitrary range, in Table 6.1, which also determines the applicability of the analysis. For the number of connections in series, as well as

Feature	Range
# Solar Cells / string	[# Segments / string , 25]
# Segments / string	[1 , 3]
# Strings / section	[1 , 5]
# Sections	[1 , 5]
# Blocking Diodes (series-connected)	[1 , 4]
# Blocking Diodes (parallel-connected)	[1 , 4]
# Bypass Diodes (series-connected)	[1 , 4]
# Bypass Diodes (parallel-connected)	[1 , 4]
Max. Acceptable Solar Cell in Short	[0 , 1]
Max. Acceptable String Failures	[0 , 1]
Resistor Case Temperature	[-60 , 150] °C
Blocking Diode Junction Temperature	[-60 , 150] °C
Connector Ambient Temperature	[-60 , 150] °C
Resistor Rated Power	[0.25 , 1] W
Resistor Dissipated Power	[0.1 , Resistor Rated Power] W
Blocking Diode Reverse Voltage	[2Voc , Voc] V

Table 6.1: Features ranges for the retrieved dataset.

their redundancy, the selected range is [0 , 4]. The dataset is eventually divided into a target vector \mathbf{y} with dimension (50000,) and an input matrix \mathbf{X} with dimension (50000, # of features).

¹For instance the total number of strings has a different impact based on the number of acceptable string failures.

6.3. Feature Importance Analysis

Two of the most common techniques to calculate the feature importance are the permutation feature importance and the column drop method. With the purpose of comparing their outcome and potentially strengthening the validity of this research, they are both implemented and applied to the retrieved dataset. The former is based on the comparison of the score relative to the benchmark dataset with the averaged one obtained by randomly shuffling N times the feature columns of the input matrix. The calculated importance is equal to the difference between the two scores. The column drop method instead, iteratively eliminates the column of the feature from X , creating a corrupted input matrix \tilde{X} , used to train a new model. Then, the difference between the new score and the benchmark score is computed to retrieve the feature importance. The difference may be either positive or negative. If the feature importance is positive, the greater its value the most relevant is the feature under analysis to correctly predict the model output. A small value, instead, indicates that the feature does not carry significant information, thus its effects on the reliability are limited. A negative feature importance is always representative of a negligible feature from a reliability perspective. Indeed, the result obtained from the column drop highlights that a higher score is achieved if the parameter is not taken into consideration, meaning that it is seen as noise/disturbance by the trained model. Please be aware that the results are as good as the ML model used.

The importance values obtained from the permutation method are shown in the box plot in Figure 6.2, while the results from the column drop method are presented in a bar chart in Figure 6.3. A comparison of the

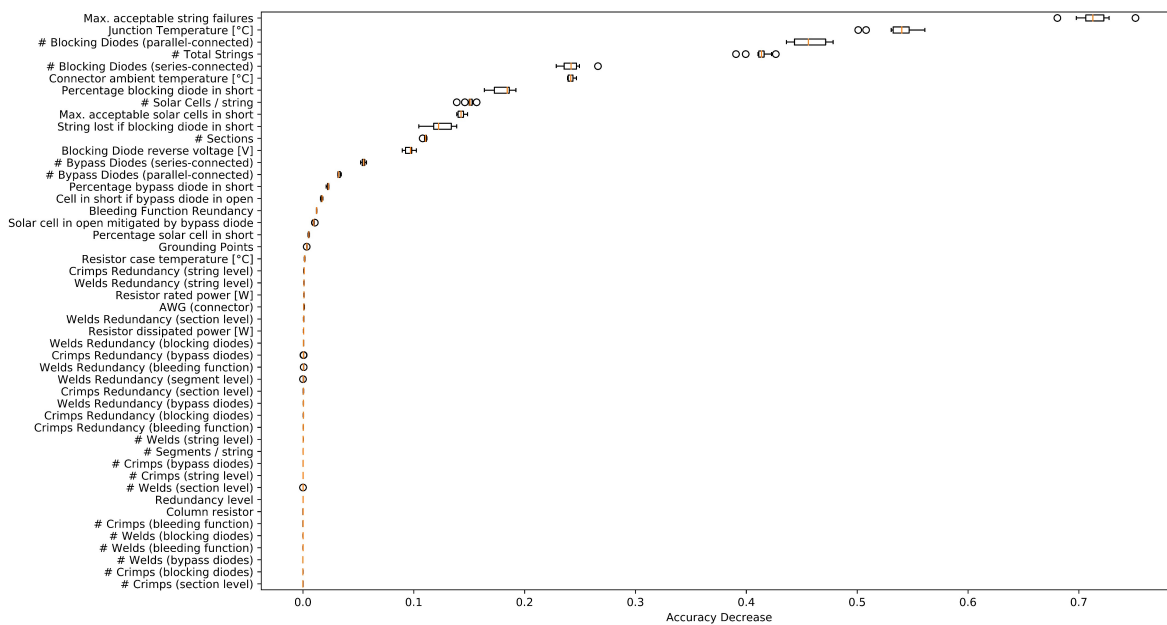


Figure 6.2: Permutation features importance: box plot.

outcome of the two methods is provided in Table 6.4. As far as the ranking is concerned, a strong agreement is registered for the first three features, even though the relative importance values of the junction temperature and the number of parallel-connected blocking diodes of the two methods are 5 p.p. apart. Furthermore, the 19 most relevant features obtained are shared between both methods and the total sum of their relative values equals 5.05 and 4.59, for the permutation and the column-drop respectively. This means that, despite some discrepancies in the importance assigned to the different features, the methods satisfyingly agree on the common value to be allocated to those features. Beyond the 19th feature, the effects on the reliability are negligible according to the techniques implemented.

By comparing Table 6.4 with the results from the sensitivity analysis in Table 5.8, it may be noted that all the features in the latter table whose reliability gain may be considered relevant (indicated by the cells with a background color) are contained within the 19 features with the highest estimated importance. In particular, the same ranking is assigned to the maximum number of acceptable string failures, connector ambient temperature, and series-connected blocking diodes.

A third method to perform features importance analysis is to apply the SHapley Additive exPlanations (SHAP)

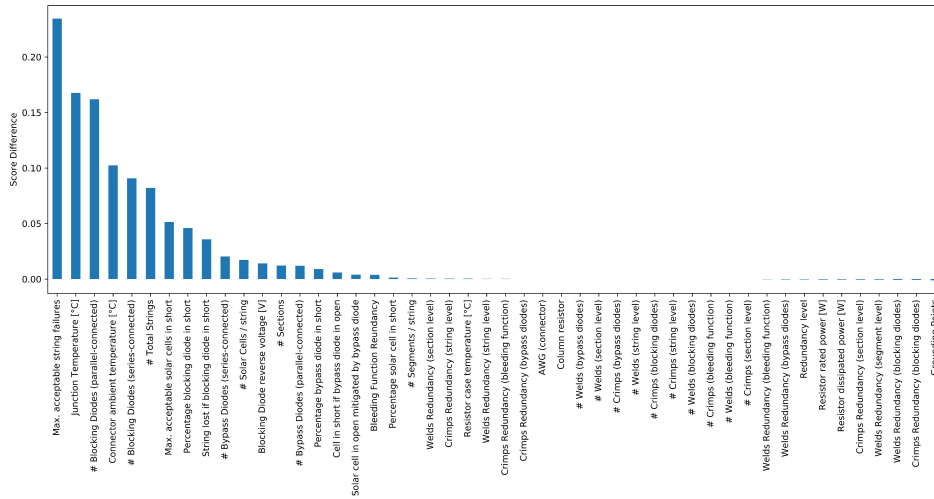


Figure 6.3: Features importance using column drop method.

Feature	Permutation		Method		Column Drop		Rank
	Feature Importance	Relative Feature Importance	Rank	Feature Importance	Relative Feature Importance		
Max. acceptable string failures	0.6849530	1.0000000	1	0.2345930	1.0000000	1	
Junction Temperature [°C]	0.5222060	0.7623970	2	0.1676490	0.7146390	2	
# Blocking Diodes (parallel-connected)	0.4442800	0.6486280	3	0.1643430	0.7005440	3	
# Total Strings	0.4073660	0.5947350	4	0.0826350	0.3522480	6	
Connector ambient temperature [°C]	0.2390640	0.3490220	5	0.1023750	0.4363940	4	
# Blocking Diodes (series-connected)	0.2279760	0.3328350	6	0.0907940	0.3870290	5	
Percentage blocking diode in short	0.1671090	0.2439710	7	0.0460670	0.1963690	8	
# Solar Cells / string	0.1505110	0.2197400	8	0.0173190	0.0738260	11	
Max. acceptable solar cells in short	0.1426390	0.2082470	9	0.0513750	0.2189980	7	
String lost if blocking diode in short	0.1159950	0.1693480	10	0.0358020	0.1526130	9	
# Sections	0.1093010	0.1595740	11	0.0121390	0.0517430	13	
Blocking Diode reverse voltage [V]	0.0986310	0.1439960	12	0.0140410	0.0598530	12	
# Bypass Diodes (series-connected)	0.0545310	0.0796130	13	0.0204140	0.0870170	10	
# Bypass Diodes (parallel-connected)	0.0302570	0.0441740	14	0.0120470	0.0513510	14	
Percentage bypass diode in short	0.0214750	0.0313520	15	0.0091500	0.0390040	15	
Cell in short if bypass diode in open	0.0156610	0.0228650	16	0.0058520	0.0249470	16	
Bleeding Function Reundancy	0.0132260	0.0193090	17	0.0038750	0.0165160	18	
Solar cell in open mitigated by bypass diode	0.0091360	0.0133370	18	0.0039790	0.0169600	17	
Percentage solar cell in short	0.0054090	0.0078970	19	0.0013510	0.0057570	19	
Grounding Points	0.0032800	0.0047880	20	-0.0011210	-0.0047800	48	
Resistor case temperature [°C]	0.0008340	0.0012180	21	0.0004040	0.0017230	23	
Resistor rated power [W]	0.0007330	0.0010700	22	-0.0004360	-0.0018590	42	
AWG (connector)	0.0006980	0.0010190	23	0.0000340	0.0001450	27	
Welds Redundancy (bleeding function)	0.0006600	0.0009630	24	-0.0001730	-0.0007390	39	
Welds Redundancy (string level)	0.0005330	0.0007780	25	0.0003140	0.0013390	24	
Crimps Redundancy (section level)	0.0005010	0.0007320	26	-0.0005190	-0.0022100	44	
Crimps Redundancy (blocking diodes)	0.0004730	0.0006910	27	-0.0007570	-0.0032270	47	
Welds Redundancy (segment level)	0.0004330	0.0006330	28	-0.0005230	-0.0022290	45	
Resistor dissipated power [W]	0.0003540	0.0005170	29	-0.0004610	-0.0019660	43	
Welds Redundancy (section level)	0.0003500	0.0005110	30	0.0005620	0.0023940	21	
Crimps Redundancy (string level)	0.0003050	0.0004450	31	0.0004360	0.0018570	22	
Crimps Redundancy (bypass diodes)	0.0002950	0.0004300	32	0.0000990	0.0004200	26	
# Crimps (bypass diodes)	0.0002800	0.0004090	33	0.0000000	0.0000000	28	
Welds Redundancy (bypass diodes)	0.0002670	0.0003900	34	-0.0002590	-0.0011060	40	
Crimps Redundancy (bleeding function)	0.0002450	0.0003580	35	0.0002390	0.0010190	25	
Welds Redundancy (blocking diodes)	0.0002250	0.0003290	36	-0.0007190	-0.0030650	46	
Column resistor	0.0001910	0.0002780	37	0.0000000	0.0000000	28	
# Segments / string	0.0001010	0.0001470	38	0.0005740	0.0024450	20	
Redundancy level	0.0000700	0.0001020	39	-0.0003190	-0.0013600	41	
# Welds (bypass diodes)	0.0000680	0.0000990	40	0.0000000	0.0000000	28	
# Welds (bleeding function)	0.0000490	0.0000710	41	0.0000000	0.0000000	28	
# Welds (string level)	0.0000470	0.0000690	42	0.0000000	0.0000000	28	
# Welds (blocking diodes)	0.0000290	0.0000420	43	0.0000000	0.0000000	28	
# Crimps (bleeding function)	0.0000240	0.0000360	44	0.0000000	0.0000000	28	
# Crimps (section level)	0.0000190	0.0000280	45	0.0000000	0.0000000	28	
# Crimps (blocking diodes)	0.0000190	0.0000280	45	0.0000000	0.0000000	28	
# Welds (section level)	0.0000160	0.0000230	47	0.0000000	0.0000000	28	
# Crimps (string level)	0.0000140	0.0000210	48	0.0000000	0.0000000	28	

Table 6.4: Comparison between permutation and column drop methods.

approach, which has been developed to explain the output of a ML model. This method is based on the calculation of the Shapley value of the feature, which refers to its averaged marginal contribution obtained by

considering the possible combinations of the other features. The contribution of each feature is computed with respect to a base value that is representative of the model's output when no input information is provided. Mathematically, it is the average of the model's predicted values over the training dataset X_{train} . The bar plot in Figure 6.4a displays the 20 most important features according to the assigned Shapley values and shows agreement with respect to the results obtained from the permutation and column-drop methods. Fur-

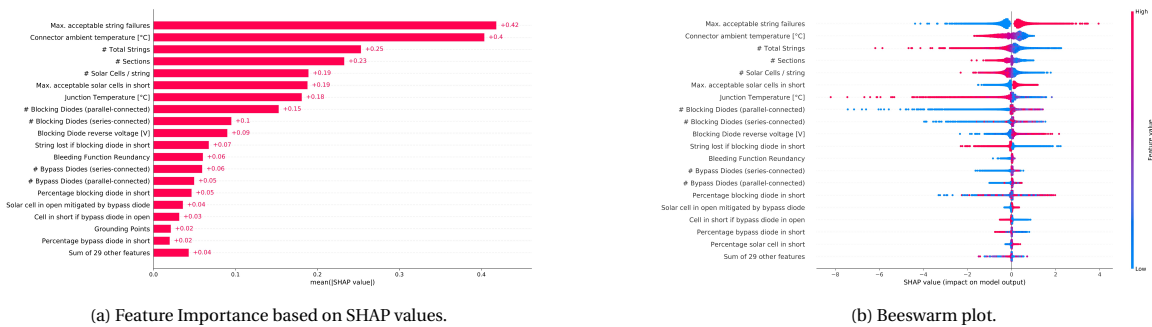
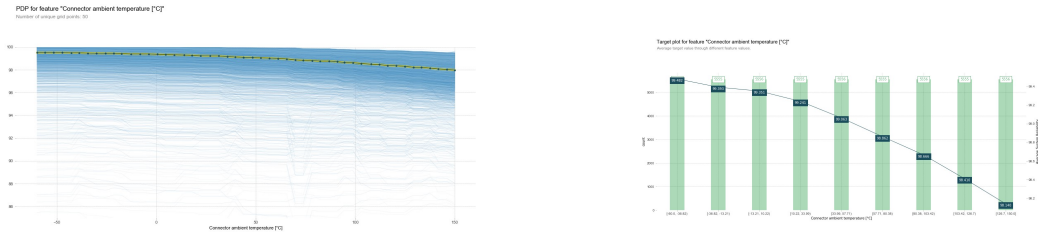


Figure 6.4: SHAP Analysis.

thermore, a beeswarm plot is provided in Figure 6.4b, providing more insights on the effects of the features on the PVA reliability. Through this graph, it is possible to analyze the whole input dataset X and investigate how the reliability is influenced based on the value assigned to each feature, which is represented by the color assumed by the data point. The color scale is associated with a value range that goes from *low* to *high* with respect to the mean value of the uniform distribution that characterizes each feature in the dataset. This allows determining the nature of the correlation between the features and the target values. A negative SHAP value highlights a negative impact on the system reliability, while a favorable impact is associated with a positive value. Consistently, a low value of the maximum number of acceptable string failures, i.e. 0 failures, decreases the reliability. The opposite occurs when the acceptable failures are increased to 1. The visible tails that are stretching off to both directions reveal that the feature under analysis may have either a strong or limited influence on the target values depending on the combination of the other features. Such dependence, however, cannot be grasped from the presented beeswarm plot. As far as the connector is concerned, in agreement with the outcome of the sensitivity analysis, an increase in its ambient temperature is detrimental to the reliability of the system. It also appears that, by evaluating all the combinations of the other features, the thermal control of the connectors tends to achieve little reliability improvements, while its inefficiency may degrade significantly its ability to perform the required function. The same consideration holds for the junction temperature of the blocking diodes. Another interesting piece of information that may be retrieved from the plot in Figure 6.4b is related to the degree of dependence between the different features. For instance, by analyzing the data points of the failure modes distribution of the blocking diode, it can be noted that, even though their pattern produces evident tails, a characterization of its effects based on the assumed value cannot be clearly defined. This is a symptom of the fact that its influence on the reliability is strongly dependent on one or multiple other features. Some of these existing dependencies are studied in Section 6.4.

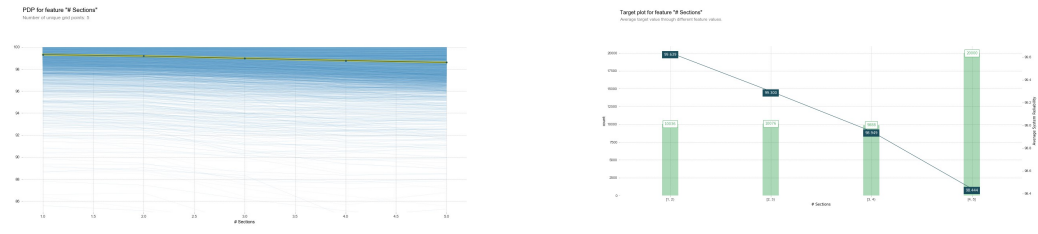
6.4. Features Effects on System Reliability

The results described in Section 6.3 allow establishing a ranking of the different features based on their relevance with respect to the PVA reliability. Moreover, the nature of the correlations, i.e. positive or negative, between a feature and the target value may be inferred from the plot in Figure 6.4b. However, the existing dependencies between the target value and the features and those between the features themselves have not been studied yet. For this purpose, Partial dependence plots (PDP) and Individual conditional expectation (ICE) plots are elaborated and the most relevant ones are presented in this section. For the assessment of the influence of a single feature, the respective 1D plots are drawn. ICE plots display a line for every row in the input matrix X , whose data points are representative of the predicted reliability value when all the features but the one under analysis are kept constant. For the latter, a value from a grid is assigned. This means that the accuracy of the plots depends on the quality of the ML model. The PDP is obtained by calculating the average of the ICE at every grid point of the feature. Furthermore, an important assumption to keep in mind is that the feature for which the partial dependence is computed is considered independent from the others. Figure 6.1 proves that this is the case for most of the features, with an exception for the connection points and



(a) Combined PDP and ICE for the connector ambient temperature. (b) Average reliability for different connector ambient temperatures.

Figure 6.5: PVA reliability dependence with the connector ambient temperature.



(a) Combined PDP and ICE for the number of sections. (b) Average reliability for different number of sections.

Figure 6.6: PVA reliability dependence on number of sections.

their respective redundancy. Nevertheless, the latter have been demonstrated to have a negligible impact on the reliability and their partial dependence is not computed. For this reason, it is possible to consider the aforementioned assumption valid. Some of the most relevant feature combinations are here investigated. The graphs retrieved from the analysis relative to the connector ambient temperature are shown in Figure 6.5. PDP and ICE are combined into a single graph in Figure 6.5a, where a negative correlation of the feature with the system reliability is visible. The result is further validated by the chart in Figure 6.5, obtained by averaging the reliability values from a subset of the original vector y . The subsets are identified by a specific range of the feature under analysis, indicated on the horizontal x . The height of the bars and the associated value is representative of the number of data points contained in the respective subset. A similar analysis may be carried out for the number of sections, and the results are shown in Figure 6.6. A negative correlation is highlighted between the feature and the reliability². From Figure 6.5 and 6.6, it is not possible to study whether any relationship exists between the connector ambient temperature and the number of sections. Nevertheless, recalling that it is assumed that two connectors are integrated for every section in the PVA, one may assume that one feature influences the effect that the other has on the system reliability. Figure

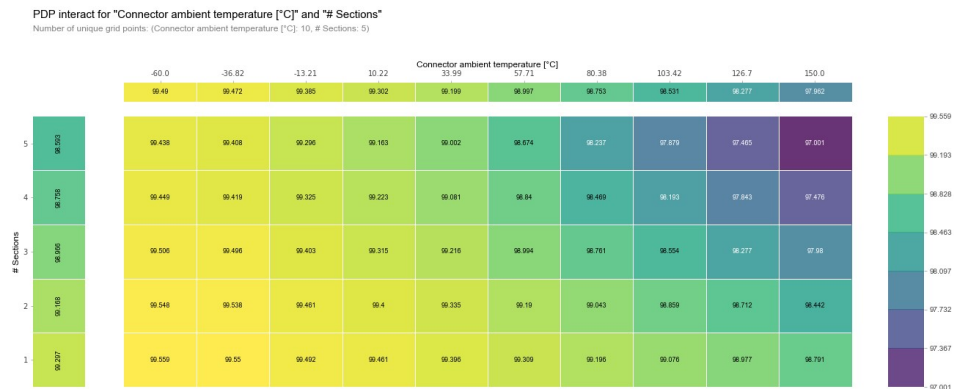
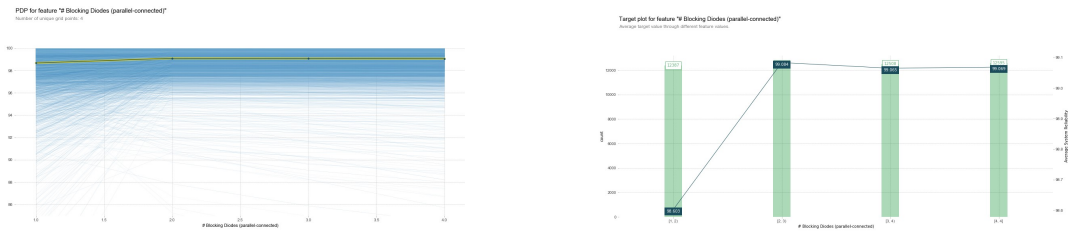


Figure 6.7: 2D PDP for connector ambient temperature and number of sections.

²Please note that the last reliability value, relative to the range [4, 5], is the result of the average of a subset that contains twice as many data points as the others. This is due to the fact that 2 different feature values characterize the subset.

6.7 offers the opportunity to clearly understand their combined impact on the target values. As expected, the reliability decreases along both axes. However, it shows that a very low temperature of the connector strongly mitigates the impact of an increased number of sections, i.e. an increased number of connectors. A different color gradient is visible across the rows, revealing a strong influence of the connector temperature for a high number of components. This is reasonable since a warmer temperature shortens the mean time to failure of the components, whose number N determines the overall reliability as $(R_{\text{connector}})^N$. As a consequence, the lowest reliability is registered for a combination of the highest temperature with the maximum number of components.

In Section 5.3.10, the blocking diode assembly is identified as one of the items which may be subjected to feasible modifications that may significantly increase the PVA reliability. For this reason, it is here analyzed in more detail. From the ICEs in Figure 6.8a, both the trend-lines obtained from the sensitivity analysis (Figure



(a) Combined PDP and ICE for the number of parallel-connected blocking diode. (b) Average reliability for different number of parallel-connected blocking diode.

Figure 6.8: PVA reliability dependence on number of parallel-connected blocking diode.

5.11) are visible. However, the PDP and the graph in Figure 6.8b show that the studied effects for *Assumption 1 = 0* are dominant. A reasonable explanation may be found by considering the influence of the failure modes distribution. As long as the short-circuit failure of the blocking diodes does not undermine the function of the whole string, the line retrieved by adding redundant components in parallel follows the same trend regardless of the percentage associated with the probability of occurrence of a particular failure. On the contrary, when *Assumption 1* is valid, the negative slope of the line in Figure 5.11 depends on the percentage assigned to the short-circuit circuit failure: the lower the latter, the more gentle is the slope and the graph tends to match the one for *Assumption 1 = 0*. This is proved by the plots provided in Figure 6.9, additional outcomes of the sensitivity analysis. The respective dependence plot of the features considered in the graphs, is proposed in

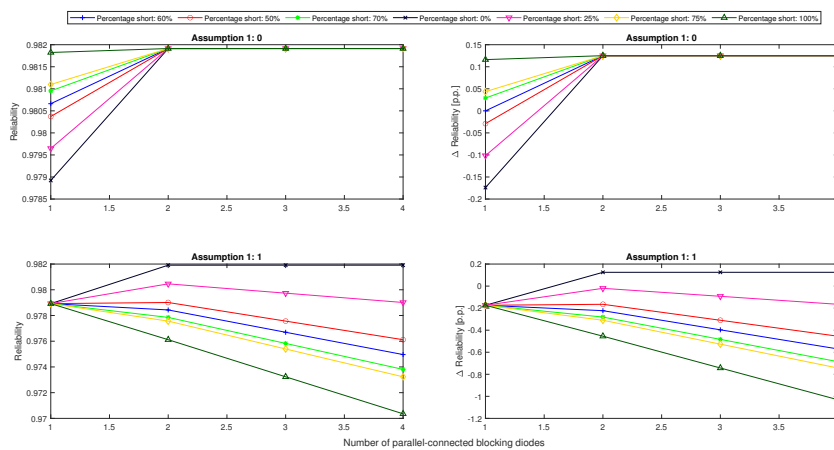


Figure 6.9: Effects of the number of parallel-connected diodes given different failure modes distributions.

Figure 6.10. However, one of the main limitations of PDPs is that the maximum number of analyzed features is constrained to 2. As a consequence, the different correlations existing with the validity of *Assumption 1* cannot be captured, and the result is the average over the predicted value for the total number of instances in the dataset X . As long as a single blocking diode is integrated for voltage mismatch protection, the graph reveals an improvement of the reliability for a higher failure rate allocated to the short-circuit failure. By

comparing the result with the graphs in Figure 6.9, it can be noted that such relationship is representative of the reality exclusively under the condition that *Assumption 1* = 0. The highest reliability is achieved for an assembly configuration that integrates multiple diodes in series with the lowest probability of experiencing a short-circuit failure. This outcome reflects the actual system response regardless of the assumption considered, as proved by the shared shape of the curve shown in Figure 6.9 under such conditions. It is here stressed that the predicted values for the reliability displayed in the PDP cannot be used to define the actual reliability of the model, since they are computed as the averages over different instances whose interval of confidence may be significantly spread.



Figure 6.10: 2D PDP for number of parallel-connected blocking diodes and failure modes distribution.

Figure 6.11 shows the 2D PDP relative to the number of parallel-connected blocking diodes and that of the maximum string failures. It may be noted that, if the system is not fault tolerant and it is not able to sustain any failure, the integration of an additional diode in parallel greatly improves the system reliability. In agreement with the results from the sensitivity analysis, the rate of improvement, however, is negligible for a number of components ≥ 2 . A small decrease in the reliability is registered between the configuration with 3 and 4 parallel diodes, a behavior that may be reasonably linked to the negative impact of this configuration under the condition *Assumption 1* = 1. By raising the acceptable number of failures to 1, the effect of the blocking diode assembly structure loses relevance, and the reliability remains constrained to a limited range with a higher mean value.

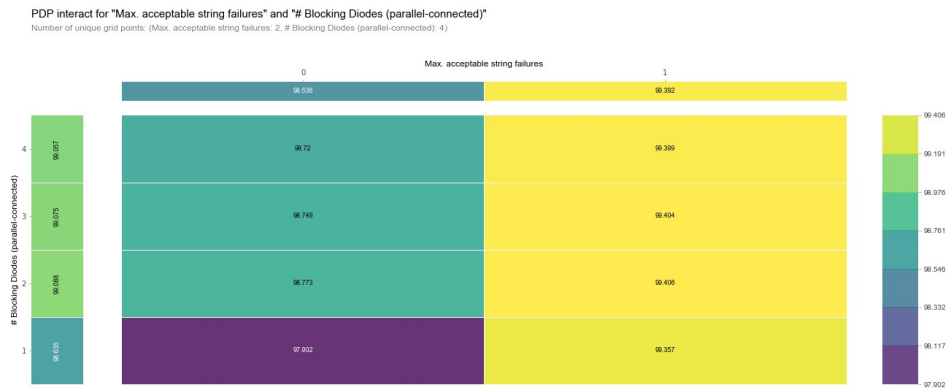


Figure 6.11: 2D PDP for number of parallel-connected blocking diodes and maximum number of acceptable string failures.

Another insightful analysis, which also shows a close agreement with Figure 5.19 from the sensitivity analysis, is the one that involves the blocking diode reverse voltage and the junction temperature. In Figure 6.12, the reliability of the system decreases towards the bottom right corner, corresponding to a low reverse voltage and a high junction temperature. Moreover, within the considered ranges, by maintaining a low junction temperature the negative impact of poorly designed safety margin with respect to the reverse voltage may be strongly mitigated. However, a thermal control of the blocking diode, as indicated in Table 5.8 may require some effort

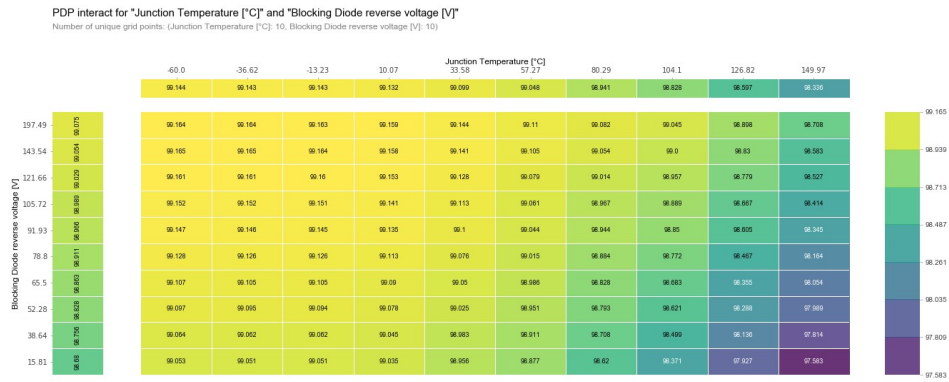


Figure 6.12: 2D PDP for the blocking diode reverse voltage and the junction temperature.

to achieve. This is mainly due to the numerous temperature cycles to which the panels are subjected in orbit. As a consequence, one may apply a different technique to constrain the reliability within acceptable values. Indeed, similarly to the aforementioned mitigation effect, by increasing the blocking diode reverse voltage, the influence of the junction temperature variation is limited.

7

Criticality Assessment

The criticality assessment is an activity of the Failure Modes, Effects and Criticality Analysis (FMECA), that is "a FMEA extended to classify potential failure modes according to their criticality, i.e. the combined measure of the severity of failure modes and their probability of occurrence" [31]. The combination of the results obtained from the simulation of the failure modes in Chapter 4 and some of the formulas used for the reliability analysis, allows performing a severity and probability classification of the failures, treated in Section 7.2 and 7.1, respectively. In Section 7.3, a criticality number is calculated and assigned to every failure.

7.1. Probability Classification

The probability levels, limits and numbers are mission-specific and agreed with the customer. In this case, the suggested values provided in [31] are used (Table 7.1). Usually, the probability classification follows a qualitative approach and the probabilities do not require to be as precise and detailed as for the reliability prediction method. They may be evaluated from:

- Heritage: by looking at prior analysis in which similar failure modes were spotted and adapt the probability to the intended mission and conditions requirements;
- Test: difficult to perform with the purpose of investigating the frequency of failures occurrence even with accelerated test;
- Engineering judgment: when the knowledge and expertise of engineers from previous missions can provide an estimation of how probable is for an event to happen with certain margins.

Nevertheless, some of the formulas proposed in Section 5.2 can be used to estimate the failure probabilities to be allocated to some of the failure modes analyzed in Chapter 4.

First of all, it is necessary to determine the failure modes for which the probability may be predicted. As far as the diodes are concerned, in Section 5.1 is assumed that the failure rate is apportioned into contributions that relate to open- and short-circuit failures, while the drift failure, i.e. a variation of the diode parameters, is not taken into account in the reliability analysis. As a consequence, the impedance fault of the diodes is not included in the criticality assessment. The same consideration holds for the impedance fault concerning the connection points, whose failure mode is identified exclusively as open-circuit in the reliability analysis. Furthermore, short- and open-circuit are also the only failure modes whose probability of occurrence is

Level	Limits	PN
Probable	$P > 1E-1$	4
Occasional	$1E-3 < P \leq 1E-1$	3
Remote	$1E-5 < P \leq 1E-3$	2
Extremely remote	$P \leq 1E-5$	1

Table 7.1: Probability classification parameters [31].

Component	Failure Mode	Failure Probability	Probability Number	Level
Intra-string Connections	Open	4.99E-05	2	Remote
Bypass Diode	Short	1.96E-03	3	Occasional
	Open	5.27E-04	2	Remote
Solar Cell	Short	1.96E-03	3	Occasional
	Open	4.90E-04	2	Remote
Blocking Diode	Short	1.77E-03	3	Occasional
	Open	1.27E-03	3	Occasional
Power Transfer (section connections + connectors)	Open	1.22E-02	3	Occasional

Table 7.2: Failure probabilities.

computed for the solar cells. Indeed, no data are available to estimate the probability of micrometeorites' impact leading to a reduced active area. Moreover, a lack of data also prevents any probability prediction for line-to-line and ground faults, therefore excluded in this analysis.

As the calculation of the failure probabilities related to the diodes, as well as to the power transfer function, have been already described in Section 5.1, the only elements whose probability of occurrence has yet to be estimated are the solar cells. The following formula is provided, where the subscript $Fmode$ refers to the failure mode considered.

$$P_{Fmode,SC} = \binom{N}{N-k} R_{Fmode,SC}^{N-k} \cdot (1 - R_{Fmode,SC})^k \quad (7.1)$$

Here N is the total number of solar cells and k is representative of the number of failures occurring, taken equal to 1 in this analysis. Since all the solar cells are identical and a single failure is considered, equation 7.1 reduces to:

$$P_{Fmode,SC} = N \cdot \left[R_{Fmode,SC}^{N-1} \cdot (1 - R_{Fmode,SC}) \right] \quad (7.2)$$

The obtained probabilities are: $P_{sc,SC} = 1.96 \times 10^{-3}$ and $P_{oc,SC} = 4.90 \times 10^{-4}$. Please keep in mind that these values concern the bare solar cells and not their assemblies.

The results of the probability classification are summarized in Table 7.2. As far as the solar cell assemblies are concerned, the table shows that the short-circuit failure of either the solar cell or the bypass diode has the highest probability of occurrence, even though classified as *occasional*. Within the same probability level fall the failure modes of the blocking diodes. It is important to highlight that these results are strictly related to the failure modes distribution assigned to the involved components. Furthermore, the power transfer function may also experience a failure with a relatively high probability. This is mainly due to the presence of 2 connectors per section, characterized with a high failure rate, as shown in Table 5.1.

7.2. Severity Classification

Severity category	Severity level	Description of consequences (failure effects)	
		Dependability effects (as specified in ECSS-Q-ST-30)	Safety effects (as specified in ECSS-Q-ST-40)
Catastrophic	1	Failure propagation (refer to 4.2c)	Loss of life, life-threatening or permanently disabling injury or occupational illness. Loss of an interfacing manned flight system. Severe detrimental environmental effects. Loss of launch site facilities. Loss of system.
Critical	2	Loss of mission	Temporarily disabling but not life-threatening injury, or temporary occupational illness. Major detrimental environmental effects. Major damage to public or private properties. Major damage to interfacing flight systems. Major damage to ground facilities.
Major	3	Major mission degradation	
Minor or Negligible	4	Minor mission degradation or any other effect	

(a) Failure consequences description.

Severity level	Severity category	SN
1	Catastrophic	4
2	Critical	3
3	Major	2
4	Negligible	1

(b) Severity number.

Table 7.3: Severity classification guidelines[31].

The consequences on the SA performance of the failure modes presented in Section 4.2 are classified into different severity categories as a fundamental activity for the FMECA. A description of the failure consequences, as well as the assigned severity numbers, is provided in [31]. When the analysis is performed at subsystem level, *loss of mission* refers to the loss of the functionality of such subsystem. The criteria for mission loss and mission degradation are defined by the customer. For this study, Table is used 7.4.

Severity Category	Severity Number	ΔP_{mp} [%]	
		Lower Bound	Upper Bound
Catastrophic	4	-25	-inf
Critical	3	-15	-25
Major	2	-5	-15
Minor/Negligible	1	NaN	-5

Table 7.4: Assigned severity criteria.

Component	Failure Mode	ΔP_{mp} [%]	Severity Number	Severity category
Intrastring Connections	Open	-12.50	2	Major
Bypass Diode	Short	-12.15	2	Major
	Open	0.00	1	Negligible
Solar Cell	Short	-12.16	2	Major
	Open	-12.50	2	Major
Blocking Diode	Short	0.13	1	Negligible
	Open	12.50	2	Major
Power Transfer (section connections + connector)	Open	-25.00	3	Critical

Table 7.5: Severity classification.

By collecting the data obtained from the simulations described in Section 4.2 and applying the criteria in Table 7.4, the severity classification is performed and the results are summarized in Table 7.5. The considered elements and components are those that are subjected to the probability classification in Section 7.1. In this case, it is assumed that an open-circuit failure of a solar cell is mitigated by the presence of the bypass diode, consistently with the configuration of the electrical model implemented for the system. For most of the failure modes, the power degradation is equivalent to the power output of one string¹, meaning that the maximum power is achieved under faulty conditions of the string, as already explained. The most severe failure involves an open-circuit at section level, affecting the power transfer function. Reasonably, since every section is built by parallel-connecting two strings, the power reduction equals the power of two strings.

7.3. Criticality Classification

According to [31], the criticality is a "combined measure of the severity of a failure mode and its probability of occurrence". Therefore, a criticality assessment of the items investigated may be directly derived from the classifications carried out in Section 7.1 and 7.2. A criticality matrix is provided by the standard and reported in Table 7.6, where the items are identified as critical if either their failure leads to catastrophic consequences or the obtained criticality number is ≥ 6 .

Severity category	SNs	Probability level			
		10 ⁻⁵	10 ⁻³	10 ⁻¹	1
		PNs			
		1	2	3	4
catastrophic	4	4	8	12	16
critical	3	3	6	9	12
major	2	2	4	6	8
negligible	1	1	2	3	4

Table 7.6: Criticality Matrix [31].

Component	Failure	Severity Number	Probability Number	Criticality Number
Intra-string connection	open-circuit	2	2	4
Bypass Diode	short-circuit	2	3	6
	open-circuit	1	2	2
Solar Cell	short-circuit	2	3	6
	open-circuit	2	2	4
Blocking Diode	short-circuit	1	3	3
	open-circuit	2	3	6
Power transfer	open-circuit	3	3	9

Table 7.7: Criticality classification.

The results of the criticality assessment are given in Table 7.7. Solar cells and bypass diodes are classified as critical in relation to their short-circuit failure. Once again, please recall the strong dependency with the assumed failure modes distributions for both components (80% short, 20% open). The power transfer function is registered as the most critical item within the PVA, for which the concern mainly involves the connectors, as previously mentioned.

The outcome of the criticality assessment is helpful to evaluate the compliance of the design with the system dependability requirement and to identify strategies that may be implemented to meet those requirements. For instance, the criticality assessment further highlights the importance of controlling the connector ambient temperature, which is selected as one of the features that may effectively increase the system reliability from the sensitivity analysis in Section 5.3.

¹Slight variations are experienced due to the voltage drop across the bypass diode of the faulty cell.

8

Conclusions

Cost and lifetime requirements are two of the main drivers for the development of complex systems involved in modern space missions. As a consequence, system reliability is a factor of primary concern that requires appropriate analyses. A closely related topic is the study of the consequences induced by failures to which the system may be subjected, necessary to identify criticalities and weaknesses within the system from which mitigation strategies may be derived and implemented. The aforementioned activities are laborious, intensive and, usually, a significant number of iterations are needed to achieve a system design that complies with the system dependability requirements. This research aims to perform a FMEA and reliability analysis on satellite solar arrays by developing a flexible modeling software, that is able to simulate the performance of any PVA configuration and to provide a reliability assessment. The latter includes a sensitivity analysis that allows deriving strategies for reliability improvement. The software, developed in MATLAB and Simulink, builds a model of the system based on the configuration defined by the user and runs different simulations. The model can be either an electrical model, when the selected analysis requires the simulation of the system performance, i.e. FMEA, or a reliability model, in case the study is related to the system reliability and its potential improvements.

A sample satellite has been modeled to perform the FMEA. A static analysis has been carried out, for which the software simulates the performance of the solar array under healthy and faulty conditions. The obtained characteristic curves are compared by the software, which outputs the performance variations related to the three main SA operating points: short-circuit, open-circuit, and maximum power. According to user-defined criteria, a severity number is assigned by the software to each simulated failure mode. As the quantitative values of current, voltage and power degradation are highly dependent on the system configuration, a qualitative assessment of the consequences of the simulated failures is provided in Table 8.1.

Component	Failure Mode	String-level	Effects	PVA-level
Bypass Diode	short-circuit	• Open-circuit voltage reduction equal to the open-circuit voltage of one solar cell.	• Inflection point at the open-circuit voltage of the faulty string.	
	open-circuit	• No effects if no current mismatch is experienced.	• No effects if no current mismatch is experienced.	
	impedance	• Decrease of the current-source region. • The slope of the curve around the maximum power point varies based on the impedance value.	• Decrease of the current-source region. • The slope of the curve around the maximum power point varies based on the impedance value.	
Blocking Diode	short-circuit	• Open-circuit voltage increase equal to the forward voltage of the shorted blocking diode.	• Negligible inflection point at the open-circuit voltage of the healthy strings.	
	open-circuit	• Loss of the string.	• Short-circuit current reduction equal to the short-circuit current of the faulty string.	
	impedance	• Decrease of the current-source region. • Decrease of the magnitude of the slope at open-circuit voltage. The slope variation depends on the impedance value.	• Decrease of the current-source region. • The slope of the curve around the maximum power point varies based on the impedance value. • Negligible increase of the open-circuit voltage.	
Harness	line-to-line	• Open-circuit voltage reduction equal to the open-circuit voltage difference of the shorted points within the PVA.	• Inflection point at the open-circuit voltage of the faulty string.	
	ground	• Open-circuit voltage reduction equal to the open-circuit voltage of the grounded point.	• Inflection point at the open-circuit voltage of the faulty string.	
	impedance	• Decrease of the current-source region. • Decrease of the magnitude of the slope at open-circuit voltage due to the increase of the series resistance. The slope variation depends on the impedance value.	• Decrease of the current-source region. • The slope of the curve around the maximum power point varies based on the impedance value.	
	open-circuit	• Loss of the string.	• Short-circuit current reduction equal to the short-circuit current of the faulty string.	
Solar Cell	shading	• Inflection point within the voltage-source region of the string consisting of the illuminated solar cells. • Output current at high voltage values limited by the shaded solar cell.	• Inflection point within the voltage-source region of the partially shaded string consisting of the illuminated solar cells. • Output current reduction due to the limited output current of the partially shaded string.	
	open-circuit	• Open-circuit voltage reduction equal to the open-circuit voltage of one solar cell.	• Inflection point at the open-circuit voltage of the faulty string.	
	reduced active area	• Inflection point within the voltage-source region of the string consisting of the healthy solar cells. • Output current at high voltage values limited by the faulty solar cell.	• Inflection point within the voltage-source region of the faulty string consisting of the healthy solar cells. • Output current reduction due to the limited output current of the faulty string.	

Table 8.1: Failure modes effects.

In addition to the evaluation of the PVA performance over its entire operating range, the software allows performing dynamic analyses by interfacing the PV array with a modeled Solar Array Regulator (SAR) connected

to a load. According to the Company's needs, two types of SAR are supported by the software, namely the Sequential Switching Shunt Regulator (S3R) and the Maximum Power Point Tracker (MPPT). The former implements a direct energy transfer method with a fully-regulated bus, in which the bus voltage is regulated through switching devices driven by the Main Error Amplifier (MEA). The S3R is particularly suitable for GEO mission. The MPPT, instead, includes a DC/DC converter that decouples the PVA from the bus. The duty cycle is defined by a controller whose software is able to constantly track the maximum power point of the solar array. This makes the implementation of the MPPT convenient for LEO mission, where large variations of temperature and irradiance are experienced. The modeling software developed for this research also includes the possibility of considering time-dependent operating conditions (temperature and irradiance). The dynamic analysis allows studying the response of the aforementioned solar array regulators to different failures and the results are summarized in Table 8.2.

Topology	Load	Effects
S3R	Resistive	<ul style="list-style-type: none"> • $I_{load} _{V_{bus}} < I_{PVA, faulty} _{V_{bus}}$: even though the operating mode of the sections may change, the solar array regulator is still able to perform its function and to maintain a constant bus voltage • $I_{load} _{V_{bus}} > I_{PVA, faulty} _{V_{bus}}$: all the sections are in feeding mode and the solar array regulator is not able to keep the bus voltage constant. Nevertheless, the load demand is always satisfied and the PVA is clamped to operate at the voltage level at which it delivers the required current. The S3R function is restored should the load profile change such that $I_{load} _{V_{bus}} < I_{PVA, faulty} _{V_{bus}}$.
	Current	<ul style="list-style-type: none"> • $I_{load} < I_{PVA, faulty} _{V_{bus}}$: even though the operating mode of the sections may change, the solar array regulator is still able to perform its function and to maintain a constant bus voltage. • $I_{PVA, faulty} _{V_{bus}} < I_{load} < I_{PVA, faulty} _{V=0}$: all the sections are in feeding mode and the solar array regulator is not able to keep the bus voltage constant. Nevertheless, the load demand is satisfied and the PVA is clamped to operate at the voltage level at which it delivers the required current. The S3R function is restored should the load profile change such that $I_{load} < I_{PVA, faulty} _{V_{bus}}$. • $I_{load} > I_{PVA, faulty} _{V=0}$: even though all the sections are in feeding mode, the load demand is not satisfied and the load drains current from the bus capacitor, decreasing the bus voltage that eventually reaches 0V. At this point the PVA operates in short-circuit conditions and does not deliver any power.
	Power	<ul style="list-style-type: none"> • $I_{load} _{V_{bus}} < I_{PVA, faulty} _{V_{bus}}$: even though the operating mode of the sections may change, the solar array regulator is still able to perform its function and maintain a constant bus voltage. • $\exists V I_{load} _V = I_{PVA, faulty} _V$: all the sections are in feeding mode and the solar array regulator is not able to keep the bus voltage constant. Nevertheless, the load demand is satisfied and the PVA is clamped to operate at the voltage level at which it delivers the required current. The S3R function is restored should the load profile change such that $I_{load} _{V_{bus}} < I_{PVA, faulty} _{V_{bus}}$. • $\exists V I_{load} _V = I_{PVA, faulty} _V$: even though all the sections are in feeding mode, the load demand is not satisfied and the load drains current from the bus capacitor, decreasing the bus voltage that eventually reaches 0V. At this point the PVA operates in short-circuit conditions and does not deliver any power.
MPPT (boost converter)	Resistive	<ul style="list-style-type: none"> • If the operating point defined by the load is not within the operational range of the converter, the MPPT cannot track the maximum power point and the PVA is clamped to operate at the operating point imposed by the load. • If the operating point defined by the load is within the operational range of the converter and belongs to the IV curve region of the faulty PVA that includes the global maximum, the maximum power point is properly tracked and the solar array operates at MPP. • If the operating point defined by the load is within the operational range of the converter and belongs to the IV curve region of the faulty PVA that includes a local maximum, the maximum power point is not properly tracked and the solar array operates at the local maximum power point.
	Current	<ul style="list-style-type: none"> • $I_{load} < I_{mp, PVA, faulty}$: the maximum power point is properly tracked and the solar array operates at MPP. • $I_{mp, PVA, faulty} < I_{load} < I_{PVA, faulty} _{V=0}$: the maximum power point does not lie within the operational range of the boost converter and the PVA is clamped to work at the voltage value such that $I_{PVA, faulty} = I_{load}$. • $I_{load} > I_{PVA, faulty} _{V=0}$: the PVA cannot satisfy the load demand and it is reverse biased, dissipating power.
	Power	Simulation not possible due to software limitation.

Table 8.2: Solar array regulators response to failures.

To estimate the reliability of the system, the software implements the mathematical model associated with the reliability block diagram derived from the user-defined solar array configuration. Three functions have been identified such that their fulfillment leads to an acceptable functionality of the solar array, namely the *power generation*, the *power transfer*, and the *bleeding function*. The failure rates of the components are calculated according to the models provided in *MIL-HDBK-217F Notice 2*. As one of the objectives of the research is to investigate strategies to improve the system reliability, the software has been featured with the capability of performing a sensitivity analysis involving different factors of interest from a reliability perspective. Table 8.3 collects those that have been found to have the most significant impact.

Feature	Delta	Reliability benchmark	- [p.p.]	+ [p.p.]	Reliability (-)	Reliability (+)	Feasibility
Max. acceptable string failures	+/- 1	0.980661933	-	0.563109382	-	0.986293027	1
Max. acceptable solar cells in short	+/- 1	0.980661933	-	0.433823463	-	0.985000168	2
# Bypass Diodes (series-connected)	+/- 1	0.980661933	-	0.19261326	-	0.982588066	1
Bleeding Function Redundancy	+/- 1	0.980661933	-	0.15148803	-	0.982176813	4
# Blocking Diodes (parallel-connected)	+/- 1	0.980661933	-	0.12510101	-	0.981912943	4
Blocking Diode reverse voltage [V]	+/- 30V	0.980661933	-0.335632164	0.062677799	0.977305611	0.981288711	5
Junction Temperature [°C]	+/- 10°C	0.980661933	0.023586597	-0.02787832	0.980897799	0.98038315	3
# Solar Cells / string	+/- 1	0.980661933	0.062388064	-0.062348399	0.981285814	0.980038449	2
# Total Strings	+/- 1	0.980661933	0.070388673	-0.070338186	0.98136582	0.979958551	1
# Blocking Diodes (series-connected)	+/- 1	0.980661933	-	-0.124961525	-	0.979412318	4
Grounding Points	+/- 1	0.980661933	-	-0.15148803	-	0.979147053	4
Connector ambient temperature [°C]	+/- 10°C	0.980661933	0.155231336	-0.157452965	0.982214246	0.979087403	3
# Bypass Diodes (parallel-connected)	+/- 1	0.980661933	-	-0.192242417	-	0.978739509	1

Table 8.3: Most relevant factors for the reliability of the sample satellite.

The outcome of the analysis identifies, for the defined PVA configuration, the factors that have the highest influence on the reliability, providing, based on their feasibility, recommendations on potential modifications

for reliability improvement.

The reliability prediction, as well as the results obtained from the sensitivity analysis, are strictly dependent on the PVA configuration and they cannot be generalized to make a characterization of satellite solar arrays. For this purpose, a machine-learning model has been developed and trained over 40000 samples. The dimension of the dataset is 47, equal to the number of features considered that may affect the reliability, which is the target variable. The dataset has been used to perform a feature importance analysis with the goal of retrieving insights about the effects on the reliability of features applicable to a general PVA. The results from three different methods are shown in Table 8.4.

Feature	Permutation		Method Column Drop		SHAP	
	Relative Feature Importance	Rank	Relative Feature Importance	Rank	Relative Feature Importance	Rank
Max. acceptable string failures	1	1	1	1	1	1
Junction Temperature [°C]	0.762397	2	0.714639	2	0.428571429	6
# Blocking Diodes (parallel-connected)	0.648628	3	0.700544	3	0.357142857	7
# Total Strings	0.594735	4	0.352248	6	0.595238095	3
Connector ambient temperature [°C]	0.349022	5	0.436394	4	0.952380952	2
# Blocking Diodes (series-connected)	0.332835	6	0.387029	5	0.238095238	8
Percentage blocking diode in short	0.243971	7	0.196369	8	0.119047619	12
# Solar Cells / string	0.21974	8	0.073826	11	0.452380952	5
Max. acceptable solar cell in short	0.208247	9	0.218998	7	0.452380952	5
String lost if blocking diode in short	0.169348	10	0.152613	9	0.166666667	10
# Sections	0.159574	11	0.051743	13	0.547619048	4
Blocking Diode reverse voltage [V]	0.143996	12	0.059853	12	0.214285714	9
# Bypass Diodes (series-connected)	0.079613	13	0.087017	10	0.142857143	11
# Bypass Diodes (parallel-connected)	0.044174	14	0.051351	14	0.119047619	12
Percentage bypass diode in short	0.031352	15	0.039004	15	0.047619048	14
Cell in short if bypass diode in open	0.022865	16	0.024947	16	0.071428571	13
Bleeding Function Redundancy	0.019309	17	0.016516	18	0.142857143	11

Table 8.4: Feature Importance Analysis Results.

The outcome from the permutation and the column drop methods show a satisfactory degree of agreement. However, the same cannot be said for the SHAP method, whose features rank and relative importance values differ significantly from the other techniques. As a consequence, the analysis has to be considered inconclusive with respect to the objective of retrieving a feature importance ranking. On the other hand, an important result is given by the fact that all the implemented methods agree on the first 17 most relevant features. This suggests that the other 30 factors may be disregarded when dealing with reliability improvement.

In addition to the feature importance, individual conditional expectation plots and their respective partial dependence plots (pdp) have been generated from the dataset to assess the dependence of the reliability on the considered factors. However, these graphs do not provide a clear visualization of the impact that a single feature has depending on different combinations of the others. Therefore, 2D partial dependence plots have been drawn to highlight this aspect.

Lastly, the software exploits the mathematical model built for the reliability analysis to estimate the probability of occurrence of different failures modes concerning diodes, solar cells, harness, and components involved in the power transfer function. The predicted probabilities are classified by the software according to the criteria in ECSS-Q-ST-30-02C and a probability number has been assigned to them. By combining the results from the probability classification and those from the severity classification derived from the FMEA, it has been possible to perform a criticality assessment of the failure for the selected PVA configuration. This allows highlighting weaknesses in the system and acting accordingly with the implementation of mitigation measures.

8.1. Limitations

As far as the electrical model is concerned, the software has been implemented in such a way to maximize its flexibility. The size of the solar array, in terms of number of involved components, is exclusively limited by the memory capability of MATLAB. Even though the verification process, both at unit and system level, has been successfully completed, some additional tests may be performed to verify the correct implementation of the influence of the environmental conditions as no experimental data were available.

Regarding the solar array regulators, the type of converter chosen for the MPPT constraints the operating range of the system, which has to be taken into account when defining the load. Indeed, as the software is

not able to recognize unstable operating points unless disturbances are introduced into the system, a power load cannot be connected to a MPPT architecture. This is due to the fact that its load line would cross the PVA IV curve in the current-source region, outside the operating range of the boost converter. Furthermore, the implemented algorithm for tracking the maximum power point is not fault-tolerant to the presence of multiple local maxima. This might deny the supply of maximum power from the PVA, clamped to an operating point away from the MPP.

Moreover, it has to be stressed that the electrical model built by the software is not representative of a complete electrical power system. The power storage, i.e. the secondary batteries, and the respective regulators, whose function is fundamental for the correct operation of the EPS, are not included in the model. This has a significant impact on the system behavior, especially when the load demand increases above the PVA capability, and has to be taken into account when investigating the results obtained from the simulations.

For what concerns the system reliability, it is of primary importance to understand the weight of the failure rates associated with the solar cells and the bypass diodes. The value of the former is taken from [3], issued in 1990, and it is commonly used and accepted for the reliability analysis of space solar arrays. Nevertheless, no reference to the failure rate of solar cells is included in any updated standards or handbook due to the cost of a test campaign on these components. Therefore, the value provided in [3] may be outdated and not representative of the modern solar cells, and it can be arguably considered an assumption. As the solar arrays are massively constituted of the aforementioned components, their failure rate highly influences the reliability prediction. A similar consideration applies for the bypass diodes, which historically were manufactured with the same technology as the solar cells, and the same manufacturing processes are supposedly followed nowadays. For this reason, solar cells and bypass diodes share the same failure rate in the reliability analysis involving solar arrays. The space community accepts this assumption, even though it affects significantly the estimation of the reliability. Despite the above discussion, it is here pointed out that the graphical user interface of the software allows the user to customize the aforementioned failure rates.

Another important aspect is the influence of the user-defined assumptions: failure modes distribution, consequences of different failures of the diodes, mitigation capability of bypass diodes. Their impact on the reliability prediction cannot be disregarded and the assumptions shall be clearly justified. Moreover, it is important to highlight that the sensitivity analysis is limited by the features considered. For instance, even though the number of connection points is included in the study, the associated factors used for the calculation of their failure rate are kept constant and equal to the value defined by the user. As a consequence, the validity of the outcome of the sensitivity and ML analysis regarding the connection points is constrained to those characterized by a similar failure rate.

Other limitations exist concerning the machine learning-based analyses. The main purpose of the latter was to extend the results obtained from the sensitivity analysis, which are strictly applicable to the modeled PVA configuration, to a broader group of solar arrays. Nevertheless, the outcome is in turn constrained to those systems that may be characterized by the ranges of parameters used to retrieve the dataset. Furthermore, the outcome of the analysis has been revealed as inconclusive with respect to the objective of retrieving an importance ranking of the different factors affecting the reliability. Then, as far as the partial dependence plots are concerned, they are limited to the analysis of two different features, denying the possibility of investigating the dependence of the reliability on more complex combinations of features.

8.2. Future Work

The research provides an exhaustive analysis of the failure modes of space solar arrays, accompanied by an investigation of the solar array regulators' response to the simulated failures. The effects of the failure modes on the three main operating points of the PVA (short-circuit, open-circuit, maximum power) are clearly explained at both string and system level, while the SAR reactions are categorized based on the type of load connected. The software provides a robust modeling approach of both PVA and SAR, from which updates may be implemented to extend its capability to achieve a complete EPS model. To date, the software supports the implementation of the S3R and a MPPT feeding an unregulated bus. Possible patches may include the possibility of choosing the desired energy transfer method and bus regulation by integrating additional solar array regulators and introducing the power storage system and the respective regulators. Moreover, as far as the MPPT is concerned, its applicability may be extended by modeling other types of converters, whose controller may be implemented by a more effective and fault-tolerant MPPT algorithm. A transition from the open-loop controller to a closed-loop controller is also possible. Another interesting update may broaden the

scope of both the FMEA and the reliability analysis from the PVA to the other modeled subsystems, allowing for a more detailed study of the EPS.

Bibliography

- [1] Umbra & penumbra. <https://en.wikipedia.org/wiki/File:Umbra01.gif>. Accessed: 2022-01-13.
- [2] Reliability modeling and prediction. Military standard MIL-STD-756B, Department of Defense, Washington, DC, 1981.
- [3] Failure rates for esa space systems. Handbook PSS-01-302, European Space Agency, Noordwijk, NL, 1990.
- [4] Reliability prediction of electronic equipment. Military Handbook ML-HDBK-217F, Department of Defense, Washington DC, 1991.
- [5] Semiconductor devices. Military Specification MIL-S-19500J, Department of Defense, Washington DC, 1994.
- [6] Reliability prediction of electronic equipment. Military Handbook ML-HDBK-217F Notice 2, Department of Defense, Washington DC, 1995.
- [7] Semiconductor device, diode, silicon, ultrafast recovery, power rectifier, types 1n5802, 1n5804, 1n5806, 1n5807, 1n5809, and 1n5811, jan, jantx, jantxv, jans, janhc, and jankc. Military Performance Specification MIL-PRF-19500/477, Military and Government Specs & Standards (Naval Publications and Form Center), Washington DC, 2019.
- [8] Resistor, fixed, film, nonestablished reliability, established reliability, and space level, style rn*90 1/. Military Performance Specification MIL-PRF-55182/9, Military and Government Specs & Standards (Naval Publications and Form Center), Washington DC, 2020.
- [9] Ji-Eun Byun, Hee-Min Noh, and Junho Song. Reliability growth analysis of k-out-of-n systems using matrix-based system reliability method. *Reliability Engineering & System Safety*, 165:410–421, 2017.
- [10] DSH Chan, JR Phillips, and JCH Phang. A comparative study of extraction methods for solar cell model parameters. *Solid-State Electronics*, 29(3):329–337, 1986.
- [11] Qi Chen, Zhigang Liu, Xiaofeng Zhang, and Liying Zhu. *Spacecraft Power System Technologies*. Springer, 2020.
- [12] Christophe Delepaut. S3r stability margins and design guidelines. In *8th European Space Power Conference*, volume 661, page 48, 2008.
- [13] Omnia S Elazab, Hany M Hasaniien, Ibrahim Alsaidan, Almoataz Y Abdelaziz, and SM Muyeen. Parameter estimation of three diode photovoltaic model using grasshopper optimization algorithm. *Energies*, 13(2):497, 2020.
- [14] Nicola Femia, Giovanni Petrone, Giovanni Spagnuolo, and Massimo Vitelli. *Power electronics and control techniques for maximum energy harvesting in photovoltaic systems*. CRC press, 2017.
- [15] FIDES Group et al. Fides guide 2009 edition a-reliability methodology for electronic systems. *AIRBUS France, Eurocopter, Nexter Electronics, MBDA missile systems, Thales Systèmes Aéroportés SA, Thales Avionics, Thales Corporate Services SAS, Thales Underwater Systems*, 2014.
- [16] Zhu Hong-yu, Zhang Bo-wen, and Zhang Dong-lai. Overview of architectures for satellite's regulated bus power system. In *2020 IEEE 1st China International Youth Conference on Electrical Engineering (CIYCEE)*, pages 1–8. IEEE, 2020.
- [17] J.F. Bürkle. Eps – solar array configuration analysis. Technical Note DNX-TUD-TN-0863 Issue 1, Delft University of Technology, Delft, NL, 2011.

- [18] Manish Kumar and Arun Kumar. An efficient parameters extraction technique of photovoltaic models for performance assessment. *Solar Energy*, 158:192–206, 2017.
- [19] Wiley J Larson and James Richard Wertz. Space mission analysis and design. Technical report, Torrance, CA (United States); Microcosm, Inc., 1992.
- [20] Wilfried Ley, Klaus Wittmann, and Willi Hallmann. *Handbook of space technology*, volume 22. John Wiley & Sons, 2009.
- [21] Chenxi Li, Yongheng Yang, Sergiu Spataru, Kanjian Zhang, and Haikun Wei. A robust parametrization method of photovoltaic modules for enhancing one-diode model accuracy under varying operating conditions. *Renewable Energy*, 168:764–778, 2021.
- [22] Fang Li, Xiaojie You, and Yan Li. Control loop design of sequential switching shunt regulator considering the influence of double section functioning. *IET Power Electronics*, 7(4):998–1007, 2013.
- [23] Shuhui Li and Bao Ke. Study of battery modeling using mathematical and circuit oriented approaches. In *2011 IEEE Power and Energy Society General Meeting*, pages 1–8, 2011. doi: 10.1109/PES.2011.6039230.
- [24] Zhisong Lin, Wei Xie, Mengxue Dong, and Jianyu Lan. Research of s3mpr engineering application on space power sources. In *2020 IEEE 4th Information Technology, Networking, Electronic and Automation Control Conference (ITNEC)*, volume 1, pages 817–823. IEEE, 2020.
- [25] Carlos R Ortiz Longo. *Method for the calculation of spacecraft umbra and penumbra shadow terminator points*, volume 3547. National Aeronautics and Space Administration, 1995.
- [26] Adel Mellit, Giuseppe Marco Tina, and Soteris A Kalogirou. Fault detection and diagnosis methods for photovoltaic systems: A review. *Renewable and Sustainable Energy Reviews*, 91:1–17, 2018.
- [27] Zhuo Meng, Yiman Zhao, Shiqing Tang, and Yize Sun. An efficient datasheet-based parameters extraction method for two-diode photovoltaic cell and cells model. *Renewable Energy*, 153:1174–1182, 2020.
- [28] Mukund R Patel. *Spacecraft power systems*. CRC press, 2004.
- [29] Dhanup S Pillai and N Rajasekar. A comprehensive review on protection challenges and fault diagnosis in pv systems. *Renewable and Sustainable Energy Reviews*, 91:18–40, 2018.
- [30] R. Teuling. Top level design of the electrical power subsystem. Technical Note DNX-TUD-TN-0019 Issue 2, Delft University of Technology, Delft, NL, 2011.
- [31] Requirements & Standards Division. Space product assurance: Failure modes, effects (and criticality) analysis (fmea/fmeca). Standard ECSS-Q-ST-30-02C, European Cooperation for Space Standardization, Noordwijk, NL, 2009. URL <https://ecss.nl/standard/ecss-q-st-30-02c-failure-modes-effects-and-criticality-analysis-fmeafmeca/>.
- [32] Requirements & Standards Division. Components reliability data sources and their use. Handbook ECSS-Q-HB-30-08A, European Cooperation for Space Standardization, Noordwijk, NL, 2011. URL <https://ecss.nl/hbstms/ecss-q-hb-30-08a-components-reliability-data-sources-and-their-use/>.
- [33] Requirements & Standards Division. Ecss system: Glossary of terms. Standard ECSS-S-ST-00-01C, European Cooperation for Space Standardization, Noordwijk, NL, 2012. URL <https://ecss.nl/standard/ecss-s-st-00-01c-glossary-of-terms-1-october-2012/>.
- [34] Requirements & Standards Division. Space engineering: Electrical and electronic. Standard ECSS-E-ST-20C Rev.1, European Cooperation for Space Standardization, Noordwijk, NL, 2019. URL <https://ecss.nl/standard/ecss-e-st-20c-rev-1-electrical-and-electronic-15-october-2019/>.
- [35] Nahla Mohamed Abd Alrahim Shannan, Nor Zaihar Yahaya, and Balbir Singh. Single-diode model and two-diode model of pv modules: A comparison. In *2013 IEEE International Conference on Control System, Computing and Engineering*, pages 210–214. IEEE, 2013.

-
- [36] Omid Shekoofa and Shahab Karbasian. Design criteria for electrical power subsystem's topology selection. In *2013 6th International Conference on Recent Advances in Space Technologies (RAST)*, pages 559–564. IEEE, 2013.
- [37] Marcelo Gradella Villalva, Jonas Rafael Gazoli, and Ernesto Ruppert Filho. Comprehensive approach to modeling and simulation of photovoltaic arrays. *IEEE Transactions on power electronics*, 24(5):1198–1208, 2009.
- [38] James R Wertz, David F Everett, and Jeffery J Puschell. *Space mission engineering: the new SMAD*. Microcosm Press, 2011.
- [39] Rui Zhang, Rui Tu, Pengfei Zhang, Jinhai Liu, and Xiaochun Lu. Study of satellite shadow function model considering the overlapping parts of earth shadow and moon shadow and its application to gps satellite orbit determination. *Advances in Space Research*, 63(9):2912–2929, 2019.
- [40] Hongyu Zhu and Donglai Zhang. Design considerations of sequential switching shunt regulator for high-power applications. *IEEE Transactions on Industrial Electronics*, 67(11):9358–9369, 2019.